Synthesis and Characterization of Pure and Doped SnO_2 for Gas Sensing Studies

This thesis is submitted as a partial fulfilment of the Ph.D. programme in Physics

by

PARUL GUPTA

(ID No. 2010RPH101)

Department of Physics

MALAVIYA NATIONAL INSTITUTE OF TECHNOLOGY JAIPUR

October 2017

Dedicated to My Husband and Parents

Supervisor's Certificate

This is to certify that the thesis entitled ***"Synthesis and Characterization of Pure and Doped SnO_2 for Gas Sensing Studies"*** describes the original research work carried out by **Ms. Parul Gupta (ID No. 2010RPH101)** for the award of the degree of Doctor of Philosophy (Physics) in Malaviya National Institute of Technology Jaipur (India). This work was done by her during the period July, 2010 to April, 2017 under my supervision.

(Dr. S. K. Sharma)
Professor
Department of Physics
MNIT Jaipur (India)

Acknowledgements

First of all, I would like to thank Almighty, by whose grace I could achieve this destination.

I would like to express deepest sense of gratitude and respect to my research supervisor, Prof. S. K. Sharma, Department of Physics, MNIT Jaipur, without his insightful guidance and encouragement this thesis would never have been accomplished. With his help and continuous supervision, I have been able to complete this work.

I also extend thanks to the former Heads of the Department for providing the administrative support. I would like to thank also the faculty members of the Department and DREC members Prof. K. C. Swami, Prof. A. K. Bhargava, Dr. K. Sachdev and Dr. S. Mandal, with whom I had an opportunity to discuss academics at various stages of my work.

I am grateful to Prof. N. Bhat, Chairperson, Centre for Nano Science and Engineering (CeNSE), IISc. Bangalore for allowing me to carry out the major part of my research work in his lab. The acknowledgement is due to Dr. Sanjeev Kumar Shrivastava, Co-ordinator, Indian Nanoelectronics User Program for allowing me to work under the INUP programme in IISc. Bangalore.

I highly acknowledge University of Rajasthan, Jaipur and Materials Research Centre at MNIT Jaipur for providing the facilities for characterization of specimens.

I acknowledge DST-INSPIRE program of the Department of Science and Technology, New Delhi for providing me the research fellowship (during July, 2010 to June, 2014).

I am also thankful to my seniors, colleagues and friends who made my research work quite enjoyable.

Last but not the least; I owe a special thanks to my family for their endless support. I would like to extend special thanks to my husband Mr. Sachin Dangayach for supporting me in every possible way and constant encouragement.

(Parul Gupta)

Abstract

This thesis contains the research work carried out on synthesis and characterization of pure and doped SnO_2 nanostructures for gas sensing studies.

Chapter 1 contains an introduction to gas sensors, metal oxides semiconductors, and explanation of the gas sensing mechanism of resistive metal oxide gas sensors. It also contains the objective of the thesis.

Chapter 2 presents detailed literature survey of research work in the field of both pure and doped SnO_2 based gas sensors for different gases. A brief discussion on surface modification of SnO_2 based sensor by thermal annealing and microwave sintering is also presented.

Chapter 3 contains fundamental understanding of materials characteristics, selection of synthesis techniques, dopants, thermal and microwave annealing which lead to good response and sensitivity. A detailed overview of characterization techniques used in the thesis have been appended under this section.

Chapter 4 describes the synthesis of pure and doped (Zn, Cu, Ni, Sb and Fe) SnO_2 using sol-gel method. These as-prepared samples have been characterized using different structural, morphological and optical characterization techniques. Zn-doped as-prepared nanostructured specimens were also subjected to microwave sintering to check the change in the electrical properties.

Chapter 5 contains the gas sensing behaviour studies of differently doped SnO_2 samples. The as-synthesized pure and doped SnO_2 pellets were investigated for gas exposure at operating temperature for different gases (H_2, H_2S and CH_4) for finding the sensitivity, response and recovery time towards particular gas.

Chapter 6 contains conclusions obtained from the present research work done and suggests future aspects of the research work.

Contents

List of Tables

List of Figures

List of Abbreviation

CGSF	Combustible gas sensing facility
Cu	Copper
EDS	Electron dispersive spectroscopy
Fe	Iron
FESEM	Field effect scanning electron microscopy
FWHM	Full width at half maxima
MFC	Mass flow controller
Ni	Nickel
PL	Photoluminescence
ppm	Part per million
SAED	Selective area electron diffraction
Sb	Antimony
SEM	Scanning electron microscopy
SnO_2	Tin Oxide
TEM	Transmission electron microscopy
UV-Vis	Ultra violet- visible
XRD	X-ray diffraction
Zn	Zinc

Chapter- 1

Introduction

1.1 Introduction

Human life becomes very comfortable and easy with the advancement of manufacturing technology, but with the development and rapid industrialization, the serious concerns of environment safety have been raised. Therefore, continuous monitoring of toxic as well as flammable gases is needed. This requires the development of a device which is able to transform physical or chemical phenomena into an electrical signal for further treatment using transducer systems. Thus arises the need for gas sensors for domestic, automotive and industrial application due to the implication of gases or dangerous emissions in environment. The major reason for gas sensors requirement is monitoring of environmental pollutants and controlling their emission. Based on the new regulations, the market demands a higher reliability in domestic and environmental gas sensors for the detection of combustible and toxic gases [1].

A variety of gas sensors has been developed so far. A real sensor era started in 1970's, when semiconductor combustible gas sensors, solid state electrolyte oxygen sensors and humidity sensors were developed and used [2]. It is noteworthy that air pollution has been continuously increasing due to the result of growing industrialization and increasing pollutants from vehicular exhaust. It is known that due to the lack of proper gas-leak alarms in cooking pipe lines in the modern house, it becomes a severe fire hazard. Thus air quality monitoring related problems are main issues of the current research activity. A key component in the product development, environment monitoring and process control etc. is the concentration measurement of one or the other gaseous component of the ambient. In such situations, the necessary

interface between the ambient and the backup electronic instrumentation to detect the target gas can be done by sensors [3-4].

A gas sensor is a device that detects a signal pointing to the presence of some chemical compound. In other words, sensor is a device that converts a physical phenomenon into electrical signal or interface between physical world and world of electrical devices. Many types of gas sensors used for gas monitoring are given below:

1. Metal oxide based gas sensors: They are also called as chemiresistor gas sensors. The principle of this gas sensor for the detection of gas is based on the change of the resistance of a thin or thick film due to the absorption of the gas molecules on the surface of a semiconductor. The density of charged carrier species in the film change the resistance of the film when the gas solid interaction takes place [5-6].

2. Capacitance based gas sensors: The principle of detection of a capacitance based gas sensor is based on the measurement of the dielectric constant change between the electrodes. This sensor relies on interdigitated electrode structure [7].

3. Calorimetric gas sensors: Principle of calorimetric gas sensors depend on the temperature change at reactant surface. The surface of this sensor consists of a film of a catalytically active metal. In this sensor the heat is produced by the combustion of the gas which is produced due to the burning of the combustible gases. Low electrical power is used to balance this heat. So, the power consumption determines the gas concentration [8].

4. Acoustic wave based gas sensors: These sensors are sound based sensors and are also called as acoustic wave based gas sensors. These sensors use piezoelectric material in any form (thin or bulk) as transducers at the surface. Then it is based on finding out the acoustic wave type which is generated and the resonant frequency of the device [9].

5. Optical gas sensors: For this sensor the principle is based on use of ellipsometry, spectroscopy and interferometry techniques [10]. In these sensors a required quantity such as refractive index, fluorescence etc. is determined by transducing elements.

6. Electrochemical gas sensors: Electrochemical gas sensors consist of chemical catalysts as an anode and a cathode. The oxidation process takes place due to anode and the reduction process is due to cathode. Thus the negative charge carriers move in the direction of anode and positive carriers towards the cathode leading to a flow of current. The output of this sensor is directly proportional to the concentration or partial pressure of the gaseous species [11].

Besides the above mentioned types, some other types of gas sensors are also available like potentiometric, infra-red (absorption band in IR region) etc. [12-13]. In the work reported here metal oxide based chemiresistor gas sensors are considered and discussed. These are based on the variation in resistance of the sensor on exposure to the target gas.

1.2 Metal-oxide semiconductor gas sensor

Metal oxide semiconductor sensors favour fast producing, dependable, low cost, easy to handle devices with the use of modern technologies. However, many sensing devices have not gained commercial viability due to the high demand of power, operating temperature and other characteristics of the sensors. So, the material which has required surface and bulk characteristics and large sensitivity, selectivity and stability are needed as semiconductor sensors materials [6].

Semiconductor metal oxides are the main materials for gas sensors, as they are physically and chemically stable and broadly studied for gas detection. Gas sensor performance, mainly sensitivity, depends upon the three independent parameters: the receptor function, transducer function and utility [14]. The capability of the oxide surface to interact with the target gas is known as receptor function. For receptor

function, the surface oxygen and its chemical properties are responsible. When an additive is added on the oxide surface, sensitivity changes considerably. Transducer function is related to the ability of the active surface to change the signal produced by the chemical reaction into an electrical signal. The measurement of current by the system which contains many grain boundaries and grains, on which a double-Schottky barrier model could apply, realized this function. Barrier height, pores size, doping of the material, film thickness, diffusion depth and target gas concentration are the parameters on which utility function depends [4].

1.3 Metal oxides: Principle of the gas sensing mechanism

The principle of gas sensing by metal oxide semiconductor gas sensor depends on the changes in depletion layer at the grain boundaries when it comes in contact with the reducing or the oxidizing gases [15]. As this contact happens, it changes the height of the energy barrier which controls the flow of the electrons/holes, so it leads to the variation in the resistance of the sensor [16]. This is schematically shown in Fig. 1.1.

In the sensor, the active surface layer of thick or thin film is made up of various interconnected grains of the metal oxide. Thus, the adsorption of oxygen (O_2) removes the electron from the grain surface layer converting into the oxygen ion species as O_2^-, O^- and O^{2-}, and this depends on temperature. Thus it forms the depletion layer around the grain boundary. The oxygen pressure and the surface properties of the metal oxides, determine the depletion layer depth [17].

The depletion layer acts as a potential barrier. So the grain boundaries provide the small passages for charge carrier mobility. Now when this sensor comes in contact with the test gas, the oxygen species (variety) O_2^-, O^- and O^{2-} on the surface react to test gas and form a combustion product [18]. Oxygen species are reduced by this reaction and make more free negative charge carriers i.e. electrons to the material and decrease the electrical resistance. This change in resistance due to a surface reaction is given by a response curve of the sensor [19].

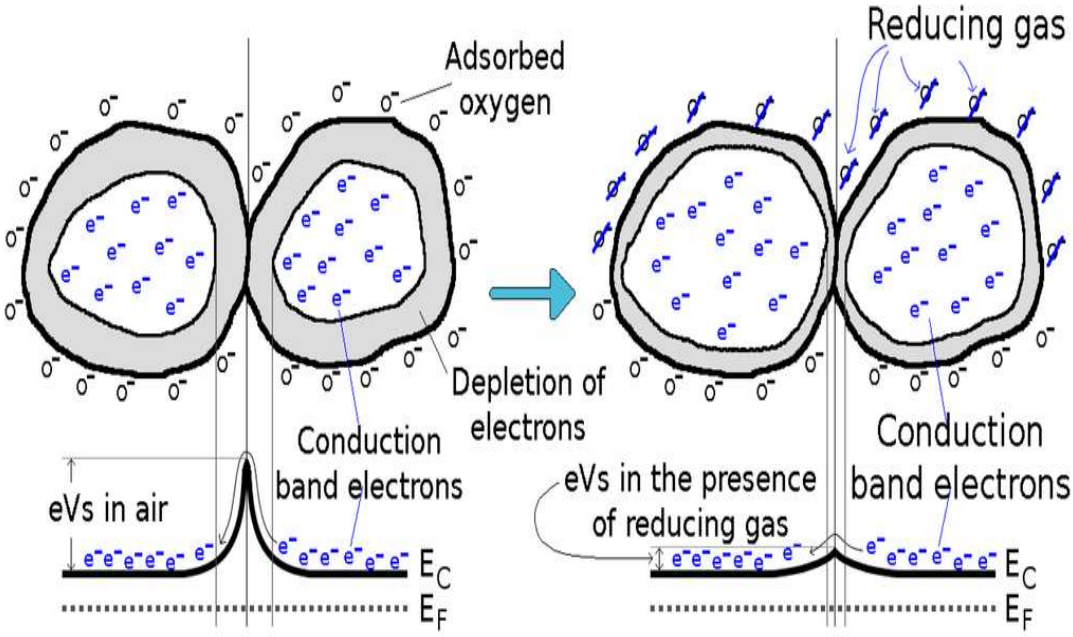

Figure 1.1: Schematic diagram of metal oxide semiconductor as gas sensor

1.3.1 Mechanism of sensitivity measurement of semiconductor sensors

The ratio of the resistance of the sample in a test gas and the resistance of the sample in the pure air determines the sensitivity of the device [20].

A better understanding of both bulk and surface properties of the sensing material is required for developing a technology for semiconductor gas sensor. Gas sensitivity is determined by the gas adsorption or desorption processes on the surface of the sensor. The basic working operation of the chemiresistive gas sensor depends on the resistance change of the sensing material when it is in contact to a target gas in environment air [21-22]. When the sensor surface adsorbs the reducing gas (CO, H_2, H_2S etc.) it acts as a surface donor, injecting the electrons into it. Similarly, when the sensor surface adsorbs the oxidizing gas (NO_2, O_2 etc.) opposite phenomena occurs. For an n-type semiconductor, when the sensor is in contact with reducing gas or vapor, the resistance of the sensor drops, whereas in the case of oxidizing gas the resistance is enhanced [23].

The other parameter that influences the sensitivity of the SnO_2 sensor is temperature. The reactivity of the semiconductor surface increases at high temperatures, so these sensors are operated at high temperatures or in other words sensor surface must be heated. Normally, resistive gas sensors operate between 300°C to 750°C temperatures, in which the oxygen vacancies are in thermodynamic equilibrium with the pressure of environmental oxygen.

Metal doping enhances the sensitivity of the sensing material towards different gases. Catalytic metals Pt, Pd etc. improve the catalytic activity of the active surface. Metal doping to metal oxide produces electronic sensitization on the space charge layer [16-17]. Metals having larger work function than electron affinity, capture electrons from the surface of the semiconductor, that increases resistance of the sensor in air. Thus doping is an important parameter in determining the sensing behaviour of a metal-oxide sensor.

1.3.2 Surface reactions change the electrical properties

Adsorption is a process in which a gas or liquid accumulates on the solid or a liquid surface (adsorbent), thus forming a molecular or atomic film. Physisorption and chemisorption are the types of adsorption. Physisorption is a type of adsorption, where the adsorbate adhere to the surface only through the van-der-Waals (weak interaction) interaction. In this process, both geometrical and electronic structure of the particle and the surface do not change, whereas chemisorption is a strong interaction between adsorbate molecules and surface. Chemisorption can take place molecularly or atomically. Chemisorption adjusts the oxidation or reducing state of adsorbate molecules. This also changes the electronic structure of the adsorbate and the surface, as a chemical bond is created [24].

In the discussion of the gas sensing mechanism ionosorption has also accompanied the physisorption and chemisorption. Chemisorption is called ionosorption when the active surface traps an electron/ hole. The ionosorbed species are always present in metal oxide surface as water molecules [25]. Chemisorption of water i.e. ionosorption produce “hydroxylated surface” where metal cation makes

bond with OH^- whereas oxide ion makes bond with H^+ ion on metal oxide surface. Oxygen is another species which is always adsorbed onto metal oxide surface.

1.3.3 Working principle of metal oxide semiconductor based gas sensors

In metal oxide semiconductor based gas sensors, i.e. chemiresistive type gas sensors, the sensing element is made up of semiconducting material with small particle size i.e. high surface to volume ratio. When the test gas interacts with the sample surface, surface reactions take place which alters the oxygen species on the surface and leads to change in resistance of the sample. That is the basic principle of detection.

The surface of metal oxide semiconductor absorbs the reactive oxygen species like O_2^-, O^- and O^{2-} at high temperature. The oxygen adsorption on the metal oxide surface process is described below:

$$O_{2\,(gas)} \leftrightarrow O_{2\,(adsorbed)} \qquad 1.1$$

$$O_{2(adsorbed)} + e^- \leftrightarrow O_2^-{}_{(adsorbed)} \qquad 1.2$$

$$O_2^-{}_{(adsorbed)} + e^- \leftrightarrow 2O^-{}_{(lattice)} \qquad 1.3$$

The sensing element captures the electron from conduction band when the adsorption of oxygen species takes place at the sensor surface. So, it decreases the charge carrier concentration (e^-) which increases the resistance of the n-type material. Thus during the chemisorption process the resistance of the sample increases and gains equilibrium. And the process through which the equilibrium is disturbed, results in the changes in resistance of the metal oxide semiconductor. This resistance change is strongly dependent on the concentration of test gas in normal air/ environmental conditions [26].

The response of the gas sensor varies according to the type of (conductivity) semiconductor metal oxide, like if n-type - then resistance decrease and if p-type

material - then resistance increases. When the n-type semiconducting material is used for the sensor, which has electrons as majority charge carriers, interacts with reducing gas, decrease in resistance occurs, but when it interacts with oxidizing gas, the charge carriers decrease and the resistance increases [5].

In contrast, when the p-type semiconducting material is used for sensor, which has positive holes as majority charge carriers, interacts with reducing gas, the resistance increases (because negative charge introduced into the material reduces the positive (hole) charge carrier concentration), but when it interacts with oxidizing gas resistance decreases (as the number of holes increases due to test gas). Response change of metal oxide semiconductor sensor for oxidizing and reducing gases are shown in Table- 1.

Table 1.1: Response changes according to the material type

Classification of material	**Oxidizing Gases**	**Reducing Gases**
n-type	Resistance increases	Resistance decreases
p-type	Resistance decreases	Resistance increases

The band bending and space charge region (electron depletion region) take place when oxygen (O_2) molecules adsorbed on the surface of metal oxides semiconductor, extract electrons from the conduction band E_c and form ions. The thickness of depletion zone is equal to the distance of the band bending.

The conductivity of the metal oxide semiconductor is affected by the band bending which occurs due to the trapping of electrons by the adsorbed molecules. The conductivity decreases when the energy band bends upward due to the oxygen species trapped the negative charges.

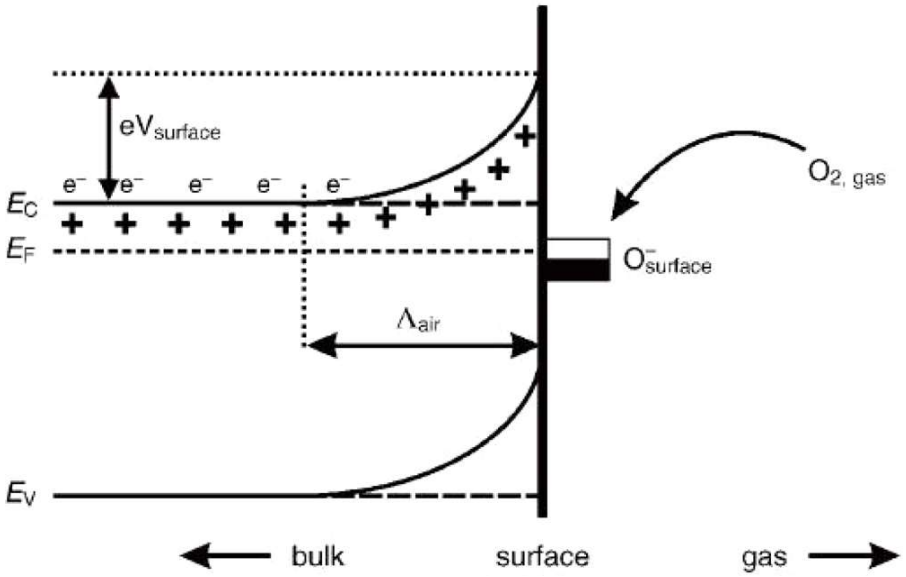

Figure 1.2: Schematic diagram of band bending after chemisorption of charged species

An increase in the conductivity results from reverse in band bending, that occurs due to the decrease in oxygen species after reaction with reducing gases or in the case of substitution of adsorbed oxygen, competitive adsorption occurs. The conductivity decreases when test gas is oxidizing [19, 27].

1.3.4 Sensing mechanism in SnO_2

As the metal oxide semiconductor gas sensor operates in oxygen rich condition i.e. in an open environment so the oxygen ionosorption study is very important. But the contribution of water molecules in the electrical properties of metal oxide gas sensor is nullified as these sensors are operated at high temperatures (400K to 800K). The SnO_2 is a highly used n-type metal oxide semiconducting material for gas sensing application among all other metal oxides [28]. The adsorption of atomic oxygen reaction is given below here. As SnO_2 based gas sensors work at the temperature range between 400K to 800K, so atomic oxygen reaction takes place on the surface in both forms, molecular (O_2^-) and atomic (O^-) [25]. The reaction is given below:

$$O_{2,\,gas} = O_{2,ads} \quad 1.4$$

$$e^- + O_{2,\,ads} = O_2^-{}_{,\,ads} \quad 1.5$$

$$e^- + ½\ O_{2,\,ads} = O^-_{ads} \quad 1.6$$

As the O^- exhibit higher activation energies in comparison to O_2^-, thus, O^- has high concentrations beyond 500K and till 500K the absorbed oxygen O_2^- dominates [17]. With the change in operating temperature, the surface reaction changes the surface conductivity, as the detecting gas comes in contact with adsorbed oxygen, the resistance of the semiconductor metal oxide surface changes.

At semiconductor metal oxide surface the ionosorbed oxygen interacts with a reducing gas molecule then the following reaction takes place, during which the resistance decreases

$$CO_{gas} = CO_{ads} \quad 1.7$$

$$CO_{ads} + O_{ads}^- = CO_{2,\,gas} + e^- \quad 1.8$$

Similarly, an oxidizing gas (NO_2) takes an electron and increases the resistance of the metal oxide semiconductor. The reaction is given below

$$NO_{2,\,gas} = NO_{2,\,ads} \quad 1.9$$

$$e^- + NO_{2,\,ads} = N\ O_2^-{}_{,\,ads} \quad 1.10$$

These are the direct adsorption reactions as the gases are strongly electronegative or electropositive.

The difficulty in the precise measurement of reaction that refers to change in resistivity, have prevented the use of this kinetics equation. The sensing of CO, could take place by direct adsorption as CO^+ [29] and by hydroxyl group reaction that produces atomic hydrogen which combines with lattice oxygen and releases a free electron [30].

1.4 Sensor performance influencing factor

Several investigations have been done on the gas interaction with material surface i.e. the property of chemiresistive metal oxide gas sensors. The base material properties, surface area, the microstructure of sensing layer, additives and temperature are such factors which influence these reactions [31-32].

So many types of metal oxide semiconductor gas sensors with thick and thin film form are commercially available in the market. But they show poor sensitivity, high response and recovery time. At high temperature only, they show appreciable sensitivity. But the selectivity of the sensors is the biggest challenge.

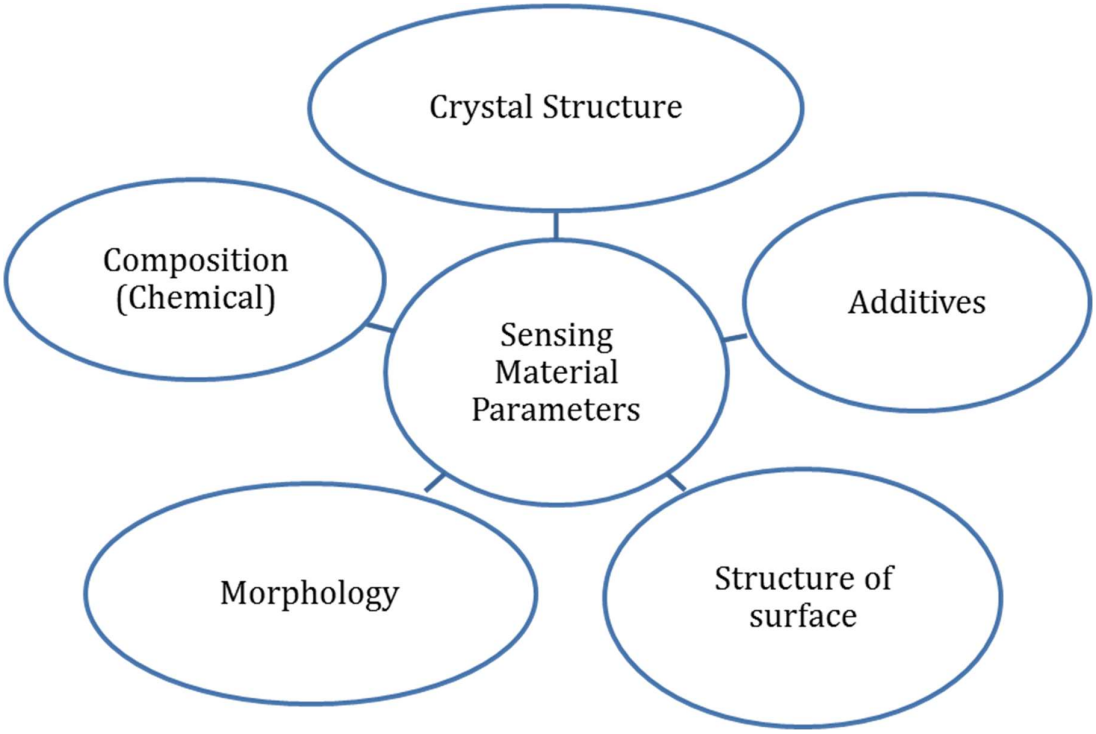

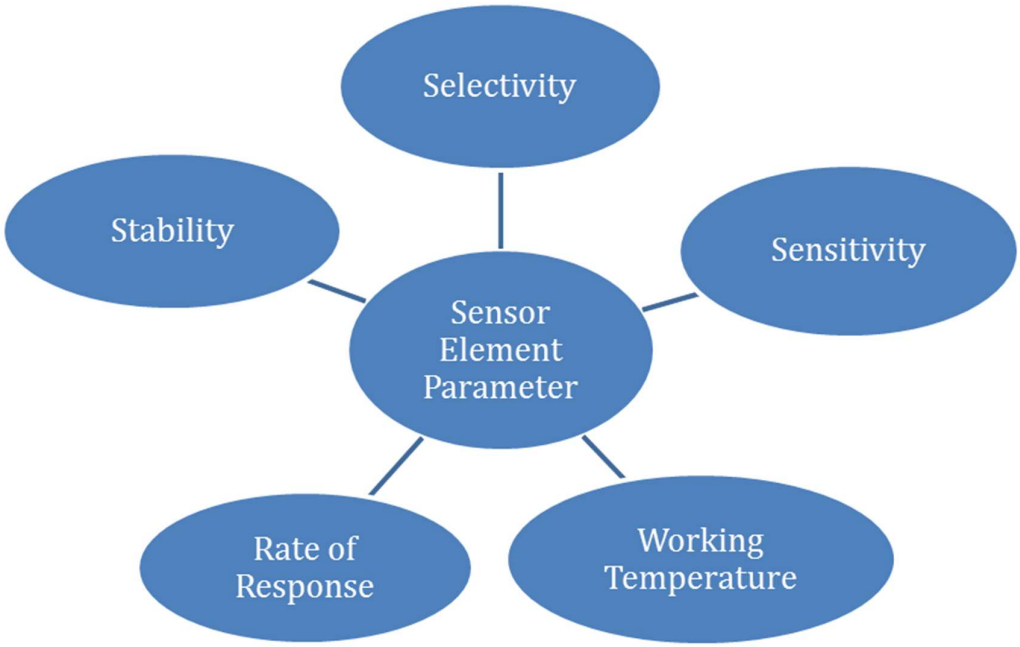

Figure 1.3: Sensing material parameters and sensor parameters

Thus the investigations need to focus on the development of metal oxide semiconductor gas sensors with improved selectivity and sensitivity. The important factors which improve the gas sensing properties of resistive gas sensors are the optimized values of grain size, morphology, grain network, porosity etc. [33].

Sensor performance is thus influenced by sensing material and the type of target gas. All parameters are interrelated, one can be improved at the cost of another parameter. Sensitivity and stability are related parameters. For higher sensor response, crystallite size should be smaller but the stability of the sensor decreased with fine crystallite size [18].

Thus, for the betterment of gas sensor performance, parameters should be altered by optimized value. These are summarized below:

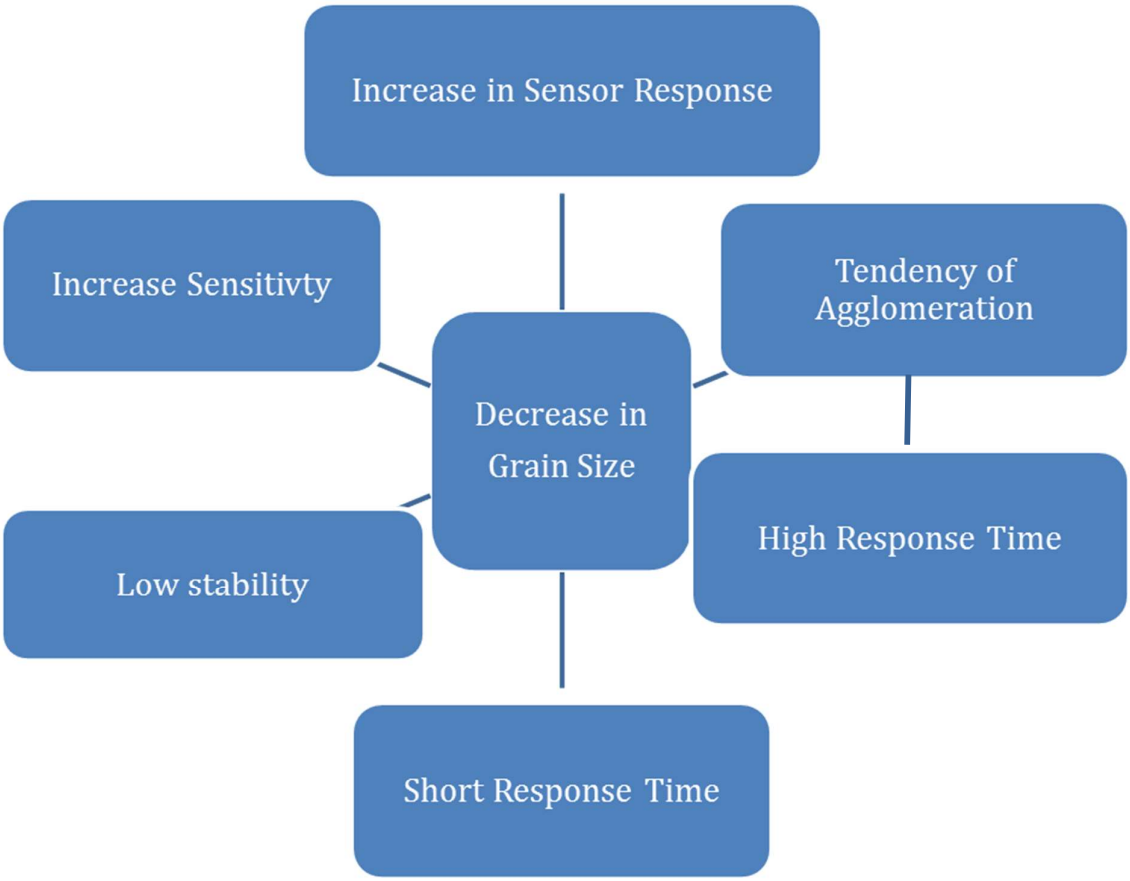

Figure 1.4: Sensor performance influenced by decrease in grain size

i. Surface reactions highly influence the gas sensing process.
ii. For each target gas, different reaction activation energy is required for different materials [34].
iii. High-dispersed catalysts are obtained by high surface areas.
iv. When the catalytic properties complement each other then composite metal oxide semiconductor gas response is better than a single component [35-36].
v. Due to spill-over effect, noble metal additive improves the sensitivity of pure metal oxides.
vi. High surface to volume ratio provides large surface area for surface and gas reaction.
vii. Sensitivity can be improved by small grain size.

viii. Operating temperature

- Response and recovery time of the sensor depend on operating temperature exponentially as the adsorption and desorption processes are temperatures activated [37-38].
- At different operating temperature different reactions take place as the chemical decomposition, co-adsorption and other reactions are temperature dependent.
- Debye length, work function and charge carrier concentration all physical properties of the metal oxide semiconductor depend on temperature.
- In some cases, at higher temperatures the sensor sensitivity decreases, this may be due to the fact that at higher temperature Debye length decreases and charge carrier concentration increases.

1.5 Role of gas sensors based on nanomaterials

Nanomaterials have unique electrical, optical and thermal properties due to their shape and size. Shape and size of nanomaterials can be controlled by many techniques, which control the material structure. Since last several years, the researchers have been working in the field of nanostructured gas sensitive materials.

The sensor performance can be increased by the reduction in crystallite size and the same has been shown by some researchers e.g. [39]. Small size crystallites with high surface to volume ratio are known to enhance the sensitivity. Various reports suggest that nanomaterials based gas sensors have a very small response and recovery time i.e. in milliseconds [40].

Nanostructured metal oxide sensors have various advantages over the normal thick and thin film sensors like:

i. High surface to volume ratio: The surface area for the reaction between the gas and the sensing material is high so it increases the sensitivity and favors the gas adsorption on the sensor surface.

ii. Large-scale production due to relatively simple preparation methods.

iii. Large stability due to high crystallinity.

iv. Large surface adsorption and catalytic activity.

1.6 Objective of the present study

The main focus of this study is on the synthesis, characterization of pure and doped SnO_2 as gas sensing material and gas sensing studies on this material. The synthesis using the sol-gel method and characterization of SnO_2 based nanostructures forms one aspect of the study, and the other aspect is gas sensing studies on this material for the combustible gases such as H_2, CH_4, H_2S. Doping, microwave sintering and thermal annealing methods have been used for structural modification of the nanostructured samples. The main objectives of the study are summarized in following points:

- To synthesize and characterize the pure and doped (doped with Zn, Cu, Ni, Fe and Sb) SnO_2 powder and to study their gas sensing behaviour for combustible gases such as H_2, CH_4, H_2S,

- To investigate the effects of doping and surface modification with annealing on gas sensing behaviour of SnO_2 based gas sensor for reducing gases (H_2, CH_4, H_2S),

- To investigate the effects of microwave sintering on gas sensing performance on some specimens of SnO_2.

The above objectives lead to some new findings in this thesis work and thus provide the additional knowledge regarding the gas sensing behaviour for particular test gas combination for a particular dopant and surface modification method. These are discussed in detail in subsequent chapters.

Chapter- 2

Literature Review

2.1 Introduction

The metal oxide semiconductor gas sensors have an extensive research interest from past several decades owing to the unique properties like high sensitivity and low response time for various gases. In some early reports, Seiyama et al. [41] suggested the use of metal oxide gas sensors to detect combustible gases. The sensors using n-type conduction like SnO_2 diagnose gases due to the change in the electrical resistance of an active surface. Gas sensors based on SnO_2, have been superior among others due to high sensitivity, quick response, resistance to corrosion, simple design, low weight and low cost etc. The gas sensing characteristics of SnO_2 based materials rely on its chemical and physical properties, which are highly controlled by the preparation conditions, dopant and grain size. These sensors are best suited for diagnosing the harmful gases at low concentration levels due to their sensitivity, stability and robustness [2]. A summarized literature survey is given here on SnO_2 based gas sensor study, which has been the focus of work reported in this thesis.

2.2 International status

SnO_2 gas sensing material has been extensively explored in the early sixties. Doped and un-doped SnO_2 films and ceramics have been grown by using several techniques, including sol-gel [42-43], screen printing [44], thermal evaporation [45], spray pyrolysis [46-47], sputtering [48], chemical vapour deposition(CVD) [49-50], ion beam sputtering [51] and hydrolysis [52] etc. The advancement in the fulfilment of these gas sensors with a reduction in particle size of SnO_2 has added power to the

investigation in this field. In addition to this, modern development in the synthesis, characterization and analysis of the physical characteristics of nanoformed SnO_2 gave the chance to enhanced the gas sensing response of nanostructured SnO_2.

Nanostructured SnO_2 were tried for several gases and gas compositions like CO, H_2S, H_2, NO, NO_2, NH_3, Cl_2, LPG, fire alarm [50-51, 53-57] and various organic compounds such as ethanol, acetone etc. [52, 58-60] by the control of crystallite size and the catalyst doping [39, 61].

The gas sensor response is related to porosity, crystal structure, surface to volume ratio and grain size [24, 40, 59, 62-67]. Therefore, the aim has been on the investigations of gas sensing properties and the variation owing to nanostructures; various kinds of one-dimensional nanomaterials were prepared as nanowires, nanotubes, nanospheres, nanorods and nanobelts [24, 68], multiwalled carbon nanotubes [69-73]. These materials confirmed the favourable sensing ascribed to the high density of surface sites, large surface area and nanoscale size [74]. S. Shukla et al. [66] proposed that the gas response of nanocrystalline SnO_2 thin film is enhanced with the decrease in the thickness of film. It suggests that the nanostructured metal oxides have become the important materials for the development of semiconducting gas sensors due to improved gas sensing properties.

The main issue in the development of SnO_2 gas sensor is to control the active layer properties to meet the necessary conditions of gas sensors like prominent sensitivity, high selectivity, small response time and recovery time, low operating temperature, low power consumption and drift of parameters [4]. The gas sensor properties can be modified, controlled and improved by doping. By adding different dopants and catalyst, some gas sensor cells are found to have the better response to a particular gas while a common response to other gases and thus these cross sensitivities need to be analyzed [66]. In this regard SnO_2 has been tested with various dopants like Pd [75], W [76], Fe [62], CuO [77-78], Ni, Mo, Sb [79] etc. SnO_2 based resistive sensors have been prepared for variety of applications in the area of combustible gases by variation in the choice of additives and operation conditions [80]. Ni, Mo, Sb promoters improve the recovery time of sensor and Ni plays an important additive role in the improvement of the gas response time of the sensors [79]. Catalytic metals Pt, Pd increases the surface reactions with gases which leads to

chemical hypersensitivity [4]. So, studies on a large-scale have been done for the improvement in sensing behaviour by doping of metals and metal oxides, grain size refinement, control of pores, catalysts adding and surface modification or defects [64-65].

In recent years, microwave sintering has made great progress in various fields including organic reactions and catalysis [81]. Microwave sintering is an effective and rapid method with low cost, for the preparation of nanocrystalline SnO_2 powders due to its homogeneous and fast-heating characteristics. It uses 2.45 GHz wavelength of microwave energy. Microwave sintering produces pure and doped precursors in very less time. Fast firing by microwaves can lead to improvement in densification and small particle size. Further stabilization methods have also been suggested which are depend on conventional thermal annealing and combined thermal/ microwave annealing [82]. Microwave sintering of Sb-doped SnO_2 leads to the synthesis of fine uniform microstructures and high densification which have enhanced electrical properties [83].

2.3 National status

There are many groups working in the field of SnO_2 gas sensors for hazardous gases in the country. SnO_2 nanopowder, thick and thin films can be synthesized by various synthesis methods [84-89]. There are many reports on SnO_2 based gas sensors from IIT Delhi group which primarily has the focus of research on the synthesis of pure nano-crystalline SnO_2 based pure and doped thin films with different doping concentrations by using sol–gel spin coating method. They investigated the sensing characteristics and response for CO, NH_3, ethanol and NO_2 gases by using different dopants like Fe, WO_3, In and MoO_3 with different concentrations [90-93]. With higher Fe-doping the sensitivity is found to increase owing to the small particle size and irregular morphology of crystallites for NH_3 and ethanol and it also produces the fast response and recovery time. In addition to this, Fe-doping increases the stability for CO gas sensing with a minimum baseline-drift [90]. They also suggested that with the addition of dopant not only the morphology of the surface changes but it also

moderate the operating temperature [91]. Indium doping in SnO_2 enhanced the response and the selectivity at lower operating temperature for NO_2 gas. Agglomeration of particles is also reduced by indium doping which lowers the stability and selectivity of synthesized films [92].

Another group from Tamilnadu (Nanotechnology Laboratory, Department of Physics, Sri Ramakrishna Mission Vidyalaya College of Arts and Science, Coimbatore, Tamilnadu) is carrying out research with IIT Delhi group and they have used the microwave assisted technique for the synthesis of tin dioxide nanoparticles with particle size of about 10 nm [94-95]. The same group has also carried out research solely which includes the reports on the sensing behaviour of thick film resistive sensors prepared by pure SnO_2. This group has also reported that the low-cost and easy microwave treatment of tin oxo-hydroxide precursor give rise to the preparation of crystalline SnO nanoplatelets. These nanoplatelets were reported to convert themselves to SnO_2 nanoparticles crystallized by the normal thermal annealing technique at comparatively low temperatures [96].

Research work on SnO_2 gas sensors is being carried out at several places which include reports from Singh et al. [97], Devi et al. [98], Ray et al. [99], Vaishampayan et al. [100], etc. The report from Singh et al. [97] is on the role of reaction temperature during synthesis of nanostructures of SnO_2 of different particle sizes and it was concluded by the authors that the sensors fabricated with small particles operate at lesser operating temperature than those with large particles. The report from Devi et al. [98] is on the synthesis of SnO_2 incorporating CuO, which was reported high sensitivity towards H_2S gas at a low operating temperature of about 100^oC. The report from Ray et al. [99] is on the deposition and characterization of multilayered un-doped and Pd-doped SnO_2 thin films prepared by sol-gel technique. These thin films were reported to be sensitive towards mild methane gas sensor at room temperature. The sensitivity of these thin film gas sensors was reported to increase with the addition of a catalyzing agent (like palladium) and formation of multiple sensing layers. A report from Vaishampayan et al. [100] reported on the synthesis of nanospherical Pd:SnO_2 which showed good response towards LPG at a lower operating temperature of 50^oC.

Table 2.1: Some references (category-wise) are given in this table.

Synthesis	**Sol-gel method**	Devi et al., Sens. Actuators B 28 (1995) 31 [98] Rella et al., Thin Solid Films 304 (1997) 339 [101] Kaur et al., Sens. Actuators B 123 (2007) 1090 [91] Zhang et al., J. Mater. Sci. 34 (1999) 3213 [102]
Characterizations	**XRD**	Bari et al., Int. J. Smart Sensing & Intelligent Systems 7(2) (2014) 610 [103] Kaur et al., Sens. Actuators B 126 (2007) 478 [92] Singh et al., Sens. Actuators B 143 (2009) 226 [97]
	SEM	Kang et al., J. Mater. Sci. 38 (2003) 4319 [104] Gnanan et al., Digest J. Nanomaterials & Biostructures 5(3) (2010) 699 [105] Chen et al., J. Nanomaterials (2014) 1 [106]
	TEM	Kaur et al., Sens. Actuators B 123 (2007) 1090 [91] Anandan et al., J. Non-oxide Glasses 2(2) (2010) 83 [107] Singh et al., Sens. Actuators B 143 (2009) 226 [97]
	UV-Vis Spectroscopy	Patil et al., Bull. Mater. Sci. 34(1) (2011) 1 [108] Tan et al., J. Nanomaterials (2011) 1 [109] Mondal et al., Bull. Mater. Sci. 33(4) (2010) 357 [110] Arivazhagan et al., J. Ovonic Research 6 (5) (2010) 221 [111] Anandan et al., J. Non-oxide Glasses 2(2) (2010) 83 [107]
	I-V measurements	Bari et al., Int. J. Smart Sensing & Intelligent Systems 7(2) (2014) 610 [103] Rai et al., Adv. Mater. Lett. 1 (2010) 55 [112]

Microwave treatment		Krishnakumar et al., Mater. Lett. 63 (2009) 896 [94] Krishnakumar et al., J. Sensors (2009) 1 [113] Rizzato et al., Physica Scripta T115 (2005) 291 [114] Krishnakumar et al., Mater. Lett. 62 (2008) 3437 [96] Zhu et al., Mater. Lett. 53 (2002) 12 [81]
Gas sensing measurements		Devi et al., Sens. Actuators B 28 (1995) 31 [98] Mishra et al., Bull. Mater. Sci. 25(3) (2002) 231 [115] Lee et al., Sens. Actuators B 67 (2000) 122 [67] Kaur et al., Sens. Actuators B 126 (2007) 478 [92] Choi et al., Nanotechnology 19 (2008) 095508 [68] Chen et al., J. Nanomaterials (2014) 1 [106]

Table 2.2: Effect of dopants on gas sensing

Dopants	**Results**	**References**
Cu	H_2S gas detection, high response at RT, high response to methanol, CO gas sensing	Wang et al., Ceramics Int. 42(8) (2016) 10006 [116] Bhardwaj et al., Phys Chem Chem Phys 18 (28) (2016) 18846 [117] Jin et al., Sens. Actuators B 213 (2015) 171 [118] Shukla et al., J. Mat. Sci. Engg A 4(3) (2014) 99 [119] Kumar et al., Sens. Actuators B 138 (2009) 587 [120] Johari et al., AIP Conf. Proc. 1591 (2014) 306 [121] Johari et al., J Nanosci Nanotech. 14 (2014) 5288 [122]

		Benzitouni et al., Adv. Nanoparticles 5 (2016) 140 [123] Karthik et al., Sensors 16 (2016) 1283 [124] More et al., Mater Lett. 57 (2003) 2177 [125] More et al. Mater Lett. 58 (2003) 205 [126]
Zn	Higher response, methanol sensing, NO_2 sensing, acetone detection	Singh et al., J. Molecular Structure 1115 (2016) 250 [127] Sakaguchi et al., J. Ceramic Soc. Japan 124 (6) (2016) 714 [128] Bari et al., Int. J. TechnoChem Research 1(2) (2015) 86 [129] Zhao et.al., Sci. Reports 5 (2015) 7874 [130] Singh et al., AIP Conf. Proc. 1675 (2015) 030042 [131] Kumar et.al., Indian J. App. Research 5(10) (2015) [132] Guan et al., Sens. Actuators B 191 (2014) 45 [133] Bagal et al., Mater Research Innovation 17 (2) (2013) 98 [134] Tian et al., J. Am. Ceram. Soc. 95 (1) (2012) 436 [135] Wang et al., Appl. Surf. Sci. 261 (2012) 890 [136] Sun et al., Cryst Eng Comm 14 (2012) 1701 [137] Bhat et al., Bull. Mater. 29 (3) (2006) 331 [138]
MoO_3	Higher sensitivity and selectivity	Ansari et al., Sens. Actuators B 87 (2002) 105 [139]
Au, Fe	Highly selective, high response	Vaishampayan et al., Mater Chem Phy., 109 (2008) 230 [140] Bose et al., Sens. Actuators B, 105 (2005) 346 [141] Ramgir et al., Appl. Surf. Sci., 252 (2006) 4298 [142] Rani et al., Sens. Actuators B, 122 (2007) 204 [90]

		Zhu et al., Sens. Actuators B, 178 (2013) 418 [143] Wang et al., Mater. Lett., 63 (2009) 917 [144] Galatsis et al., Sens. Actuators B, 93 (2003) 562 [62] Yin et al., J. Mater. Sci., 25 (11) (2014) 4960 [145]
WO_3, Sb, In, MoO_3	Lowering of operating temperature, good sensitivity, high stability, high response	Gupta et al., AIJRFANS 15-138 (2015) 46 [146] Verma et al., IJSRET, 1 (2) (2012) 49 [147] Kaur et al., Sens. Actuators B, 123 (2007) 1090 [91] Krishnakumar et al., J. Sensors, 980965 (2009) 7 [95] Kaur et al., Sens. Actuators B, 126 (2007) 478 [92] Kaur et al., Sens. Actuators B, 133 (2008) 650 [148] Zhang et al., Sens. Actuators B, 135 (2009) 610 [149]
Ni	Good selectivity towards higher alcohols like n-butanol, higher response	Jain et al., Sens. Actuators B, 113 (2006) 823 [150] Liu et al., Sens. Actuators B, 152 (2011)162 [151] Lin et al., Sens. Actuators B, 239 (2017) 501 [152] Chen et al., Sens. Actuators B, 166 (2012) 61 [153] Yogamalar et al., Chem Asian J., 5(11) (2010) 2379 [154] Rahman et al., Biosens. Bioelectronics, 28 (2011) 127 [155]

Chapter -3

Materials and Methods

3.1 Introduction

Knowledge of material's properties is essential to use it as a gas sensing material. The structural and chemical characteristics are predominantly derived from the important properties of sensing materials like sensitivity, stability, selectivity and operating temperature. Therefore, preparation of a unique sensing layer with better properties can be done using the knowledge of material's characteristics. Higher sensitivity, operating temperature and sometimes cross sensitivity could be improved by the preference of preparation technique, doping of elements and proper surface treatment. The techniques and methods which have been used in this study like synthesis method, basic characterization and surface modification methods are described in this chapter.

3.2 SnO_2: An embryonic metal oxide for gas sensing

Tin dioxide (SnO_2) is a metal oxide semiconductor with large band-gap of 3.6 eV at 300 K, it has an n-type conduction behaviour ascribed to large electrons and intrinsic defects. It behaves as a good insulator when it is in stoichiometric form. Non stoichiometry form i.e. oxygen deficiency generally, makes it a conductor. The formation energy values in SnO_2 for oxygen vacancies and tin interstitials are small and such defects are easily formed. This is the reason due to which it is often seen that the large conductivity values are exhibited by pure but non stoichiometric, SnO_2. The electrical characteristics of SnO_2 are strongly dependent on the stoichiometry of oxygen, amount and nature of impurities or dopants and also on its shape and size of nanostructures [20]. SnO_2 is widely studied over decades because of its wide range of

applications as gas sensors, solar cells, transistors, LCD and catalysts owing to its unique electrical, optical and electrochemical properties [156]. SnO_2 as a gas sensing material has been extensively explored in early sixties. The performance of SnO_2 based materials for gas sensing applications depends on its chemical and physical properties, which are critically rely on the preparation conditions, dopant and grain size.

3.2.1 Basic properties of SnO_2

Tin oxide (SnO_2) is an n-type oxide with wide band gap of 3.6 eV. The crystal structure of SnO_2 is tetragonal rutile type with the space group of $P4_2/mnm$. Cassiterite phase is the predominant form of naturally occurring SnO_2, with the tetragonal rutile structure. Rutile has tetragonal D_{4h}^{14} symmetry. Molar mass of SnO_2 is 150.71 g/mol. It is of white appearance and presence of iron causes yellow. The density of tin oxide is 6.95 g/cm^3. Its melting point is 1630°C and boiling point is 1800-1900°C. It is insoluble in water. The SnO_2 crystal structure is shown in Fig. 3.1.

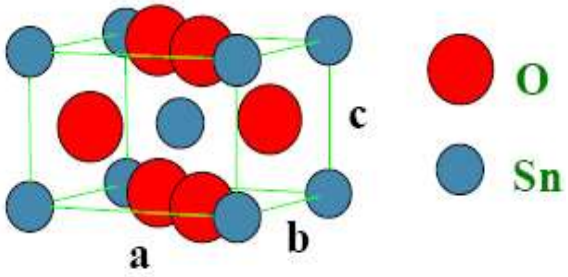

Figure 3.1: Crystal structure of SnO_2

The unit cell consists of eight tin atoms at the corners and one in the middle of the cell. Four oxygen atoms are located at cell faces, while the other two are totally inside the unit cell. Each tin atom is surrounded by an octahedron of oxygen atom in the lattice. The appearance of transparency and conductivity is the unique feature of SnO_2, among the IV group elements of the periodic table. The top of the valance band consists of O (p) states, whether the conduction band bottom has an anti-bonding character arising from the Sn (4s) and O (p) states, in the direct band structure of

SnO_2. SnO_2 conductivity is caused by a high number of lattice defects like oxygen vacancies and Sn interstitials.

SnO_2 is a non-symmorpic crystal. SnO_2 lattice constants are a=b because it has a tetragonal structure, where a = 4.737 Å and c = 3.186 Å. The ratio of c/a and internal constant define the atomic positions. The ionic radius for O_2 and Sn^{4+} are 1.40 and 0.71 Å, respectively. Metal atoms i.e. cations are located at (0, 0, 0) and (½, ½, ½) places and the oxygen atoms i.e. anions are lying at ± (u, u, 0) and ± (½+u, ½-u, ½) in the unit cell, where u is the internal parameter and its value is 0.307. In each cation two anions are present at d_1 = 2ua (2.053 Å) and four at $d_2 = \sqrt{2(½ - u)^2 + (c/2a)^2}$ a. Metal atoms are present in octahedral coordinates whereas oxygen is present in planar three coordinates in this crystalline structure. Chemical bonding in SnO_2 is usually carried out by the linear combination of O 2s and 2p orbitals with Sn 5s and 5p orbitals. SnO_2 has high chemical stability due to its chemical properties.

In SnO_2, Sn possesses a dual valency and has the oxidation state of 2+ or 4+ preferably. SnO has a low band gap i.e. 2.5 - 3 eV in comparison to SnO_2 i.e. 3.6 eV at room temperature (RT). During reduction of SnO_2, the Sn cations convert from a 4+ to a 2+ valence state and oxygen vacancies generates. So the Sn 5s states are significantly vacant for Sn (4+) which become occupied by Sn 2+ and become valence band unit [40].

3.2.2 Doped SnO_2 gas sensor

The sensing characteristics like sensitivity, response time and consistency for a specific gas for a SnO_2 based gas sensor are enhanced by acceptable additives, like Ag, Au, Zn, Pt, Pd and metal oxides. The additives generally increase the concentration of reaction or lower the activation energy, or even both. The following three models explained the effect of additives as metal oxides:

a) Catalytic effect
b) Spill-over effect
c) Fermi energy control

It is assumed in the above models that the additives whether metal or metal oxide in dispersed cluster form or bulk form, lie on the surface of the sensing oxide. Palladium and platinum are presumed to work as a bulk donor or acceptor sort of dopants in bulk doping form.

Catalytic Effect- There is no consequence on the resistance of the SnO_2 based sensor, but it shortens the response time because in this model the metal cluster available on the surface of SnO_2 ease the reaction between the target gas and the environmental oxygen.

Spill-over effect- This model accelerates the reaction, results in higher sensitivities and shorter response time, because the metallic clusters assemble the reaction and the reaction output spill over on the metal oxide support from the clusters in this effect. The catalyst on the active area are capable to trigger assured gas molecules, e.g. segregation of O_2/H_2.

Fermi energy control- Semiconductor electronic contact with the additives produces the sensor signal in this process. This creates an arrangement of the metal oxide Fermi energy with the dopant. Under atmospheric conditions, Pd and Ag, which are frequent additives, exist as PdO and Ag_2O. The higher work function reduces the conductivity of the oxidized additives. Combustible gases exposure reduces the additives to metal which forms less band bending of SnO_2 and consequently lower work function so give an increased conductivity [65].

3.2.3 Effect of temperature on SnO_2

The sensitivity of the gas sensors is highly dependent on temperature as it effects the physical characteristics of semiconductors (change of the free charge carrier concentration, Debye length etc.). The dependence of sensor on temperature is more critical because sensor operation is influenced by surface processes. Adsorption, desorption, surface coverage by molecular and ionic species, chemical decomposition, reactive sites are the temperature dependent surface phenomena. Thus the changing characteristics of the sensors like response time, recovery time etc. are also temperature dependent [65].

3.3 Sample preparation technique

The preparation technique used for synthesis of SnO_2 nanostructure powder is sol-gel method. For gas sensing studies, these as-prepared nanopowders were pelletized in pellet form using hydraulic pellet press.

3.3.1 Sol-Gel method

The sol-gel process is one of the promising deposition methods; it is a wet chemical process that facilitates formation of metal oxides, ceramics and glasses from aqueous solution. For nanomaterial formation it is wet chemical based self-assembly process. It involves the production of networks through the growth of a sol which act as precursor for the gel formation. Metallic ions and ligands, which are elements enclosed by different reactive species are the precursors used for synthesizing the colloids. Some homogenizing agents are used as mutual solvents to facilitate miscibility of these materials. Following four steps occur in sol-gel formation:

1. Hydrolysis and alcoholysis
2. Condensation of water and alcohol to produce particles
3. Development of particles
4. Particle agglomeration proceed from the production of structure through the liquid surrounding in thick gel

These steps are dependent on several initial conditions such as pH value of sol, time of reaction, temperature of reaction, nature and concentration of catalyst, reagent concentration, time of gel formation, aging temperature and molar ratio.

The structural, electrical and optical properties of the sol- gel derived inorganic network over a wide range can be changed by controlling these parameters. After gel formation, there are several ways to convert the gel into desired solid. This gel can be converted into various forms such as aerogel, xerogel, gelled spheres, nanopowder, thin film, nanostructured layers etc., depending on the deposition and drying process or conditions. Fig. 3.2 and Fig. 3.3 show the sol-gel process and its flow chart, respectively.

It is feasible to produce novel materials by this process through the preparation of organic and inorganic mixture. In the sol-gel preparation method, costly setups and

significant environmental conditions like high vacuum or neutral gas atmosphere are not required. Meanwhile, this method permits one to make sample with large doping gradient and nanocrystalline structure [87, 157]. The prime benefits of this technique are its capability to produce well-defined oxides with superior homogeneity, to selectively dope a material with high purity and need little for the reactive equipment [56]. It is one of the most widely used methods employed to obtain SnO_2 powder. The hydrated oxide is obtained from precipitation when ammonia is added to an aqueous solution of tin tetra-chloride ($SnCl_4$), it is followed by washing in water for removing the chloride contamination results in the formation of SnO_2 precipitate. The precipitate thus obtained would be used to produce the pellets of SnO_2 for gas sensing measurements.

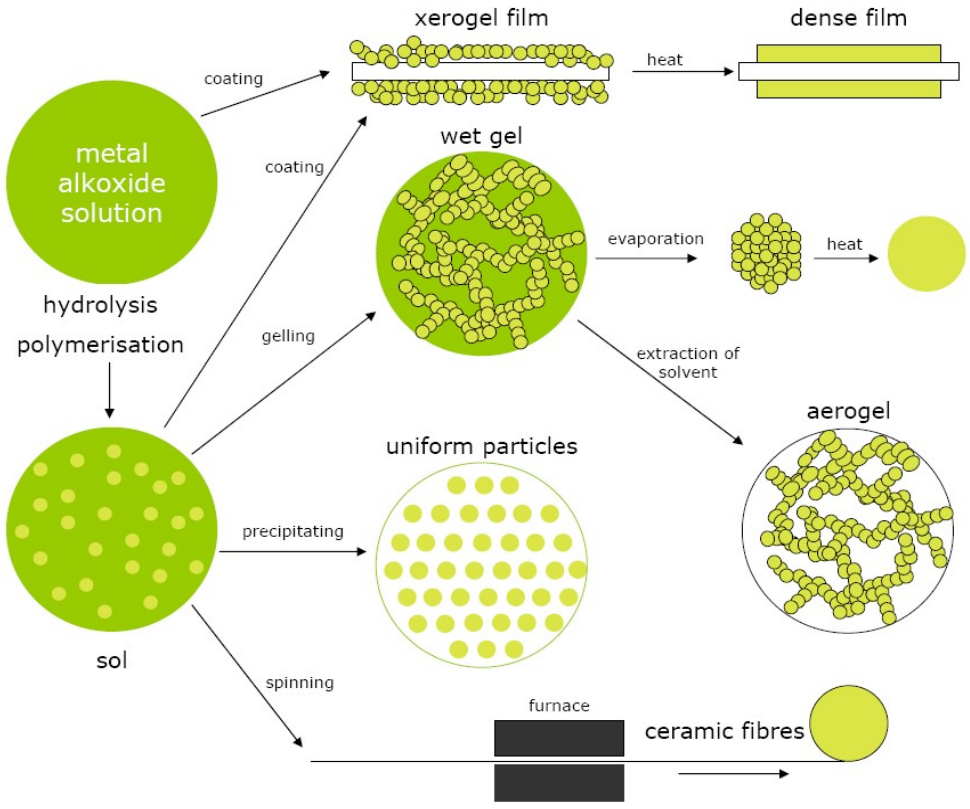

Figure 3.2: Sol-gel method

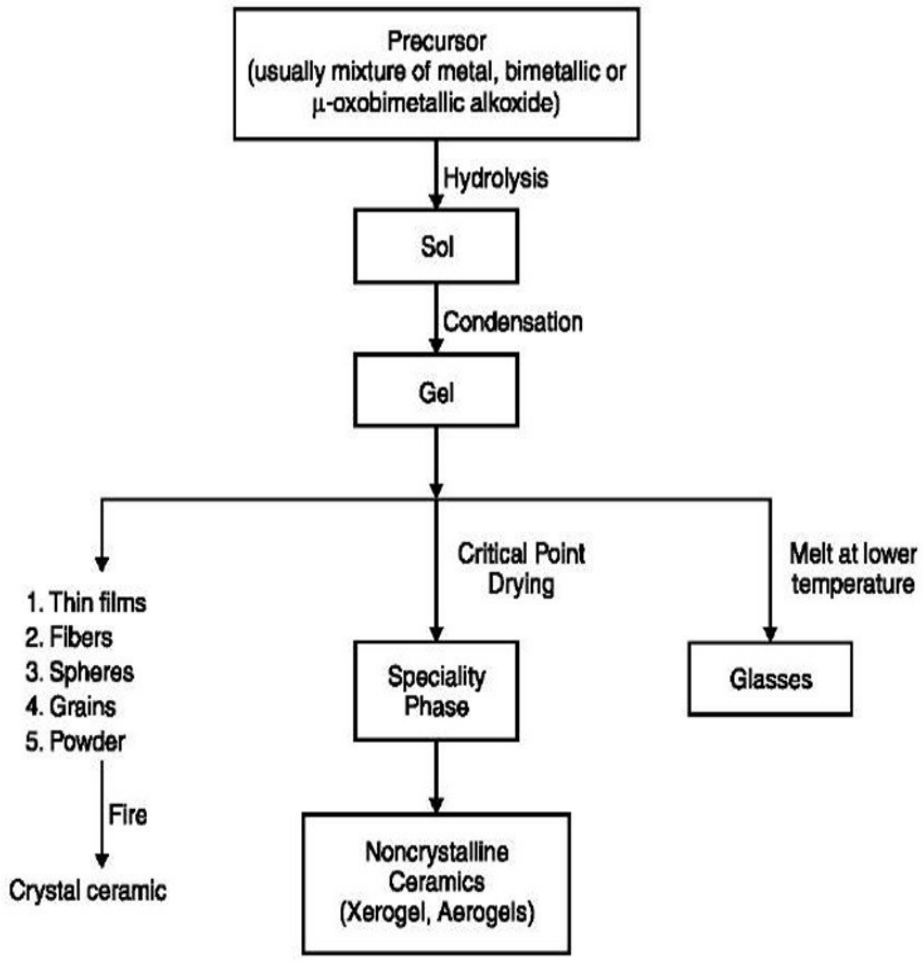

Figure 3.3: Flow chart to represent the sol-gel process

3.4 Surface modification techniques

The gas detection mechanism is based on the reaction that occurs at the sensor surface, so it is the surface condition that can be changed by using surface modification treatment. Surface modification techniques modify the crystallite size, shape, defect concentrations which result in the change in surface conductivity and interaction between the gases and surface. Gas sensing properties of the materials can be drastically changed with surface modification techniques. Three techniques doping, microwave sintering and thermal annealing were used for surface modification in the present work which change the sensing layer characteristics.

3.4.1 Microwave sintering

Use of microwave radiation for sintering of ceramic elements has currently behaved as a newly attracted scientific approach. Microwave heating has the possibility for homogeneous and quick heating as the energy is absorbed straight inside the heated object, instead of conducted from the outside. Uniformity in heating is important because it will prevent temperature gradients. In conventional heating, energy is absorbed only at surface of the material and then it transferred into the bulk by conduction. Gradients in temperature exist in the fired sample until it achieves thermal equilibrium. Fast firing by microwaves can lead to improvement in densification [82-83]. Microwave sintering is predicted to have numerous benefits like quick and volumetric heating, enhanced production rate, improvement in densification and grain growth constraint in ceramics. Microwave heating thus occurs due to an interaction between electromagnetic waves and material molecules. There are reports [94, 158-164] from research workers citing the impact of microwave radiation on sintering behaviour of oxide materials. Microwave heating has numerous advantages, like time and energy saving, quick heating rates, significantly lower processing cycle time and temperature, fine microstructure and enhanced mechanical properties, superior product performance etc. Reduced temperature densification is larger in microwave heating in comparison to conventional heating. The higher densification noticed at the time of microwave sintering is generally ascribed to enhanced grain boundary diffusion. At the time of microwave sintering, along with heating, the increase in temperature is followed by an increase in grain diameter and a consequent decrease in the porosity during densification. Fig. 3.4 and Fig. 3.5 show the schematic diagram of microwave sintering furnace with ceramic cavity in which microwave sintering takes place.

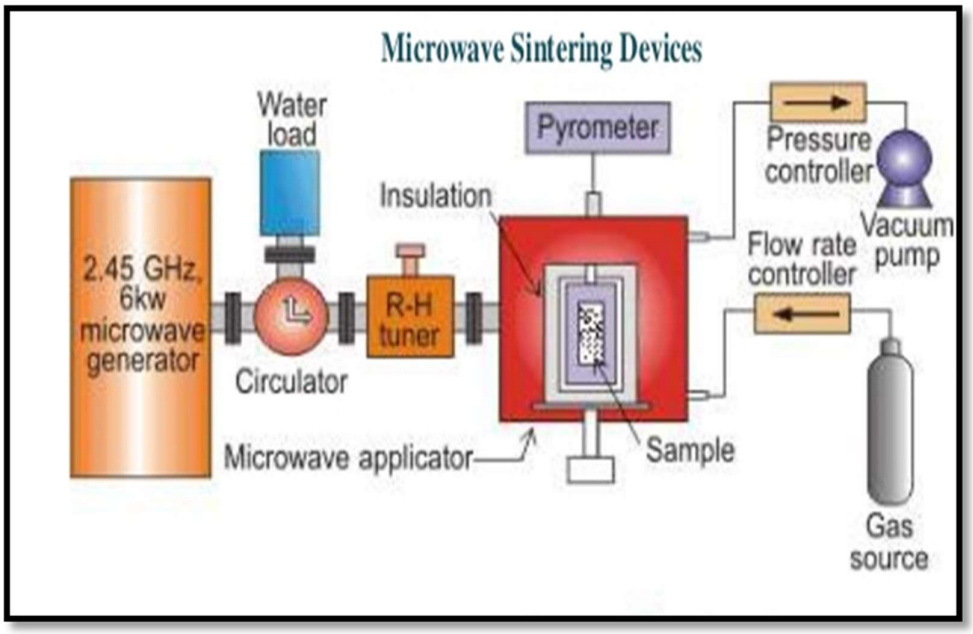

Figure 3.4: Microwave sintering furnace schematic diagram

Figure 3.5: Microwave sintering furnace with its ceramic cavity

3.4.2 Doping

Doping is basically a process of deliberately adding impurity to an extremely pure material, for the reason of modifying its electrical and chemical properties. In other words, the implantation of foreign atoms into a defined lattice structure is called doping. These atoms influence the conductivity due to the change in the concentration of free charge carriers in the crystal. The optical, electronic and magnetic properties of the material can be tuned by doping. There are several reports suggesting the effect of dopants on the change in the sensitivity of the gas sensor and its grain size e.g. Cu [117, 119-120], Zn [129, 165-167], Sb [83, 146, 168], In [92], Fe [141]. The incoming dopant atom is reported to change the structure of the host and its affinity towards gas sensing. Therefore, it is a suitable modification method to tune the properties of SnO_2 combustible gas sensors. For this purpose, various dopant atoms (like Cu, Zn, Ni, Fe and Sb) have been introduced in SnO_2 lattice during synthesis of specimens.

3.4.3 Thermal annealing

Annealing is a heat treatment which changes the physical and occasionally chemical properties of the material to make it more practical. The annealing temperature influences the film surface morphology, crystalline structure, optical and electrical properties. The gas sensing characteristics of SnO_2 films are highly affected by surface morphology. Fig. 3.6 represents the tubular furnace schematic diagram. With the increase in annealing temperature, the percentage of crystallinity and grain size are also increased [169].

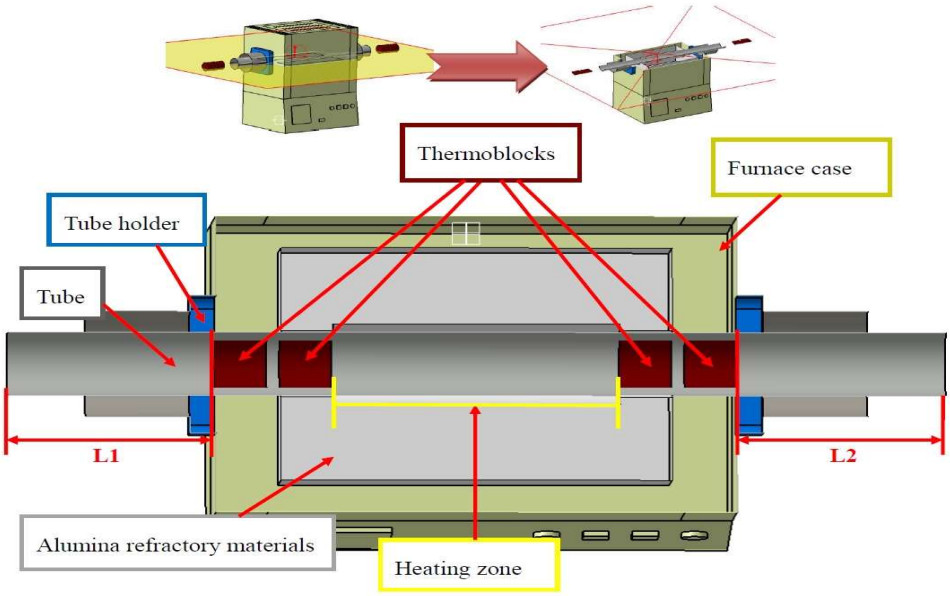

Figure 3.6: Thermal annealing furnace

3.5 Sample characterization techniques

Following techniques were used to characterize the SnO_2 nanopowders or pellets and they are divided into the subsequent categories:

- Structural and morphological characterization
  X-ray diffraction (XRD)
  Scanning electron microscopy (SEM)
  Energy dispersive spectroscopy (EDS)
  Transmission electron microscopy (TEM)
- Optical characterization
  UV- Vis spectroscopy
- Electrical measurements
  I-V measurement
  Gas sensing measurement

3.5.1 Structural and morphological characterization

3.5.1.1 X-ray diffraction

X-ray diffraction is a method which is used to obtain the crystal structure of solids, containing orientation of single crystals, favoured orientation of poly-crystals, defects, stresses, lattice constants and geometry, recognition of unidentified materials etc. It is a quick and non-destructive technique. It gives information on unit cell dimension. In year 1913, Sir W.H. Bragg and his son Sir W.L. Bragg, the physicists generated the relation to explain why the faces of crystals reflect X-ray beams at particular angles of incidence (theta, θ); it is known as Bragg's Law [170]

$$n\lambda = 2d \sin \theta \qquad 3.1$$

where λ is the incident X-ray wavelength, n is an integer and d is the distance between atomic layers in a crystal. This is an instance of X-ray wave interference, usually known as X-ray diffraction (XRD). In XRD an X-ray beam is incident on the specimen and is diffracted by its crystalline phases depending on Bragg's law. Fig. 3.7 represents a schematic diagram which explains Bragg Law given by equation 3.1.

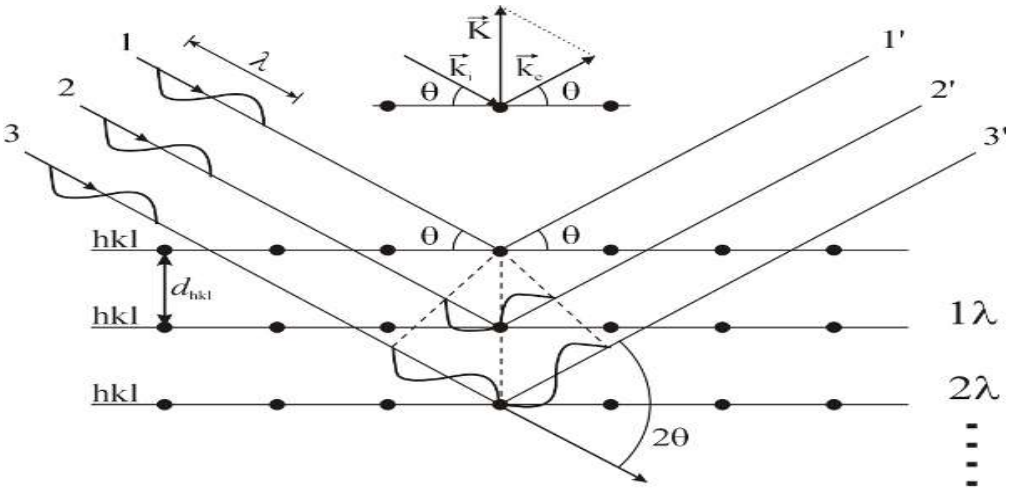

Figure 3.7: Schematic diagram shows the diffraction from lattice planes explaining Bragg's Law

The diffraction angle (2θ) and the orientation of specimen are used in the analysis of the intensity of the diffracted X-rays. The crystallinity, phases of specimen

and other structural characteristics can be identified by using the diffraction pattern. XRD is non-destructive technique. XRD is highly used technique for material characterization due to the fact that it doesn't need complicated sample preparation. It is the preferred method for characterizing the homogeneous and inhomogeneous strains in the specimen from an analysis of the diffraction peak positions. Diffraction peak positions are shifted due to the homogeneous or uniform elastic strain. The change in d-spacing can be measured from the shift in peak positions that is due to the outcome of the change in lattice constants under a strain. Diffraction peak broadening is the result of inhomogeneous strains, which changes from crystallite to crystallite or in a single crystallite. It increases with sin θ. Finite size of crystallite also induces peak broadening but this broadening is not related to sin θ. It needs a different and precise determination of peaks shape, when crystallite size and inhomogeneous strain both contribute to peak width.

When no inhomogeneous strain is present, the crystallite size D, can be calculated from the peak width with the Scherrer's formula [170-171]:

$$D = \frac{K\lambda}{\beta \cos\theta} \qquad 3.2$$

where θ is a diffraction angle, λ is an X-ray wavelength, K is a Scherrer's constant (order of unity) and β is FWHM (full width at half maximum) of diffraction peak.

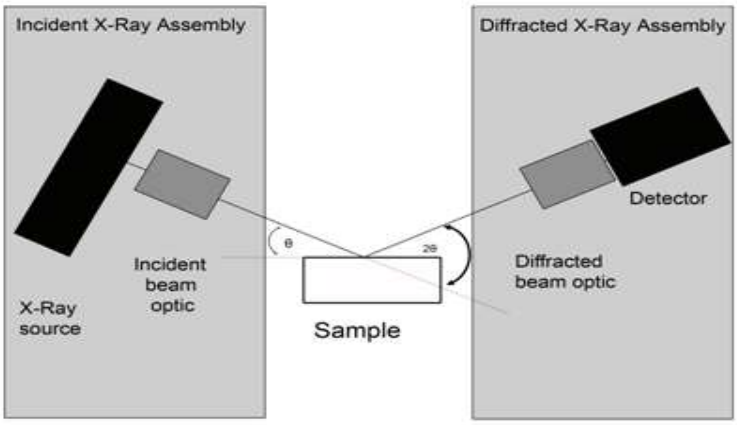

Figure 3.8: Basic beam optics diagram of the X-ray diffraction

X-ray diffraction technique gives only the cumulative facts about the crystallite sizes and generally needs a sizable quantity of powder. This method is very helpful in characterizing the nanostructures. XRD is also used to calculate the film thickness of epitaxial and highly textured thin films.

Fig. 3.8 represents the basic design of XRD instrument. Figure explains the XRD technique. X-rays are produced in an X-ray source when electrons are bombarded on the target material. Then this X-ray is guided to the sample and produces a diffraction pattern. Then detector detects the pattern and the data thus generated from the sample are interpreted.

3.5.1.2 Scanning electron microscopy (SEM)

The scanning electron microscope (SEM) is a type of electron microscope, efficient to create high-resolution images of the specimen surface by scanning it with a beam of electrons in a raster scan pattern. In SEM, the secondary electrons signal after the electron interaction with the atoms of the specimen are collected, and these signals give information about specimen's surface morphology and composition.

In a conventional SEM, an electron beam with a very small spot size of ~ 5nm is focused on the specimen surface. This beam has energy between few hundred eV to 50 keV that is rastered over the surface of the specimen by deflection coils. Production of SEM image is due to the penetration of electron when it strikes through the specimens surface, due to which a multiple interactions take place that ejects electrons and photons from the samples. These collected emitted electrons create the image on a cathode ray tube (CRT).

SEM produced signals include secondary electrons, back-scattered electrons (BSE), characteristic X-rays, light photons (cathodoluminescence) and transmitted electrons. This schematic diagram of SEM representing the image formation procedure are shown in Fig. 3.9 and the Fig. 3.10.

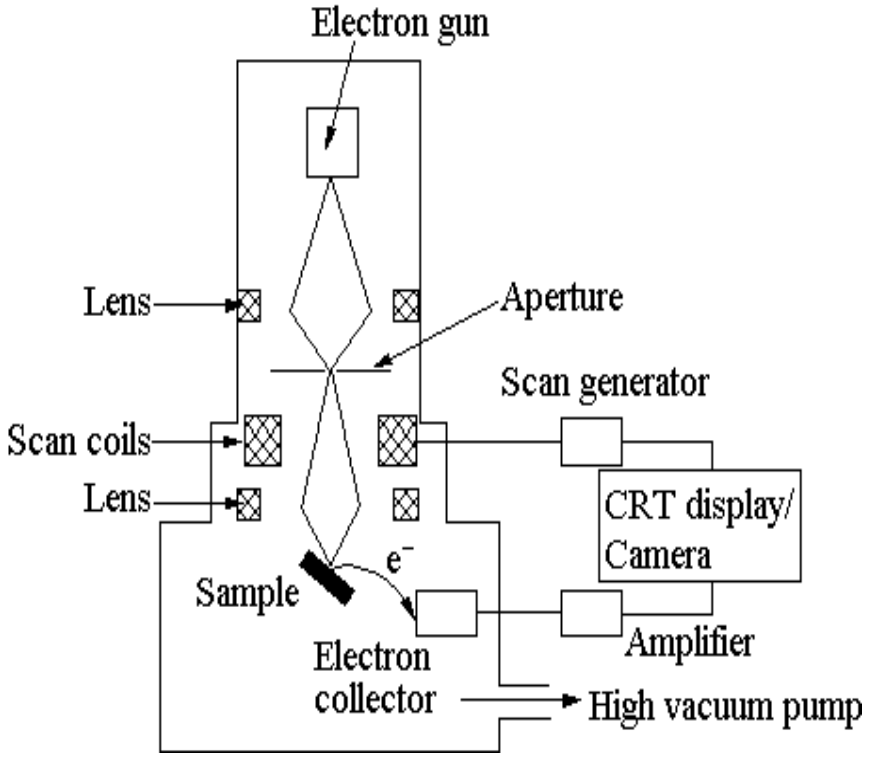

Figure 3.9: Schematic diagram of image composition process in SEM

SEM consists of an electron gun, producing a beam of monochromatic electrons. The beam is then condensed by the first condenser lens. This condenser lens is used for both, for the electron stream and for the control of the quantity of current in the stream. It is used in combination with the condenser aperture to remove the large angle electrons from the stream. The stream (beam) is then compressed by the condenser aperture, removing some large angle electrons. A thin, tight, coherent beam of electrons is formed by using the second condenser lens, it is normally restrained by the "fine probe current knob". Large angle electrons from the stream are removed by the user selectable objective aperture. Then the coil set scans the stream in a pattern, according to the scan speed time. The objective lens focuses the scanning beam on the specimen, when this beam strikes on the sample interactions happens in the specimens, which are detected by devices. These devices count the number of interactions before the beam goes to the next dwell point and display a pixel image on a CRT. Until the grid scan is completed this process is repeated. The whole image is scanned multiple (about 30) times per second.

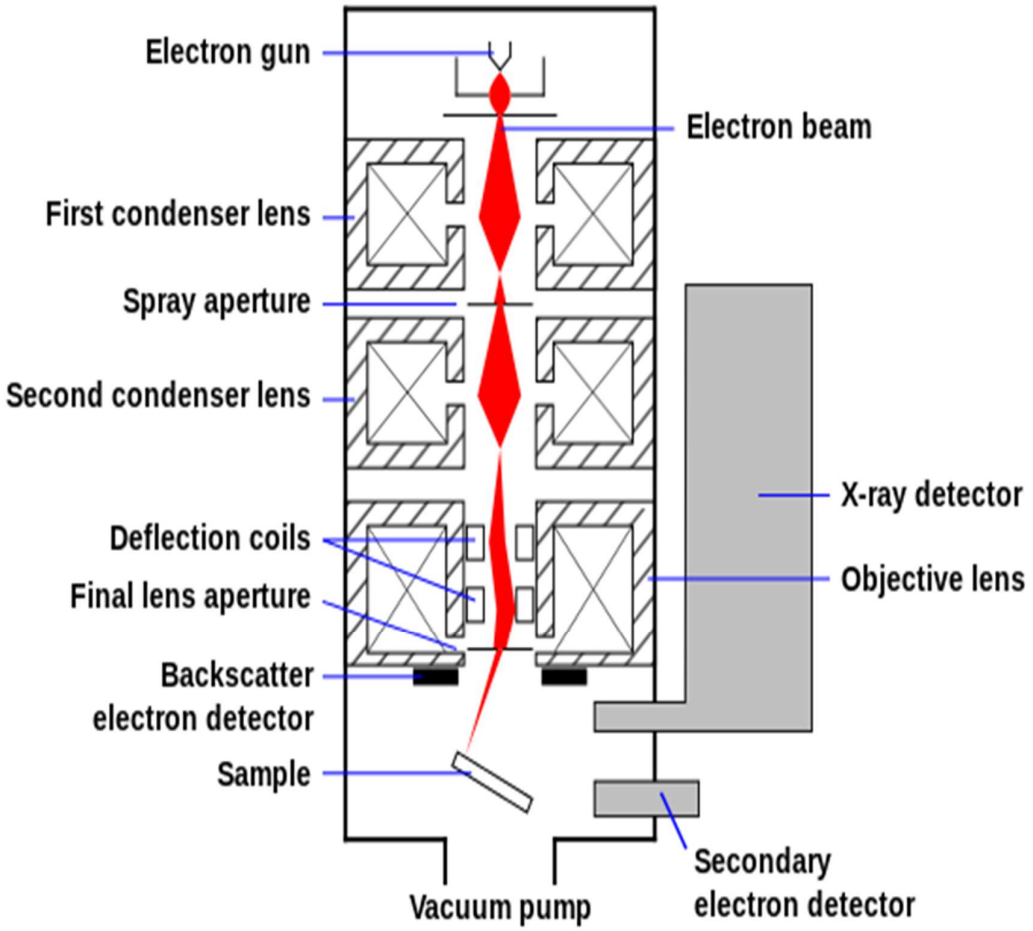

Figure 3.10: Schematic diagram of probing formation in SEM

3.5.1.3 Electron dispersive spectroscopy (EDS)

Energy-dispersive X-ray microanalysis or spectroscopy (EDX or EDS) is complementary to scanning electron microscopy (SEM) or transmission electron microscopy (TEM). It permits the user to find the composition of the sample in the SEM image. The concept of EDX is to detect the x-rays emitted from the sample at the time of bombardment of electron beam to find the elemental composition of the considered volume. These X-rays which are emitted from elements have energies characteristics of the element, so it is useful in determining the element as well as their concentration also. Three main parts to a usual EDX system are: X-ray detector, pulse processor which is used to determine the voltage pulses comparable to the X-ray

energies and a computer. The X-rays emitted from the sample are energy analyzed by the X-ray detector. When these X-rays enter the detector, they produce a small current that is changed into the voltage pulse. This voltage pulse size is proportional to the X-ray energy.

The voltage pulse for a particular time is analyzed on a computer and a histogram is plotted. This histogram represents a spectrum of the X-ray energies which were determined. The presented elements can also be determined by reviewing the spectrum.

3.5.1.4 Transmission electron microscopy (TEM)

In transmission electron microscopy (TEM), the acceleration of electrons at higher energy i.e. few hundred keV takes place. These electrons then are projected onto a thin specimen (< 200 nm) with the help of a condenser lens system and then penetrate the specimen thickness. The main benefits of TEM are its higher magnification range (50 to 10^6) and its capability to give both micrograph and diffraction data of a single specimen.

The particular facts are generated by the electrons scattering process when it passes through the specimen. Diffraction patterns rises with elastic scattering without loss of energy. But inelastic scattering induces complex absorption, scattering effect, which leads to intensity change of transmitted electrons, it happens between the primary electrons and specimen electrons at diversities like dislocations, grain boundaries, defects and many more. In TEM technique by modifying the power of intermediate lens, switching between micrograph and diffraction pattern is possible.

In TEM the magnification and resolution are controlled by the characteristics of the electron beam. The electron wavelength (λ) is interpreted by the de Broglie relationship [170]:

$$\lambda = \frac{h}{(2mqV)^{1/2}} \qquad 3.3$$

where m is the mass of electron, h is Planck's constant, q is the charge of electron and V is the potential difference for electron acceleration. In TEM instrument a high operating voltage corresponds to greater resolution. Fig. 3.11 represents schematic diagram of TEM. Image formation process in TEM depends on Fourier transform. In the formation of primary image, the objective lens generates the diffraction pattern at its back focal plane. This pattern is a Fourier transform of the scattered electron wave and the primary image is the Fourier transform of the diffraction pattern. This is the basis of the TEM image.

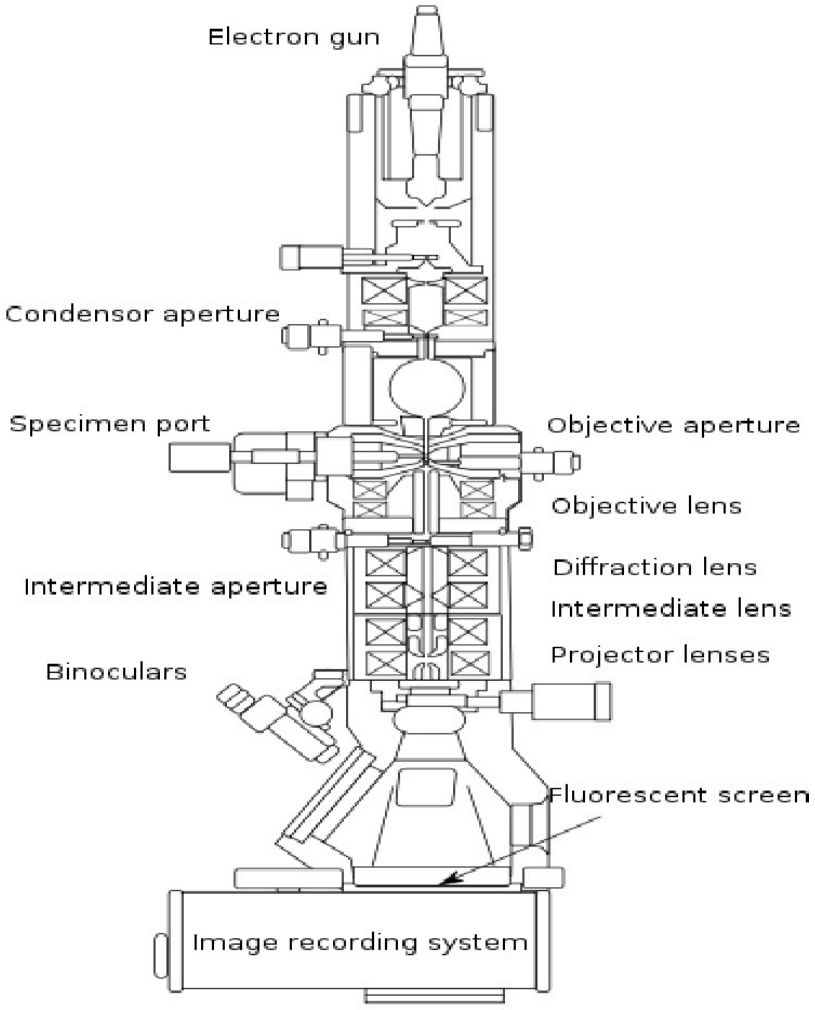

Figure 3.11: Schematic diagram of Transmission electron microscope

Selected –area diffraction (SAED) provides an exclusive ability to find the crystal structure of particular nanostructure, like nanowire, nanoparticle etc. In SAED parallel illumination at the sample is produced by the defocusing of the condenser lens

and to limit the diffracting area a selected area aperture is used. The bravais lattices and the lattice parameters of the crystalline materials are determined by SAED pattern same as in XRD.

3.5.2 Optical characterization

For proper application in semiconductor electronics it is essential to investigate the optical characterization of semiconducting material. Reflectance, absorption and transmittance of light at different wavelength and angles of the beams are the fundamental optical properties. The atoms and the electromagnetic wave electric field interaction determine the optical properties of a semiconducting material.

3.5.2.1 UV-Vis spectroscopy

Ultraviolet- visible spectroscopy (UV-Vis) is the absorption spectroscopy or reflectance spectroscopy in the UV-Vis spectral region (200 -400 nm). Light in the visible region, near –UV and near- infrared (NIR) regions are used in this process. The excitation of the electrons from the ground level to higher energy level is the output of absorption of the UV radiations. The absorbed UV energy is equal to the difference between the energy of the ground level and higher energy level.

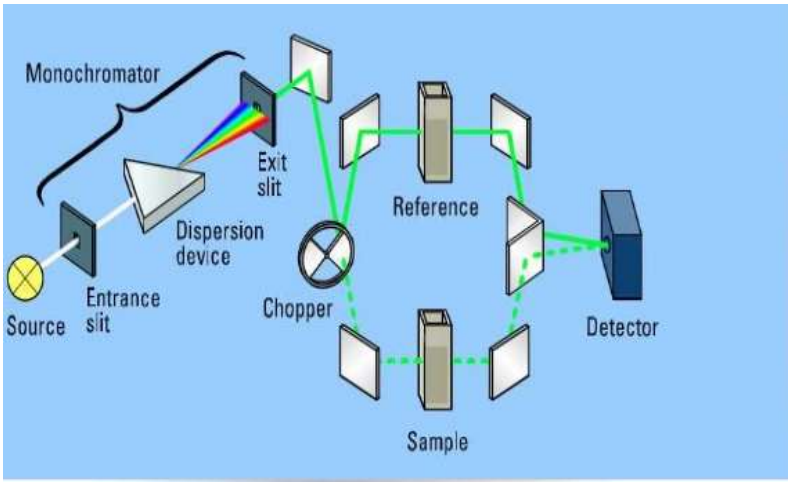

Figure 3.12: UV-Vis spectrometer working process

UV-Vis spectroscopy follows the Beer- Lambert law, according to which, the rate of change in intensity of the beam with respect to absorbing substance through which the monochromatic light beam comes, is proportional to the intensity of incident beam and solution concentration. The Beer-Lambert law is given by the following equation:

$$A = \log (I_o / I) = \varepsilon c l \qquad 3.4$$

where, A is absorbance, I_o is the intensity of light incident upon specimen cell, I is intensity of light leaving specimen cell, ε is molar absorptivity, l is the length of the sample cell and c is molar concentration of sample.

It is used to characterize the optical adsorptions of materials. The relationship between the adsorption coefficient α and the photon energy hν for direct allowed transitions are related as [170]

$$(\alpha h\nu)^2 = B (h\nu - E_g) \qquad 3.5$$

where E_g is the apparent optical band gap, B is a constant characteristic of the semiconductor, hν is the photon energy, and α is the absorption coefficient. The direct band gap is calculated with the help of this equation, when the straight portion of the Tauc plot is extrapolated to intersect the energy axis at α = 0.

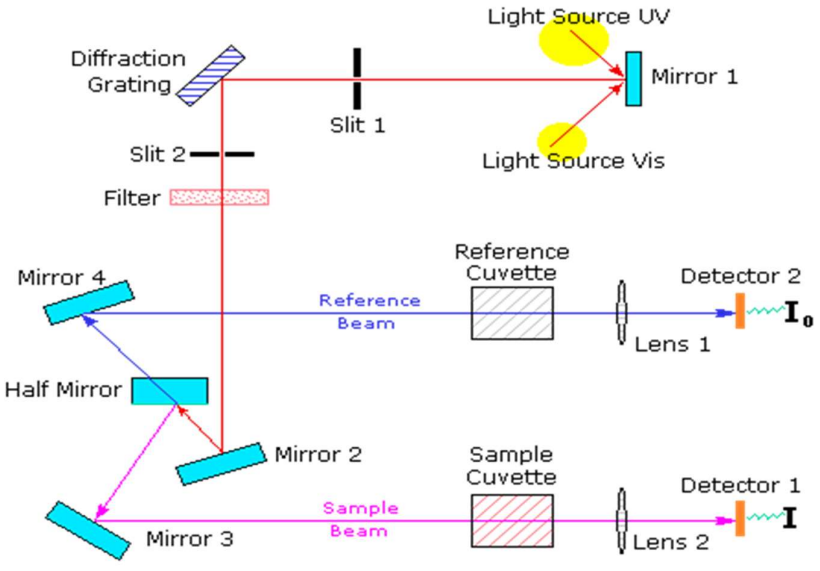

Figure 3.13: The schematic diagram of UV-Vis spectroscopy

According to this law, higher the number of molecules which can absorb the light of a particular wavelength, the higher absorption of light occurs. Fig. 3.13 represents the schematic diagram of the conventional spectrometer. Fig. 3.12 and 3.13 explain the working that a prism or diffracting grating is used to separate the beam of light from visible and/ or UV light source into its component wavelength. Half mirrored device divides each monochromatic beam of light into two equal intensity beams. The specimen beam travels through a transparent tube (cuvette) which contains a solution for study. The second beam or the reference beam travels through an identical cuvette which contains the solvent only. Detectors are used to determine the intensities of these beams and are compared. The reference beam (no light absorption) intensity is defined as I_o. The sample beam intensity is defined as I.

3.5.3 Electrical measurements

Electrical characterizations i.e. gas sensing behaviour studies for the application part of the thesis were carried out in Gas Sensing Lab., at Centre for Nano Science and Engineering (CeNSE), IISc. Bangalore. In addition to this, other electrical characterizations i.e. I-V characterizations and R-T characterizations were executed in Combustible Gas Sensing Facility (CGSF) at Materials Research Laboratory (MRL), Physics Department, MNIT Jaipur.

3.5.3.1 I-V measurements

When the sensor is in test atmosphere, then the resistance is monitored for the resistive gas sensors. The free charge carrier's changes when the target gas interacts with the sensing film. When the resistor is used as an equivalent sensing element the current- voltage (I-V) characteristic should be linear, but it may show non -linear behaviour also. Therefore, I-V characteristics knowledge is necessary to know about the behaviour of gas sensor device.

The possible carrier transport mechanisms depend on tunnelling and that may happen between metal-semiconductor junction and the inter-crystalline boundaries. Depletion width is the important parameter that figure outs which mechanism takes place. Tunnelling takes place for high donor concentrations, therefore, in semiconductor material the donor concentration is main factor which tells about the electron transport mechanism. Therefore, I-V measurement is important for each specimen. Silver paste is used to make contacts for taking I-V characteristics. These characteristics were carried out using Keithley 2400 SMU. This meter is used to source voltage and to measure current (or vice-versa) in two-point contact mode at a particular temperature. The substrate heater, on which the sample is placed, is connected with proportional-integral-derivative controller (PID controller) to maintain a particular temperature.

Figure 3.14: Custom built I-V measurement and gas sensing set up

Fig. 3.14 and Fig. 3.15 show the custom built I-V measurement and Gas sensing set up and front panel diagram of I-V measurement, respectively. For I-V measurement of semiconducting specimen, it is coupled with Keithley 2400 and integrated with a PC controlled by National Instruments, Labview 2010 software.

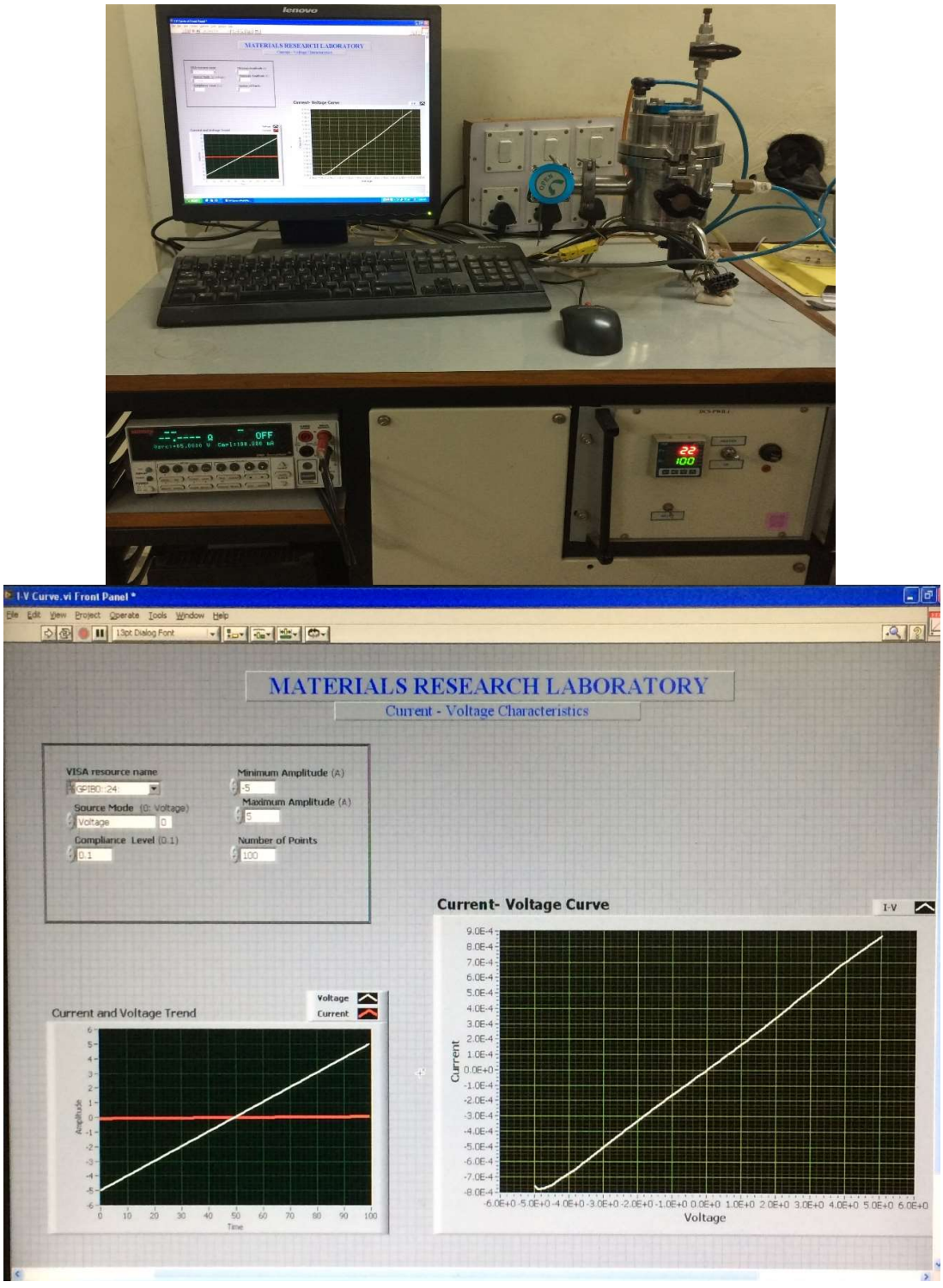

Figure 3.15: Custom built gas sensing set up and I-V measurement front panel

3.5.3.2 Gas sensing characteristics

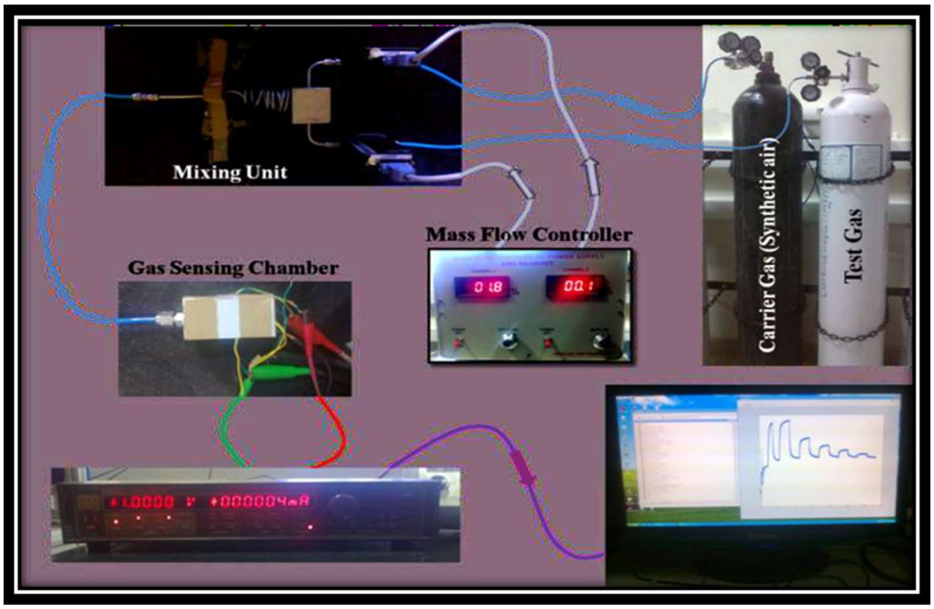

Figure 3.16: Gas sensing experiment setup. Arrow shows gas flow direction

Gas sensing setup used for study is shown in Fig. 3.16. This system is custom built in CeNSE, IISc. Bangalore, to study the gas sensing behaviour of various specimens. In this set-up a mass flow controller is used to control the mixer unit to mix test gas and carrier gas in the ratio required to obtain the desired gas concentration. The output of the mixer is connected to the gas sensing chamber. Two Keithley source meters are used to apply voltage to heater and sensing electrodes separately. The Keithley source meter which is connected to sensing electrode is also connected to a computer to acquire current variation with gas concentration. Carrier gas used here is synthetic air (N_2 80% and O_2 20%). Sensing is carried out by sensing synthetic air first to stabilize the sensing material resistance to its base value and then the target gas at a particular concentration is tested.

Gas sensing parameters

The sensor performance is basically defined using few of the parameters. These parameters with respective definitions are given below [4, 40]:

Sensitivity: This is the sensor characteristic of detecting a change in physical or chemical properties of the sensing material under gas exposure. In other words, it

offers the detection of gas concentration at ppm level. The fundamental of sensing is the change in the electrical resistivity by the adsorption of reducing or oxidizing gases on the surface of the material.

Gas sensitivity: For oxidizing gas (e.g.: NO_2, CO_2 etc.)

$$S = \frac{\left[R_g - R_a\right]}{R_a} \qquad 3.6$$

For reducing gas (e.g.: CO, CH_4, H_2 etc.)

$$S = \frac{\left[R_a - R_g\right]}{R_g} \qquad 3.7$$

Selectivity: This sensor characteristic is associated to the discrimination capacity of semiconductor gas sensing device in a mixture of gases or we can say it is detection of specific gases in a mixed gas environment.

Stability: Basically it is the capability of the sensor to give same results for a definite time period. The all other parameters like sensitivity, selectivity, response and recovery time should be retained in that.

Detection limit: Under given conditions, particularly the given temperature, the smallest concentration of the gas that the sensor can detect is called detection limit.

Resolution: The smallest concentration change that can be determined by the device.

Dynamic range: The gas concentration range bounded by the detection limit and the highest concentration.

Linearity: A comparable change from ideal straight line to an experimentally calibrated plot is called linearity.

Response time: The time which is required to respond to a particular change in concentration from zero to a certain value for sensor. In other words, the required time to attain 90% of the full sensing signal value in test gas environment.

Recovery time: The time when the device is again exposed to the carrier gas, the resistance will again go to the value before the target gas period or at the base value.

The recovery time defines the time until the signal has reached 90% of its background signal again. It indicates the dead time of sensor.

Working temperature: It is usually defined as the temperature at which it attains higher sensitivity.

Life cycle: The time interval for which the sensor can work regularly.

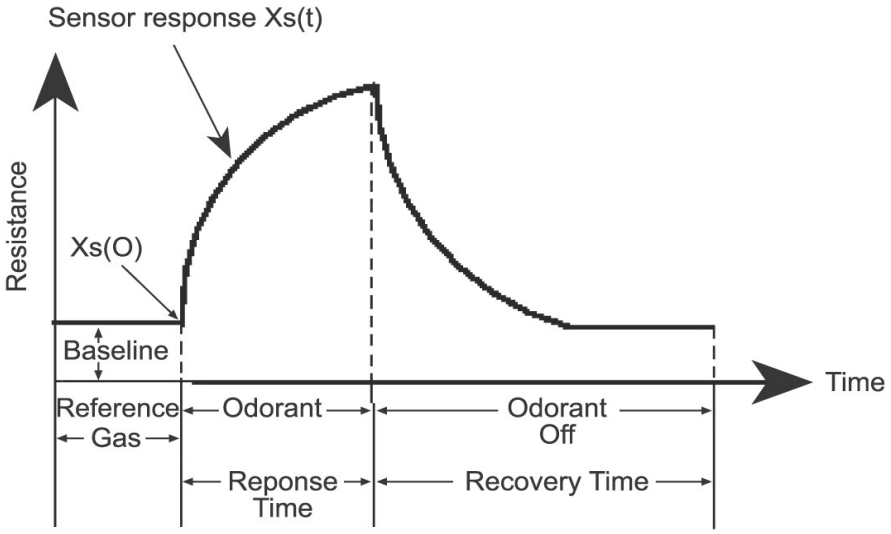

Figure 3.17: Schematic diagram of gas sensing parameters

All these parameters are used to characterize the properties of the gas sensing material. Fig. 3.17 shows schematic diagram of gas sensing parameters from gas sensing curve. High sensitivity, good selectivity, long term stability, dynamic range, low detection limit, linearity, shorter response time and long life cycle are the characteristics of the ideal gas sensor. Usually, investigators make efforts to approach only some of these characteristics, not all, because this is really a difficult task to create an ideal sensor.

3.5.4 Instrumentation used in this work

The crystal structure of the specimens was determined by X-ray diffraction (XRD). These XRD patterns have been obtained using PANalytical's X'Pert PRO Materials Research Diffractometer with monochromatized CuKα incident radiation (λ

= 1.5406 Å), with the current of 35 mA and an operating voltage of 40 kV. Data were collected in 2θ range from 20° to 70°, the step size was 0.015° and time per step was 0.50 s.

Figure 3.18: Image of PANalytical's X'Pert PRO-PW3040 diffractometer

Surface morphology of the specimens was characterized by SEM (ZEISS - EVO18) and Nova Nano FESEM 450 (FEI). These electron microscopes were operated at 20kV and 10 kV, respectively. For SEM observations, SnO_2 nanopowders were coated with Au coating unit.

Figure 3.19: Image of SEM (ZEISS - EVO18) and Nova Nano FESEM 450 (FEI)

Transmission Electron Microscopy (TEM) images were taken using FEI Techani G^2 20 S-Twin (200keV) electron microscope which is operated at 200 kV at 0.24 nm point resolution. For TEM measurements, the powder specimen was ultrasonically dispersed in a solution and then deposited on carbon grid. Image processing was done using Digital Micrograph software.

Figure 3.20: Image of FEI Techani G^2 20 S-Twin (200keV)

UV-Vis measurements were made with Shimadzu UV-1800 spectrophotometer and LAMBDA 750 (Perkin Elmer UV-Vis spectrophotometer.

Figure 3.21: Image of Shimadzu UV-1800 spectrophotometerand LAMBDA 750 (Perkin Elmer) spectrophotometer

I-V and R-T characteristics were carried out with the help of a custom-built set-up connected with Keithley- 2400 SMU operated in Two-point mode by sourcing voltage and measurement of current in a custom-built chamber with substrate heater that is controlled by LabVIEW software. The electrode contacts were made using silver paste on pellets.

Figure 3.22: Image of custom-built setup using Keithley- 2400 SMU

Gas sensing measurements were carried out on a custom built set up at CeNSE, IISc Bangalore.The mass flow controller was used to control the mixer unit to mix test gas and carrier gas in the ratio required to obtain the desired gas concentration. Two Keithley source meters were used to apply voltage to heater and sensing electrodes separately. Carrier gas used here was synthetic air (N_2 80% and O_2 20%).

Figure 3.23: Image of custom built gas sensing set up at CeNSE, IISc. Bangalore

Chapter -4

Synthesis and Characterization

4.1 Introduction

The previous chapters have highlighted the suitability of SnO_2 for gas sensing due to its unique physical and chemical properties as well as its low cost in comparison to other materials. Now the goal is to synthesize the material in such a way which can preserve the sensitivity, selectivity and the response increase without affecting its cost. This can be done by adding a foreign metal to SnO_2 lattice i.e. doping of metals since an optimum amount of doping may promote better response towards a particular gas and enhance the sensing property of the material [92]. This chapter details the synthesis and characterization of pure, metal doped and surface modified SnO_2 nanostructures which were further used for gas sensing application for different gases. The synthesis of pure and doped (Zn, Cu, Ni, Sb and Fe) SnO_2 has been done using sol-gel method, these as-prepared samples were then characterized using different structural, morphological and optical characterization techniques.

4.2 Pure SnO_2 nanoparticles

4.2.1 Synthesis of pure SnO_2 nanoparticles

Synthesis of pure tin dioxide nanopowder was done by using three different methods based on sol-gel route which is a simple, inexpensive method and offers ability to control the grain size, with the objective of optimization of processing parameters for synthesis of SnO_2 nanopowder. The following procedures were employed to synthesize nanostructured SnO_2 powder:

1. Nanoparticles of tin dioxide SnO_2 powder were prepared by adding ammonia water to the 0.1 M solution of $SnCl_4.5H_2O$. The precipitate was separated from rest of the liquid by filtering and drying. Then the sample was annealed at 600°C for 3 hours resulting in the formation of a yellow SnO_2 powder [97].

2. Tin dioxide nanopowder was prepared by means of dissolving 0.1 M of $SnCl_4.5H_2O$ in 50 ml water – ethylene glycol mixture (1:1) as a solvent. An aqueous ammonia solution of 0.1 M was added to the above solution drop wise under stirring. The resulting gel was filtered and dried. Then annealed it at 600°C for 3 hours. Finally, black colored tin oxide nanopowder was formed [105].

3. 0.1 M of an aqueous solution of $SnCl_4$ was neutralized with aqueous NH_3 solution to obtain a precipitate. The precipitate was filtered, thoroughly washed with deionized (DI) water to remove excess ammonia and dried. Then it was annealed at 600°C for 3 hours [98].

The comparative study of the structural and optical properties of SnO_2 nanopowders prepared by three different routes along with the commercially available SnO_2 (Alfa Aesar-99.99%) was done which is discussed below.

4.2.2 Characterization of pure SnO_2 samples

The crystalline structure of SnO_2 nanopowders was characterized by XRD using PANalytical's X'Pert PRO- PW3040 Diffractometer with CuKα X-ray radiation (λ = 1.5406 Å). The SEM images were recorded by ZEISS make EVO18 model to study the morphology of the samples. Transmission Electron Microscopy (TEM) images were taken using FEI Techani G^2 20 S-Twin (200keV) electron microscope which is operated at 200 kV. For TEM measurements, the powder specimen was ultrasonically dispersed in a solution and then deposited on carbon grid. UV-Vis measurements were made with a UV-1800 spectrophotometer. PL measurements were carried out at RT using 275 nm as excitation wavelength with a Shimadzu make RF5301 PC spectrofluorophotometer.

4.2.3 Results and discussions

4.2.3.1 XRD studies

Fig. 4.1 shows the XRD patterns of differently synthesized SnO_2 nanopowders. All of the peaks in the XRD spectra were readily indexed to tetragonal rutile structure which is suggestive of the synthesis of pure nanostructured SnO_2. No characteristic peaks of other impurities were observed indicating that the product has high purity. The crystallite size was estimated using the Scherrer's formula [171] and is given in Table 4.1. The crystallite size of pure SnO_2 prepared by method 1 and method 2 was almost same and in the range of commercially available sample (S4), while method 3 gave larger sized nanoparticles of SnO_2 after the same annealing treatment at 600°C.

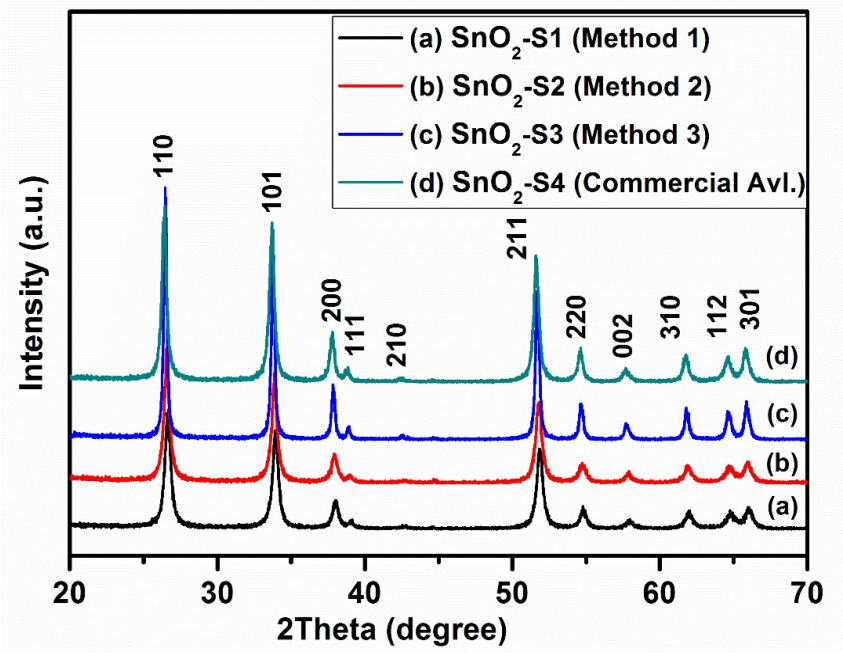

Figure 4.1: XRD of pure SnO_2 powder prepared by three different methods (1-3) and compared to the commercially available SnO_2 nanopowder

4.2.3.2 Electron microscopy studies

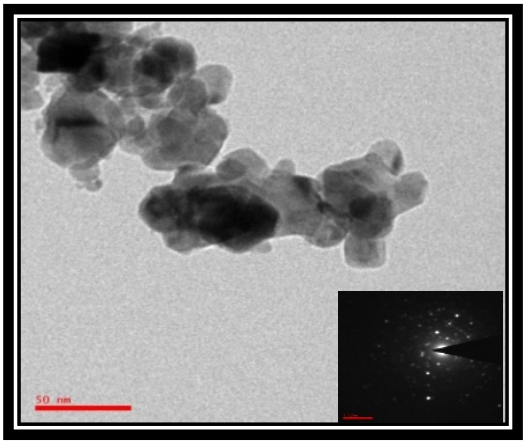

Figure 4.2: TEM images of pure SnO_2 nanopowder

TEM image of as-synthesized pure SnO_2 nanopowder and corresponding SAED pattern (inserted right bottom of the figure) are shown in Fig. 4.2. From the figure it has been observed that the nanoparticles showed agglomerated structure. TEM pattern indicates small particle size ~ 19 nm which is in a good agreement with the particle size calculated by XRD as indicated in Table 4.1.

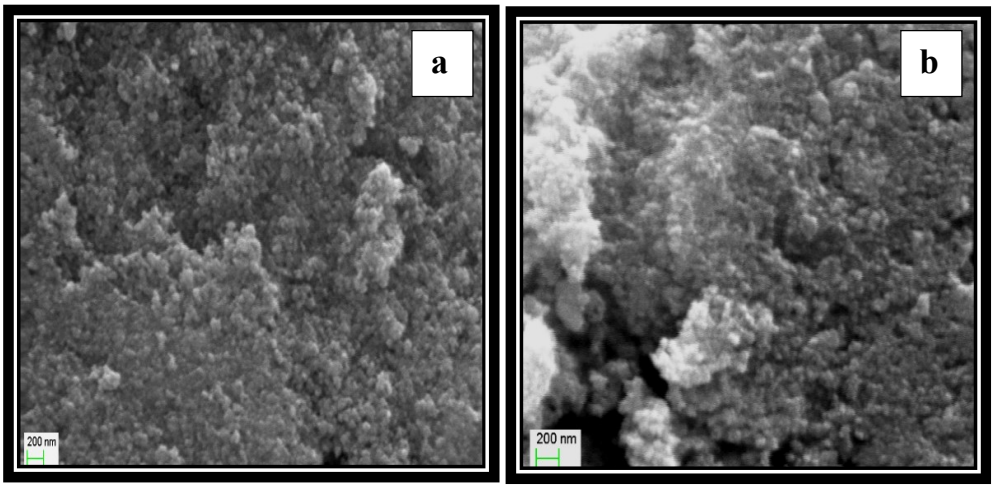

Figure 4.3: SEM image of SnO_2 nanopowder synthesized by (a) method 1, (b) method 2

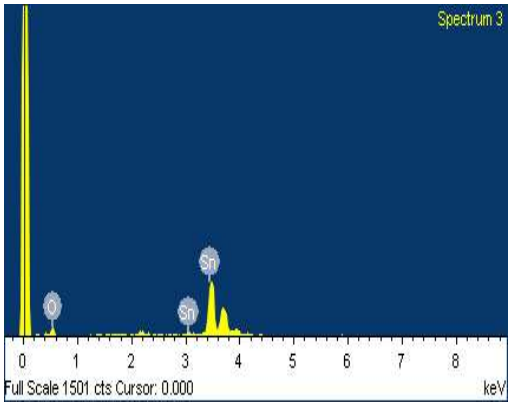

Figure 4.4: EDX image of SnO_2 nanopowder synthesized by method 1

SEM micrographs of pure SnO_2 pellets are shown in Fig. 4.3. As shown in Fig. 4.3 (a) and 4.3 (b), the as synthesized samples consist of fine tiny nanoparticles, which seem to be well crystallized with slightly agglomerated structures having small crystallite size. SEM micrograph of method 3 showed similar morphology as Fig. 4.3 (a), with comparatively larger grains. Fig. 4.4 shows the EDX spectra of pure SnO_2 sample indicating the presence of elements Sn and O. No impurities were detected in the EDX spectrum suggesting a good purity for the specimen.

4.2.3.3 UV-Vis and PL spectroscopy studies

UV-Vis and PL spectroscopy were used to characterize the optical properties of SnO_2 nanopowders. UV-Vis spectroscopy gave the optical absorption spectra of SnO_2 nanoparticles. Fig. 4.5 shows the Tauc plot [171] corresponding to the pure SnO_2 nanopowders. The band gap for each specimen is calculated and mentioned in Table 4.1, suggesting its dependence on particle size. The increase in band gap with decrease in particle size has been attributed to quantum size effect [109].

Fig. 4.6 shows PL emission spectra wherein the broad emission peak is appearing in all spectra at ~ 366 nm and is usually attributed to the free exciton electron hole recombination [109]. The broad emission peak is also suggestive of the formation of oxygen deficient nanostructured SnO_2 [172]. The PL intensity was also

correlated with particle size which revealed its decrease with increase in particle size of SnO_2.

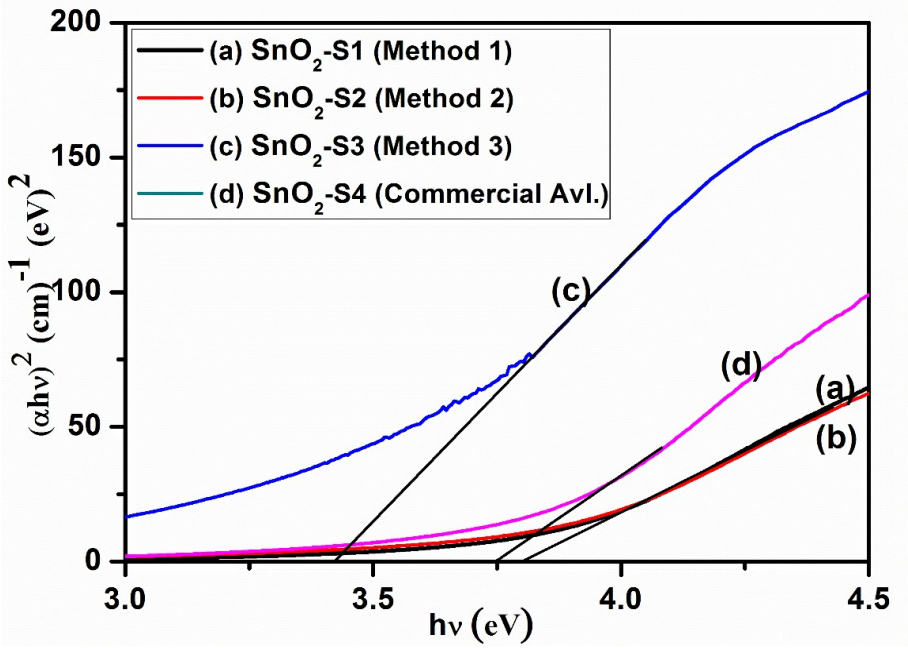

Figure 4.5: Tauc plots of SnO_2 nanopowders synthesized by different methods

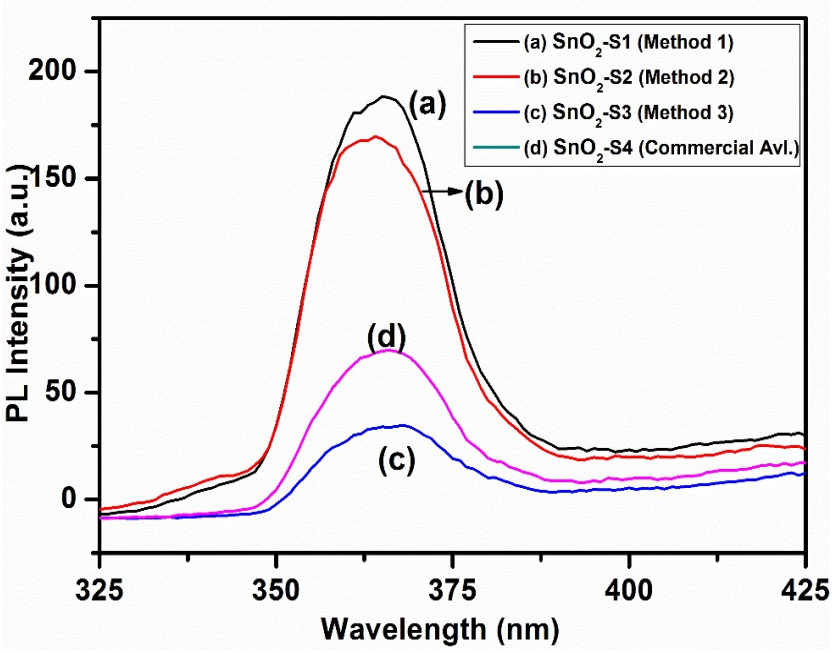

Figure 4.6: PL spectroscopy of SnO_2 nanopowders synthesized by different methods

It is noted here that method 1 and 2 yielded almost same particle size while method 3 gave larger sized nanoparticles of SnO_2 after the same annealing treatment at 600°C. Further, it was relatively easier to synthesize SnO_2 nanopowder using method 1 in comparison to method 2 and 3. In addition to this, the particle size control was found to be much better in case of method 1 during repeated synthesis of SnO_2.

Table 4.1: Crystallite size and band gap estimation using Scherrer's formula and UV-Vis spectroscopy, respectively

Method	Crystallite size	E_g using UV-Vis
1.	17±1 nm	3.78 eV
2.	18±1 nm	3.78 eV
3.	34±1 nm	3.40 eV
4.	21±1 nm	3.75 eV

Further, among all three routes employed for synthesis, method 1 gave comparatively small particle size in repeated synthesis [173].

4.3 Zn-doped SnO_2 nanoparticles

4.3.1 Synthesis of Zn-doped SnO_2 nanoparticles

Pure and Zn-doped SnO_2 with variable concentration of Zn (1 wt%, 3 wt% and 5 wt%) have been synthesized using sol-gel method. The main precursors which have been used are tin tetrachloride pentahydride ($SnCl_4.5H_2O$) and zinc chloride ($ZnCl_2$). For the preparation of nanostructured SnO_2 powder, a very small quantity of hydrochloric acid was added to $SnCl_4$ solution to prevent it from rapid hydrolysis. The aqueous ammonia solution was added drop-wise into the aforesaid solution under vigorous stirring at room temperature till the pH of the solution reaching about 2.8. The resultant white solution was heated at 60°C for 30 min under vigorous stirring. After aging for two days, the gel was filtered /washed and dried. Then the final product was annealed at 600°C for 3 hours.

For preparation of Zn-doped SnO_2 nanopowder, an appropriate amount of $ZnCl_2$ was added to the pH balanced solution and mixture was stirred for 2 hours at 60°C before aging [165]. The rest of the procedure is same as for obtaining pure SnO_2 powder. The flow chart of the above method is shown below. These as-synthesized nanopowders were pelletized using hydraulic press machine at a pressure of 5 ton and then sintered at 400°C in an open air tubular furnace for 3 hours. These pellets were then used for scanning electron microscopy and gas sensing measurements.

Flow Chart of Synthesis Process:

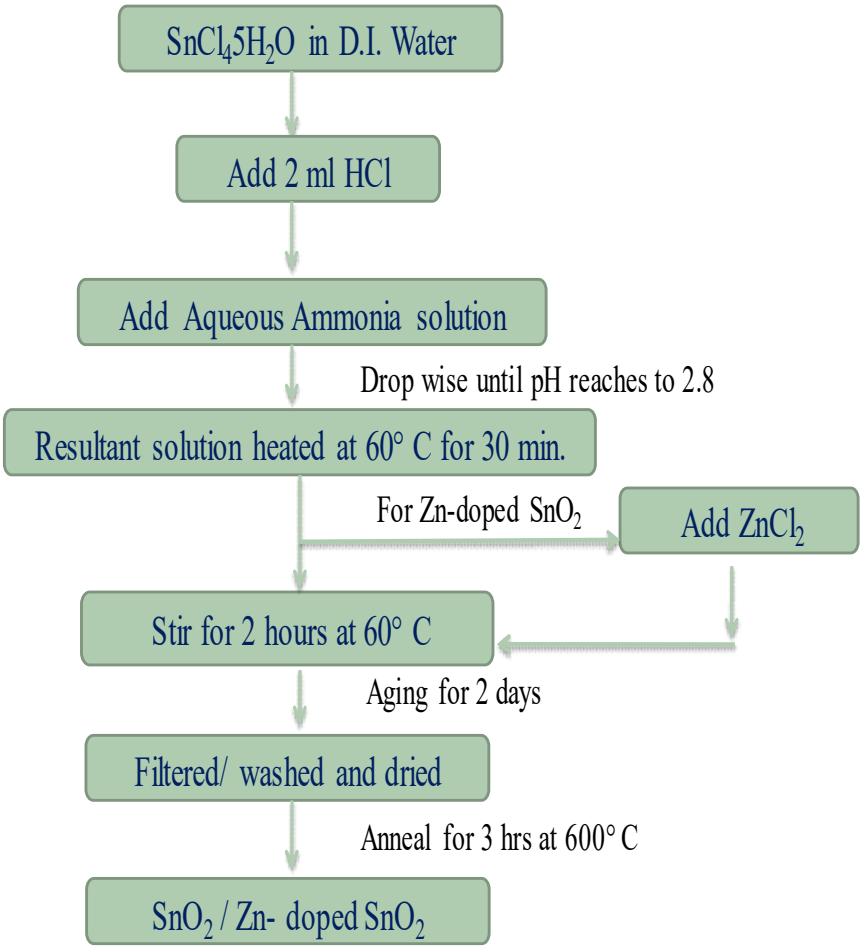

4.3.2 Characterization of Zn-doped SnO_2 samples

X-ray powder diffraction (XRD) technique has been used to characterize the crystal structure of as-prepared samples using the PANalytical's X'Pert PRO-PW3040 diffractometer with Cu K_α X-ray radiation (λ = 1.5406 Å). The morphology of the samples was recorded using Field Emission Scanning Electron Microscope (FESEM) model Nova Nano FESEM 450 (FEI). TEM images were taken using FEI Techani G^2 20 S-Twin (200keV) electron microscope which is operated at 200 kV. For TEM measurements, the powder specimen was ultrasonically dispersed in a solution and then deposited on carbon grid. UV-Vis spectra were taken on Shimadzu UV-1800 spectrophotometer.

4.3.3 Results and discussions

4.3.3.1 XRD studies

The diffraction patterns of the pure and Zn-doped SnO_2 nanopowders with different Zn concentrations, i.e. 1, 3 and 5 wt%, are indicated in Fig. 4.7 (a-d). Good crystallinity of the samples is suggested by the sharp diffraction peaks of the recorded pattern. In the present investigation, all diffraction peaks in the pattern of Fig. 4.7 indicate the formation of tetragonal rutile structure of synthesized pure SnO_2. It has been found that the addition of Zn broadens the FWHM of diffraction peaks which is indicative of smaller particle size. However, XRD pattern did not show any peak pertaining to Zn/ ZnO phase in doped SnO_2 specimens, which is probably due to the low content of Zn-dopant since the amount of Zn in nanopowder is confirmed by EDX image shown by Fig. 4.9. Scherrer's formula [171] was used for particle size estimation which are shown in Table 4.2. The particle size calculations exhibit the decrease in particle size from 16 ± 1 nm (pure SnO_2) to 9 ± 1 nm (5 wt% Zn-doped SnO_2) with Zn-doping. In some investigations similar decrease in particle size due to increase in Zn-doping concentration have earlier been reported [174].

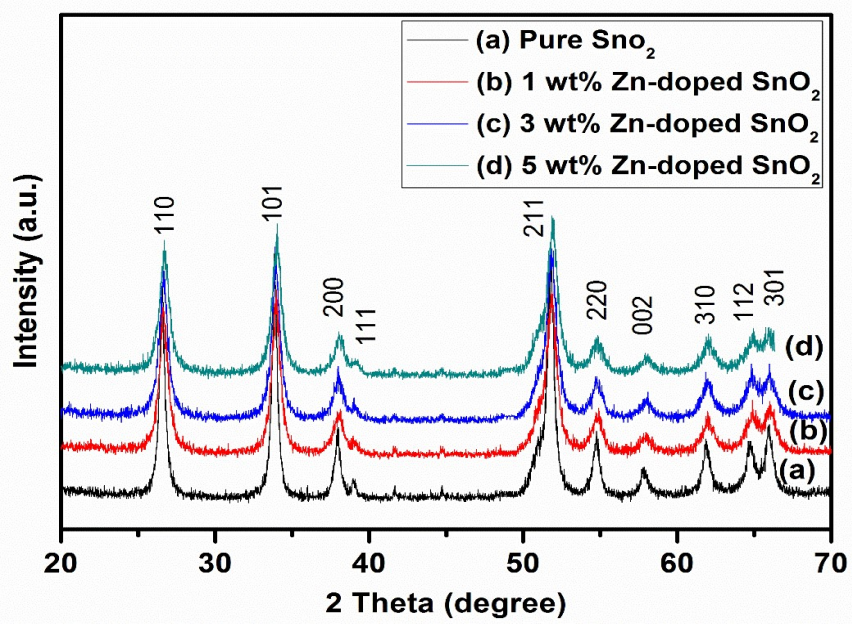

Figure 4.7: XRD pattern of Zn-doped SnO_2 nanopowder

Table 4.2: Variation in crystallite size and band gap with Zn concentration in SnO_2

Zn concentration in wt%	Crystallite size (nm)	Band-gap (E_g) (eV)
Pure SnO_2	16 ± 1	3.5
1 wt% Zn-doped SnO_2	12 ± 1	3.6
3 wt% Zn-doped SnO_2	10 ± 1	3.7
5 wt% Zn-doped SnO_2	9 ± 1	3.78

4.3.3.2 Electron microscopy studies

Fig. 4.8 indicates the FESEM images for pure and Zn-doped SnO_2 nanopowders. This Fig. suggests that the nanopowder consists of fine tiny nanoparticles which show nearly identical morphology with spherical shape of particles with different doping concentration. It is apparently seen that the crystallite size of the nanostructured material decreases with the increase in doping concentration. The surface of the pellet is approximately homogeneous with some agglomerates. SnO_2 doped with 1, 3 and 5 wt% Zn showed less homogeneity and

comparatively high clustering [Fig. 4.8 (b-d)]. Fig. 4.9 shows the EDX spectra of Zn-doped SnO_2 sample which confirms the presence of Zn in the specimens.

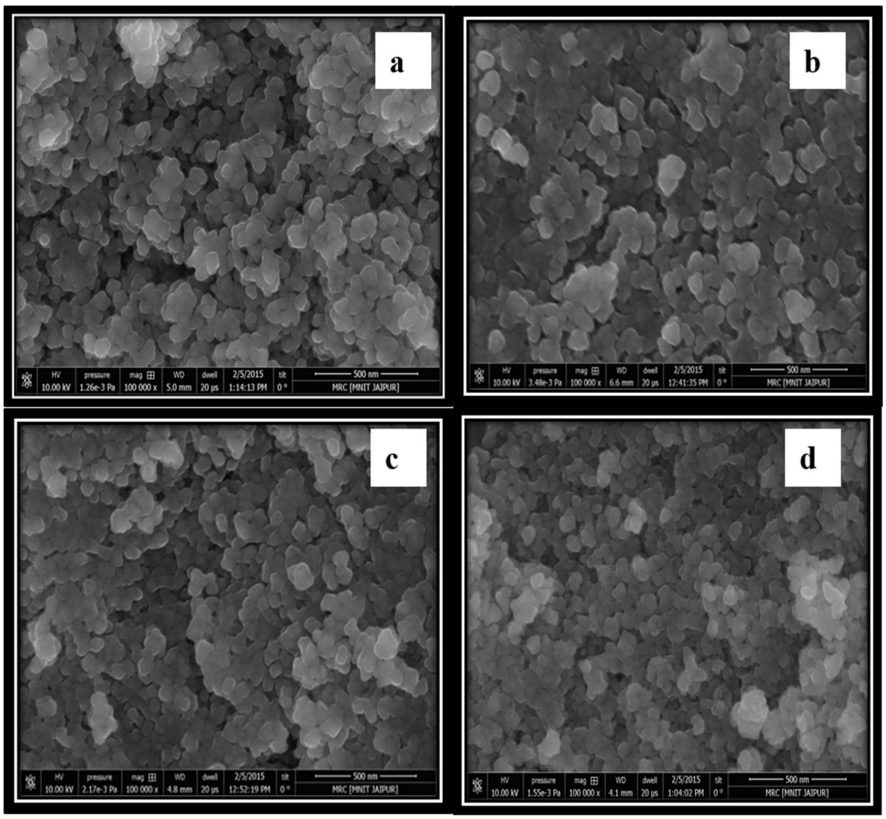

Figure 4.8: FESEM pattern of SnO_2 nanopowder (a) Pure SnO_2 (b) 1 wt% Zn, (c) 3 wt% Zn, (d) 5 wt% Zn incorporation

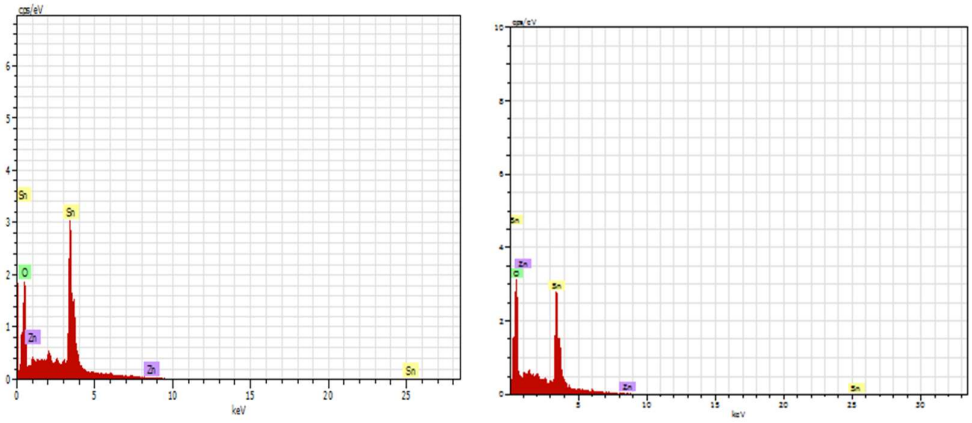

Figure 4.9: EDX pattern of Zn-doped SnO_2 nanopowder

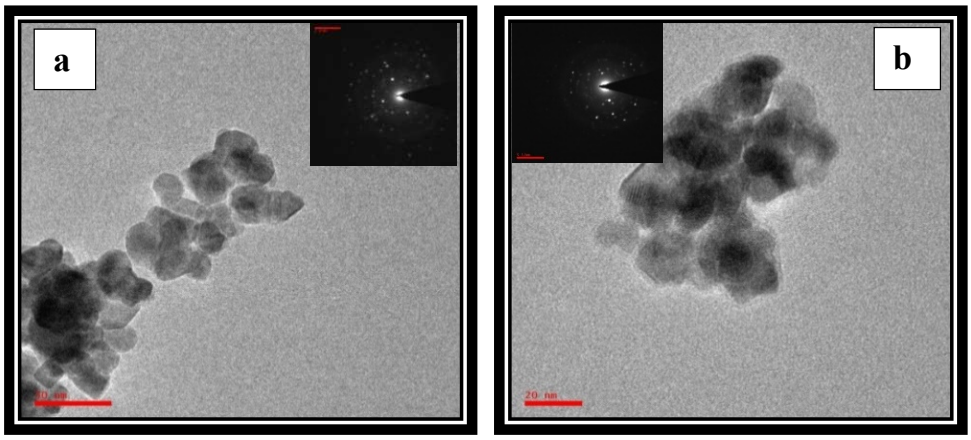

Figure 4.10: TEM pattern of SnO_2 nanopowder (a) Pure SnO_2 (b) 5 wt% Zn incorporation

TEM image of Zn-doped SnO_2 nanopowders and corresponding SAED pattern inserted on the top of the figure are shown in Fig. 4.10. TEM images indicates the uniformity in the particle size. SAED pattern indicates the clear crystalline structure. TEM pattern indicates the small particle size (~18 nm and ~10 nm) which is in good agreement with the particle size calculated by XRD.

4.3.3.3 UV-Vis spectroscopy studies

The UV-Vis spectra for pure and Zn-doped nanoparticles plotted as Tauc plots [165] to deduce the band gap, are given in Fig. 4.11. For the determination of the band gap, the straight area of the Tauc plot is extrapolated to intersect the energy axis at $\alpha=0$. The estimated band gap is mentioned in Table 4.2. It has been found that the estimated band gap increases with the increase in Zn-doping in SnO_2 from 3.5 eV (pure SnO_2) to 3.78 eV (5 wt% Zn-doped SnO_2) This is due to the reduced particle size as a result of Zn-doping. The increase in band gap due to reduced particle size has been attributed to quantum size effect [109, 165, 172].

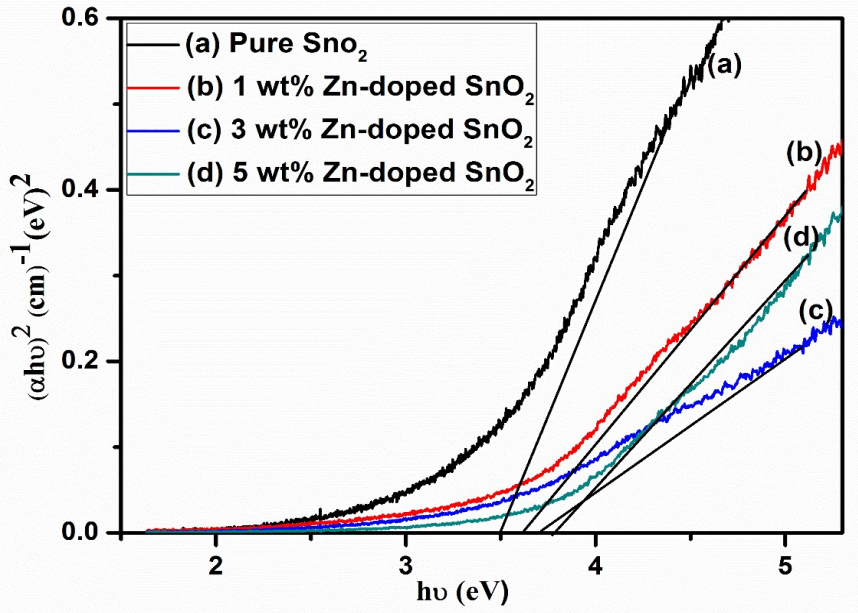

Figure 4.11: Tauc plots of SnO_2 nanopowder (a) Pure SnO_2 (b) 1 wt% Zn, (c) 3 wt% Zn, (d) 5 wt% Zn incorporation

4.4 Cu-doped SnO_2 nanoparticles

4.4.1 Synthesis of Cu-doped SnO_2 nanoparticles

Pure and Cu-doped SnO_2 with variable concentration of Cu (1 wt%, 3 wt% and 5 wt%) have been synthesized using sol-gel method. The main precursors which have been used are tin tetrachloride pentahydride ($SnCl_4.5H_2O$) and copper chloride ($CuCl_2$). For the preparation of nanostructured SnO_2 powder, same procedure was followed as described earlier in Sec. 4.3.1.

For preparation of Cu-doped SnO_2 nanopowder, an appropriate amount of $CuCl_2$ was added to the pH balanced solution and mixture was stirred for 2 hours at 60°C before aging, rest procedure is same as pure SnO_2. Flow chart explaining the synthesis process is given below. These as-synthesized nanopowders were pelletized using hydraulic press machine at a pressure of 5 ton and then sintered at 400°C in an open air tubular furnace for 3 hours.

Flow Chart of Synthesis Process:

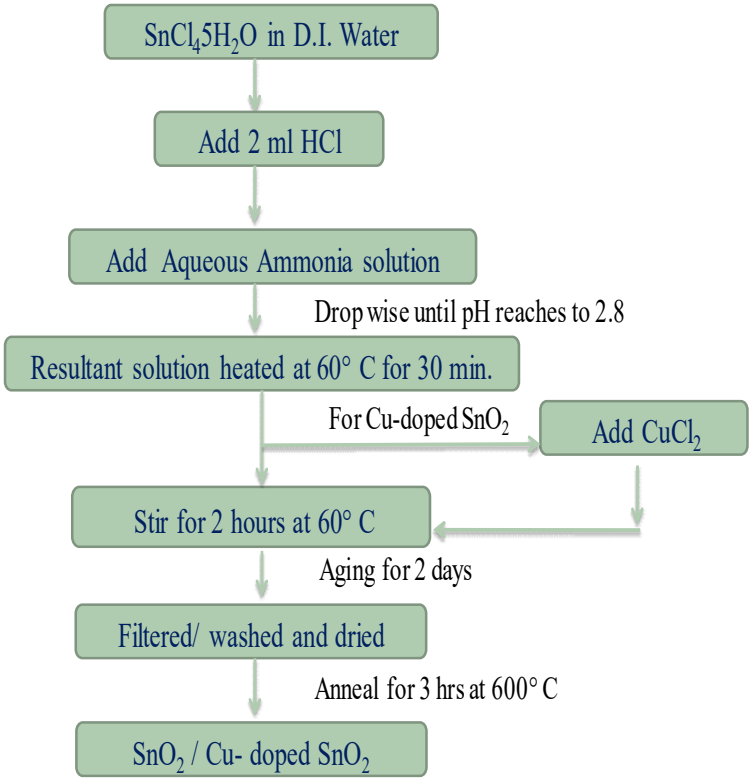

4.4.2 Characterization of Cu-doped SnO_2 samples

The specimens of pure and Cu-doped SnO_2 were characterized by XRD, SEM, TEM and UV-Vis spectroscopy using characterization tools mentioned in section 4.3.2.

4.4.3 Results and discussions

4.4.3.1 XRD studies

The X-ray diffraction pattern of all powders could be indexed to tetragonal phase of SnO_2 with lattice parameters consistent with the reported values (JCPDS card

no. 41-1445). The diffraction data of the pure and Cu-doped SnO_2 nanopowders with different Cu concentrations, i.e. 1, 3 and 5 wt%, are indicated in Fig. 4.12 (a-d). Good crystallinity of the samples is suggested by the sharp diffraction peaks of the recorded pattern. In the present investigation, all diffraction peaks in the pattern of Fig. 4.12 indicate the formation of tetragonal rutile structure, that is suggestive of the synthesis of pure SnO_2. It has been found that the addition of Cu broadens the FWHM of diffraction peaks, suggesting a decrease in particle size. And no peak pertaining to Cu/ CuO phase was detected in doped SnO_2 specimens, which is probably due to the low content of Cu-dopant. These results are similar to reported data [125, 175-179]. Scherrer's formula [171] has been used for particle size estimation and these are mentioned in Table 4.3. It is seen from Table 4.3 that the particle size decreases from 16 ± 1 nm (pure SnO_2) to 7 ± 1 nm (5 wt% Cu-doped SnO_2) with Cu-doping. In some investigations similar decrease in particle size due to increase in Cu-doping concentration has earlier been reported [121, 180-181]. This decrease in grain size of SnO_2 suggests that the growth is suppressed by doping of Cu into Sn-site [182].

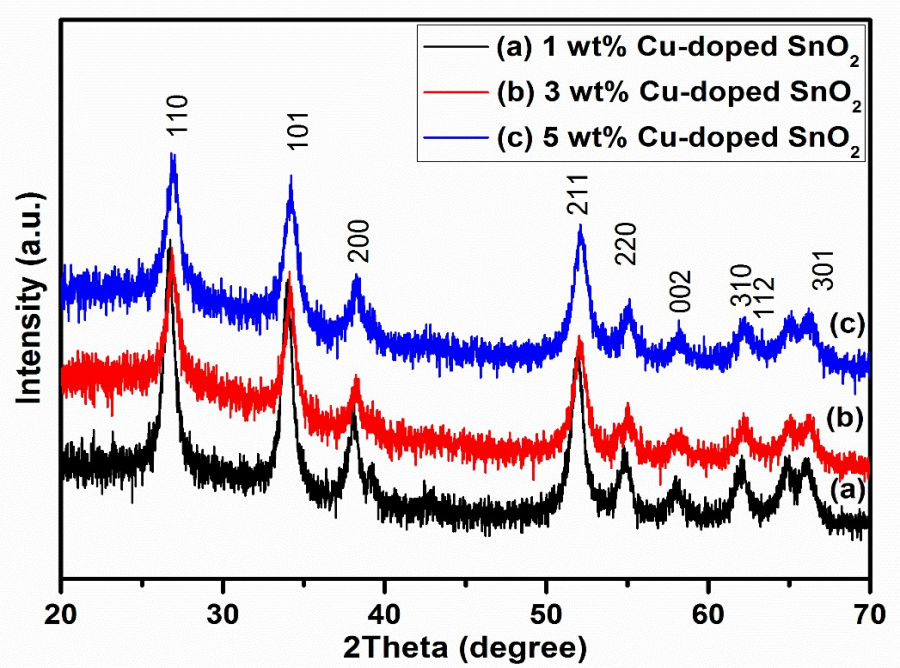

Figure 4.12: XRD pattern of Cu-doped SnO_2 nanopowder

Table 4.3: Variation in crystallite size with Cu-doping concentration in SnO_2

Cu concentration in wt%	Crystallite size (nm)
Pure SnO_2	16 ± 1
1 wt% Cu-doped SnO_2	11 ± 1
3 wt% Cu-doped SnO_2	9 ± 1
5 wt% Cu-doped SnO_2	7 ± 1

4.4.3.2 Electron microscopy studies

Fig. 4.13 indicates the FESEM images for Cu-doped SnO_2 nanopowders. This figure suggests that the nanopowder consists of fine tiny nanoparticles, which show form like structure with spherical shape of particles of SnO_2 powder with different doping concentration. The particles are agglomerated because of the increase in physical bonding among the nano scale particles. These images show micro-structural homogeneities and exhibit remarkably different morphology for SnO_2 powder with different doping concentration. The grain size distribution seems to be uniform from FESEM micrographs. It is apparently seen that the crystallite size of the nanostructured material decreases with increasing doping concentration. Similar type of morphology is also reported in another investigation [183].

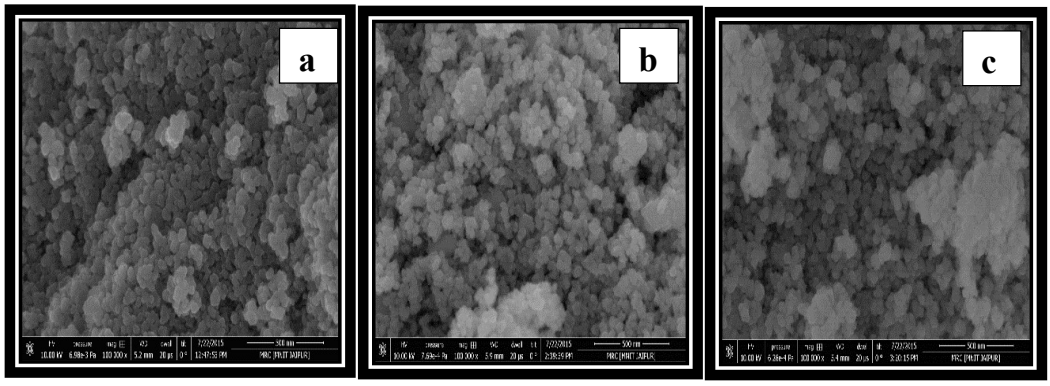

Figure 4.13: FESEM pattern of Cu-doped SnO_2 nanopowder (a) 1 wt% Cu (b) 3 wt% Cu, (c) 5 wt% Cu, incorporation

Figure 4.14 shows the TEM images of (a) 1 wt% Cu (b) 5 wt% Cu doped SnO_2 nanoparticles. The average particle size of the samples ranges from 10 to 7 nm. These results are in good estimation with crystallite size calculated by XRD (shown in Table 4.3). These patterns also indicate the uniformity in the particle size. The SAED 'halo' ring pattern of both figures indicates that the both samples have crystalline structure. M.Parthibavarman et al. [181] have reported similar behaviour of Cu-doped SnO_2.

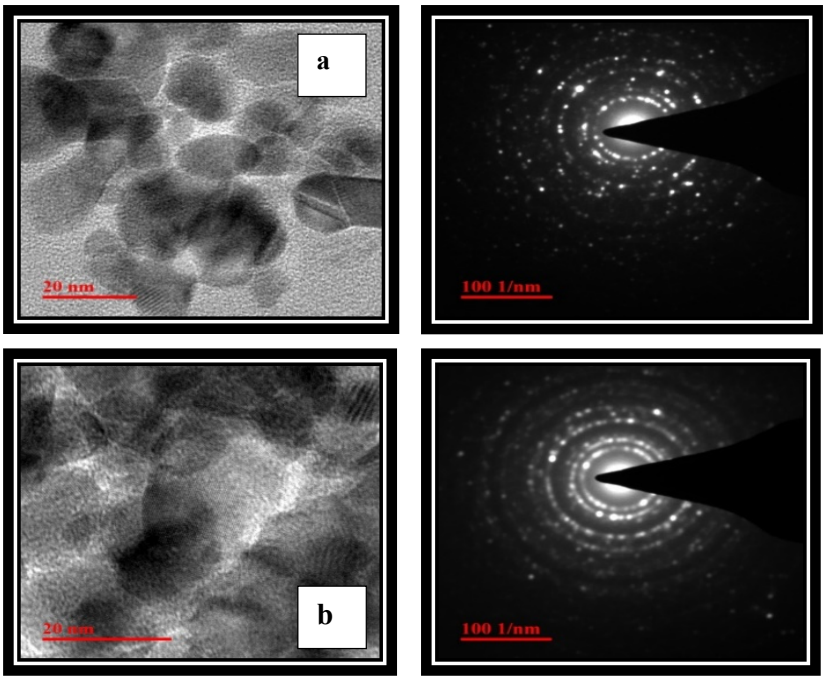

Figure 4.14: TEM pattern of (a) 1 wt% Cu-doped SnO_2 (b) 5 wt% Cu-doped SnO_2 nanopowder

4.4.3.3 UV-Vis spectroscopy studies

The UV-Vis spectra for Cu-doped nanoparticles were plotted as Tauc plots [171] to deduce the band gap, and are given in Fig. 4.15. For the determination of the band gap, the straight area of the Tauc plot is extrapolated to intersect the energy axis at $\alpha=0$. It has been found that the estimated band gap increased with increase in Cu-doping in SnO_2 from 3.35 eV (1 wt% Cu-doped SnO_2) to 3.76 eV (5 wt% Cu-doped SnO_2). The reduced particle size as a result of Cu-doping suggests that there is a blue

shift in the absorption edge. The increase in band gap due to reduced particle size has been attributed to quantum size effect [109, 165, 172, 180]. The reason for the optical band gap variation which have been noticed is might be the variation in band structure [180,183].

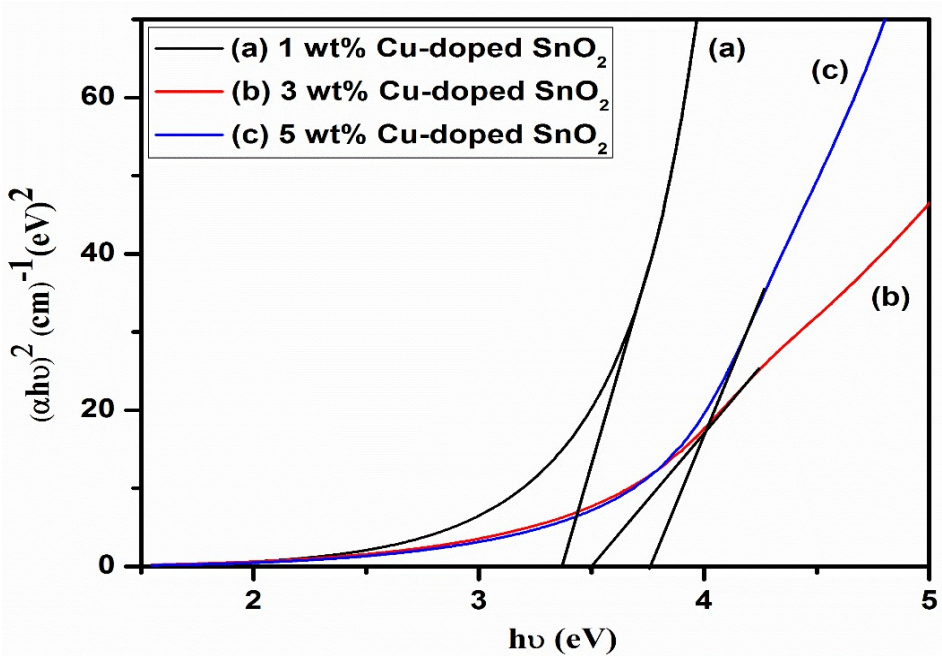

Figure 4.15: Tauc plots of SnO_2 nanopowder with (a) 1 wt% Cu, (b) 3 wt% Cu, (c) 5 wt% Cu incorporation

4.5 Ni-doped SnO_2 nanoparticles

4.5.1 Synthesis of Ni-doped SnO_2 nanoparticles

Ni-doped SnO_2 nanopowder was synthesized using tin tetrachloride pentahydride ($SnCl_4.5H_2O$) and nickel chloride ($NiCl_2$) as main precursor. Pure and Ni-doped SnO_2 with variable concentration of Ni (1 wt%, 3 wt% and 5 wt%) have been synthesized using sol-gel method. The preparation of nanostructured SnO_2 powder was done by the method, as mentioned in section 4.3.1.

For preparation of Ni-doped SnO_2 nanopowder, an appropriate amount of $NiCl_2$ was added to the pH balanced solution and the mixture was stirred for 2 hours at

60°C before aging. Rest of the procedure is same as for pure SnO_2. Flow chart for the synthesis process is given below. These as-synthesized nanopowders were pelletized using hydraulic press machine.

Flow Chart of Synthesis Process:

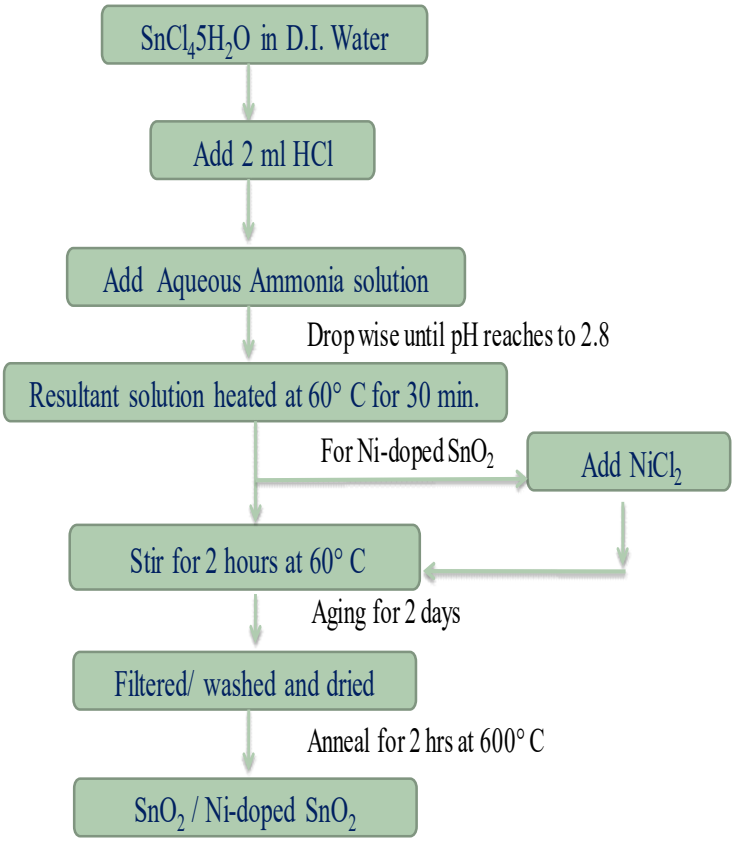

4.5.2 Characterization of Ni-doped SnO_2 samples

Crystallinity, structure and crystallite size of the as-prepared pure and Ni-doped SnO_2 were characterized by X-ray powder diffraction (XRD) technique using the PANalytical's X'Pert PRO-PW3040 diffractometer with Cu K_α X-ray radiation (λ = 1.5406 Å) in 2θ range from 20° to 70°. The other characterizations by FESEM, TEM and UV-Vis spectroscopy were done using the machines as mentioned in section 4.3.2.

4.5.3 Results and discussions

4.5.3.1 XRD studies

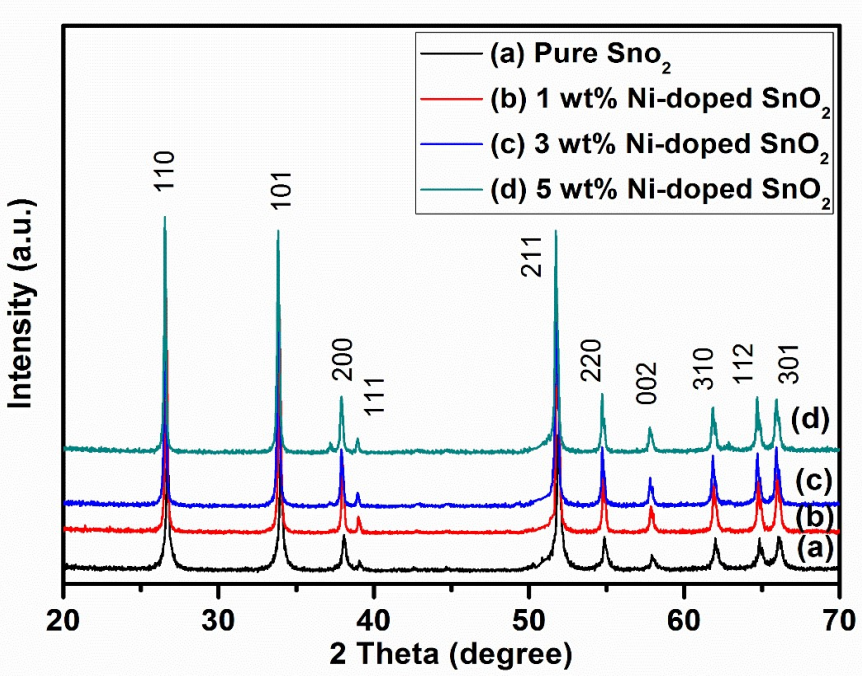

Figure 4.16: XRD pattern of Ni-doped SnO_2 nanopowder

The diffraction patterns of the pure and Ni-doped SnO_2 nanopowders with different Ni concentrations i.e. 1, 3 and 5 wt% are shown in Fig. 4.16 (a-d). All diffraction peaks in the pattern indicate the formation of tetragonal rutile structure of pure SnO_2. The sharp diffraction peaks of the recorded pattern suggested the good crystallinity of the samples. It has been found that the addition of Ni decreases the FWHM of diffraction peaks, that is suggestive of the increase in particle size. However, this is contrary to the reported data where the particle size decreases with increase in doping concentration [150, 152, 184]. Further, XRD pattern did not show any peak relevant to Ni/ NiO phase in doped SnO_2 specimens. Scherrer's formula [171] has been used for particle size estimation and results are shown in Table 4.4 which exhibit the increase in particle size from 24 ± 1 nm (pure SnO_2) to 50 ± 1 nm (5 wt% Ni-doped SnO_2) with Ni-doping.

Table 4.4: Variation in crystallite size with Ni-doping concentration in SnO_2

Ni concentration in wt%	Crystallite size (nm)
Pure SnO_2	24 ± 1
1 wt% Ni-doped SnO_2	34 ± 1
3 wt% Ni-doped SnO_2	36 ± 1
5 wt% Ni-doped SnO_2	50 ± 1

4.5.3.2 Electron microscopy studies

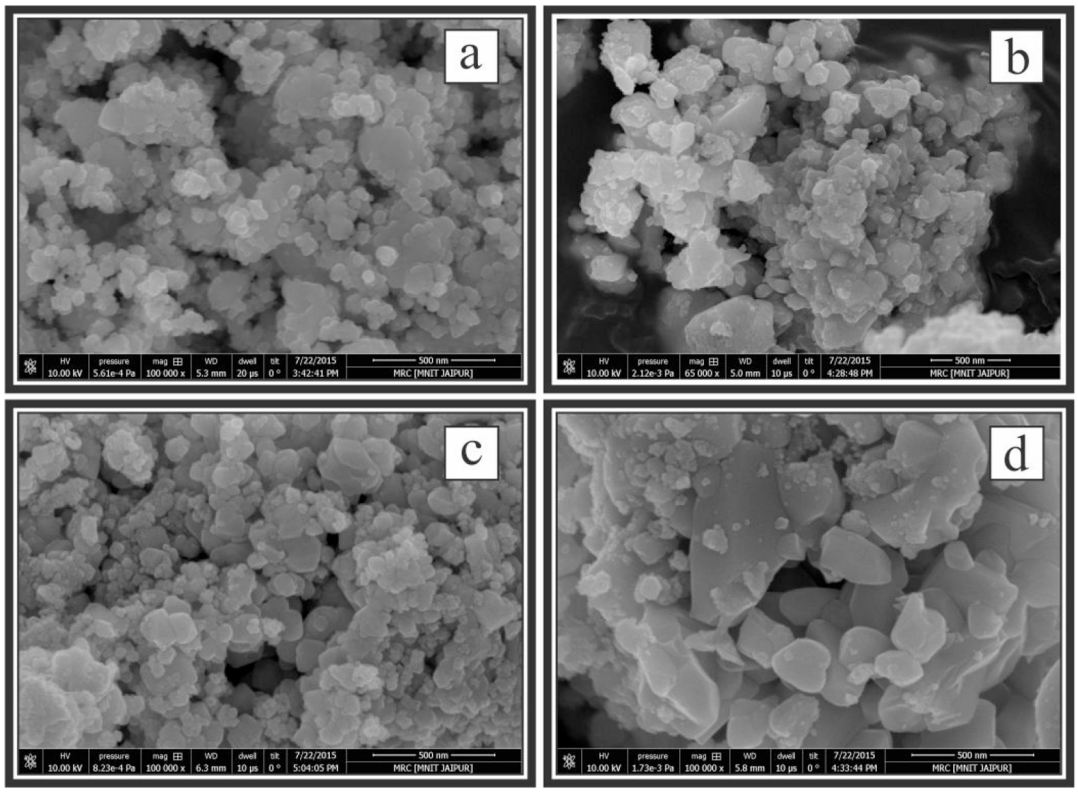

Figure 4.17: FESEM pattern of Ni-doped SnO_2 nanopowder (a) Pure SnO_2 (b) 1 wt% Ni (c) 3 wt% Ni, (d) 5 wt% Ni, incorporation

FESEM images of pure and Ni-doped SnO_2 nanopowders are exhibited in Fig. 4.17(a-d). These images show micro-structural homogeneities and remarkably different morphology for SnO_2 powder with different doping concentration. The crystallite size of the nanoparticles increases with the increasing doping concentration. The grain size distribution seems to be uniform (upto 3% Ni-doping) from FESEM micrographs. These images show aggregated nanoparticles shapes in doped nanostructured materials. All nanostructured powders up to 3 wt% Ni-doping composed of spherical particle-like shapes of the aggregated Ni-doped SnO_2. The results are in agreement with reported data [155, 184].

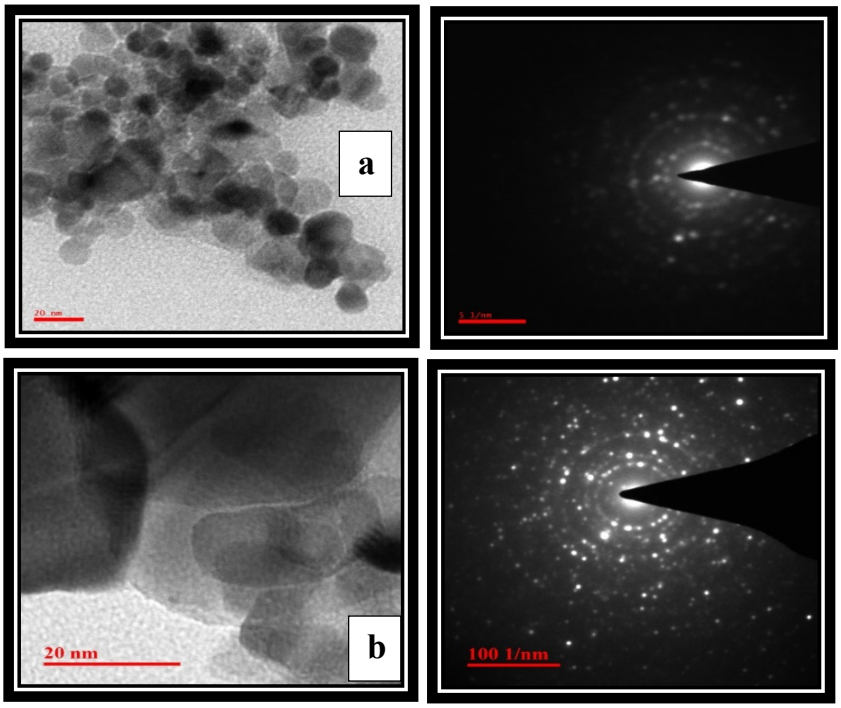

Figure 4.18: TEM pattern of (a) Pure SnO_2 (b) 5 wt% Ni-doped SnO_2 nanopowder

Fig. 4.18 shows the TEM pattern of pure and 5 wt% Ni-doped SnO_2 nanoparticles. Fig. 4.18 indicates the grains of SnO_2 have spherical morphology. TEM study reveals the increase in particle size with the increase in doping concentration. SAED pattern indicates very good crystallinity of the specimen.

4.6 Fe-doped SnO_2 nanoparticles

4.6.1 Synthesis of Fe-doped SnO_2 nanoparticles

Fe-doped SnO_2 nanopowders were synthesized using $SnCl_4.5H_2O$ and $FeCl_3$ as a main precursor. Pure and Fe-doped SnO_2 with variable concentration of Fe (1 wt%, 3 wt% and 5 wt%) have been synthesized using sol-gel method. The synthesis of nanostructured SnO_2 powder was done using the method as mentioned in section 4.3.1.

For preparation of Fe-doped SnO_2 nanopowder, an appropriate amount of $FeCl_3$ was added to the pH balanced solution and mixture was stirred for 2 hours at 60°C before aging, rest procedure is same as pure SnO_2. Synthesis process is also explained by flow chart which is given below. These as-synthesized nanopowders were pelletized using hydraulic press machine.

Flow Chart of Synthesis Process:

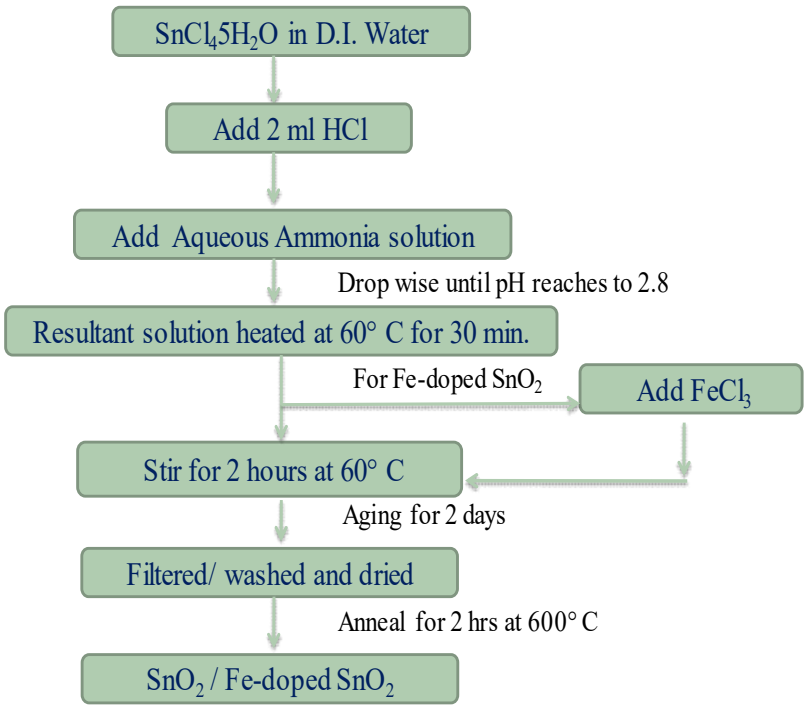

4.6.2 Characterization of Fe-doped SnO_2 samples

The specimens of pure and Fe-doped SnO_2 were characterized by XRD and TEM using characterization tools mentioned in section 4.3.2.

4.6.3 Results and discussions

4.6.3.1 XRD studies

The diffraction patterns of the pure and Fe-doped SnO_2 nanopowders with different Fe concentrations i.e. 3 and 5 wt% are shown in Fig. 4.19 (a-c). All diffraction peaks in the pattern indicate the formation of tetragonal rutile structure of pure SnO_2. The sharp diffraction peaks of the recorded pattern suggested the good crystallinity of the sample. It has been found that the addition of Fe decreases the FWHM of diffraction peaks, that is suggestive of the increase in particle size, this is controversial from the reported data [185]. However, XRD pattern did not show any peak relevant to Fe/ Fe_2O_3 phase in doped SnO_2 specimens. Crystallite size has been estimated by using Scherrer's formula [171], which is shown in Table 4.5 and it is suggested that the particle size increases from 19 ± 1 nm (pure SnO_2) to 37 ± 1 nm (5 wt% Fe-doped SnO_2) with Fe-doping.

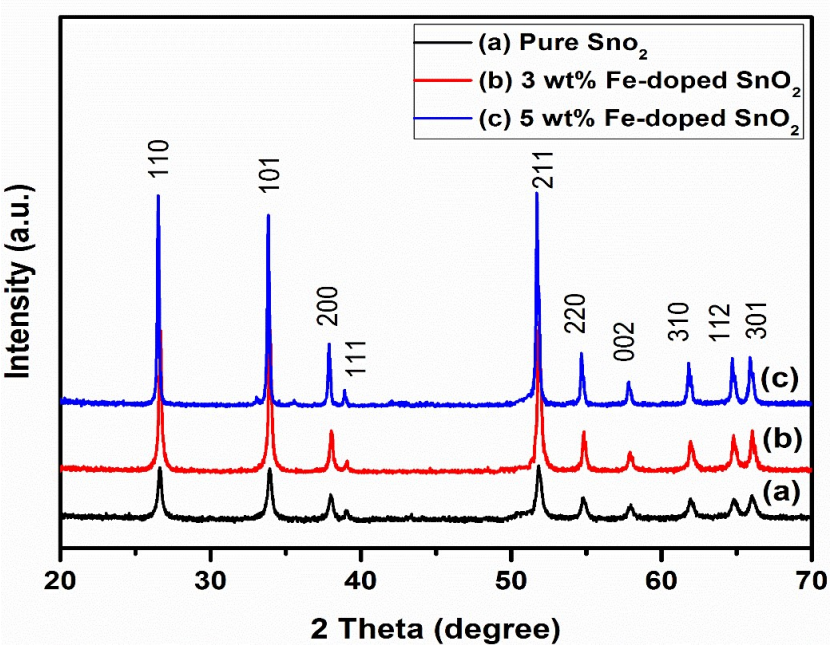

Figure 4.19: XRD pattern of Fe-doped SnO_2 nanopowder

Table 4.5: Variation in crystallite size with Fe-doping concentration in SnO_2

Fe concentration in wt%	Crystallite size (nm)
Pure SnO_2	19 ± 1
3% Fe-doped SnO_2	27 ± 1
5% Fe-doped SnO_2	37 ± 1

4.6.3.2 Electron microscopy studies

The TEM image of as-synthesized Fe-doped SnO_2 nanoparticle and corresponding SAED pattern inserted right bottom of the figure are shown in Fig. 4.20. The figure suggested that the nanoparticles showed fine agglomerated structure. TEM pattern indicates the particle size ~ 20 to 35 nm, i.e. a good agreement with the particle size calculated by XRD. TEM study reveals the uniformity in particle size.

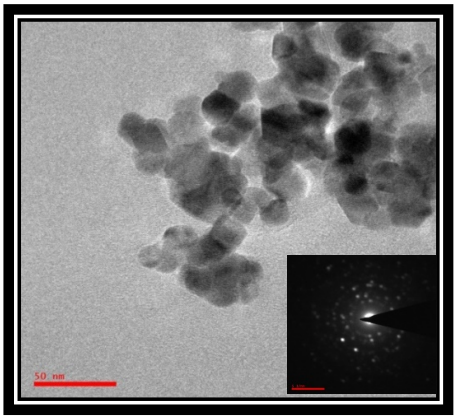

Figure 4.20: TEM images of 3 wt% Fe-doped SnO_2 powder

4.7 Sb-doped SnO_2 nanoparticles

4.7.1 Synthesis of Sb-doped SnO_2 nanoparticles

Sb-doped SnO_2 nanopowders were synthesized using $SnCl_4.5H_2O$ and $SbCl_3$ as a main precursor. The synthesis of nanostructured SnO_2 powder was done using the method mentioned in section 4.3.1.

For preparation of Sb-doped SnO_2 nanopowder, an appropriate amount of $SbCl_3$ was added to the pH balanced solution and mixture was stirred for 2 hours at 60°C before aging, rest procedure is same as pure SnO_2. These as-synthesized nanopowders were pelletized using hydraulic press machine.

4.7.2 Characterization of Sb-doped SnO_2 samples

The specimens of pure and Sb-doped SnO_2 were characterized by XRD, TEM and UV-Vis spectroscopy using characterization tools mentioned in section 4.3.2.

4.7.3 Results and discussions

4.7.3.1 XRD studies

The diffraction patterns of the pure and Sb-doped SnO_2 nanopowders with different Sb concentrations i.e. 3 and 5 wt% are shown in Fig. 4.21 (a-c). The sharp diffraction peaks of the recorded pattern suggested the good crystallinity of the sample. It has been found that the addition of Sb decreases the FWHM of diffraction peaks, that is suggestive of the increase in particle size, this is controversial from the reported data [146, 186]. All diffraction peaks in the pattern indicate the formation of tetragonal rutile structure of pure SnO_2. However, XRD pattern did not show any peak relevant to Sb/ Sb_2O_5 phase in doped SnO_2 specimens, which is probably due to the low content of Sb-dopant since the amount of Sb in nanopowder is confirmed by EDX. The crystallite size calculated from XRD are shown in Table 4.6.

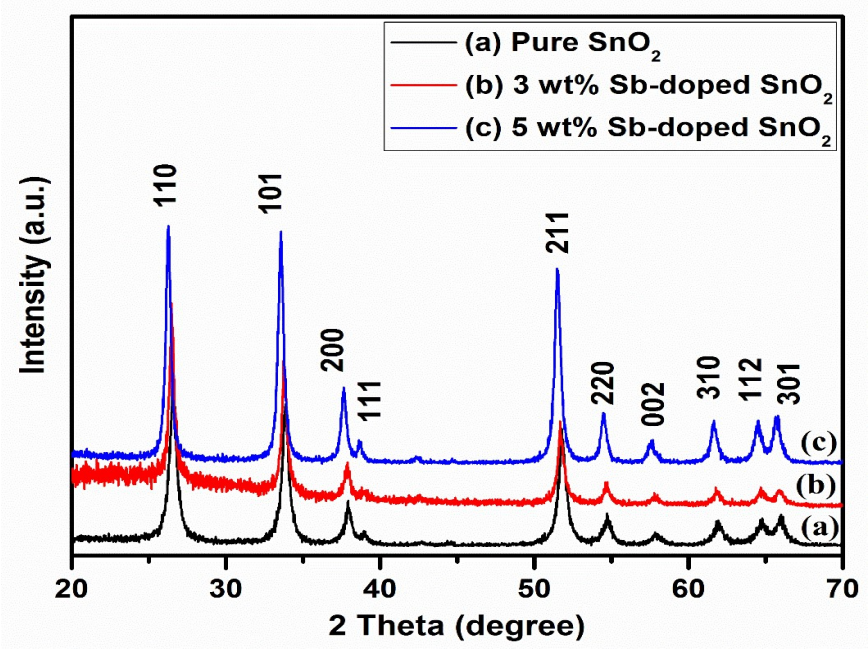

Figure 4.21: XRD pattern of Sb-doped SnO_2 nanopowder

Table 4.6: Variation in crystallite size and band gap with Sb concentration in SnO_2

Sb concentration in wt%	Crystallite size (nm)	Band-gap (E_g) (eV)
Pure SnO_2	10 ± 1	3.6
3 wt% Sb-doped SnO_2	12 ± 1	3.4
5 wt% Sb-doped SnO_2	18 ± 1	3.2

4.7.3.2 Electron microscopy studies

TEM micrograph of 3 wt% Sb-doped (antimony-doped) SnO_2 nanoparticles and corresponding SAED pattern inserted on the right top of the image are shown in Fig. 4.22. Small size particle is clearly observed. Fig. 4.23 shows the EDX spectra of Sb-doped SnO_2 sample which confirms the presence of Sb in the specimens.

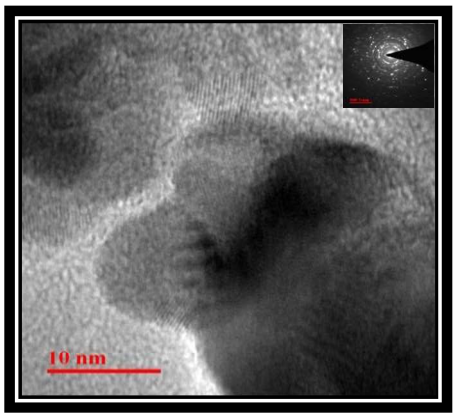

Figure 4.22: TEM image of 3 wt% Sb-doped SnO_2

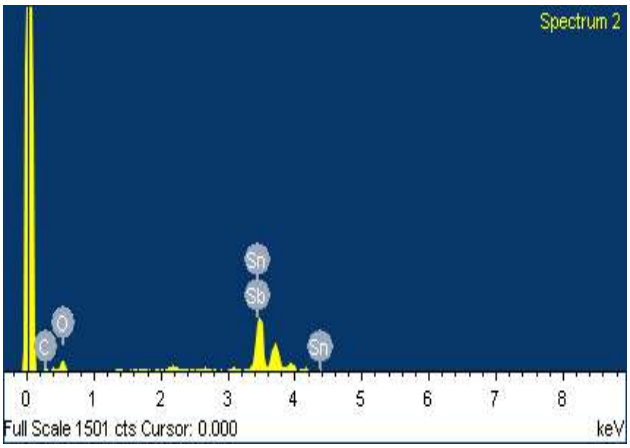

Figure 4.23: EDX spectra of 3 wt% Sb-doped SnO_2

4.7.3.3 UV-Vis spectroscopy studies

Fig. 4.24 shows the UV-Vis spectra of Sb-doped nanoparticles, which was plotted as Tauc plot [171] to deduce the band gap. It has been found that the estimated band gap was decrease with the increase in Sb-doping in SnO_2.

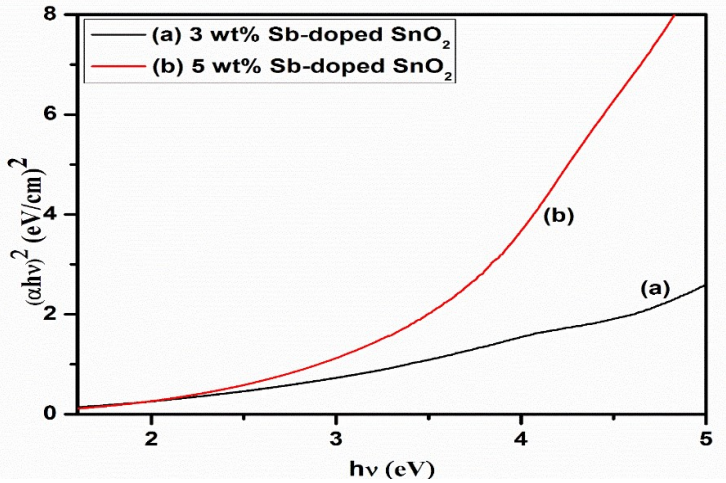

Figure 4.24: Tauc plots of Sb-doped SnO_2 nanopowder

4.8 Thermal Annealing

Annealing is a heat treatment which changes the physical and occasionally chemical properties of the material to make it more practical. The annealing temperature influences the film surface morphology, crystalline structure, optical and electrical properties. The gas sensing characteristics of SnO_2 films are highly affected by surface morphology. With the increase in annealing temperature, the percentage of crystallinity and grain size was also increased [169].

4.8.1 Synthesis of pure SnO_2 nanoparticles

To study the effect of thermal annealing on the sample, the pure SnO_2 was synthesized using method 1, which we have discussed earlier. Briefly its mentioned here also. Initially 0.1 M $SnCl_4$ solution was made by dissolving $SnCl_4.5H_2O$ in distilled water. Ammonium hydride solution was added slowly to the above solution, and stirred for 30 minutes. The resultant tin hydride precipitate was separated from the rest of the solution by filtering. The precipitate was then washed and dried. The final product was divided into four parts to study the effect of different annealing temperature on structural, morphological and sensing characteristics of SnO_2 powder and each part was annealed with 600°C, 700°C, 800°C and 900°C, respectively for 3 hours. For I-V measurements and gas sensing measurements, these as-synthesized

nanopowders were pelletized in a hydraulic press at the pressure of 5 ton and then sintered at 400°C in an open air tubular furnace for 3 hours.

4.8.2 Characterization of thermal annealed samples

The crystalline structure of as-prepared nanopowders were characterized by X-ray diffraction (XRD) using PANalytical X'Pert PRO-PW3040 diffractometer with CuK_α X-ray radiation (λ = 1.5406 Å). The surface morphology of the specimens was characterized using ZEISS make EVO18 model scanning electron microscope (SEM). UV-Vis measurements were made using UV-1800 spectrophotometer. The I-V and R-T measurements were performed using Keithley 2400 SMU in two-point mode by sourcing voltage and measurement of current in a custom built chamber with substrate heater controlled by LabVIEW software. The electrode contacts were made using silver paste on pellets.

4.8.3 Results and discussions

4.8.3.1 XRD studies

The XRD patterns of the pure SnO_2 nanopowders with different annealing temperatures i.e. 600°C, 700°C, 800°C and 900°C are shown in Fig. 4.25 (a-d). The XRD patterns of all plots exhibited sharp diffraction peaks, which indicate a good crystallinity of the samples. XRD patterns of all the plots were indexed to pure tetragonal rutile structure which is suggestive of the synthesis of pure SnO_2 powder. For higher annealing temperature it has been found that there is decrease in FWHM, which is indicative of increase in crystallite size. However, XRD pattern did not exhibit any impurity peak. The crystallite size 'D' was estimated from the peak width with Scherrer's formula,

$$D = K \lambda / \beta \cos\theta$$

where λ is the X-ray wavelength, β is the full width at half maximum (FWHM) of diffraction peak, θ is the diffraction angle, and K is the Scherrer's constant [171].

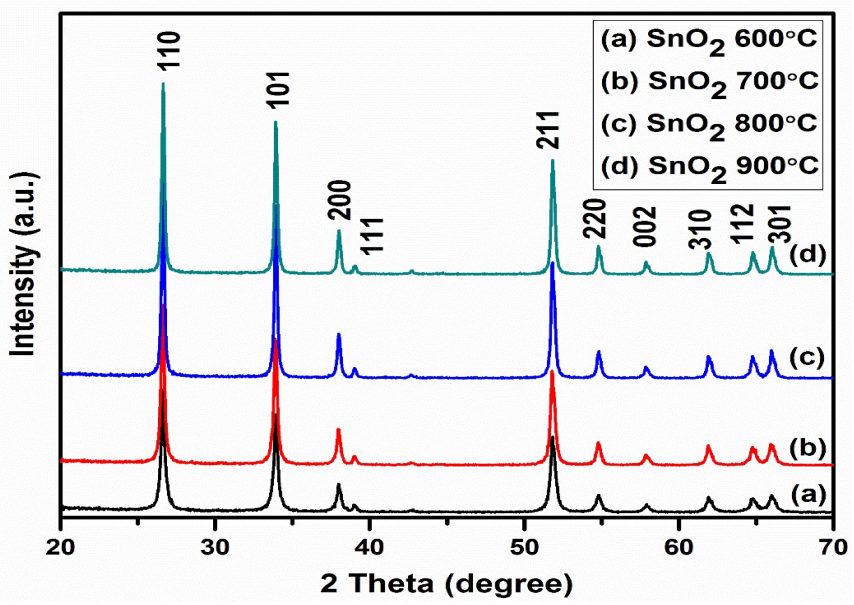

Figure 4.25: XRD pattern of pure SnO_2 powder annealed at different temperature (a) 600° C (b) 700° C (c) 800° C (d) 900° C

The crystallite size calculations were performed on three main intense diffraction peaks [110], [101] and [211] using the Scherrer's formula. The crystallite size was found to increase from 23±1 nm to 38±1 nm with increased annealing temperature which is shown in Table 4.7.

Table 4.7: Variation in crystallite size and band-gap of SnO_2 with annealing temperature

Sample Name	Crystallite Size using XRD	E_g using UV-Vis Spectroscopy
SnO_2 600°C	23 ±1 nm	3.87 eV
SnO_2 700°C	27 ±1 nm	3.84 eV
SnO_2 800°C	35 ±1 nm	3.85 eV
SnO_2 900°C	38 ±1 nm	3.90 eV

4.8.3.2 Electron microscopy studies

The SEM micrographs for nanostructured SnO_2 annealed at different temperatures are shown in Fig. 4.26 [a-d]. These figures show microstructural homogeneities and remarkably different morphology for SnO_2 powder with different annealing temperature. It is clearly seen that the crystallite size of the nanoparticles increases with the annealing temperature. The grain size distribution seems to be uniform from SEM micrographs.

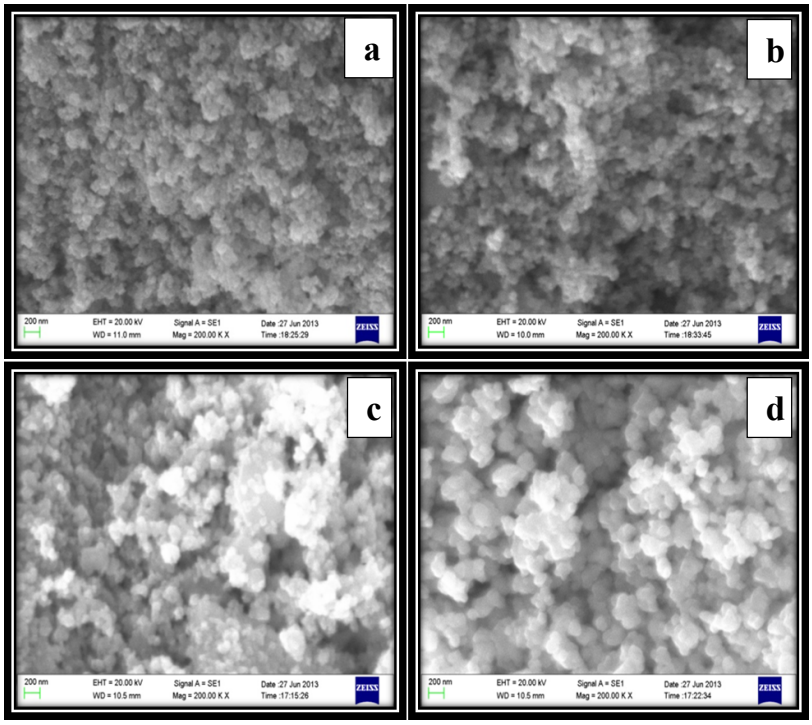

Figure 4.26: SEM micrograph of pure SnO_2 annealed at (a) 600°C (b) 700°C (c) 800°C and (d) 900°C

4.8.3.3 UV-Vis spectroscopy studies

Fig. 4.27 shows the UV-Vis spectra for SnO_2 nanopowders annealed at different temperature plotted as Tauc plots [171] to deduce the bandgap.

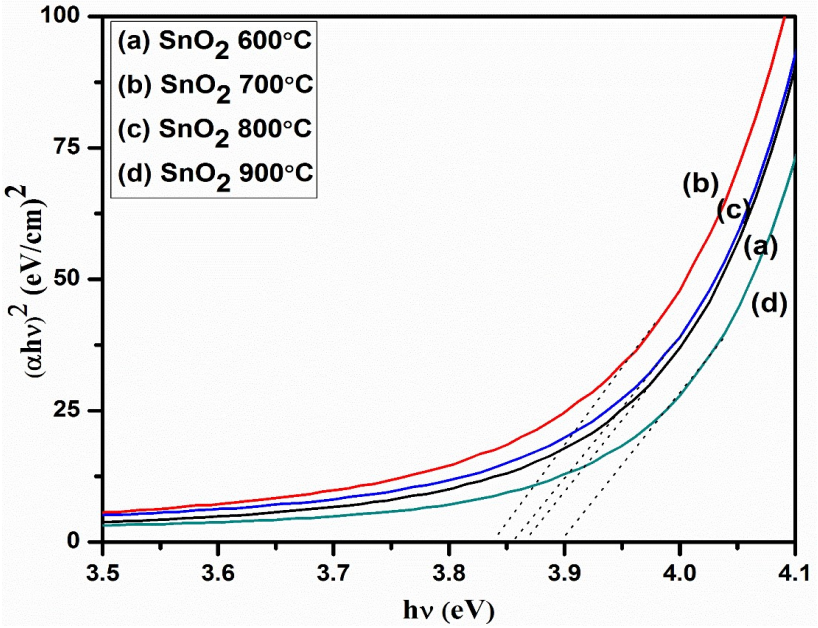

Figure 4.27: Tauc plots of pure SnO_2 powder annealed at different temperature (a) 600° C (b) 700° C (c) 800° C (d) 900° C

4.8.3.4 Electrical measurements

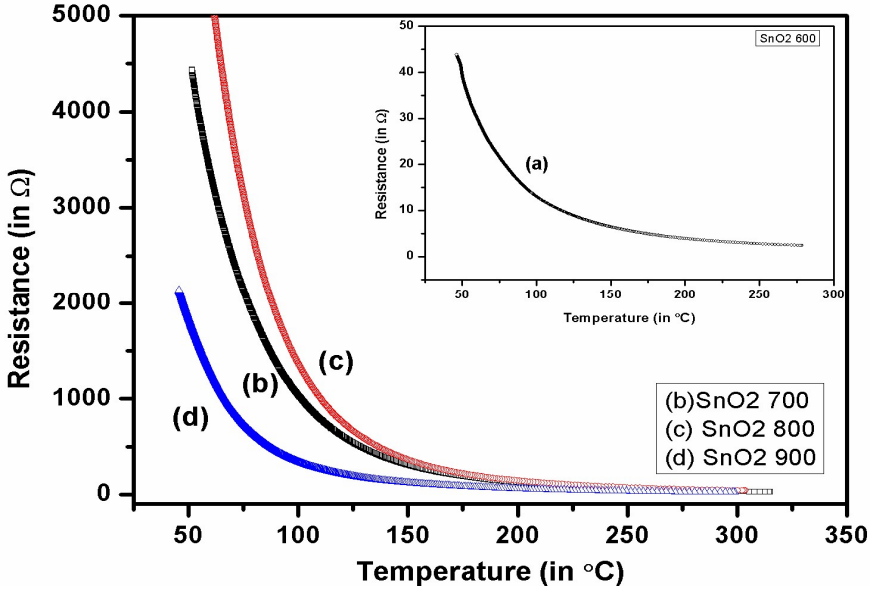

Figure 4.28: R-T plot of pure SnO_2 powder annealed at different temperature

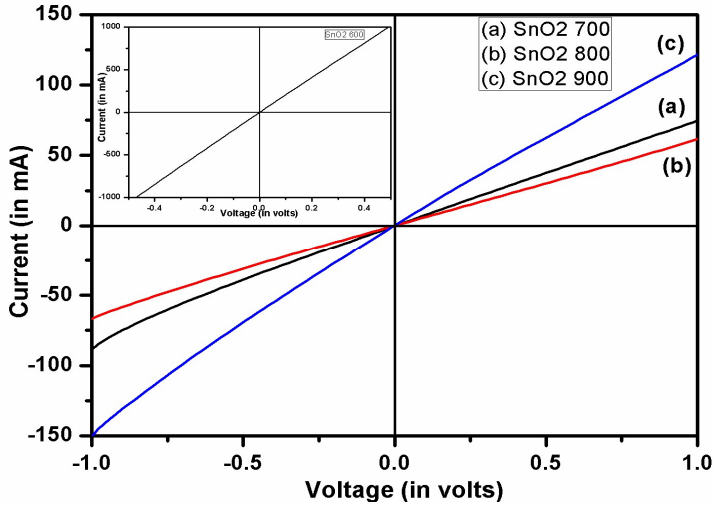

Figure 4.29: I-V measurements of pure SnO_2 (a) 600°C (b) 700°C (c) 800°C and (d) 900°C

Fig. 4.28 shows the resistance variation with temperature for SnO_2 specimens. R-T measurements suggest good thermal stability in the operating temperature region [112]. The decrease in resistance with increase in temperature could also be attributed to negative temperature coefficient and semiconducting nature [181]. Fig. 4.29 shows the current-voltage characteristics for SnO_2 pellets. The current voltage characteristics are almost linear which is indicative of ohmic nature of the specimens.

4.9 Microwave sintering

Microwave heating has the possibility for homogeneous and quick heating as the energy is absorbed straight inside the heated object, instead of heat being conducted from the outside as in conventional heating. Uniformity in heating is important because it will prevent temperature gradients. In conventional heating, energy is absorbed only at surface of the material and then it transferred into the bulk by conduction. Gradients in temperature exist in the fired sample until it achieves thermal equilibrium. Fast firing by microwaves can lead to improvement in densification [82-83]. Microwave sintering is predicted to have numerous benefits like quick and volumetric heating, enhanced production rate, improvement in densification and grain growth constraint in ceramics. Microwave heating is an output

of an interaction between electromagnetic waves and material molecules. Reduced temperature densification is larger in microwave heating in comparison to conventional heating. The higher densification noticed at the time of microwave sintering is generally ascribed to enhanced grain boundary diffusion.

Microwave sintering is a way of surface modification, as it is a rapid and volumetric heating. Microwave sintering of Zn-doped SnO_2 pellets was done in the microwave sintering furnace with the ceramic cavity where samples were placed for microwave sintering. Microwave sintering was carried out at 600°C for 30 mins.

4.9.1 Characterization

The specimens were characterized by XRD, FESEM and UV-Vis spectroscopy using characterization tools mentioned in section 4.3.2.

4.9.2 Results and discussions

4.9.2.1 XRD studies

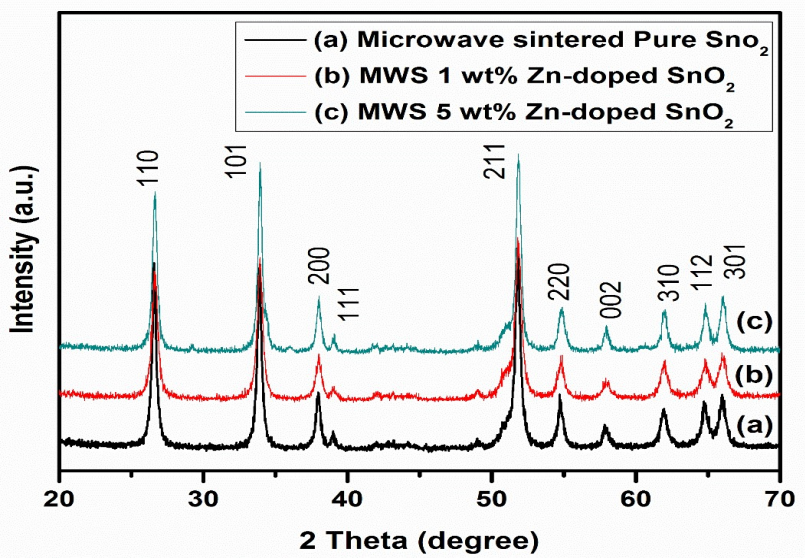

Figure 4.30: XRD pattern of microwave sintered SnO_2 nanopowder (a) Pure SnO_2 (b) 1 wt% (c) 5 wt% Zn incorporation

The diffraction patterns of microwave sintered pure and Zn-doped SnO_2 nanopowders with different Zn concentrations i.e. 1 and 5 wt% are indicated in Fig. 4.30 (a-c). The sharp diffraction peaks suggested the good crystallinity of the samples. In the present investigation, all diffraction peaks in the pattern of Fig. 4.30 indicate the formation of tetragonal rutile structure, which indicates the synthesis of pure SnO_2. The addition of Zn broadens the FWHM of diffraction peaks, which is suggestive of the decrease in particle size. However, XRD pattern did not show any peak pertaining to Zn/ ZnO phase in doped SnO_2 specimens, which is probably due to the low content of Zn-dopant since the amount of Zn in nanopowder is confirmed by EDX shown earlier in Fig. 4.9. The crystallite size is increased (as shown in Fig. 4.30) due to microwave sintering in comparison to un-sintered sample as shown in Fig. 4.7.

4.9.2.2 Electron microscopy studies

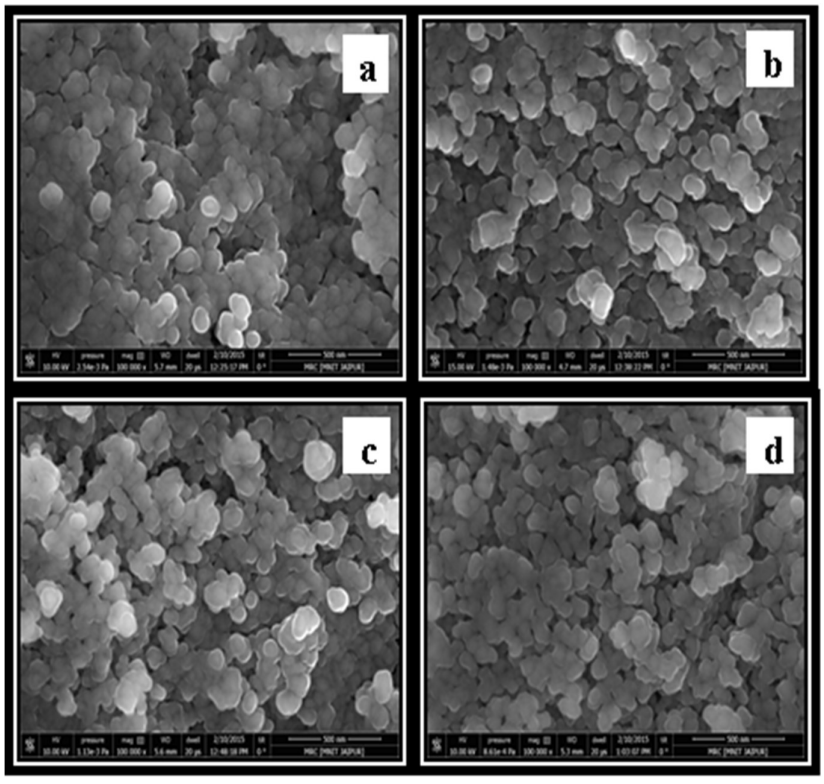

Figure 4.31: FESEM images of microwave sintered SnO_2 nanopowder (a) Pure SnO_2 (b) 1 wt% Zn, (c) 3 wt% Zn, (d) 5 wt% Zn incorporation

The FESEM micrographs of microwave sintered pure and Zn-doped SnO_2 nanopowders are showed in Fig. 4.31. These figures show uniform morphology with spherical shape of particles with different doping concentration. It is apparently seen that the crystallite size of the nanostructured material decreases with the increasing doping concentration. The surface of the pellet is approximately homogeneous with some agglomerates. SnO_2 doped with 1, 3 and 5 wt% Zn showed comparatively high clustering [Fig. 4.31 (b-d)]. Fig. 4.9 shows the EDX spectra of Zn-doped SnO_2 sample which confirms the presence of Zn in the specimens. Fig. 4.31 is in same agreement with Fig. 4.8, only crystallite size is increased as a result of microwave sintering.

4.10 Conclusion

Pure and doped (Zn, Cu, Ni, Fe and Sb) SnO_2 nanopowders with different concentration (1 wt%, 3 wt% and 5 wt%) of doping were synthesized by sol-gel method. These as-synthesized nanopowders show good crystallinity with tetragonal rutile phase. No impurity peak was seen in the XRD pattern by any of the nanopowder. It has been found in the case of Zn and Cu doping that with the increase in dopant concentration the crystallite size decreases and the band gap increases. But in the case of Ni, Fe and Sb doping the crystallite size increases with doping concentration. The variation is also observed to change the surface morphology of resultant product. After thermal annealing of the SnO_2 nanopowders the phase of the sample does not change with higher annealing temperature, but the crystallite size increases. The surface morphology of powder shows the uniformity in the grain size of the samples and crystallite size of the nanoparticles goes on increasing as the annealing temperature increases. From I-V and R-T measurements it is found that high temperature annealed specimens have low conductivity and good thermal stability up to 300°C. Microwave sintering of Zn-doped SnO_2 pellets resulted in an increase in grain size after sintering.

Chapter -5

Gas Sensing Behaviour Studies

5.1 Introduction

As SnO_2 is an n-type semiconductor, it is generally believed that the gas sensing characteristics of SnO_2 originate from the reaction between the test gas and the chemisorbed oxygen ions on the surface of SnO_2 nanoparticles, such as O_2^-, O^-, O^{2-} [187], resulting in a change in the concentration of absorbed oxygen. Oxygen ions absorbs onto the material surface removing electrons from the bulk and creating a potential barrier that limits electron movement and conductivity. When reactive gases (reducing gases like H_2, CH_4, H_2S etc.) combine with the oxygen, the height of the barrier is reduced results the increasing conductivity. This change in conductivity is directly related to the amount of a specific gas present in the environment resulting in a quantitative determination of gas presence and concentration. Principle of sensing is the modification of the surface electrical conductivity of tin dioxide by the absorption of reducing or oxidizing gases onto its surface [40].

Gas sensitivity: For oxidizing gas (e.g. NO_2, CO_2 etc.)

$$S = \frac{\left[R_g - R_a\right]}{R_a} \qquad 5.1$$

For reducing gas (e.g. CO, CH_4, H_2 etc.)

$$S = \frac{\left[R_a - R_g\right]}{R_g} \qquad 5.2$$

where: R_a = Resistance in air

R_g = Resistance in testing gas

The electrode contacts were made using silver paste on pellets. The optimum operating temperature for sensing was chosen as 300°C based on the poor observed response at temperatures below and above 300°C refer section 5.2. The gas sensing

response was determined by calculating the sensitivity (S) to reducing gas using the expression:

$$S = \frac{\left[R_a - R_g\right]}{R_g} \qquad 5.3$$

where R_a is the resistance of the sample in air, and R_g is the resistance in the presence of test gas.

Figure 5.1: Gas sensing set up at CeNSE

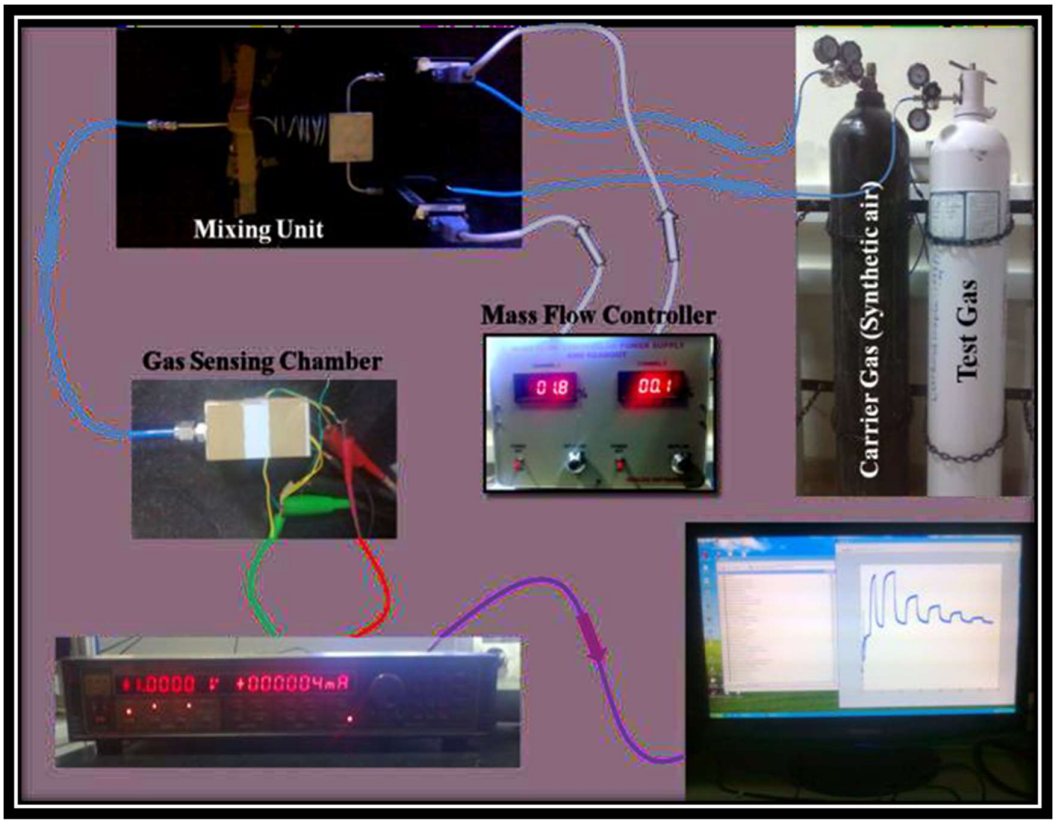

Figure 5.2: Gas sensing experiment setup. Arrow shows gas flow direction

5.2 Gas sensing study for Hydrogen (H_2) gas

Hydrogen gas is an extremely flammable gas. Its molecular formula is H_2. At room temperature (RT), it is a tasteless, odourless and colourless gas. H_2 gas is highly dangerous for humans as it has low ignition energy. It forms explosive mixtures with air and oxidizing agents. Molecule of H_2 is very small with low viscosity so it is prone to leakage, this leaking hydrogen can accumulate and reach to a flammable concentration. So, it is highly required to develop a H_2 gas sensor with good response and low cost.

It is a well-known fact that the gas sensing characteristics are highly influenced by the operating temperature of the semiconductor metal oxide sensors [188-189]. For the determination of optimum operating temperature, the sensing response curve of the pure and doped (Zn, Cu, Ni, Fe and Sb) SnO_2 pellet with respect to temperature is plotted as Fig. 5.3. Here these samples are tested for 5000 ppm of 1% H_2 gas at the operating temperature range of 100°C to 350°C. Fig. indicates that the gas response of each sample increases and reaches to its maximum value at a particular temperature, which is called the optimum operating temperature, then it decreases quickly with further increase in operating temperature. The optimum operating temperature for the samples are 300°C.

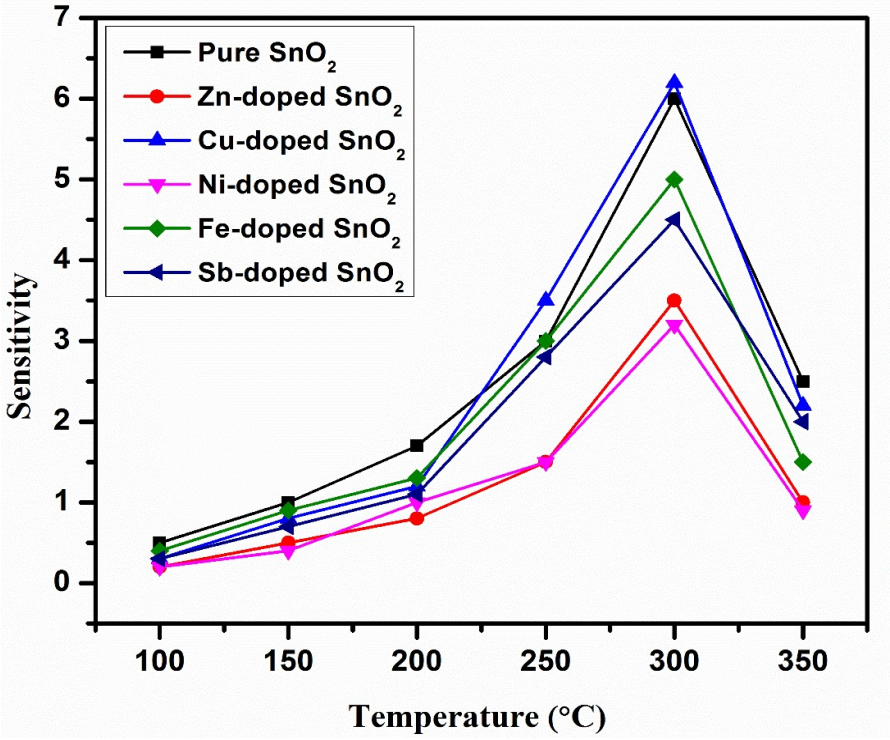

Figure 5.3: Sensitivity versus operating temperature of the sensing samples

Initially the sensing response or sensitivity increases upto 300°C then suddenly decreases with the increase in temperature. This is a common phenomenon for pure and doped SnO_2. At lower operating temperature 100°C to 300°C, the response increases due to the chemical reaction of oxygen species with H_2 gas that dominates adsorption of the oxygen ions (O^{2-} and O^-) and desorption of water. Thus at higher temperature the sensor response increases. But with the further increase in operating

temperature the sensor response decreases that is due to the desorption of reducing gas and oxygen from the sample surface [135, 190-192].

5.2.1 Pure SnO_2

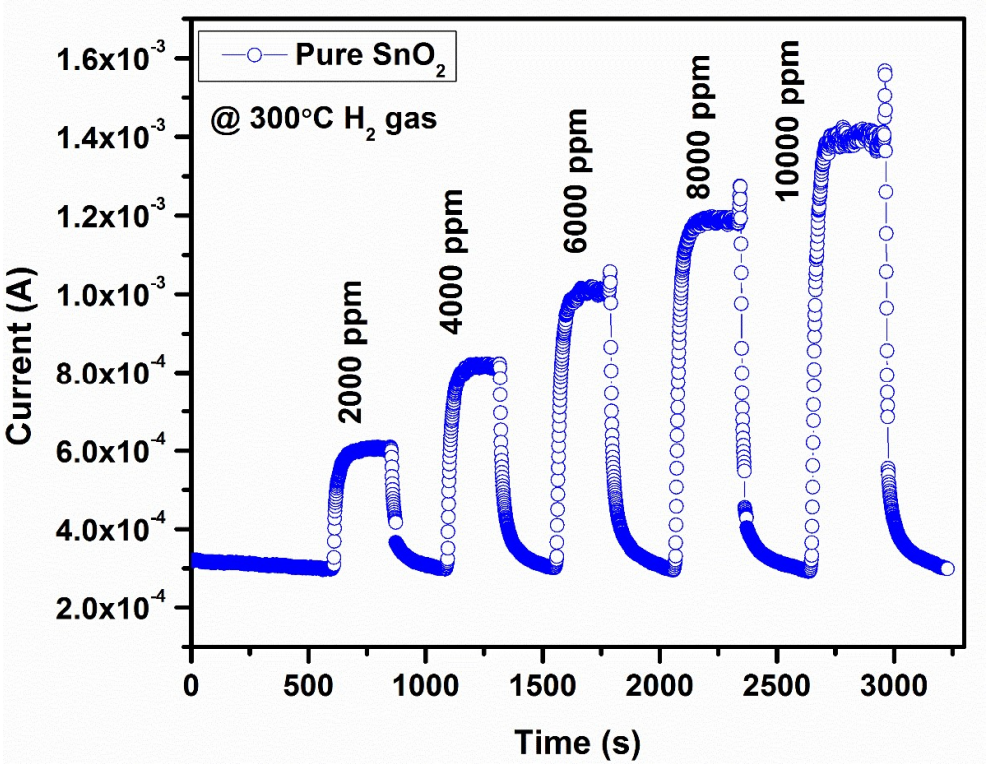

Figure 5.4: H_2 sensing characteristics shown by pure SnO_2 for 2000 ppm to 10000 ppm H_2 concentration at 300°C

The gas sensing characteristics of pure SnO_2 for (1%) H_2 is represented in Fig. 5.4 at an operating temperature of 300°C. Fig. 5.5 shows the gas sensing characteristics of pure SnO_2 prepared by method 2 (S2) for (1%) H_2 at an operating temperature of 300°C. These are some typical H_2 gas sensing curves for SnO_2 samples for 2000 to 10000 ppm at 300°C operating temperature in synthetic gas (80% N_2 and 20% O_2) environment. These curves are plotted as the change in current with the exposure of test gas i.e. H_2. Here initially the synthetic air was used to stabilize the sensing material current (resistance) and then the target gas (H_2) at a particular

concentration is tested so the current increases (resistance decreases) as SnO_2 is a n-type material and H_2 is a reducing gas. H_2 being a reducing gas, donate electrons in reaction and hence the resistance of n-type sensing material (SnO_2) decreases and current increases in its presence. As the concentration of the target gas increases, the change in current also increases. When this current is stabilized at particular concentration again we flow the synthetic gas in absence of test gas so the current goes to its base value.

Response and recovery time can be calculated by these current-time plot. These sensing curve are reproducible. In addition to this, SnO_2 pellets were also tested for 100°C, 150°C, 200°C and 250°C but at low temperatures the base current was not stable and 250°C the sensing signal is very weak (data not discussed here).

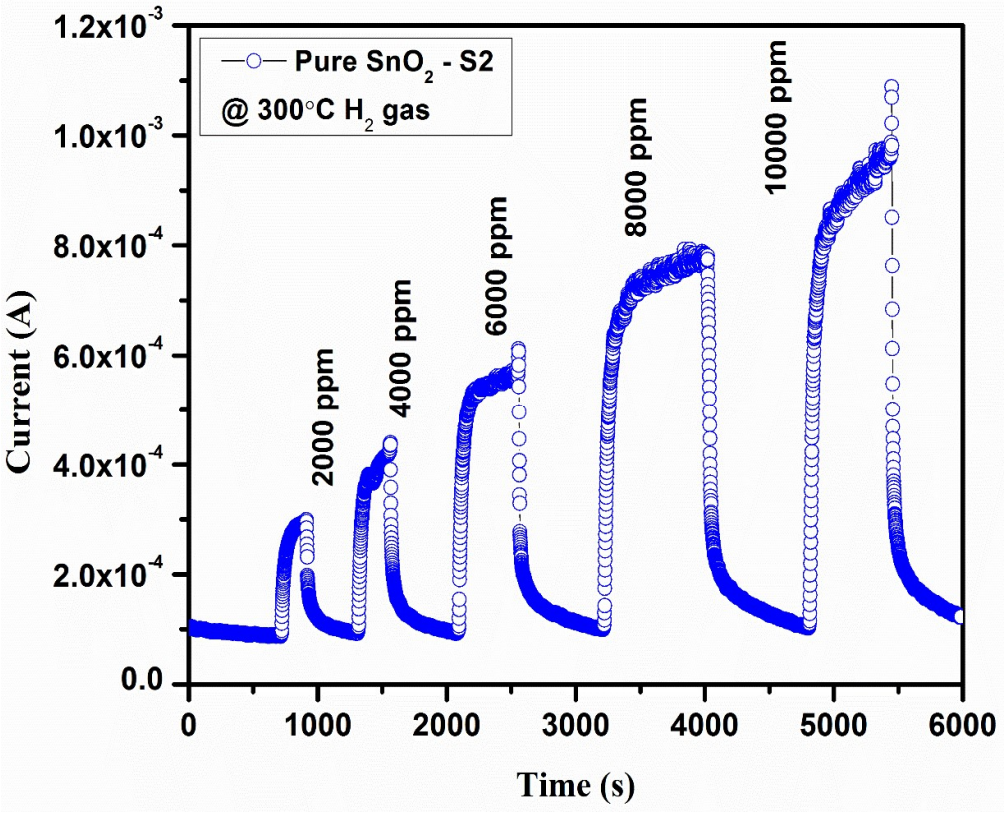

Figure 5.5: H_2 sensing characteristics shown by pure SnO_2 (S2) for 2000 ppm to 10000 ppm H_2 concentration at 300°C

The Fig. 5.6 shows the plot between gas concentration and sensitivity towards 1% H_2 gas. The linear fit of the data in Fig. 5.6 indicates the stability in the sensitivity values at 300°C operating temperature. The plot for S1 (SnO_2 prepared by method 1) shows the maximum stability after linear fitting at all concentrations. The response time are 151 s, 206 s, 227 s and 206 s, respectively for S1 (SnO_2 prepared by method 1), S2 (SnO_2 prepared by method 2), S3 (SnO_2 prepared by method 3) and S4 (commercially available SnO_2) at 2000 ppm 1% H_2 gas concentration. Similarly, recovery time for the samples are 165 s, 243 s, 269 s and 291 s, respectively for S1, S2, S3 and S4 SnO_2 at 2000 ppm 1% H_2 gas concentration. The response time and recovery time for S1 sample is low in comparison to other (S2, S3 and S4) samples. Commercially available SnO_2 (S4) shows maximum sensitivity at low concentration but at maximum concentration the value of sensitivity for S1 and S4 are almost same. Due to this increasing trend between sensitivity and gas concentration it can be concluded that pure SnO_2 specimens are suitable for H_2 detection.

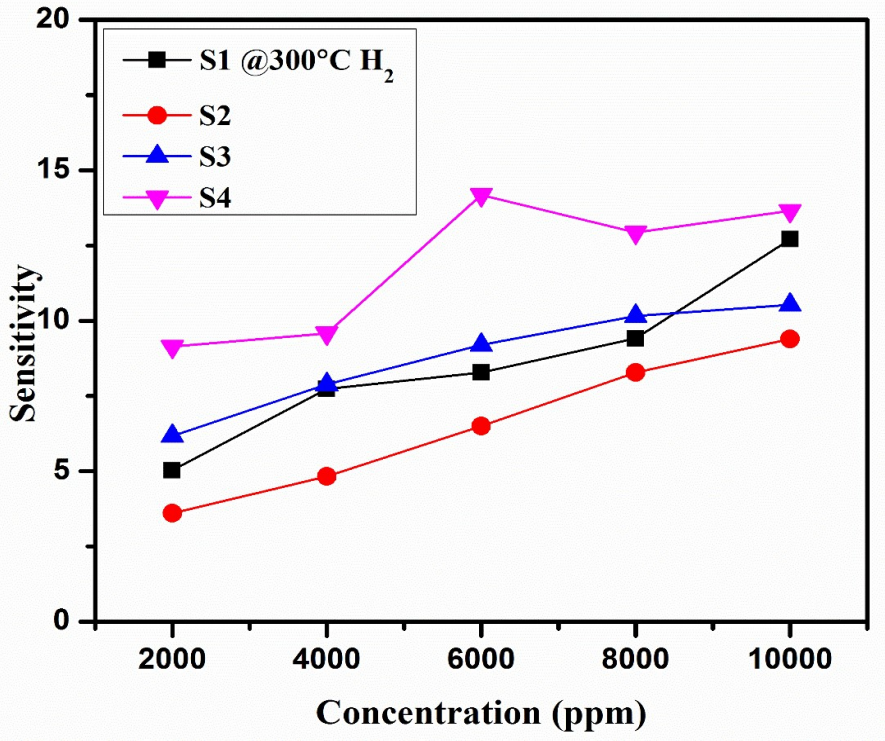

Figure 5.6: Selective response of pure SnO_2 for different concentration of H_2 (1%) at 300°C where S1- SnO_2 prepared by method 1, S2 - SnO_2 prepared by method 2, S3 - SnO_2 prepared by method 3 and S4 - commercially available SnO_2

This H_2 gas sensing mechanism is based on the chemisorption process. When metal oxide semiconductor gas sensing sample or sensor is at elevated temperature in normal air or synthetic gas environment, the oxygen species get adsorbed on the sensor surface and are ionized by free electron capture from conduction band [193]. Now when this sample is exposed to test gas (here its H_2), at a working temperature, H_2 reacts with the oxygen species and release the free electron into the conduction band and the resistance decreases (current increases).

5.2.2 Zn-doped SnO_2

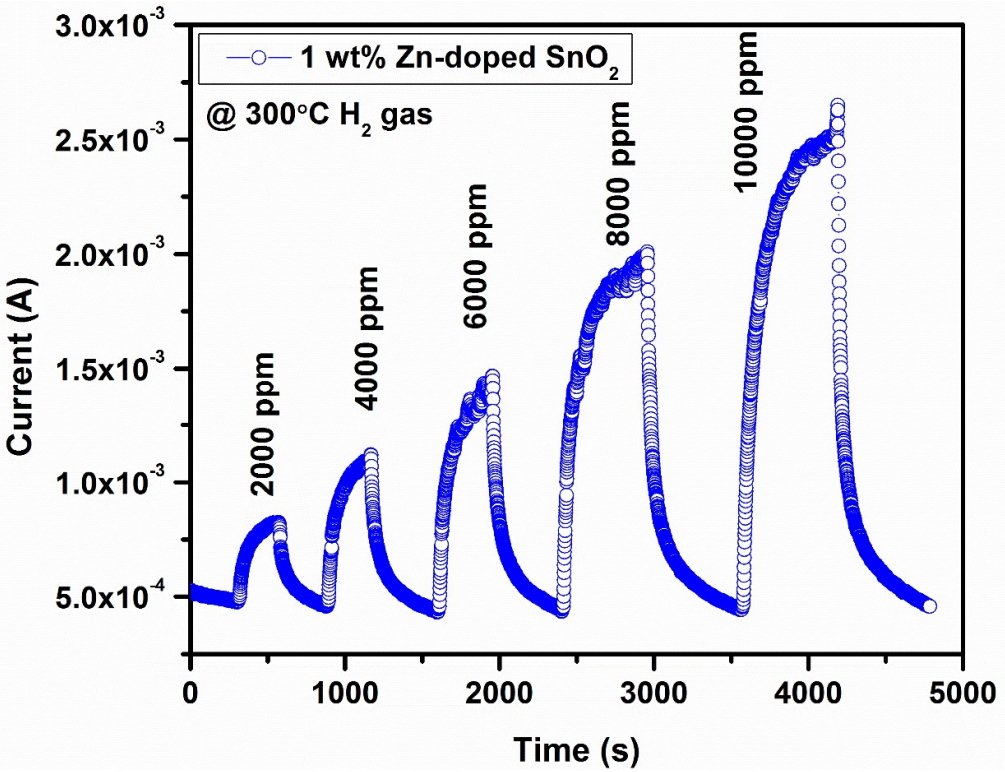

Figure 5.7: H_2 sensing characteristics shown by Zn-doped SnO_2 for 2000 ppm to 10000 ppm H_2 concentration at 300°C

The typical gas sensing characteristics curve of Zn-doped SnO_2 was evaluated at an operating temperature of 300°C for 1% H_2 gas and is represented by Fig. 5.7. This curve shows the H_2 gas sensing of Zn-doped SnO_2 sample for 2000 to 10000 ppm concentration. It is plotted between the current which changes with the exposure

of test gas i.e. H_2 and the gas concentration. The gas sensing curve characteristics are already discussed in section 5.2.1.

The sensitivity curve for differently doped Zn-doped SnO_2 are shown in Fig. 5.8. This figure indicates that Zn-doped SnO_2 can effectively detect the hydrogen. Investigations on Zn-doped SnO_2 gas sensing response for hydrogen are available in the literature [128, 194]. Fig. 5.8 shows the sensing response of Zn-doped SnO_2 samples versus 1% H_2 gas concentration ranging from 2000 ppm to 10000 ppm at 300°C temperature and indicates the increase in sensitivity with the increase in gas concentration. The highly doped (5 wt% Zn-doped SnO_2) sensing material showed the maximum sensitivity even at lower concentrations. The response and recovery times are important parameters for gas sensing. The response and recovery time for pure SnO_2, 1 wt% Zn-doped SnO_2 and 5 wt% Zn-doped SnO_2 are 216 s and 225 s, 258 s and 259 s, 301 s and 387 s, respectively at 2000 ppm H_2 gas.

The gas sensing mechanism is based on the change in the depletion layer by the adsorption of test gas to surface of sensing sample [195-198]. When the Zn-doped SnO_2 sample is exposed to air, the oxygen molecules adsorbed on to the surface. These adsorbed oxygen convert into oxygen ions (O_2^-, O^{2-}, O^-) by capturing the electrons from the conduction band of Zn-doped SnO_2, this leads to increase in resistance of the sensing material. And when this sensing material or sensor is exposed to reducing gas like H_2, the adsorbed oxygen reacts to H_2 molecules on the sample surface, so the trapped electrons release back to conduction band which tends to increase the charge carriers of Zn-doped SnO_2 and the resistance of the sensor decreases [199]. The surface reaction between the H_2 gas molecule and surface oxygen is given by

$$H_2 + 2O^- \rightarrow O + H_2O + 2e^- \qquad 5.4$$

An important parameter for sensor performance is the capability of sensing material to adsorb and ionize the oxygen species. The reason of the high sensitivity of the Zn-doped SnO_2 is, the doping of Zn which decreases the grain size. Thus the surface of nanostructured sensing material becomes more reactive which means more adsorption of oxygen and ionization of oxygen species. It also increases the surface area of doped SnO_2, so the reaction rate also increases. The another reason is

substitution of Zn^{2+} for Sn^{4+}, which increases the amount of oxygen vacancies in Zn-doped SnO_2. This also results in the more surface reactions and thus lead to an increase in the sensor response.

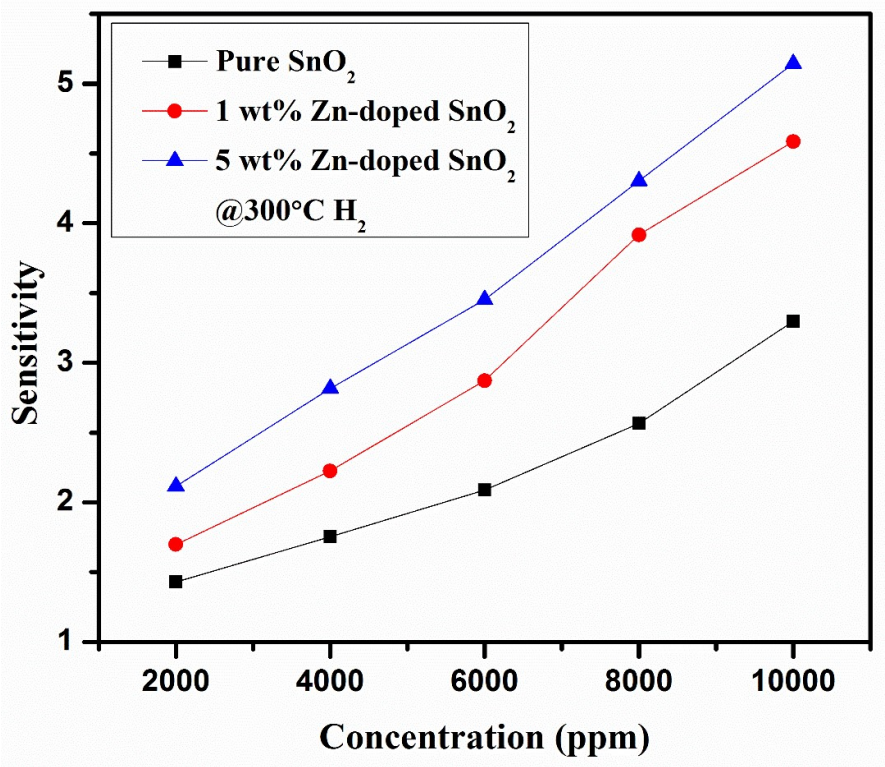

Figure 5.8: Selective response of pure SnO_2 for different concentration of H_2 (1%) at 300°C

5.2.3 Cu-doped SnO_2

The gas sensitivity of the sample is highly dependent on operating temperature and doping concentration. For the determination of optimum operating temperature, the sensitivity of the sample with 5000ppm of H_2 gas concentration at different operating temperatures have been tested which is shown in Fig. 5.3. According to this the optimal operating temperature of Cu-doped SnO_2 for H_2 is 300°C.

It is due to the fact that chemical activation leads to inert sensitivity at low operating temperature, while in very high operating temperature range, the absorbed gas molecules escape before reaction happens and so sensitivity becomes low as well [200].

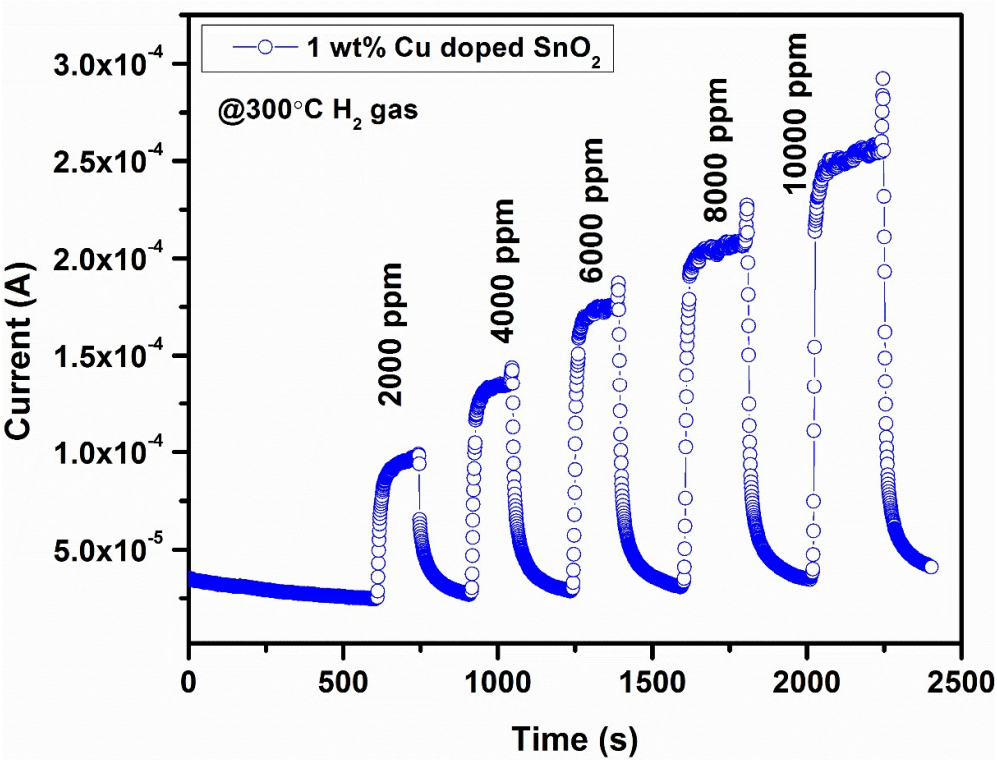

Figure 5.9: H_2 sensing characteristics for 1 wt% Cu-doped SnO_2 for 2000 ppm to 10000 ppm H_2 concentration at 300°C

The response and recovery characteristics or the gas sensing characteristics of 1 wt% Cu-doped SnO_2 and 3 wt% Cu-doped SnO_2 are shown in Fig. 5.9 and Fig.5.10, respectively. According to these curves the response and recovery time for 1 wt% Cu-doped SnO_2 is small in comparison to 3 wt% Cu-doped SnO_2 samples. The response time are 118 s, 211 s, and 162 s for 1 wt%, 3 wt% and 5 wt% Cu-doped SnO_2 at 2000 ppm 1% H_2 gas concentration, respectively. Similarly, recovery time for the samples are 164 s, 193 s and 388 s for 1 wt%, 3 wt% and 5 wt% Cu-doped SnO_2 at 2000 ppm 1% H_2 gas concentration, respectively.

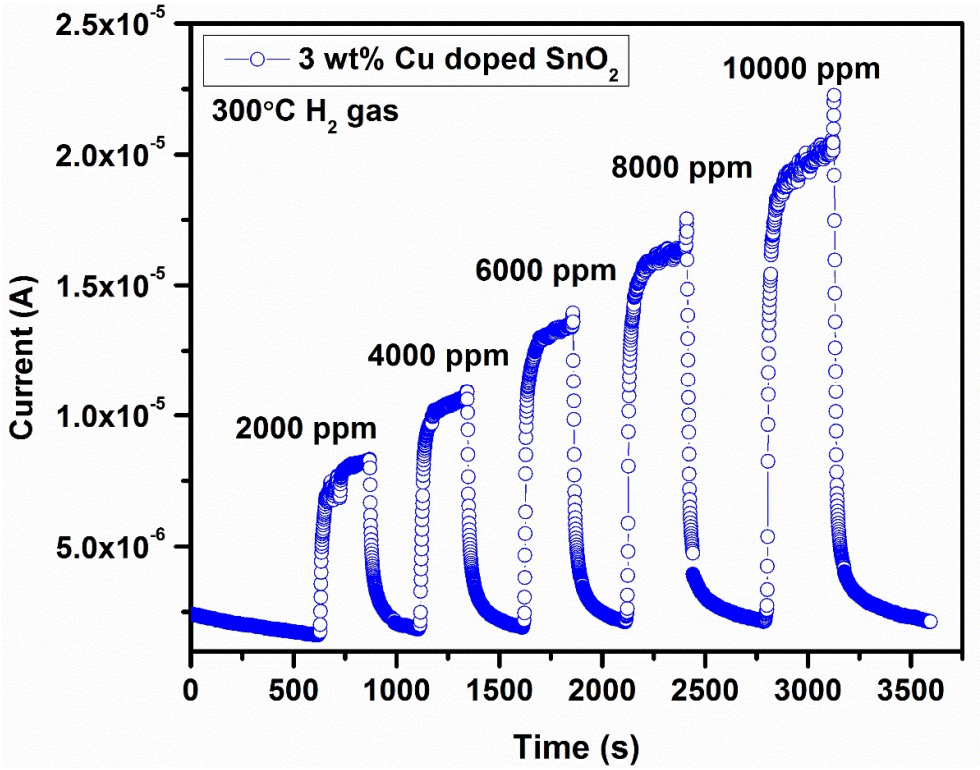

Figure 5.10: H_2 sensing characteristics of 3 wt% Cu-doped SnO_2 for 2000 ppm to 10000 ppm H_2 concentration at 300°C

The sensitivity curve for Cu-doped SnO_2 samples at operating temperature of 300°C are shown in Fig. 5.11. According to this plot, the sensitivity or sensing response increases with increase in gas concentration. Cu-doped SnO_2 shows better sensitivity in comparison to pure SnO_2 this may be due to better surface properties of Cu-doped samples like small particle size (refer section 4.4.3.1) which refers to large surface area, high pore density which provides transport of molecules and enhances the sensing performance. At 3 wt% Cu-doping the sensitivity becomes higher than the 5 wt% Cu-doping, the reason could be the deactivation of the surface area of SnO_2 with higher doping. Same type of behaviour is also reported in literature [123]. Such measured data with 1 to 11 wt% Cu-doping is available in literature [201], wherein higher sensitivity is obtained for 9 wt% Cu-doping at 230°C temperature. The doping leads to change in chem-sensing and electrical properties and also to an enhancement in electron concentration due to which more oxygen vacancies related defects are

produced. By oxygen vacancies, more adsorption sites for molecules are given which make sensor surface more reactive and thus enhance the sensing properties.

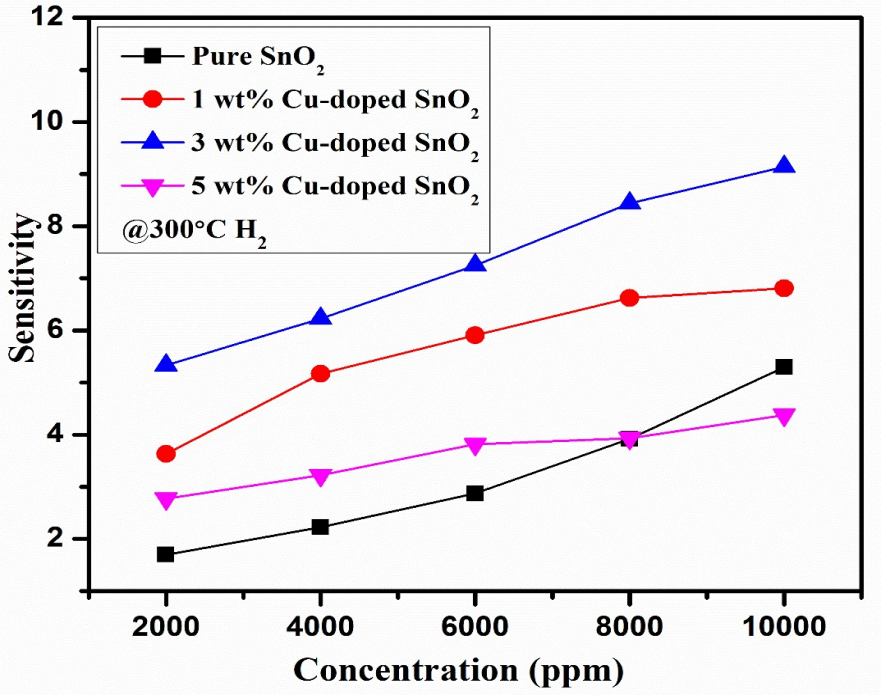

Figure 5.11: Selective response of Cu-doped SnO_2 for different concentration of H_2 (1%) gas at 300°C

The sensing mechanism can also be explained by equations:

$$O_{2\,(gas)} \rightarrow O_{2\,(ads)} \qquad 5.5$$

$$O_{2\,(ads)} + e^- \rightarrow O_2^- \qquad 5.6$$

$$O_2^- + e^- \rightarrow 2O^- \qquad 5.7$$

$$H_2 + 2O^- \rightarrow O + H_2O + 2e^- \qquad 5.8$$

It is worth mentioning here that the gas response of the Fig. 5.11 follows almost linear behaviour which suggests that the Cu-doped SnO_2 is a promising material for H_2 sensing.

5.2.4 Ni-doped SnO_2

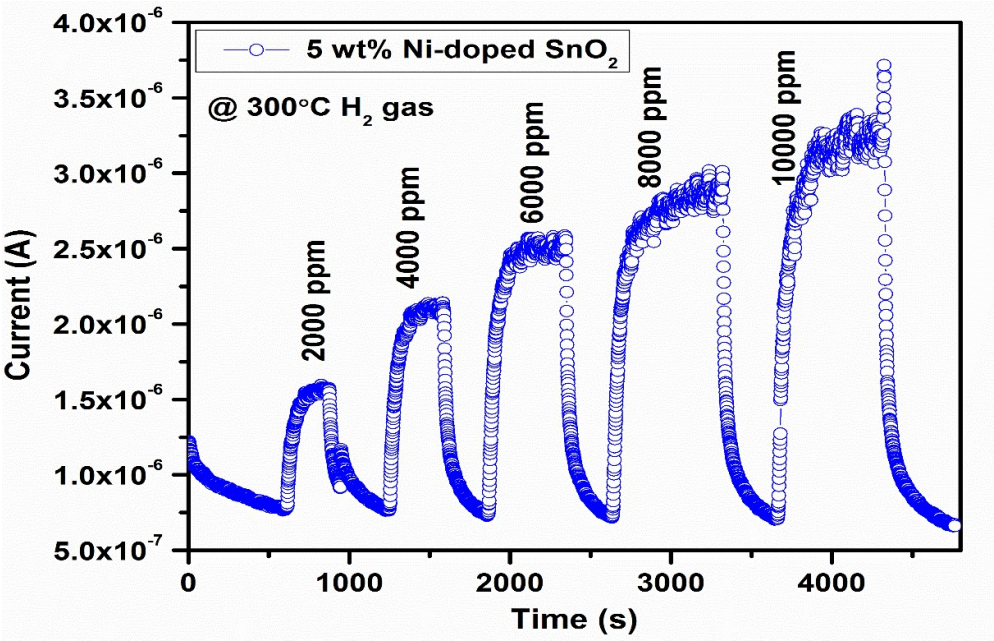

Figure 5.12: H_2 sensing characteristics of 5 wt% Ni-doped SnO_2 for 2000 ppm to 10000 ppm H_2 concentration at 300°C

A typical gas sensing curve for 5 wt% Ni-doped SnO_2 is represented in Fig. 5.12. The operating temperature as mentioned earlier is taken as 300°C. It was shown in Fig. 5.3 wherein the sensitivity versus temperature curve were plotted. It is suggested from this figure that the operating temperature value is 300°C for Ni-doped SnO_2 for 5000 ppm H_2 gas. The H_2 sensing characteristic curve for 5 wt% Ni-doped sample is shown in Fig. 5.12. Similar sensing plots of pure, 1 wt% and 3 wt% Ni-doped SnO_2 were obtained (not shown here).

Fig. 5.13 shows the H_2 gas concentration dependent sensitivity values of pure and Ni-doped SnO_2 samples. This figure indicates that the gas response or sensitivity increases significantly with increase in gas concentration, while the pure SnO_2 shows slow increase with higher concentration.

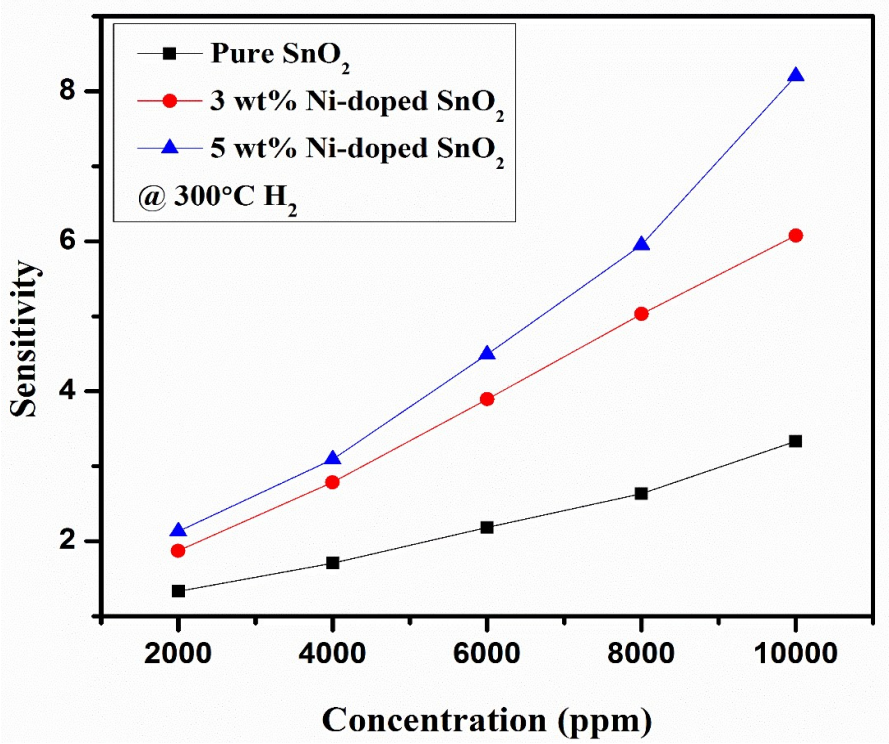

Figure 5.13: Selective response of Ni-doped SnO_2 for different concentration of H_2 (1%) gas at 300°C

According to Fig. 5.13 at initial concentrations the value of sensitivity is not significantly different for pure and doped specimens. For higher concentrations the Ni-doped SnO_2 samples gave better gas response in comparison to pure SnO_2 samples. The 5 wt% Ni-doped SnO_2 gives high sensitivity for H_2 gas. Some other reports are also available in literature for Ni-doped SnO_2, but these are for ethanol sensing [151]. The reducing gas sensing characteristics depend on the interaction between the reducing gas like H_2 or H_2S or CH_4 etc. and the chemisorbed oxygen ions (O_2^-, O^- and O^{2-}) on active surface of sensor. Refer section 5.2.2 for sensing mechanism. The increased sensitivity in the case of Ni-doped SnO_2 can be attributed to the fact that possibly at the interface between SnO_2 and NiO, Ni^{2+} acceptor ions are incorporated at

the Sn^{4+} site. The other reason may be the p-n junction formation between SnO_2 and NiO. It has been reported earlier that the decrease in donor due to the incorporation of an acceptor increases the gas response [202]. When the small amount of p-type NiO grains in n-type SnO_2 material (large amount) combines with SnO_2 materials, it forms a p-n junction, due to which sensor resistance and barrier height increases, so it enhances the sensor response [153]. The response time are 212 s, 258 s, and 199 s for pure, 3 wt% and 5 wt% Ni-doped SnO_2, respectively at 2000 ppm 1% H_2 gas concentration. Similarly, recovery time for the samples are 235 s, 247 s and 352 s for pure, 3 wt% and 5 wt% Ni-doped SnO_2, respectively at 2000 ppm 1% H_2 gas concentration.

5.2.5 Fe-doped SnO_2

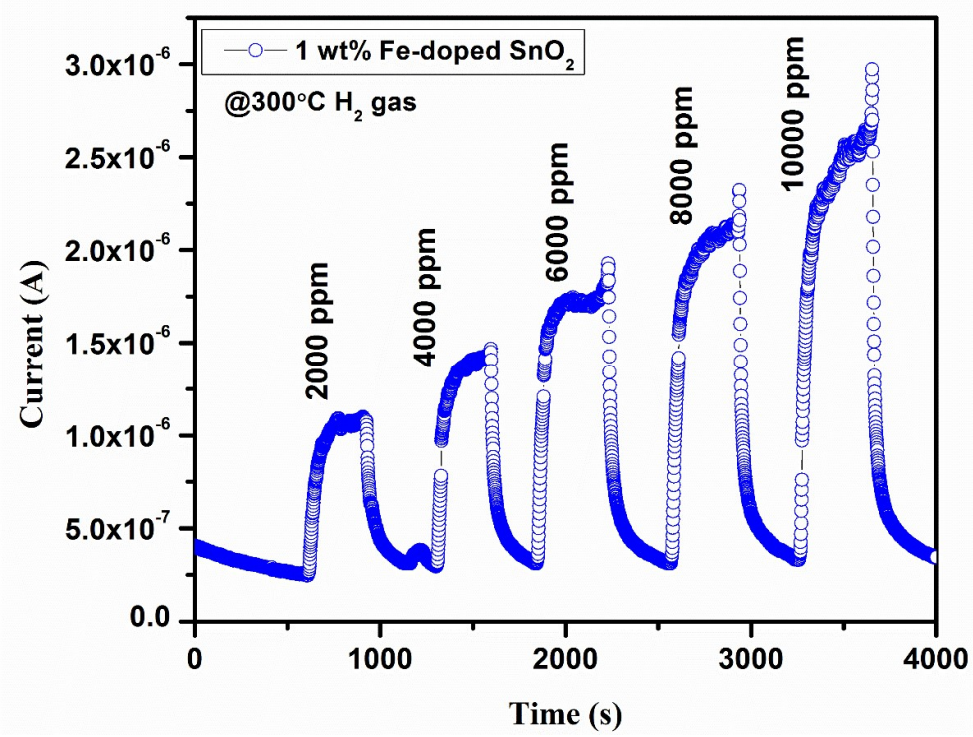

Figure 5.14: Fe-doped SnO_2 sensing characteristics for 2000 ppm to 10000 ppm H_2 concentration at 300°C

The typical gas sensing curve or the response-recovery curve of Fe-doped SnO_2 for 1% H_2 gas at 300°C is given by Fig. 5.14. According to this curve, the current increases with the increase in gas concentration with shows the better response with concentration. The sensitivity curves of the Fe-doped SnO_2 with respect to concentration are given in Fig. 5.15. Here the sensitivity increases with the increase in gas concentration for both pure and Fe-doped samples. But only upto 1 wt% Fe-doping the sensitivity increases then after that the sensitivity for higher Fe-doped SnO_2 go below the pure SnO_2 sensitivity signal. It may be due to the deactivation of the surface area of SnO_2 with higher doping. Same type of behaviour is also reported in the literature [123]. The response time are 106 s, 282 s, 127 s and 416 s for pure, 1 wt%, 3 wt% and 5 wt% Fe-doped SnO_2, respectively at 2000 ppm 1% H_2 gas concentration. Similarly, recovery time for the samples are 224 s, 274 s, 114 s and 384 s for pure, 1 wt%, 3 wt% and 5 wt% Fe-doped SnO_2, respectively at 2000 ppm 1% H_2 gas concentration.

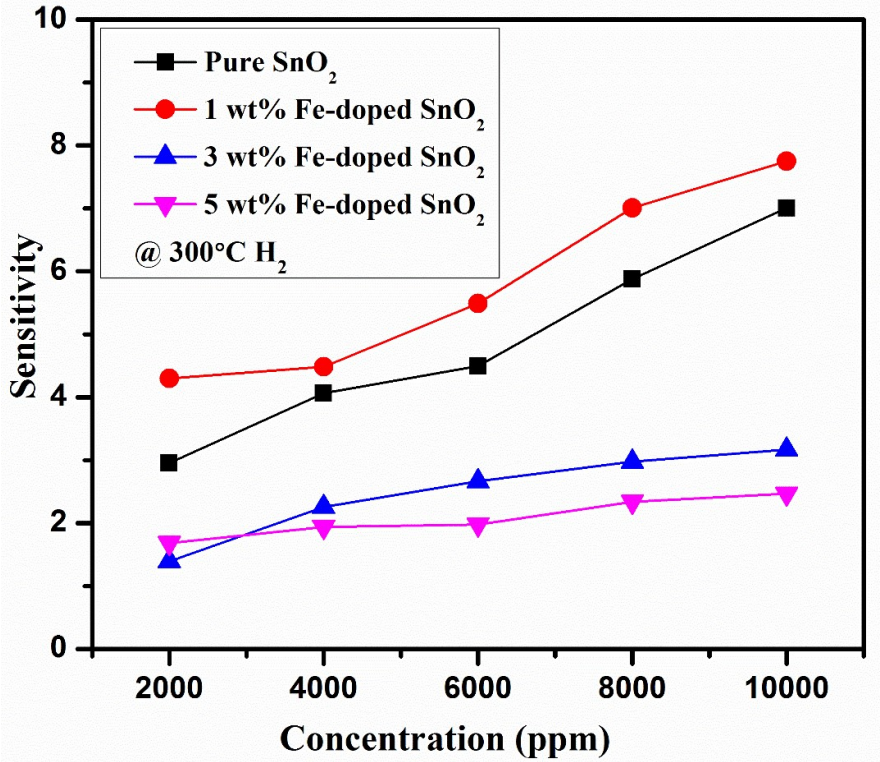

Figure 5.15: Selective response of Fe-doped SnO_2 for different concentration of H_2 (1%) gas at 300°C

1 wt% Fe-doped SnO_2 shows maximum sensitivity towards H_2 gas. The gas sensing characteristics of metal oxides semiconductors are dependent on the change in electrical properties of the material that is due to the surface reactions on sensor [203]. The sensing mechanism is already given in section 1.3.4 and 5.2.2. The Fe-doping effect on the gas sensing characteristics could be explained by defect chemistry model of SnO_2 doped with acceptor atoms as given by Fukui and Nakane et al. [204]. Here Fe^{3+} ion behaves as an acceptor for SnO_2, which increases the sample resistivity and enhances the sensor performance.

5.2.6 Sb-doped SnO_2

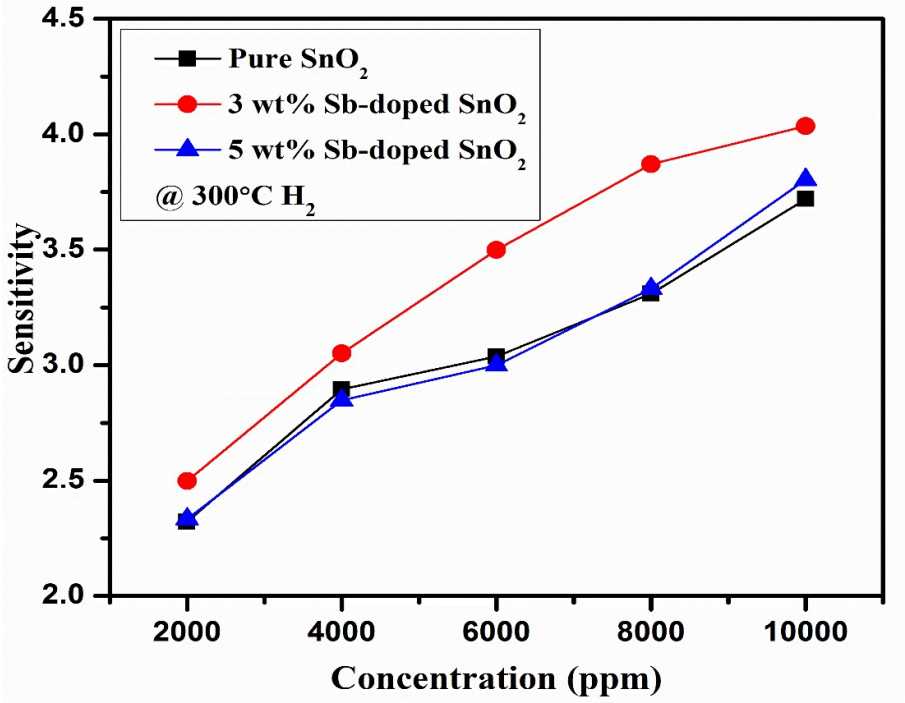

Figure 5.16: Selective response of Sb-doped SnO_2 for different concentration of H_2 (1%) gas at 300°C

The sensitivity curve for pure SnO_2, 3 wt% Sb-doped SnO_2 and 5 wt% Sb-doped SnO_2 with respect to H_2 gas concentration from 2000ppm to 10000 ppm at 300°C in given by Fig. 5.16. The 300°C is the operating temperature for Sb-doped SnO_2. It has been determined by Fig. 5.3 which is plot between the sensitivity and

temperature, which suggests the operating temperature value for Sb-doped SnO_2 for 5000 ppm H_2 gas. The sensitivity of 3 wt% Sb-doped SnO_2 is higher with respect to pure SnO_2 and 5 wt% Sb-doped SnO_2. The response and recovery times are 194 s, 234 s, 194 s and 344 s, 438 s, 335 s for pure, 3 wt% and 5 wt% Sb-doped SnO_2, respectively at 2000 ppm 1% H_2 gas concentration. It is a known fact that the gas sensing characteristic are the surface phenomenon and in metal oxides it depends on adsorbed oxygen species. So it could be a reason that Sb-doping give rise to various oxygen species and active surface sites, resulting in an increase in gas response. The decrease in the sensitivity of 5 wt% Sb-doped SnO_2 could be due to the deactivation of the surface area of SnO_2 with higher doping [123, 146]. It could also be associated with poor morphology and crystallinity.

5.2.7 Thermal Annealed SnO_2

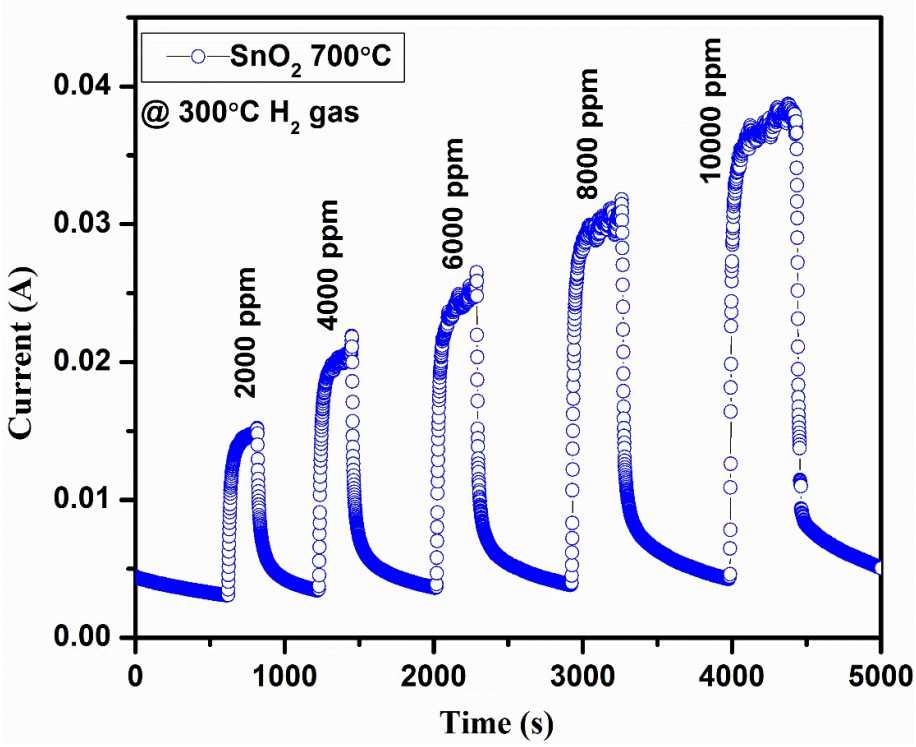

Figure 5.17: Thermal annealed pure SnO_2 sample sensing characteristics for H_2 concentration 2000 ppm to 10000 ppm at 300°C

The gas sensing characteristics of pure SnO_2 annealed at 700°C for (1%) H_2 is represented in Fig. 5.17 at an operating temperature of 300°C. This is a typical H_2 gas sensing curves for SnO_2 samples for 2000 to 10000 ppm at 300°C operating temperature. Fig. 5.18 shows the gas sensing characteristics of pure SnO_2 samples annealed at different temperatures for (1%) H_2 concentration at an operating temperature of 300°C. 300°C is the optimum operating temperature which is determined by sensitivity versus temperature curve shown in Fig. 5.3. In Fig. 5.3 it was shown that the sensitivity is increased till a particular value of temperature and then decreased. The optimum operating temperature is the temperature where the sensitivity is maximum for H_2 gas at 5000 ppm.

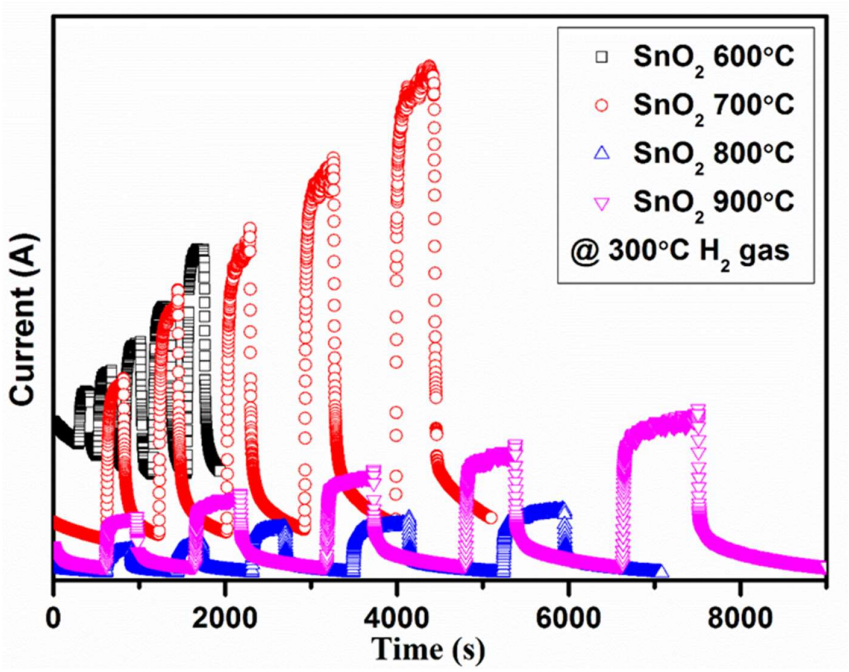

Figure 5.18: Differently annealed pure SnO_2 samples sensing characteristics for H_2 concentration 2000 ppm to 10000 ppm at 300°C

Fig. suggests that as the concentration of the target gas increases, the change in current also increases. Response and recovery time increases with the increase in annealing temperature. The response time is 102 s, 178 s, 281 s and 298 s and

recovery time is 83 s, 369 s, 477 s and 820 s for SnO_2 annealed at 600°C, SnO_2 annealed at 700°C, SnO_2 annealed at 800°C and SnO_2 annealed at 900°C, respectively at 2000 ppm 1% H_2 gas concentration. In this case, SnO_2 annealed at 600°C have low response and recovery time according to Fig. 5.18, but the sensitivity of this sample is small in comparison to other samples.

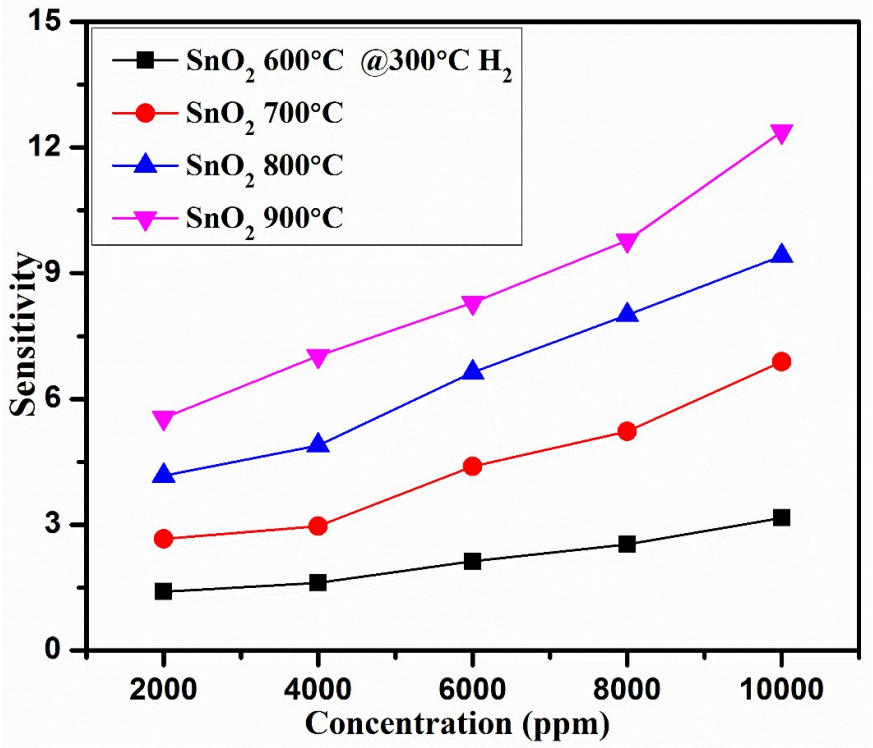

Figure 5.19: Selective response of differently annealed pure SnO_2 sample for different concentration of H_2 (1%) gas at 300°C

The sensitivity curve for pure SnO_2 samples annealed at 600°C, 700°C, 800°C and 900°C with respect to H_2 gas concentration from 2000 ppm to 10000 ppm at 300°C are given in Fig. 5.19. This figure indicates that sensitivity increases with increase in gas concentration. The almost linear fitting of the data in Fig. 5.19 indicates the stability in the sensitivity values at 300°C operating temperature irrespective of the grain size.

SnO_2 annealed at 600°C gives low gas response and with the increase in annealing temperature the sensitivity increases. SnO_2 annealed at 900°C shows maximum sensitivity. Xu et al. [205] explained that the sensitivity depends upon the grain boundary contacts and neck contacts. SnO_2 crystallites are connected by grain

boundary contacts or by neck contacts with their neighbours. When the crystallites are connected by grain boundary contacts then conduction electrons move across the potential barrier at every grain boundary, the height of this barrier is modified with the surrounding atmosphere. In this case the sensitivity is independent of grain size.

5.2.8 Microwave sintered Zn-doped SnO_2

The gas response curves for microwave sintered pure and Zn-doped (1 wt%, 3 wt% and 5 wt%) SnO_2 samples with respect to H_2 gas concentration from 2000 ppm to 10000 ppm at 300°C in given by Fig. 5.20. This figure indicates the sensitivity increases with the increase in gas concentration. In H_2 detection, using microwave sintered Zn-doped SnO_2 samples, the sensitivity changes considerably for 1 wt% Zn-doping and decreases with further addition of Zn concentration.

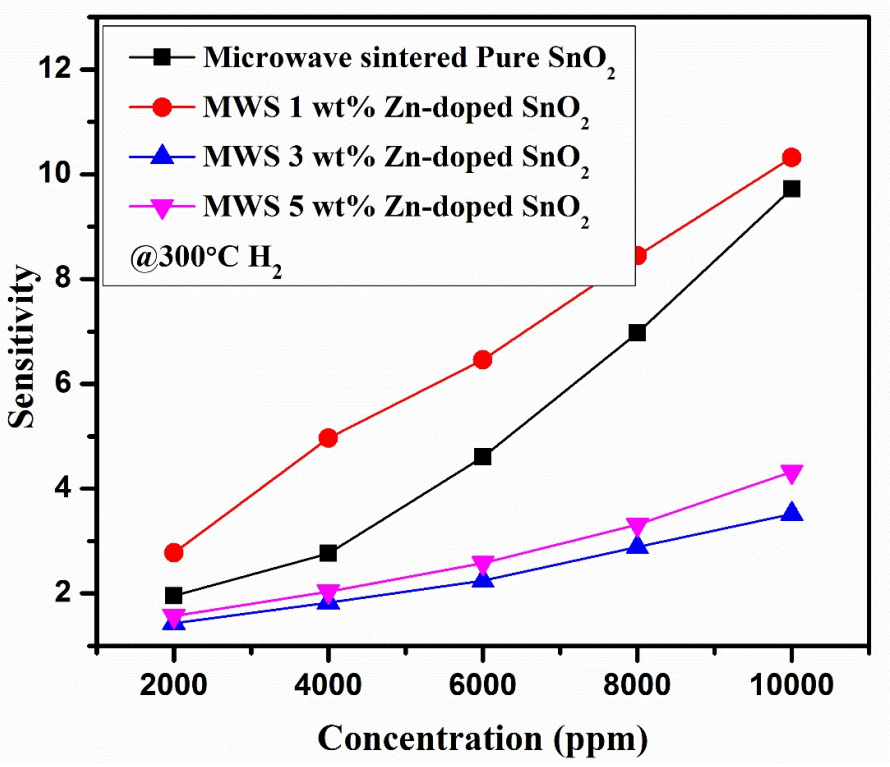

Figure 5.20: Sensitivity curve at 300°C of microwave sintered Zn-doped SnO_2 for different concentration of H_2 (1%)

The 1 wt% Zn-doped SnO_2 was discovered to be the most suitable for H_2 detection. It is important to note here that the high doping of Zn display less chances for H_2 sensing in comparison to low doping concentrations for microwave sintered samples. The microwave sintered Zn-doped SnO_2 samples thus show the highest sensitivity for 1 wt% Zn-doping for H_2 gas sensing. The particle size of the samples is not same as for un-sintered Zn-doped SnO_2 (for this refer section 5.2.2) but due to microwave sintering, the particle size increases (refer section 4.9.2) further so the active area for gas reaction decreases. For higher Zn-doping, the gas response should increase, as particle size decreases but due to the microwave sintering effect the particle size increases which leads to a lower value of gas response. It is fascinating to note here that microwave sintered samples show good sensing behaviour for pure and low doping concentration of Zn (1 wt% Zn) for H_2 gas.

Fig. 5.21 shows the sensitivity versus concentration plot for the comparative study of un-sintered and microwave sintered pure and Zn-doped samples towards H_2 gas sensing. This plot suggests an increase in sensitivity with increase in gas concentration. However, a considerably high change in sensitivity with respect to concentration is only visible in microwave sintered pure and 1 wt% Zn-doped SnO_2. In H_2 detection using microwave sintered Zn-doped SnO_2 samples, the sensitivity changes considerably initially for Zn-doping but it decreases with higher addition of Zn concentration. The microwave sintered 1 wt% Zn-doped SnO_2 was discovered to be the most suitable for H_2 detection. It can also be concluded here that microwave sintered samples show good sensing behaviour for the pure and low doping concentration of Zn for H_2 gas. The response and recovery times are important parameters for gas sensing. The response and recovery time for microwave sintered pure SnO_2, 1 wt% Zn-doped SnO_2, 3 wt% Zn-doped SnO_2 and 5 wt% Zn-doped SnO_2 are 101 s and 189 s; 229 s and 307 s; 205 s and 228 s; 197 s and 433 s, respectively at 2000 ppm H_2.

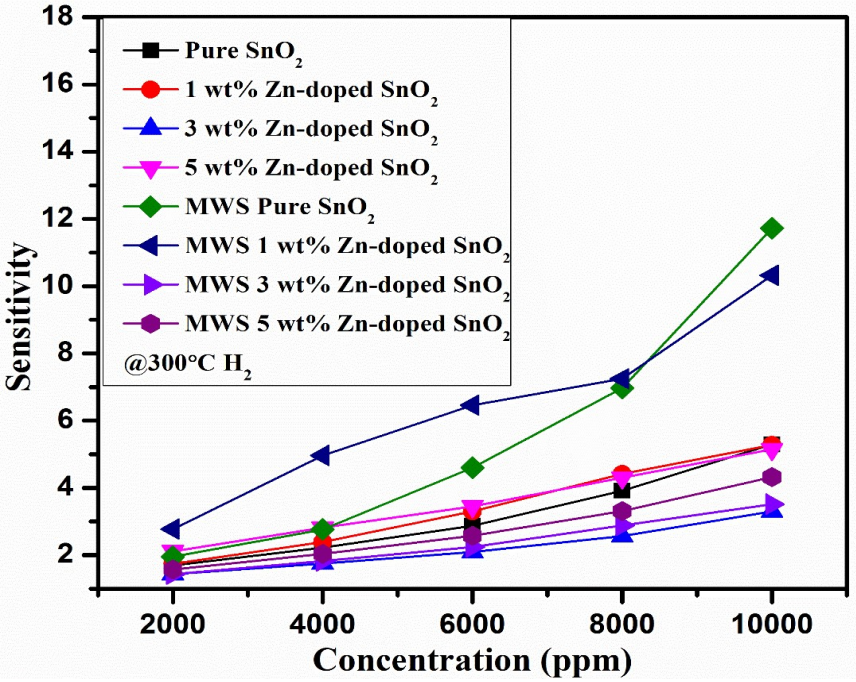

Figure 5.21: Microwave treated or untreated Zn-doped SnO_2 response for different concentration of H_2 gas at 300°C

Some of the important parameters for making a gas sensor are high sensitivity, low response and recovery time. It is observed from Table 5.1 that in the case of H_2 gas sensing at low concentration of 2000 ppm doped SnO_2 specimens used in this thesis do not show significant sensitivity for H_2 detection. However, for higher concentrations e.g. 10000 ppm, there is significant increase in sensitivity, but at the same time the response and recovery time are also observed to show an increase. For H_2 gas sensing, pure SnO_2 gave better results (~9) than (Zn, Cu, Ni , Fe and Sb) doped SnO_2. Among all the used dopants 3 wt% Cu doped SnO_2 and 1 wt% Fe doped SnO_2 gave high sensitivity (e.g. for 3 wt% Cu-doped SnO_2 sensitivity is 5.3), whereas Ni-doped and Sb-doped specimens shows low sensitivity values (refer Table 5.1). In general, for H_2 sensing high sensitivity is also obtained with significant rise in response and recovery time. Therefore, for H_2 gas detection, optimum values of these parameters need to be determined for each dopant.

Table 5.1: Response, recovery time and sensitivity values of pure and doped SnO_2 for H_2 gas at an operating temperature of 300°C

Sample	Response Time (s)	Recovery Time (s)	Sensitivity	
			2000ppm	10000ppm
S1 - SnO_2 (method 1)	151	165	5	12.7
S2 - SnO_2 (method 2)	206	243	3.6	9.4
S3 - SnO_2 (method 3)	227	269	6	10.5
S4 - SnO_2 (comm.)	206	291	9	13.6
1 wt% Zn-doped SnO_2	258	259	1.7	4.6
5 wt% Zn-doped SnO_2	301	387	2.1	5.14
1 wt% Cu-doped SnO_2	118	164	3.6	6.8
3 wt% Cu-doped SnO_2	211	193	5.3	9.14
5 wt% Cu-doped SnO_2	162	388	2.8	4.4
1 wt% Ni-doped SnO_2	212	235	1.3	3.3
3 wt% Ni-doped SnO_2	258	247	1.8	6
5 wt% Ni-doped SnO_2	199	352	2.1	8.2
1 wt% Fe-doped SnO_2	282	274	4.2	7.7
3 wt% Fe-doped SnO_2	127	114	1.4	3.17
5 wt% Fe-doped SnO_2	416	384	1.7	2.5
3 wt% Sb-doped SnO_2	234	438	2.5	4
5 wt% Sb-doped SnO_2	194	335	2.3	3.8
SnO_2 600°C	102	83	1.4	3.16
SnO_2 700°C	178	369	2.6	6.89
SnO_2 800°C	281	477	4.1	9.4
SnO_2 900°C	298	820	5.5	12.38
MW sintered 0 wt% Zn-doped SnO_2	101	189	2	12
MW sintered1 wt% Zn-doped SnO_2	229	307	2.7	10
MW sintered 3 wt% Zn-doped SnO_2	205	228	1.4	3.5
MW sintered 5 wt% Zn-doped SnO_2	197	433	1.5	4.3

5.3 Gas sensing study for Hydrogen Sulfide (H_2S) gas

H_2S is an extremely hazardous, flammable, corrosive and colourless gas with very bad smell. It is heavier than air and mixture of H_2S and air can be explosive. H_2S exposure effects on oxygen utilization and central nervous system. Low concentration

of H_2S leads to irritation in the eyes, nose, throat and respiratory system, whereas H_2S exposure at very high concentration leads to quick death. Thus highly reliable, selective and low cost sensor is needed for H_2S detection.

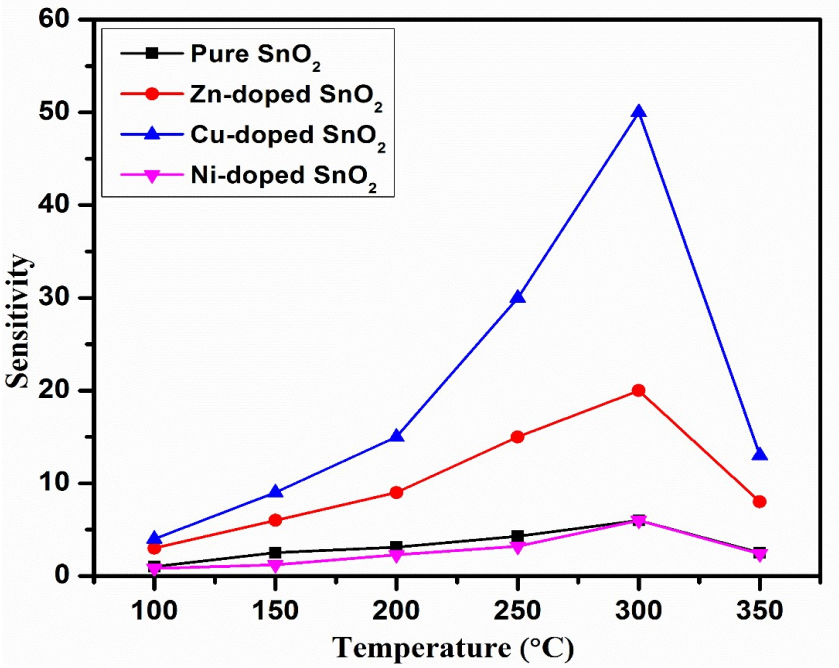

Figure 5.22: Sensitivity versus operating temperature of the sensing samples

The gas sensing characteristics are mainly dependent on the operating temperature of the semiconductor metal oxide sensors [188-189]. The sensitivity versus temperature curves were plotted to examine the optimum operating temperature. The sensing response curves are plotted for pure and doped (Zn, Cu and Ni) SnO_2 pellet in Fig. 5.22. Here, these samples were tested for 3 ppm of H_2S gas at the operating temperature range of 100°C to 350°C. Low concentration of H_2S gas have been used as it is extremely hazardous gas. For other dopants like Fe and Sb, no sensing response was found towards H_2S gas. This figure shows that the gas response of each sample increases and reaches to its maximum value at a particular temperature, which is called the optimum operating temperature, then it decreases quickly with further increase in operating temperature. The optimum operating temperature for the samples are 300°C. Cu-doped SnO_2 samples shows maximum sensitivity towards H_2S gas. At lower operating temperature 100°C to 300°C, the response increases due to the chemical reaction of oxygen species with H_2S gas that

dominates adsorption of the oxygen ions (O^{2-} and O^{-}) and desorption of water. Thus the sensor response increases with increasing temperature. But with further increase in operating temperature the sensor response decreases and this is most likely due to the desorption of reducing gas and oxygen from the sample surface [190-192].

5.3.1 Zn-doped SnO_2

The sensing of semiconductor based gas sensors is dependent on the chemisoprtion of the oxygen at the active surface of the oxide and the corresponding reactions between the oxygen species and target gas, due to which resistance/ current of the sample changes [206]. The gas sensing characteristics of 1 wt% Zn-doped SnO_2, 3 wt% Zn-doped SnO_2 and 5 wt% Zn-doped SnO_2 for H_2S gas are shown in Fig. 5.23, Fig. 5.24 and Fig. 5.25, respectively. It is noticeable here that for H_2S gas all samples show a considerably good sensing even at very low amount of gas i.e. 1 ppm. Response and recovery time can be calculated by these curves, which is not low in the case of Zn-doped SnO_2 for H_2S gas.

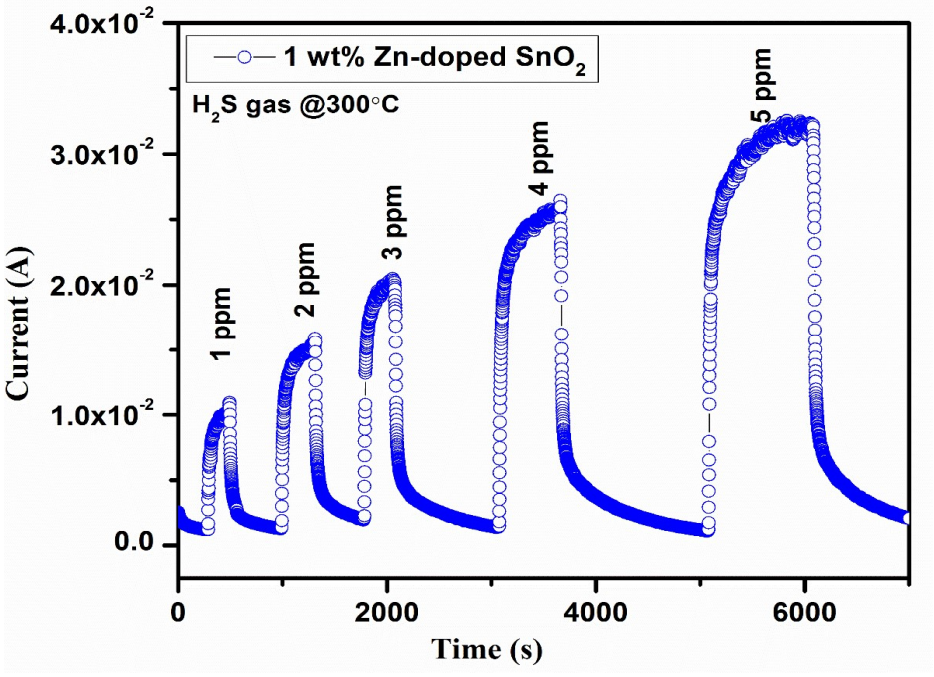

Figure 5.23: Sensing characteristics of 1 wt% Zn-doped SnO_2 sample for 1 ppm to 5 ppm H_2S gas concentration at 300°C

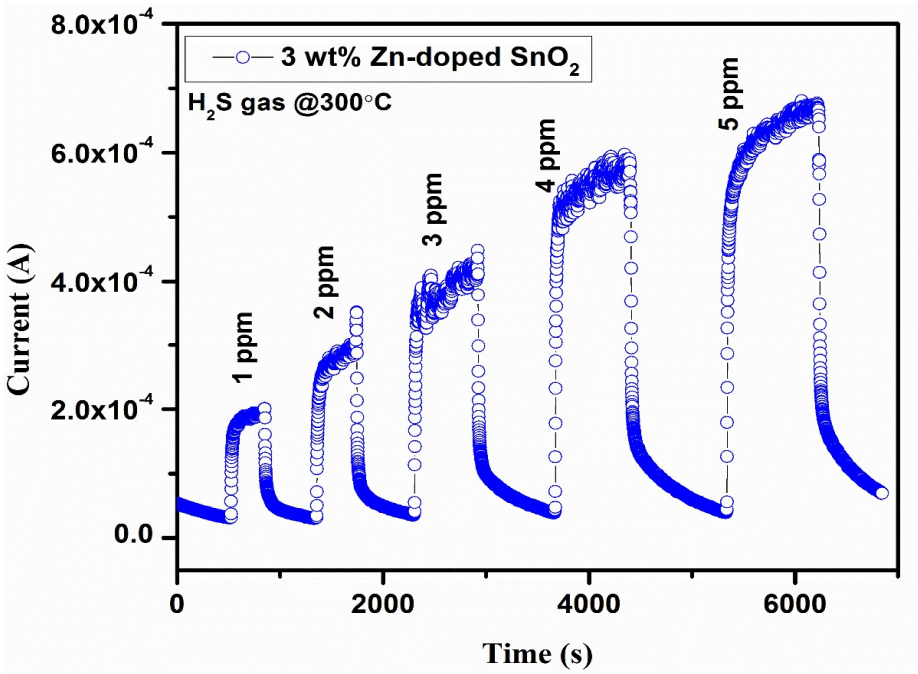

Figure 5.24: Sensing characteristics of 3 wt% Zn-doped SnO_2 sample for 1 ppm to 5 ppm H_2S gas concentration at 300°C

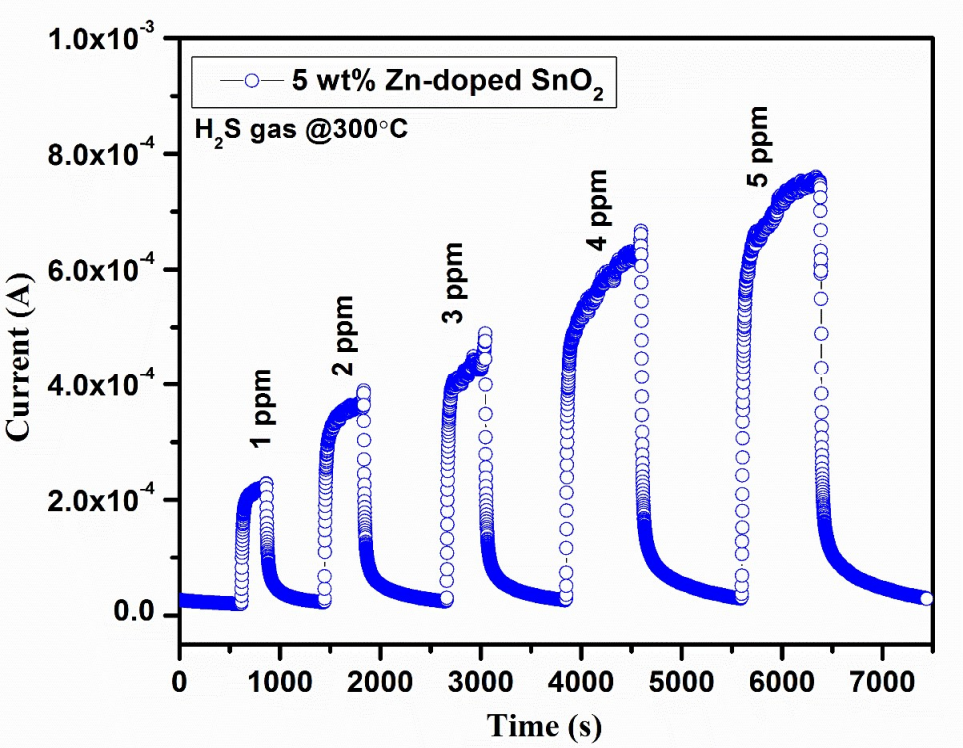

Figure 5.25: Sensing characteristics of 5 wt% Zn-doped SnO_2 sample for 1 ppm to 5 ppm H_2S gas concentration at 300°C

Fig. 5.26 shows the H_2S gas concentration dependent sensitivity values of pure and Zn-doped SnO_2 samples. This figure shows that the sensitivity increases significantly with increase in gas concentration even at 1ppm of H_2S concentration. For H_2S gas sensing pure SnO_2 shows high sensitivity in comparison to Zn-doped SnO_2, thus pure SnO_2 is much more reliable than Zn-doped SnO_2 for H_2S detection. According to Fig. 5.26 1 wt% and 3 wt% Zn-doped samples have small sensitivity but it is higher in the case of 5 wt% Zn-doped SnO_2 than for the 1 wt% and 3 wt% Zn-doped samples, whereas in the case of pure SnO_2 it is the highest. The response and recovery times are important parameters for gas sensing. The response and recovery time for pure SnO_2, 1 wt% Zn-doped SnO_2, 3 wt% Zn-doped SnO_2 and 5 wt% Zn-doped SnO_2 are 205 s and 501 s, 176 s and 459 s, 301 s and 466 s, 241 s and 503 s, respectively at 1 ppm H_2S.

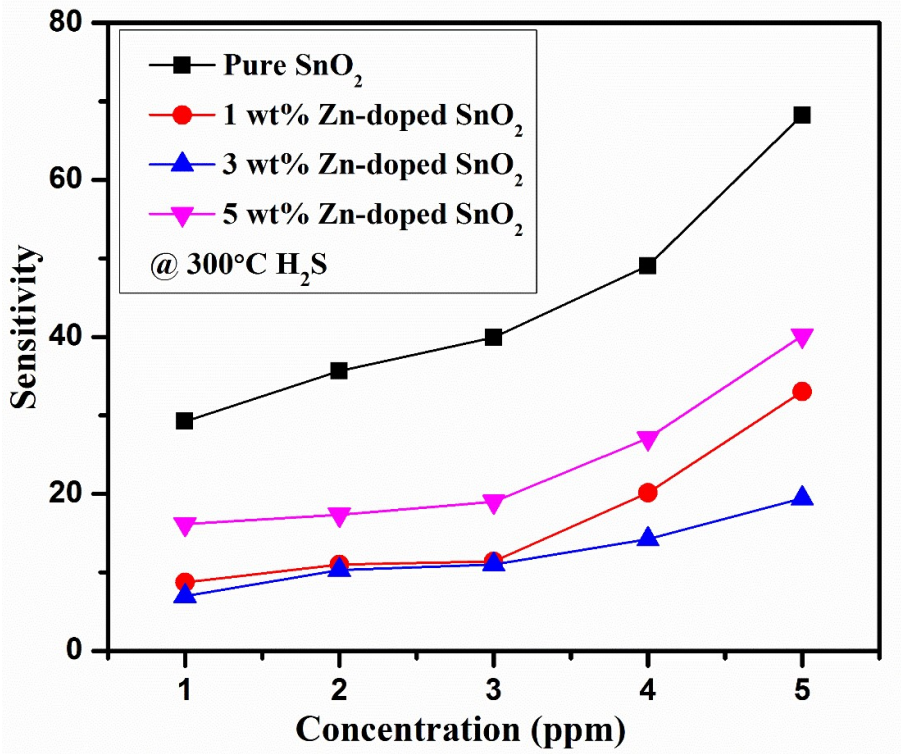

Figure 5.26: Gas response curve for Zn-doped SnO_2 for different concentration of H_2S gas at 300°C

5.3.2 Cu-doped SnO_2

The operating temperature of 300°C was determined by using the Fig. 5.22 for Cu-doped SnO_2. Cu-doped samples show maximum sensitivity towards H_2S gas. Fig. 5.27 and Fig. 5.28 represent the response and recovery curves for 1 wt% and 3 wt% Cu-doped SnO_2, respectively. These curves depict the gas sensing characteristics of Cu-doped samples. By using these curves, response time and recovery time can be calculated. There are many studies reported for the Cu-doped SnO_2 for H_2S gas sensing in the literature e.g. [116, 119, 207].

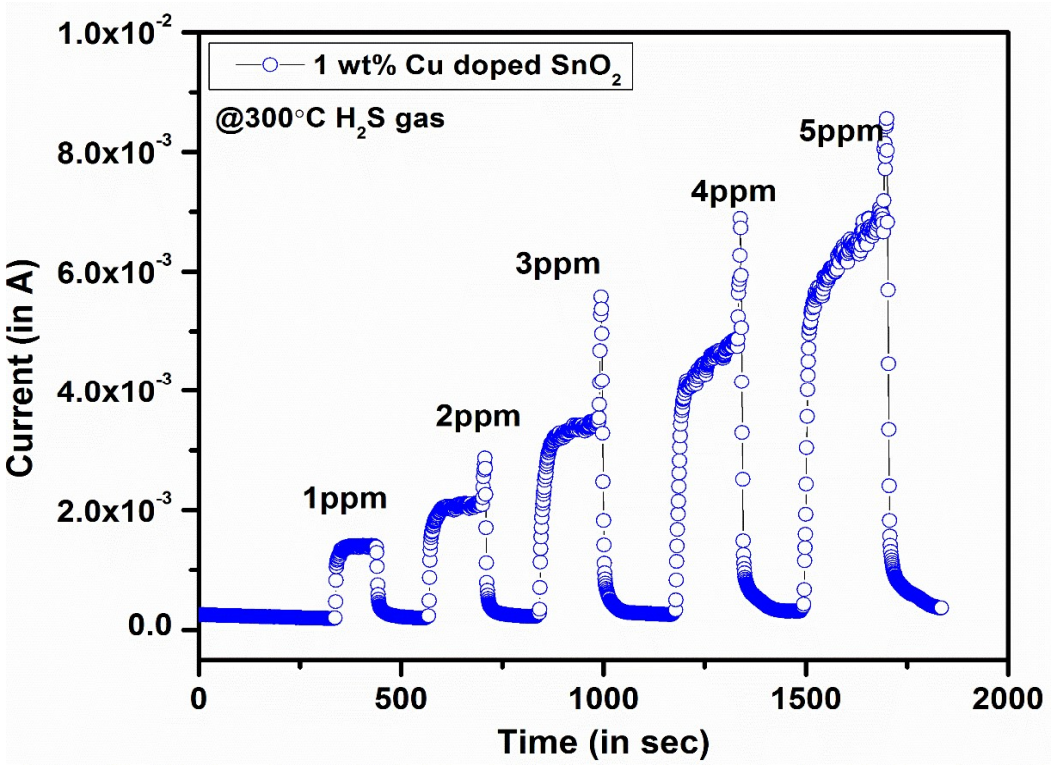

Figure 5.27: Sensing characteristics of 1 wt% Cu-doped SnO_2 sample for 1 ppm to 5 ppm H_2S gas concentration at 300°C

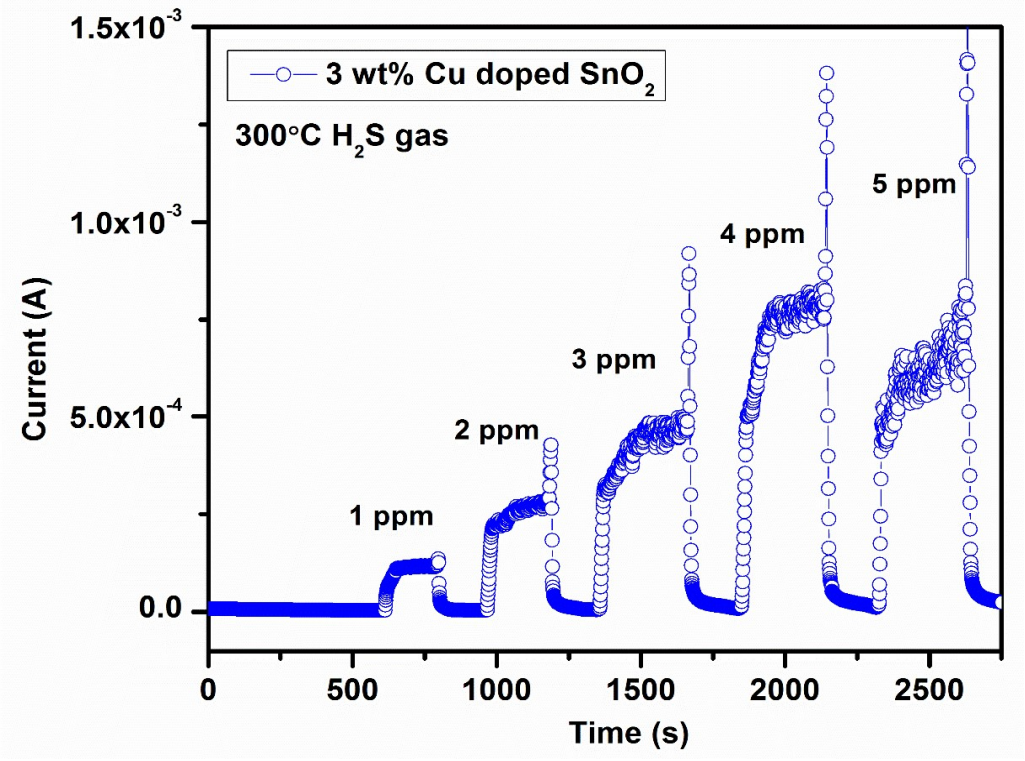

Figure 5.28: Sensing characteristics of 3 wt% Cu-doped SnO_2 sample for 1 ppm to 5 ppm H_2S gas concentration at 300°C

Fig. 5.29 represents the gas response curve for Cu-doped SnO_2 with respect to 1 ppm to 5 ppm H_2S gas concentration at 300°C operating temperature. In this plot pure and low concentration (1 wt% Cu) doped SnO_2 shows a reasonable sensitivity towards H_2S gas but with further increase in gas concentration, sensitivity increase is very small. However, in the case of high doping i.e. 3 wt% Cu-doping, it reaches to a high value which more than 150 sensitivity. The response time are 205 s, 80 s, and 153 s for pure, 1 wt% and 3 wt% Cu-doped SnO_2, respectively at 1 ppm H_2S gas concentration. Similarly, recovery time for the samples are 501 s, 84 s and 147 s for pure, 1 wt% and 3 wt% Cu-doped SnO_2, respectively at 1 ppm H_2S gas concentration.

Increase in current (decrease in resistance) of SnO_2 nanostrucutre on the exposure of reduced gas in the gas sensing mechanism was explained earlier in section 5.2.3. But in the case of Cu-doping, Cu acts an p-type semiconductor and SnO_2 is n-type material, so in Cu-doped SnO_2 sample it behaved as a p-n juction, so resistance between both of them creating as a p-n juction and it goes high in comparision to

nanostrucutre. It is due to the high concentration which is responsible for creating more conduction sites. The surface reaction ig given by

$$Cu + H_2S \rightarrow CuS + H_2O \qquad 5.9$$

$$CuS + 3/2\ O_2 \rightarrow Cu + SO_2 \qquad 5.10$$

CuS formation has been reported in the literature [208-209]. Another reason for high sensitivity could be the doping of Cu^{2+} ions on Sn^{4+} site, which results in the production of more oxygen vacancies for achieving the charge neutrality. For the enhancement of gas sensing characteristics of SnO_2 nanostructures, this increase in oxygen deficiency is reported in the literature [210].

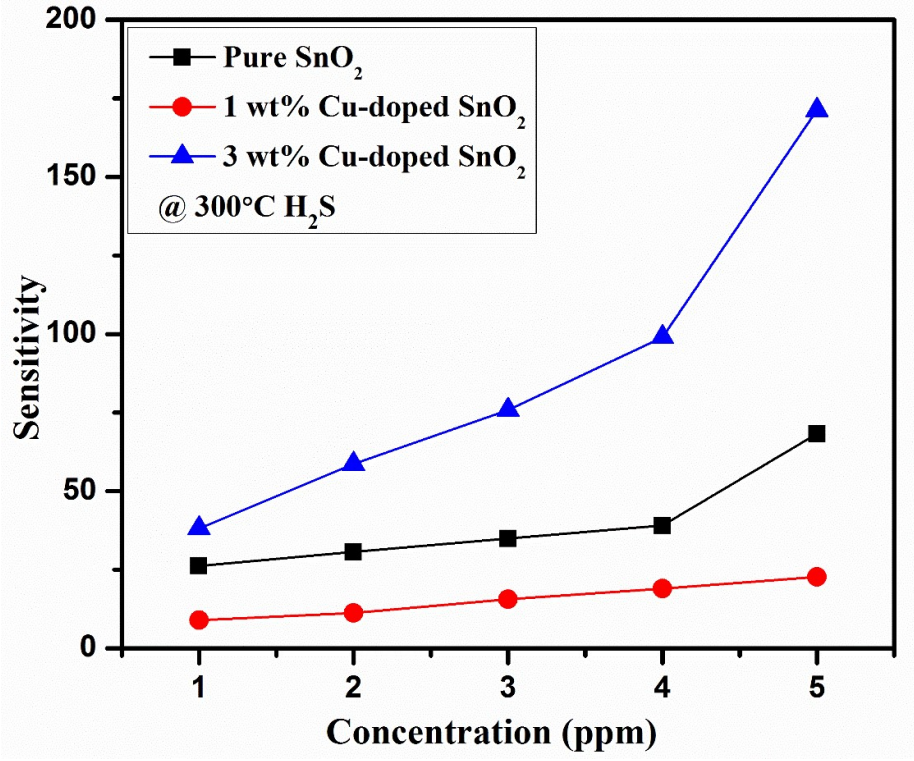

Figure 5.29: Gas response curve for Cu-doped SnO_2 for different concentration of H_2S gas at 300°C

5.3.3 Ni-doped SnO_2

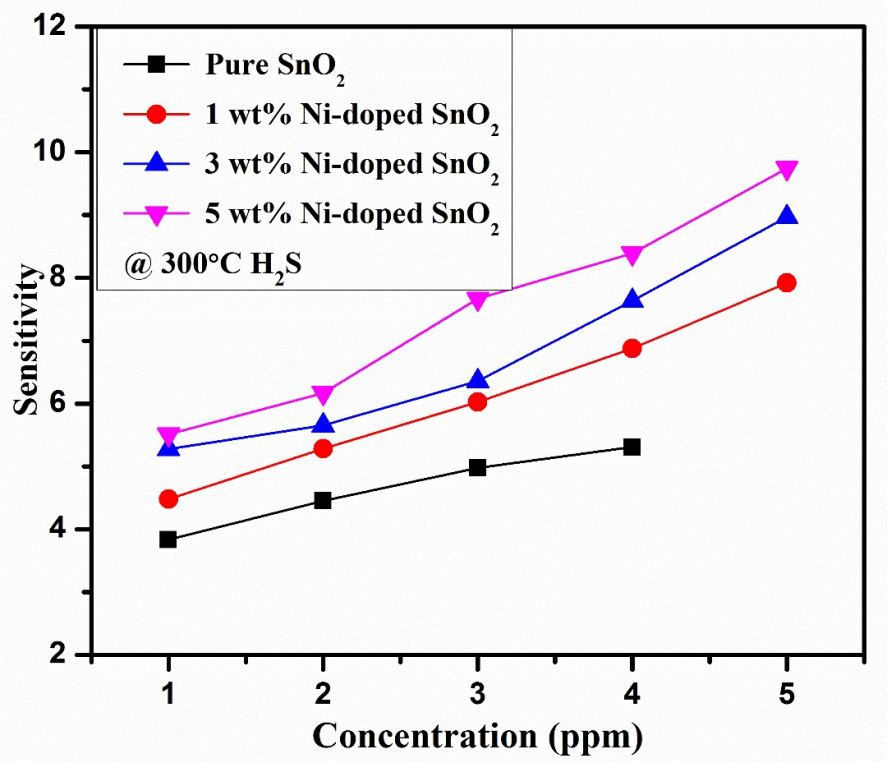

Figure 5.30: Gas response curve for Ni-doped SnO_2 for different concentration of H_2S gas at 300°C

The optimum operating temperature for Ni-doped SnO_2 was determined from the gas response plot shown in Fig. 5.22 and a value of 300°C is suggested for the operating temperature value for Ni-doped SnO_2 for 3 ppm H_2S gas. Fig. 5.30 shows the H_2S gas concentration dependent sensitivity values of Ni-doped SnO_2 samples. This indicates that the gas sensitivity increases significantly with increase in gas concentration. According to Fig. 5.30 sensitivity of Ni-doped samples towards H_2S gas shows higher sensitivity value in comparison to H_2 gas, which suggests Ni-doped SnO_2 are better for H_2S gas sensitivity. Some other reports are also available in literature for Ni-doped SnO_2, but they are for ethanol sensing [211]. Refer section 5.2.4 for the sensing mechanism of Ni-doped SnO_2. The response time are 106 s, 274 s, 88 s and 228 s for pure, 1 wt%, 3 wt% and 5 wt% Ni-doped SnO_2, respectively at 1 ppm H_2S gas concentration. Similarly, recovery time for the samples are 125 s, 438 s, 137 s and 382 s for pure, 1 wt%, 3 wt% and 5 wt% Ni-doped SnO_2, respectively at 1 ppm H_2S gas concentration.

5.3.4 Thermal Annealed SnO_2

The gas sensing curve for pure SnO_2 annealed at 700°C for H_2S gas is represented in Fig. 5.31 at an operating temperature of 300°C. This is a typical H_2S gas sensing curves for SnO_2 samples for 1 to 5 ppm concentration of H_2S gas at 300°C operating temperature. 300°C is the optimum operating temperature which is determined by sensitivity versus temperature curve shown in Fig. 5.22 for H_2S gas.

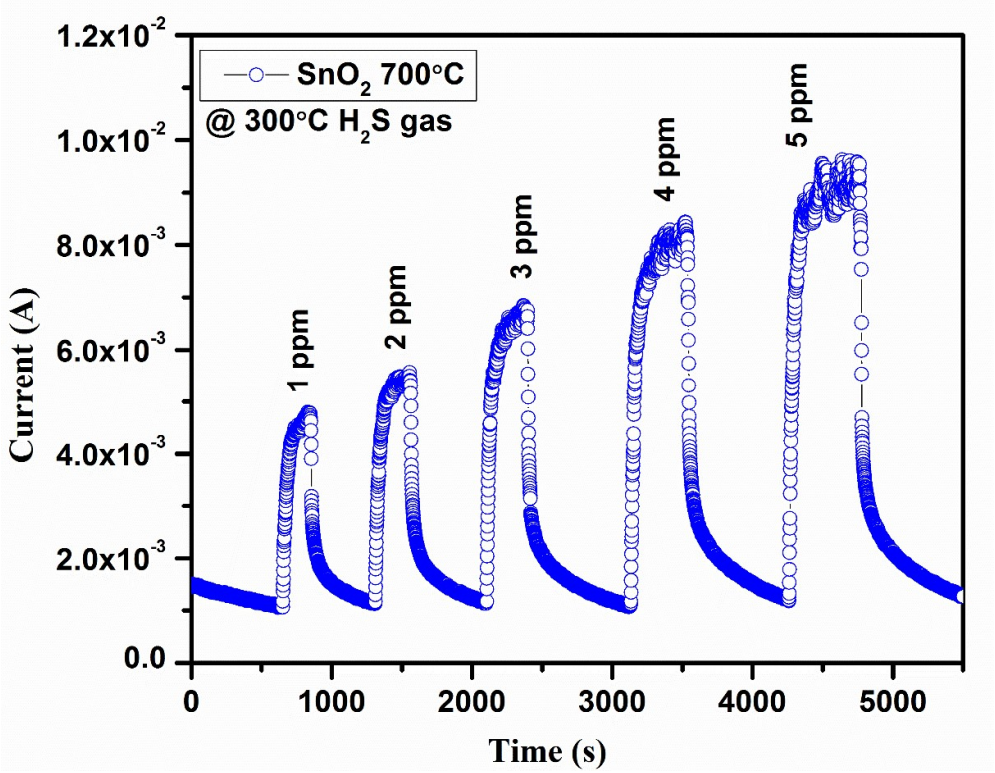

Figure 5.31: Thermal annealed pure SnO_2 sample sensing characteristics for 1 ppm to 5 ppm H_2S concentration at 300°C

The gas response curve for pure SnO_2 sample annealed at 700°C with respect to H_2S gas concentration from 1 ppm to 5 ppm at 300°C are given in figure. The values of response time are 191 s, 281 s and 279 s and recovery time are 310 s, 477 s and 624 s for SnO_2 annealed at 700°C, 800°C and 900°C, respectively at 1 ppm H_2S gas concentration. This curve indicates that sensitivity increases with increase in gas concentration. The almost linear behaviour of the data in Fig. 5.32 indicates the stability in the sensitivity values at 300°C operating temperature irrespective of the grain size.

SnO_2 annealed at 700°C, 800°C and 900°C shows enhanced sensitivity with respect to annealing temperature. SnO_2 annealed at 900°C shows maximum sensitivity. These results are same as H_2 gas sensing only the values of sensitivity are increased in the case of H_2S gas detection. The gas sensitivity depends on grain boundary is already explained in section 5.2.7.

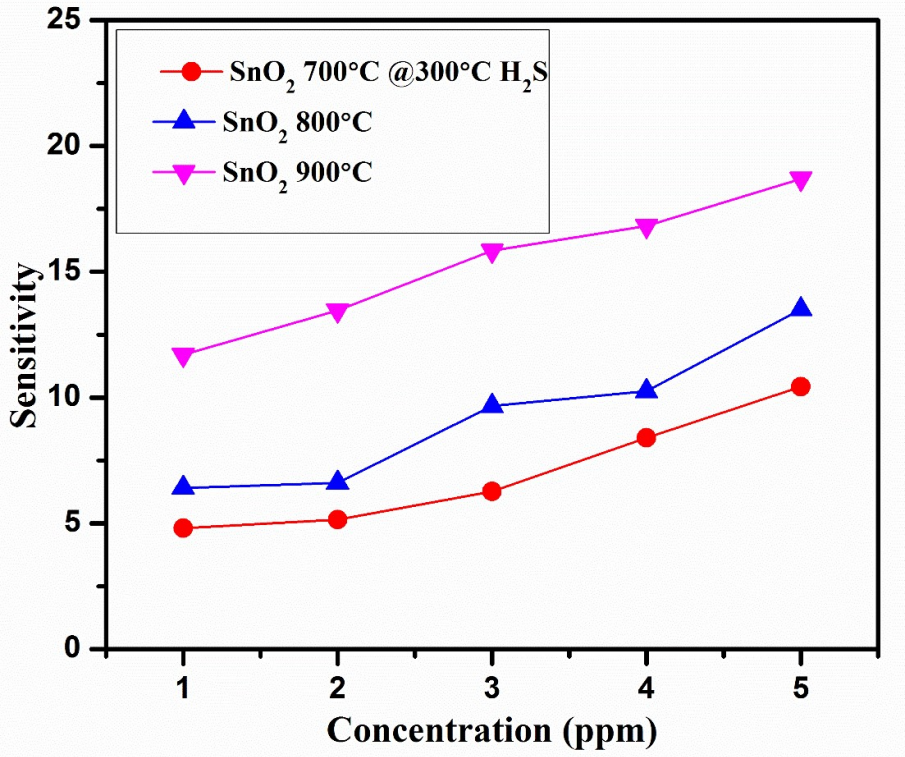

Figure 5.32: Gas response curve of thermal annealed pure SnO_2 for different concentration of H_2S gas at 300°C

5.3.5 Microwave sintered Zn-doped SnO_2

The response and recovery characteristic curves for microwave sintered 1 wt% Zn-doped SnO_2, 3 wt% Zn-doped SnO_2 and 5 wt% Zn-doped SnO_2 are shown in Fig. 5.33, Fig. 5.34 and Fig.5.35, respectively. According to these curves the response and recovery time for 5 wt% Zn-doped SnO_2 is small in comparison to 1 and 3 wt% Zn-doped SnO_2 samples.

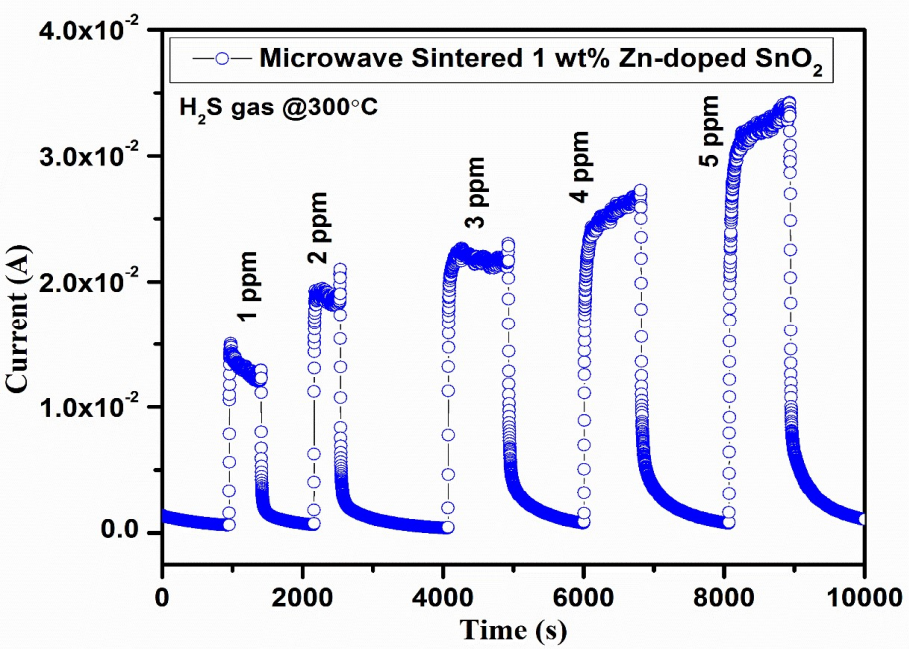

Figure 5.33: Microwave sintered 1 wt% Zn-doped SnO_2 sample sensing characteristics for 1 ppm to 5 ppm H_2S concentration at 300°C

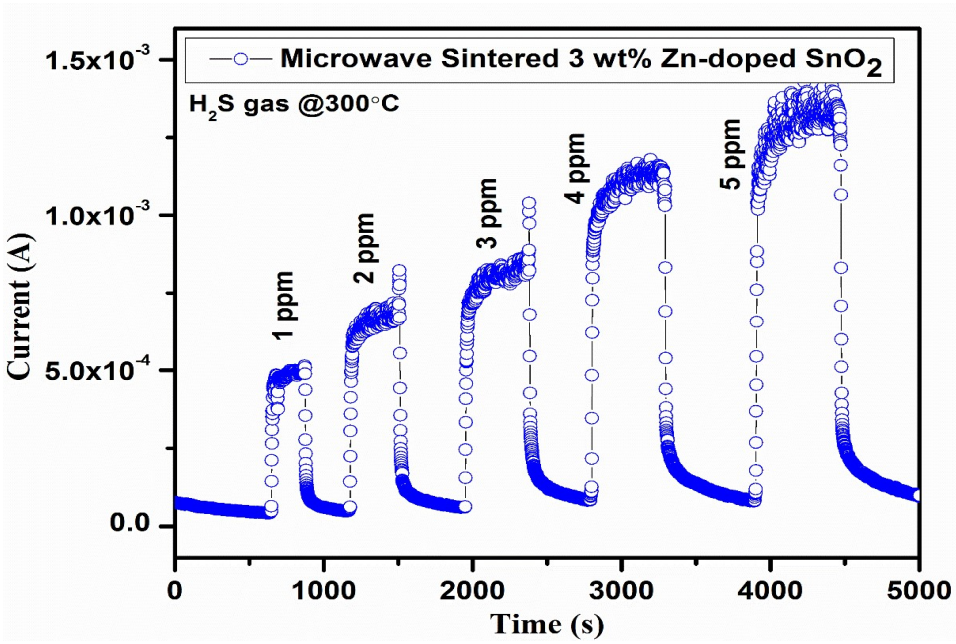

Figure 5.34: Microwave sintered 3 wt% Zn-doped SnO_2 sample sensing characteristics for 1 ppm to 5 ppm H_2S concentration at 300°C

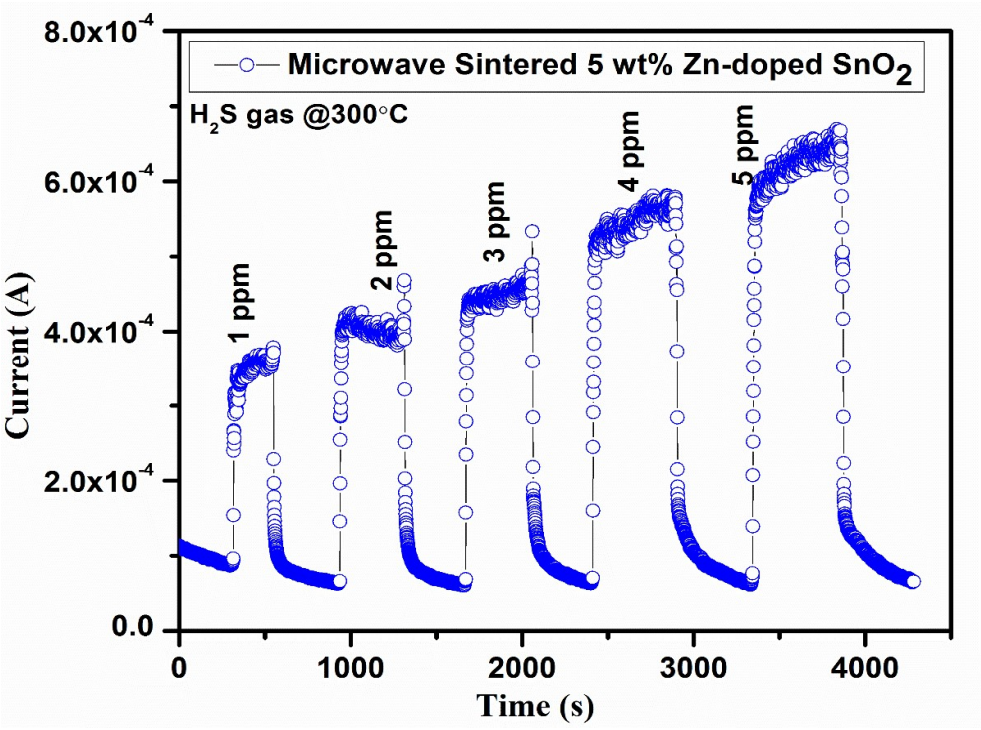

Figure 5.35: Microwave sintered 5 wt% Zn-doped SnO_2 sample sensing characteristics for 1 ppm to 5 ppm H_2S concentration at 300°C

The response time values are 398 s, 270 s and 193 s for microwave sintered 1 wt%, 3 wt% and 5 wt% Zn-doped SnO_2, respectively at 1 ppm H_2S gas concentration. Similarly, recovery time for the samples are 597 s, 282 s, and 266 s for 1 wt%, 3 wt% and 5 wt% Zn-doped microwave sintered SnO_2, respectively at 1 ppm H_2S gas concentration.

The gas sensitivity curves for microwave sintered pure and Zn-doped (1 wt%, 3 wt% and 5 wt%) SnO_2 samples with respect to 1 ppm to 5 ppm H_2S gas concentration at 300°C are given in Fig. 5.36. This figure shows an increase in sensitivity with the increase in gas concentration. In H_2S detection using microwave sintered Zn-doped SnO_2 samples, the sensitivity decreased with increase in Zn-doping concentration. The 1 wt% Zn-doped SnO_2 was found to be the most suitable for H_2S detection. It is worth mentioning here that the higher doping of Zn displays less chances for H_2S sensing in comparison to low doping concentrations for microwave sintered samples. The sensitivity of microwave sintered Zn-doped samples towards H_2S gas shows higher sensitivity value in comparison to H_2 gas, which suggests Zn-

doped SnO_2 are better for H_2S gas detection even at low gas concentration. The microwave sintered Zn-doped SnO_2 samples showed the highest sensitivity for 1 wt% Zn-doping for H_2S gas sensing. The particle size of the samples is not same as un-sintered Zn-doped SnO_2 (for this refer section 5.2.2) but due to microwave sintering, the particle size increases further so the active area for gas reaction decreases. For higher Zn-doping, the gas response should increase, as particle size decreases but due to the microwave sintering effect the particle size increases which leads to decrease the final gas response to a lower value. It is fascinating to note here that microwave sintered samples show good sensing behaviour for the pure and low doping concentration of Zn for H_2S gas.

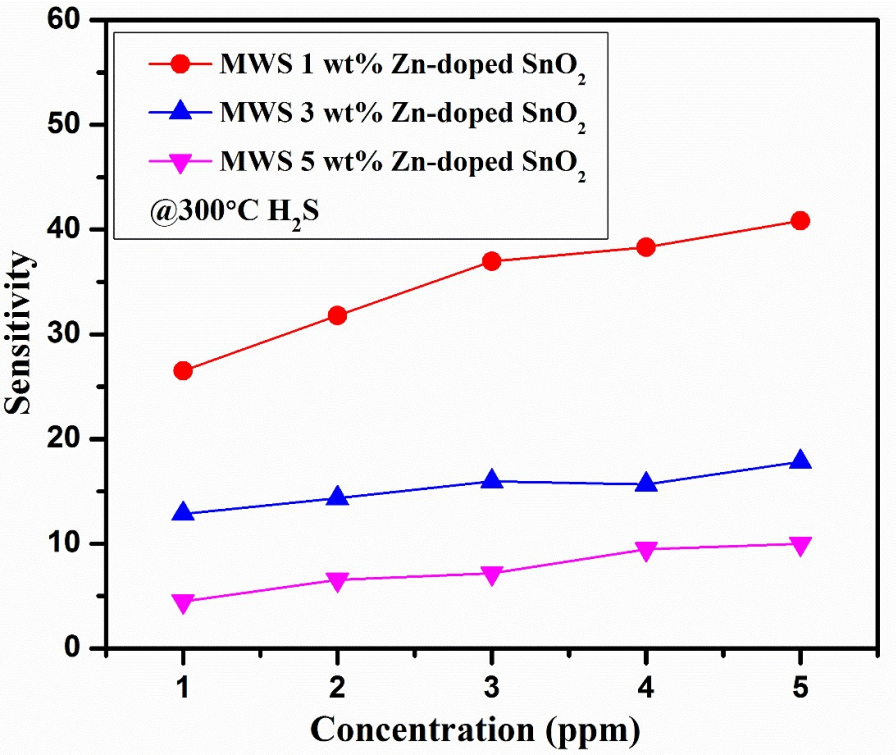

Figure 5.36: Sensitivity curve of microwave sintered Zn-doped SnO_2 for 1 ppm to 5 ppm H_2S concentration at 300°C

High sensitivity, low response and recovery time are the important parameters for a gas sensor, these parameters are interdependent. It have been observed from Table 5.2 that in the case of H_2S gas sensing, SnO_2 based sensors are perferred choice as, in general, higher sensitivity values are obtained with low response and recovery times

for pure (30 at 1 ppm) and 3 wt% Cu-doped SnO_2 (38 at 1 ppm). Also 5 wt% Zn-doped SnO_2 shows high sensitivity but here response and recovery time also rises (refer Table 5.2). Ni-doped specimens show comparatively low sensitivity values and for all concentrations of Ni the values are practically in same range. Table 5.2 shows response, recovery time and sensitivity values of pure and doped SnO_2 for H_2S gas at an operating temperature of 300°C. Microwave sintered 1 wt% Zn-doped sample also shows good sensitivity.

Table 5.2: Response, recovery time and sensitivity values of pure and doped SnO_2 for H_2S gas at an operating temperature of 300°C

Sample	Response Time (s)	Recovery Time (s)	Sensitivity	
			1ppm	5ppm
Pure SnO_2	101	189	30	68
1 wt% Zn-doped SnO_2	229	307	9	33
3 wt% Zn-doped SnO_2	205	228	7	19
5 wt% Zn-doped SnO_2	197	433	17	40
1 wt% Cu-doped SnO_2	80	84	9	23
3 wt% Cu-doped SnO_2	153	147	38	171
1 wt% Ni-doped SnO_2	274	438	4.5	8
3 wt% Ni-doped SnO_2	88	137	5.2	9
5 wt% Ni-doped SnO_2	228	382	5.5	10
SnO_2 700°C	191	310	4.8	10.5
SnO_2 800°C	281	477	6.4	13.5
SnO_2 900°C	279	624	11.8	18.7
MW sintered 1 wt% Zn-doped SnO_2	398	597	26.5	40.8
MW sintered 3 wt% Zn-doped SnO_2	270	282	12.8	17.8
MW sintered 5 wt% Zn-doped SnO_2	193	266	4.5	10

5.4 Gas sensing study for Methane (CH_4) gas

CH_4 is a highly flammable, combustible and toxic gas. It is an odourless gas and highly available organic compound on earth. It is lighter than air. Methane is violently reactive with oxidizers, halogen and some halogen containing compounds. It

may displace oxygen in an enclosed space and therefore there is a need for development of a highly reliable, selective and cost effective sensor.

As shown earlier in section 5.2 and 5.3 we have determined the optimum operating temperature for H_2 and H_2S gas, respectively, which is 300°C. Generally metal oxide semiconductors sensors operated at high temperature only so, for comparison purpose also the same operating temperature is used for detection of CH_4 gas.

5.4.1 Pure SnO_2

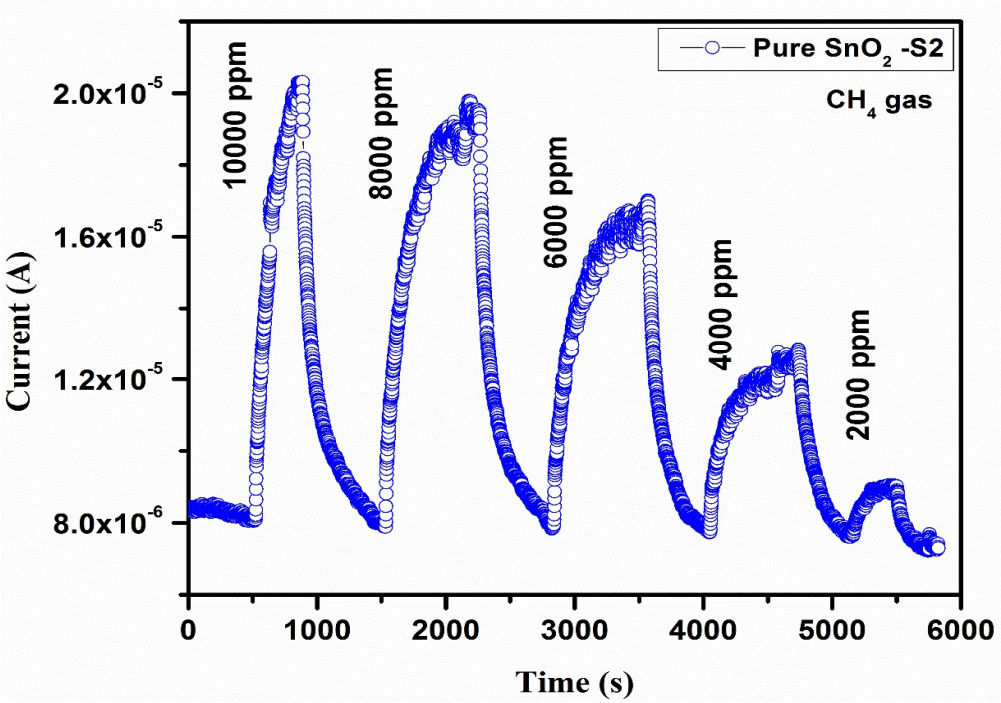

Figure 5.37: Gas sensing characteristics of pure SnO_2 sample (S2) for 10000 ppm to 2000 ppm CH_4 concentration at 300°C

The gas sensing characteristics of pure SnO_2 prepared by method 2 (S2) for CH_4 gas is represented in Fig. 5.37 at an operating temperature of 300°C. This gives typical sensing curve of SnO_2 samples for 10000 ppm to 2000 ppm CH_4 gas concentration at 300°C operating temperature. This curve is plotted as the change in current with the exposure of CH_4 test gas. In this process initially the synthetic air was used to stabilize the sensing material current (resistance) and then the target gas (CH_4) at a particular concentration is tested, and thus the current increases (resistance decreases) as SnO_2 is a n-type material and CH_4 is a reducing gas. When this current is stabilized at particular concentration again we flow the synthetic gas in absence of test gas so the current goes to its base value. In addition to this, SnO_2 pellets were also tested for 100°C, 150°C, 200°C and 250°C but at low temperatures the base current was not stable and 250°C the sensing signal is very weak (data not shown here).

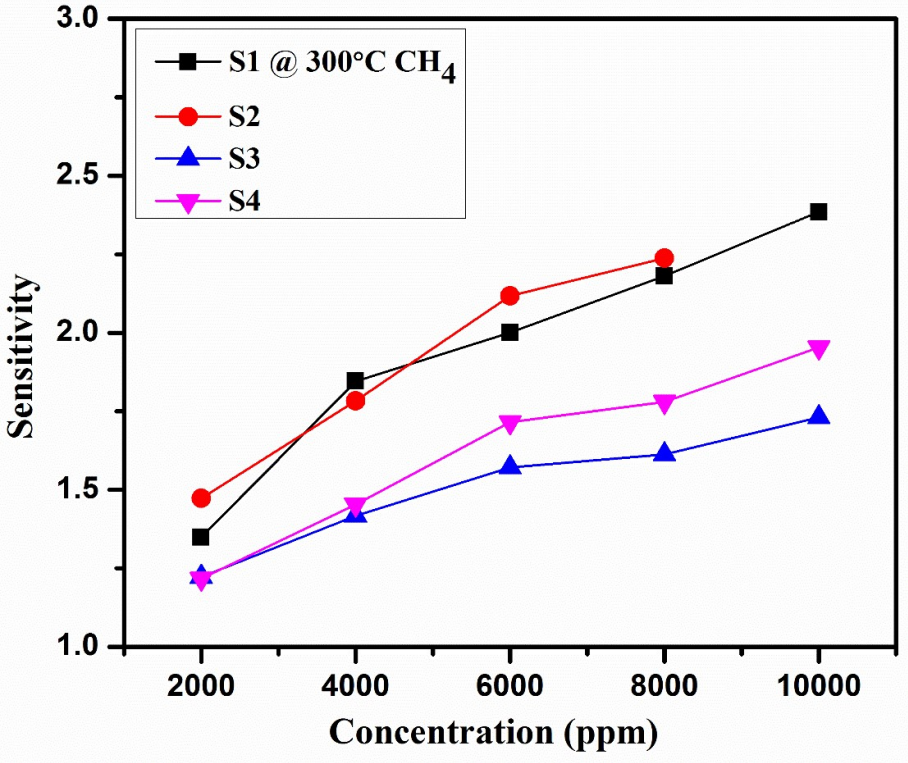

Figure 5.38: Sensitivity curve of pure SnO_2 samples prepared by different methods for 2000 ppm to 10000 ppm CH_4 concentration at 300°C

The values of response time are 258 s, 274 s, 274 s and 175 s for S1, S2, S3 and S4 SnO_2, respectively at 2000 ppm CH_4 gas concentration. Similarly, recovery time for the samples are 216 s, 273 s, 232 s and 188 s for S1, S2, S3 and S4 SnO_2, respectively at 2000 ppm CH_4 gas concentration. The Fig. 5.38 shows the plot between gas concentration and sensitivity towards CH_4 gas. The almost linear behaviour of data in Fig. 5.38 indicates the stability in the sensitivity values at 300°C operating temperature. The plots for S1 and S2 (SnO_2 prepared by method 1 and method 2, respectively) show the maximum stability and linear behaviour at all concentrations. Due to this linear relationship between sensitivity and gas concentration pure SnO_2 can detect CH_4, but due to the small sensitivity values it can be concluded that SnO_2 based gas sensors are poor sensors for CH_4 detection.

5.4.2 Ni-doped SnO_2

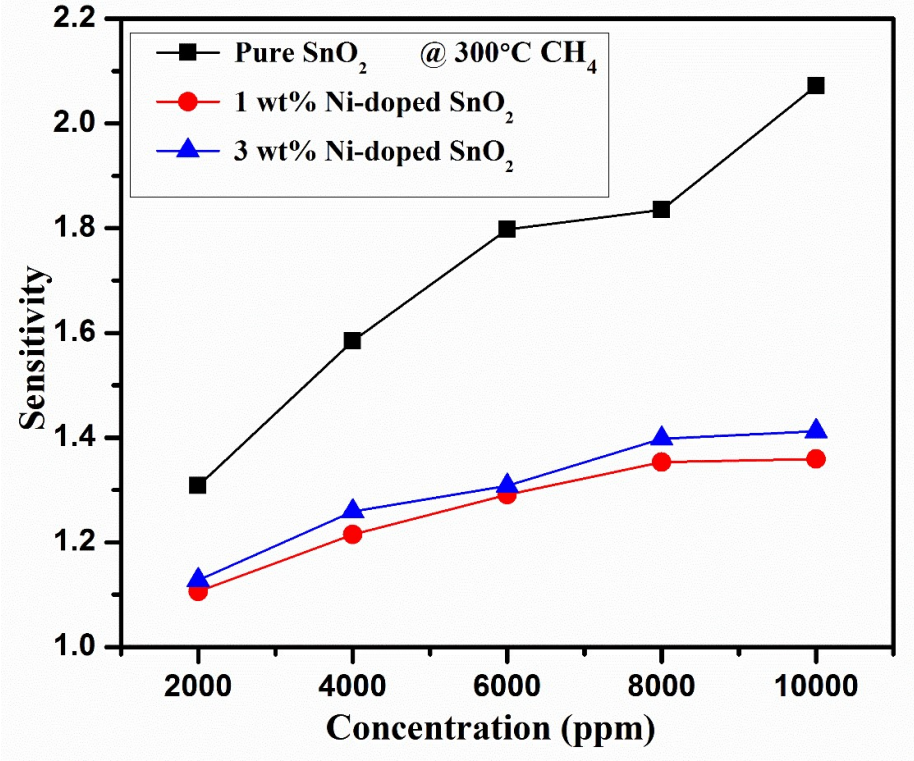

Figure 5.39: Gas response curve of Ni-doped SnO_2 samples for 2000 ppm to 10000 ppm CH_4 concentration at 300°C

Fig. 5.39 shows the CH_4 gas concentration dependent sensitivity values of pure and Ni-doped SnO_2 samples. According to this curve, the gas response or sensitivity increases significantly with increase in gas concentration. The pure SnO_2 sample shows higher sensitivity in comparison to Ni-doped SnO_2 samples. Fig. 5.39 shows that 1 wt% Ni-doped and 3 wt% Ni-doped SnO_2 have very small increase in sensitivity value for CH_4 detection. This is in the range of 1.1 to 1.3 only for doped specimens, whereas pure SnO_2 shows approximately 1.3 to 2.1. This is comparatively higher than for Ni doped sample, but not significantly higher.

The response time are 446 s, 112 s, and 205 s for pure, 1 wt% and 3 wt% Ni-doped SnO_2, respectively at 2000 ppm CH_4 gas concentration. Similarly, recovery time for the samples are 727 s, 164 s and 121 s for pure, 1 wt% and 3 wt% Ni-doped SnO_2, respectively at 2000 ppm CH_4 gas concentration.

It has been observed from Table 5.3 that SnO_2 specimens not show reasonable sensitivity for CH_4 gas as for the dopants investigated here, therefore it is not a good choice for CH_4 sensing. Table 5.3 shows response, recovery time and sensitivity values of pure and doped SnO_2 for CH_4 gas at an operating temperature of 300°C. From these results it can be concluded that Ni-doped SnO_2 specimens are poor sensors for CH_4 detection.

Table 5.3: Response, recovery time and sensitivity values of pure and doped SnO_2 for CH_4 gas at an operating temperature of 300°C

Sample		**S1**	**S2**	**S3**	**S4**	**1 wt% Ni-doped SnO_2**	**3 wt% Ni-doped SnO_2**
Response Time (s)		258	274	274	175	112	205
Recovery Time (s)		216	273	232	188	164	121
Sensitivity	2000 ppm	1.34	1.47	1.22	1.21	1.10	1.12
	10000 ppm	2.38	2.5	1.73	1.95	1.4	1.41

5.5 Conclusions

From the results presented and discussed in this chapter, the following conclusions can be drawn:

Gas sensing studies have been done for H_2, H_2S and CH_4 gases on pure and doped SnO_2. In all the plots and from Table 5.1, Table 5.2 and Table 5.3, it has been observed that the sensing response increases with increase in gas concentration. Pure SnO_2 showed a high sensitivity towards H_2 gas. The 5 wt% Zn-doped SnO_2 shows the maximum sensitivity for H_2 gas among other Zn-doped samples. The 3 wt% Cu-doped SnO_2 shows better sensitivity (5.3) in comparison to other copper concentrations. Among all Ni-doped SnO_2 samples, 5 wt% Ni-doped SnO_2 gives high sensitivity for H_2 gas. 1 wt% Fe-doped SnO_2 shows the highest sensitivity among the other Fe-doped samples. The sensitivity of 3 wt% Sb-doped SnO_2 is higher than other Sb-doped SnO_2.

SnO_2 annealed at 600°C gives low gas response and with the increase in annealing temperature the response increases. SnO_2 annealed at 900°C shows maximum sensitivity i.e. 5.5 at 1 ppm. The 1 wt% Zn-doped microwave sintered SnO_2 was discovered to be the most suitable for H_2 detection. Microwave sintered samples show good sensing behaviour for the pure and low doping concentration of Zn for both H_2 and H_2S gas.

Thus, for H_2 gas sensing, pure SnO_2 gave better results (~9) than (Zn, Cu, Ni , Fe and Sb) doped SnO_2. Among all the used dopants 3 wt% Cu-doped and 1 wt% Fe-doped SnO_2 gave high sensitivity (e.g. for 3 wt% Cu-doped SnO_2 sensitivity is 5.3), whereas Ni-doped and Sb-doped specimens shows low sensitivity values (refer Table 5.1). In general, for H_2 sensing high sensitivity is also obtained with significant rise in response and recovery time. Therefore, for H_2 gas detection, optimum values of these parameters need to be determined for each dopant.

For H_2S gas sensing pure SnO_2 shows high sensitivity. 5 wt% Zn-doped SnO_2 shows highest sensitivity among other concentrations of Zn-doping for H_2S detection. 3 wt% Cu-doping shows highest sensitivity (171 at 5 ppm) among all other dopants and concentrations. Ni-doped samples towards H_2S gas shows higher sensitivity value

in comparison to H_2 gas, which suggests Ni-doped SnO_2 are better for H_2S gas sensitivity. Even at 1 ppm of H_2S gas the samples show the good sensitivity.

With increase in annealing temperature the sensitivity for H_2S gas also increases. SnO_2 annealed at 900°C shows maximum sensitivity i.e. 11.8 at 1 ppm. Here sensing behaviour is same as H_2 gas sensing but the values of sensitivity are increased in the case of H_2S gas detection. Microwave sintered 1 wt% Zn-doped SnO_2 shows high sensitivity.

Thus SnO_2 based sensors are perferred choice for H_2S sensing as, in general, higher sensitivity values are obtained with low response and recovery time values for pure and 3 wt% Cu-doped SnO_2.

SnO_2 based sensors show poor sensitivity for CH_4 gas as for the dopants investigated here, therefore it is not a good choice for CH_4 sensing and thus it can be concluded that SnO_2 gas sensors are poor sensors for CH_4 detection.

Chapter- 6

Conclusions and Future Aspects

6.1 Introduction

The main focus of the present study was on the study of synthesis and characterization of pure and doped SnO_2 based nanostructures and their use in gas sensing studies for the combustible gases: H_2, CH_4, H_2S. Structural modifications of the nanostructured samples were carried out using doping, microwave sintering and thermal annealing methods. The main objectives of the study have been summarized as 'objectives of the present study' in Chapter 1.

The investigations have been carried out on the sol-gel synthesized SnO_2 nanostructures in order to achieve these objectives. The conclusions of the research work carried out in this study and the scope of this thesis are described below.

6.2 Conclusions

The main results of the research work reported in this thesis can be summarized as follows:

I. Pure and doped (Zn, Cu, Ni, Fe and Sb) SnO_2 nanopowders with different concentration (1 wt%, 3 wt% and 5 wt%) of doping were synthesized by sol-gel method. These as-synthesized nanopowders show good crystallinity with tetragonal rutile phase. No impurity peak was shown by any of the nanopowder in XRD plots. In the case of Zn-doping and Cu-doping, it has been found that with the increase in Zn-doping or Cu-doping concentration the crystallite size decreases and the band gap increases (e.g. for 1 wt% and 3 wt% Zn-doped SnO_2 crystallite size are 12 ± 1 nm and 10 ± 1 nm and

corresponding bandgap values are 3.6 eV and 3.7 eV, respectively, see Table 4.2. But in the case of Ni, Fe and Sb doping the crystallite size increases with doping concentration (Refer Table 4.4, Table 4.5 and Table 4.6). Further, the variation in dopant concentration is also observed to change the surface morphology of resultant product.

II. With thermal annealing of the SnO_2 nanopowders the phase of the sample does not change with higher annealing temperature, but the crystallite size increases. The surface morphology of powder shows the uniformity in the grain size of the samples and crystallite size of the nanoparticles goes on increasing from 23±1 nm to 38±1 nm as the annealing temperature increases in the range of 600°C to 900°C, refer Table 4.7. From I-V and R-T measurements, it is found that high temperature annealed specimens have low conductivity and good thermal stability up to 300°C. Microwave sintering of Zn-doped SnO_2 pellets resulted in an increase in grain size after sintering.

III. Gas sensing studies have been done for H_2, H_2S and CH_4 gases on pure and doped SnO_2. In all the plots and from Table 5.1 it has been observed that the sensing response increases with increase in gas concentration.

- The 5 wt% Zn-doped SnO_2 shows the maximum sensitivity for H_2 gas among other Zn-doped samples (Fig. 5.8).
- The 3 wt% Cu-doped SnO_2 shows better sensitivity in comparison to other copper concentrations (Fig. 5.11).
- Among all Ni-doped SnO_2 samples, 5 wt% Ni-doped SnO_2 gives high sensitivity for H_2 gas in comparison to other concentrations (Fig. 5.13).
- 1 wt% Fe-doped SnO_2 shows the highest sensitivity among the other Fe-doped samples (Fig. 5.15).
- The sensitivity of 3 wt% Sb-doped SnO_2 is higher than other Sb-doped SnO_2 (Fig. 5.16).
- SnO_2 annealed at 900°C shows maximum sensitivity at 1 ppm (Fig. 5.19).
- It is observed that pure SnO_2 showed a highest sensitivity value (sensitivity ~ 9) towards H_2 gas (Fig. 5.6).

Thus, for H_2 gas sensing, pure SnO_2 gave better results than (Zn, Cu, Ni, Fe and Sb) doped SnO_2. Among all the used dopants the highest sensitivity for H_2 gas is observed for 3 wt% Cu-doped SnO_2 (sensitivity is 5.3) and for 1 wt% Fe doped SnO_2 (sensitivity is 4.2), whereas Ni-doped and Sb-doped specimens shows low sensitivity values (refer Table 5.1). However, it is observed that sensitivity values for H_2 gas sensing considerably increase as the gas concentration increases for all the dopants investigated here.

In general, it is also observed (Table 5.1) that for H_2 sensing high sensitivity is also obtained with significant rise in response and recovery time. Therefore, it is concluded that for H_2 gas detection, optimum values of these parameters need to be determined and considered for each dopant.

IV. In H_2S gas sensing, the samples show the good sensitivity even at 1 ppm of H_2S gas refer Table 5.2.

- Pure SnO_2 shows high sensitivity for H_2S gas (Fig. 5.26).
- 5 wt% Zn-doped SnO_2 shows highest sensitivity among other concentrations of Zn-doping for H_2S detection (Fig. 5.26).
- 3 wt% Cu-doping shows highest sensitivity (171 at 5 ppm) among all other dopants and concentrations (Fig. 5.29).
- Ni-doped samples towards H_2S gas shows higher sensitivity value in comparison to H_2 gas, which suggests Ni-doped SnO_2 are better for H_2S gas sensitivity (Fig. 5.30 and Fig. 5.13).
- SnO_2 annealed at 900°C shows maximum sensitivity i.e. 11.8 at 1 ppm (Fig. 5.32). Here sensitivity behaviour is same as for H_2 gas sensing but the values of sensitivity are increased in the case of H_2S gas detection.

Further, it is noteworthy from Table 5.2 that in the case of H_2S gas sensing, higher sensitivity values are obtained with low response and recovery times for pure SnO_2 (30 at 1 ppm) and 3 wt% Cu-doped SnO_2 (38 at 1 ppm). Also 5 wt% Zn-doped SnO_2 shows high sensitivity but here response time and recovery time also rise (refer Table 5.2). Ni-doped specimens show comparatively low sensitivity values and for all concentrations of Ni the values are practically in same range. It is observed from all sensitivity plots or Table 5.2 that sensitivity values for H_2S gas sensing considerably increase as the gas

concentration increases for all the dopants investigated here. Thus, both pure and doped SnO_2 specimens are perferred choice for H_2S sensing.

V. SnO_2 samples detect CH_4, but do show rather poor sensitivity for CH_4 gas for all the dopants investigated here (Fig. 5.38, Fig. 5.39 and Table 5.3). Therefore, pure and doped SnO_2 specimens investigated here do not represent a good choice for CH_4 sensing.

VI. Microwave sintered samples show good sensing behaviour for the pure and low doping concentration of Zn for both H_2 and H_2S gas refer Table 5.1 and Table 5.2. The values of sensitivity are increased in the case of H_2S gas detection. The 1 wt% Zn-doped microwave sintered SnO_2 was found to be the most suitable for both H_2 and H_2S gas detection among all other higher Zn-doping concentrations of microwave sintered samples (Fig. 5.20, Fig. 5.36 and Table 5.1, Table 5.2). It is noteworthy that the sensitivity of Zn-doped specimens after microwave sintering for H_2 as well as H_2S gas is considerably enhanced. This leaves a good scope for further research on this aspect of the problem.

VII. The desirable parameters for making a gas sensing device require low response and recovery times and high sensitivity at an optimum operating temperature. From the above analysis in points (III), (IV) and (V) it is concluded that:

a) In the case of hydrogen gas (H_2) sensing, high sensitivity is obtained with significant rise in response and recovery times. For this gas, therefore, optimum values of these parameters need to be determined for each dopant. Our results show pure SnO_2 seems to present a better choice for H_2 gas sensing in comparision to doped SnO_2 investigated here.

b) In the case of hydrogen sulphide gas (H_2S), both pure and doped (with Cu and Zn) SnO_2 specimens seem to be a perferred choice. It is noteworthy here that higher sensitivity values also correspond to low response and recovery time values for pure, Cu and Zn dopants, thus making it a preferred choice for H_2S detection.

c) Pure SnO_2 and Ni-doped SnO_2 based specimens do not seem to be a good choice for CH_4 gas sensing as the sensitivity values are quite low. For other dopants (Zn, Cu, Fe and Sb) the sensitivity was below detection limit.

The results reported in this thesis are novel and add to the gas sensing database as the measurements have been made first time on the investigated concentrations of various dopants (Zn, Cu, Ni, Fe and Sb) and target gas (H_2, H_2S, CH_4) combination in this study. In addition, the effect of microwave sintering on the gas sensing behaviour has been investigated first time on pelletized specimens of pure and Zn-doped SnO_2.

6.3 Future aspects

Based on the experimental work and the results obtained in the present investigations, there is a good scope for doing further research on the following points:

- Further characterization by FTIR and Hall measurements would be useful and add to the understanding of the mechanism of gas sensing.
- Comparative study of the thin film and thick film of pure and doped nanostructured SnO_2 will be very useful, particularly for developing a sensor device.
- Efforts to improve the response and recovery time of the sensor are required by carrying out studies on specimens with varying dopant concentration over a much wider range.
- To plan a comprehensive study on pure and low concentration doped microwave sintered SnO_2 for some other dopants for enhancement in gas sensing behaviour.

- The SnO_2 nanocomposites could be studied for various gases and a comparative study with other nanostructures for gas sensing behaviour may be useful.

References:

[1] R. Díaz, Tin Oxide Gas Sensors: An Electrochemical Approach, 2002.

[2] N. Yamazoe, Toward innovations of gas sensor technology, Sensors Actuators B Chem. 108 (2005) 2–14. doi:10.1016/j.snb.2004.12.075.

[3] S.C. Gadkari, M. Kaur, V. Katti, V. Bhandarkar, K.P. Muthe, S.K. Gupta, Solid State Sensors for Toxic Gases, (2005) 49–60.

[4] V. Aroutiounian, Metal oxide hydrogen, oxygen, and carbon monoxide sensors for hydrogen setups and cells, Int. J. Hydrogen Energy. 32 (2007) 1145–1158. doi:10.1016/j.ijhydene.2007.01.004.

[5] G.F. Fine, L.M. Cavanagh, A. Afonja, R. Binions, Metal oxide semi-conductor gas sensors in environmental monitoring, Sensors. 10 (2010) 5469–5502. doi:10.3390/s100605469.

[6] N. Barsan, D. Koziej, U. Weimar, Metal oxide-based gas sensor research: How to?, Sensors Actuators B Chem. 121 (2007) 18–35. doi:10.1016/j.snb.2006.09.047.

[7] T. Ishihara, S. Matsubara, Capacitive Type Gas Sensors, J. Electroceramics. 2 (1998) 215–228. doi:10.1023/A:1009970405804.

[8] N.-H. Park, T. Akamatsu, T. Itoh, N. Izu, W. Shin, Calorimetric thermoelectric gas sensor for the detection of hydrogen, methane and mixed gases., Sensors (Basel). 14 (2014) 8350–62. doi:10.3390/s140508350.

[9] J. Liu, Y. Lu, Response mechanism for surface acoustic wave gas sensors based on surface-adsorption, Sensors (Basel). 14 (2014) 6844–6853. doi:10.3390/s140406844.

[10] F. Rathgeb, G. Gauglitz, Optical Gas Sensors in Analytical Chemistry: Applications, Trends and General Comments, in: Encycl. Anal. Chem., John Wiley & Sons, Ltd, Chichester, UK, 2006. doi:10.1002/9780470027318.a0709.

[11] C.O. Park, J.W. Fergus, N. Miura, J. Park, A. Choi, Solid-state electrochemical gas sensors, Ionics (Kiel). 15 (2009) 261–284. doi:10.1007/s11581-008-0300-6.

[12] J. Park, Nanostructured semiconducting metal oxides for use in gas sensors, 2010.

[13] S. Capone, A. Forleo, L. Francioso, R. Rella, P. Siciliano, J. Spadavecchia, D.S. Presicce, Solid State Gas Sensors: State of the Art and Future Activites, 5 (2003) 1335–1348.

[14] S. Basu, P.K. Basu, N. Saha, S.K. Jana, H. Saha, A.L. Spetz, Schottky junction methane sensors using electrochemically grown nanocrystalline-nanoporous ZnO thin films, J. Sensors. 2009 (2009). doi:10.1155/2009/790476.

[15] S.Y. Yurish, Modern sensors, transducers and sensor networks, IFSA, 2012.

[16] P. Shankar, J.B.B. Rayappan, Gas sensing mechanism of metal oxides : The role of ambient atmosphere , type of semiconductor and gases - A review ScienceJet, Sci. Jet. 4 (2015) 126.

[17] N. Yamazoe, G. Sakai, K. Shimanoe, Oxide Semiconductor Gas Sensors, Catal. Surv. from Asia. 7 (2003) 63–75. doi:10.1023/A:1023436725457.

[18] C. Wang, L. Yin, L. Zhang, D. Xiang, R. Gao, Metal oxide gas sensors: Sensitivity and influencing factors, Sensors. 10 (2010) 2088–2106. doi:10.3390/s100302088.

[19] R.J.B. Balaguru, B.G. Jeyaprakash, Mimic of a Gas sensor , Metal Oxide Gas Sensing Mechanism , Factors Influencing the Sensor Performance and Role of nanomaterials based gas sensors, School of Electrical & Electronics Engineering, (n.d.) 1–30.

[20] T. a Miller, S.D. Bakrania, C. Perez, M.S. Wooldridge, Nanostructured Tin Dioxide Materials for Gas Sensor Applications, Funct. Nanomater. (2006) 1–24.

[21] J. Rebholz, U. Weimar, N. Barsan, Influence of Conduction Mechanism Changes on the Sensor Performance of SMOX Based Gas Sensors, Procedia Eng. 87 (2014) 20–23. doi:10.1016/j.proeng.2014.11.256.

[22] S.M. Kanan, O.M. El-Kadri, I.A. Abu-Yousef, M.C. Kanan, Semiconducting metal oxide based sensors for selective gas pollutant detection, Sensors. 9 (2009) 8158–8196. doi:10.3390/s91008158.

[23] J. Huang, Q. Wan, Gas sensors based on semiconducting metal oxide one-dimensional nanostructures, Sensors. 9 (2009) 9903–9924. doi:10.3390/s91209903.

[24] G. Korotcenkov, Metal oxides for solid-state gas sensors: What determines our choice?, Mater. Sci. Eng. B Solid-State Mater. Adv. Technol. 139 (2007) 1–23. doi:10.1016/j.mseb.2007.01.044.

[25] N. Barsan, U. Weimar, Conduction model of metal oxide gas sensors, J. Electroceramics. 7 (2001) 143–167. doi:10.1023/A:1014405811371.

[26] G.F. Fine, L.M. Cavanagh, A. Afonja, R. Binions, Metal Oxide Semi-Conductor Gas Sensors in Environmental Monitoring, Sensors. 10 (2010) 5469–5502. doi:10.3390/s100605469.

[27] N. Barsan, U. Weimar, T. Chemistry, Fundamentals of Metal Oxide Gas Sensors, IMCS 2012- 14th Int. Meet. Chem. Sensors. (2012) 618–621. doi:10.5162/IMCS2012/7.3.3.

[28] J. Mizsei, How can sensitive and selective semiconductor gas sensors be made?, Sensors Actuators B Chem. 23 (1995) 173–176. doi:10.1016/0925-4005(94)01269-N.

[29] S.. Hahn, N. Bârsan, U. Weimar, S.. Ejakov, J.. Visser, R.. Soltis, CO sensing with SnO2 thick film sensors: role of oxygen and water vapour, Thin Solid Films. 436 (2003) 17–24. doi:10.1016/S0040-6090(03)00520-0.

[30] N. Barsan, U. Weimar, Understanding the fundamental principles of metal oxide based gas sensors; the example of CO sensing with SnO_2 sensors in the presence of humidity, J. Phys. Condens. Matter. 15 (2003) R813–R839. doi:10.1088/0953-8984/15/20/201.

[31] R. Vargas-Bernal, G. Herrera-Pérez, Nanotechnology for optics and sensors Importance of the Nanostructured Ceramic Materials on Gas Sensing, n.d.

[32] A. Cabot, A. Diéguez, A. Romano-Rodríguez, J.R. Morante, N. Bârsan, Influence of the catalytic introduction procedure on the nano-SnO_2 gas sensor performances: Where and how stay the catalytic atoms?, Sensors Actuators, B Chem. 79

(2001) 98–106. doi:10.1016/S0925-4005(01)00854-1.
[33] H. Gu, Z. Wang, Y. Hu, Hydrogen Gas Sensors Based on Semiconductor Oxide Nanostructures, 2012. doi:10.3390/s120505517.
[34] M. Hübner, R. Pavelko, J. Kemmler, N. Barsan, U. Weimar, Influence of Material Properties on Hydrogen Sensing for SnO_2 Nanomaterials, Procedia Chem. 1 (2009) 1423–1426. doi:10.1016/j.proche.2009.07.355.
[35] L.I. Trakhtenberg, G.N. Gerasimov, V.F. Gromov, T. V Belysheva, O.J. Ilegbusi, Gas Semiconducting Sensors Based on Metal Oxide Nanocomposites, J. Mater. Sci. Res. 1 (2012). doi:10.5539/jmsr.v1n2p56.
[36] A.A. Firooz, Effect of different morphologies of nanostructured SnO_2 and their nanocomposites on sensing behavior, J. Math. Nanosci. JMNS. 3 (2013) 13–16.
[37] A. Helwig, G. Müller, G. Sberveglieri, M. Eickhoff, M. Eickhoff, On the Low-Temperature Response of Semiconductor Gas Sensors, J. Sensors. 2009 (2009) 1–17. doi:10.1155/2009/620720.
[38] P. Mitra, A. Halder, Effect of initialization time on application potentiality of a ZnO thin film based LPG sensor, Mater. Res. 12 (2009) 329–332. doi:10.1590/S1516-14392009000300013.
[39] C. Xu, J. Tamaki, N. Miura, N. Yamazoe, Grain size effects on gas sensitivity of porous SnO_2-based elements, Sensors Actuators B. Chem. 3 (1991) 147–155. doi:10.1016/0925-4005(91)80207-Z.
[40] S. Das, V. Jayaraman, SnO_2: A comprehensive review on structures and gas sensors, Prog. Mater. Sci. 66 (2014) 112–255. doi:10.1016/j.pmatsci.2014.06.003.
[41] T. Seiyama, A. Kato, K. Fujiishi, M. Nagatani, A New Detector for Gaseous Components Using Semiconductive Thin Films., Anal. Chem. 34 (1962) 1502–1503. doi:10.1021/ac60191a001.
[42] M. Ivanovskaya, P. Bogdanov, G. Faglia, P. Nelli, G. Sbeerveglieri, A. Taroni, On the role of catalytic additives in gas-sensitivity of SnO_2 -Mo based thin film sensors, Sensors Actuators B. Chem. 77 (2001) 268–274.
[43] C. Cobianu, C. Savaniu, P. Siciliano, S. Capone, M. Utriainen, L. Niinisto, SnO_2 sol-gel derived thin films for integrated gas sensors, Sensors And Actuators. 77 (2001) 496–502.
[44] T. Becker, S. Ahlers, C. Bosch-v.Braunmühl, G. Müller, O. Kiesewetter, Gas sensing properties of thin- and thick-film tin-oxide materials, Sensors Actuators, B Chem. 77 (2001) 55–61. doi:10.1016/S0925-4005(01)00672-4.
[45] A. Salehi, The effects of deposition rate and substrate temperature of ITO thin films on electrical and optical properties, Thin Solid Films. 324 (1998) 214–218. doi:10.1016/S0040-6090(98)00371-X.
[46] V. Brinzari, G. Korotcenkov, V. Golovanov, J. Schwank, V. Lantto, S. Saukko, Morphological rank of nano-scale tin dioxide films deposited by spray pyrolysis from $SnCl_45H_2O$ water solution, Thin Solid Films. 408 (2002) 51–58.
[47] G. Korotcenkov, V. Brinzari, J. Schwank, M. Dibattista, A. Vasiliev, Peculiarities of SnO_2 thin film deposition by spray pyrolysis for gas sensor application, Sens. Actuators, B. 77 (2001) 244–252.
[48] A. Salehi, Selectivity enhancement of indium-doped SnO_2 gas sensors, Thin Solid Films. 416 (2002) 260–263. doi:10.1016/S0040-6090(02)00626-0.
[49] A. Rosental, A. Tarre, A. Gerst, T. Uustare, V. Sammelselg, Atomic-layer chemical vapor deposition of SnO_2 for gas-sensing applications, Sensors Actuators B. 77 (2001) 297–300.
[50] A. Salehi, A highly sensitive self heated SnO_2 carbon monoxide sensor, Sensors Actuators, B Chem. 96 (2003) 88–93. doi:10.1016/S0925-4005(03)00490-8.
[51] Y.-S. Choe, New gas sensing mechanism for SnO_2 thin-film gas sensors fabricated by using dual ion beam sputtering, Sensors Actuators B Chem. 77 (2001) 200–208. doi:10.1016/S0925-4005(01)00731-6.
[52] H.C. Wang, Y. Li, M.J. Yang, Fast response thin film SnO_2 gas sensors operating at room temperature, Sensors Actuators, B Chem. 119 (2006) 380–383. doi:10.1016/j.snb.2005.12.037.
[53] Y. Shimizu, A. Jono, T. Hyodo, M. Egashira, Preparation of large mesoporous SnO_2 powder for gas sensor application, Sensors Actuators, B Chem. 108 (2005) 56–61. doi:10.1016/j.snb.2004.10.047.
[54] G. Korotchenkov, V. Brynzari, S. Dmitriev, SnO_2 thin film gas sensors for fire - alarm systems, Sensors Actuators B. 54 (1999) 191–196.
[55] X. Lou, C. Peng, X. Wang, W. Chu, Gas-sensing properties of nanostructured SnO_2-based sensor synthesized with different methods, Vacuum. 81 (2007) 883–889. doi:10.1016/j.vacuum.2006.10.007.
[56] A. Dieguez, A. Romano-Rodríguez, M.J. R, J. Kappler, N. Barsan, W. Gopel, Nanoparticle engineering for gas sensor optimisation : improved sol – gel fabricated nanocrystalline SnO 2 thick film gas sensor for NO_2 detection by calcination , catalytic metal introduction and grinding treatments, Sensors Actuators B. Chem. 60 (1999) 125–137.
[57] A. Khodadadi, A. Miri, S.S. Mohajerzadeh, Y. Mortazavi, Fabrication of SnO_2-Based Semiconductor Gas Sensors for Combustible and Pollutant Gases, 12 Int. Conf. Microelectron. (2000) 317–320.
[58] G.X. Wang, J.S. Park, M.S. Park, X.L. Gou, Synthesis and high gas sensitivity of tin oxide nanotubes, Sensors Actuators, B Chem. 131 (2008) 313–317. doi:10.1016/j.snb.2007.11.032.
[59] Y. Wang, X. Wu, Y. Li, Z. Zhou, Mesostructured SnO_2 as sensing material for gas sensors, Solid. State. Electron. 48 (2004) 627–632. doi:10.1016/j.sse.2003.09.015.
[60] Y. Liu, E. Koep, M. Liu, A Highly Sensitive and Fast-Responding SnO_2 Sensor Fabricated by Combustion Chemical Vapor Deposition, Chem. Mater. 17 (2005) 3997–4000. doi:10.1021/cm050451o.
[61] J.C. Kim, H.K. Jun, J.-S. Huh, D.D. Lee, Tin oxide-based methane gas sensor promoted by alumina-supported Pd catalyst, Sensors Actuators B Chem. 45 (1997) 271–277. doi:10.1016/S0925-4005(97)00325-0.
[62] K. Galatsis, L. Cukrov, W. Wlodarski, P. McCormick, K. Kalantar-Zadeh, E. Comini, G. Sberveglieri, P- and n-type Fe-doped SnO_2 gas sensors fabricated by the mechanochemical processing technique, Sensors Actuators, B Chem. 93 (2003) 562–565. doi:10.1016/S0925-4005(03)00233-8.
[63] C.M. Ghimbeu, M. Lumbreras, J. Schoonman, M. Siadat, Electrosprayed metal oxide semiconductor films for sensitive and selective detection of hydrogen sulfide, Sensors. 9 (2009) 9122–9132. doi:10.3390/s91109122.
[64] M.E. Franke, T.J. Koplin, U. Simon, Metal and Metal Oxide Nanoparticles in Chemiresistors: Does the Nanoscale

Matter?, Small. 2 (2006) 36–50. doi:10.1002/smll.200500261.
[65] V.E. Bochenkov, G.B. Sergeev, Nanomaterials for sensors, Russ. Chem. Rev. 76 (2007) 1011–1020. doi:10.1070/RC2007v076n11ABEH003735.
[66] S. Seal, S. Shukla, Nanocrystalline SnO gas sensors in view of surface reactions and modifications, Jom. 54 (2002) 35–38. doi:10.1007/BF02709091.
[67] S.W. Lee, P.P. Tsai, H. Chen, Comparison study of SnO_2 thin- and thick-film gas sensors, Sensors Actuators, B Chem. 67 (2000) 122–127. doi:10.1016/S0925-4005(00)00390-7.
[68] Y.-J. Choi, I.-S. Hwang, J.-G. Park, K.J. Choi, J.-H. Park, J.-H. Lee, Novel fabrication of an SnO(2) nanowire gas sensor with high sensitivity., Nanotechnology. 19 (2008) 95508. doi:10.1088/0957-4484/19/9/095508.
[69] L. Liu, J. Zhuang, K. Liu, L. Wang, S. Li, W. Li, X. Li, Improved and excellent ethanol sensing properties of SnO_2/multiwalled carbon nanotubes, Chinese Sci. Bull. 55 (2010) 382–385. doi:10.1007/s11434-009-0722-1.
[70] X.-J. Huang, Y.-K. Choi, Chemical sensors based on nanostructured materials, Sensors Actuators B Chem. 122 (2007) 659–671. doi:10.1016/j.snb.2006.06.022.
[71] D.R. Kauffman, A. Star, Carbon Nanotube Gas and Vapor Sensors, Angew. Chemie Int. Ed. 47 (2008) 6550–6570. doi:10.1002/anie.200704488.
[72] Kong, Franklin, Zhou, Chapline, Peng, Cho, Dai, Nanotube molecular wires as chemical sensors, Science. 287 (2000) 622–5. http://www.ncbi.nlm.nih.gov/pubmed/10649989 (accessed January 12, 2017).
[73] T.P. Hülser, H. Wiggers, F.E. Kruis, A. Lorke, Nanostructured gas sensors and electrical characterization of deposited SnO_2 nanoparticles in ambient gas atmosphere, Sensors Actuators, B Chem. 109 (2005) 13–18. doi:10.1016/j.snb.2005.03.012.
[74] A. Kolmakov, M. Moskovits, Chemical Sensing and Catalysis by One Dimensional Metal Oxide Nanostructures, Annu. Rev. Mater. Res. 34 (2004) 151–180. doi:10.1146/annurev.matsci.34.040203.112141.
[75] G. Korotchenkov, V. Brynzari, S. Dmitriev, SnO_2 films for thin film gas sensor design, Mater. Sci. Eng. B. 63 (1999) 195–204. doi:10.1016/s0921-5107(99)00136-1.
[76] J.H. Park, K.H. Kim, Improvement of long-term stability in SnO_2 -based gas sensor for monitoring offensive odor, Sensors And Actuators. 56 (1999) 50–58.
[77] J. Liu, X. Huang, G. Ye, W. Liu, Z. Jiao, W. Chao, Z. Zhou, Z. Yu, H_2S Detection Sensing Characteristic of CuO/SnO_2 Sensor, Sensors. 3 (2003) 110–118. doi:10.3390/s30500110.
[78] M.N. Rumyantseva, M. Labeau, J.P. Senateur, G. Delabouglise, M.N. Boulova, A.M. Gaskov, Influence of copper on sensor properties of tin dioxide films in H_2S, Mater. Sci. Eng. B. 41 (1996) 228–234. doi:10.1016/S0921-5107(96)01601-7.
[79] S.C. Lee, H.Y. Choi, S.J. Lee, W.S. Lee, J.S. Huh, D.D. Lee, J.C. Kim, The development of SnO_2-based recoverable gas sensors for the detection of DMMP, Sensors Actuators B Chem. 137 (2009) 239–245. doi:10.1016/j.snb.2008.12.051.
[80] C. Moldovan, S. Sosin, O. Nedelcu, U. Kaufmann, S. Dimov, P. Petkov, R. Dorey, K. Persson, D. Gomez, P. Johander, F. Karlsruhe, M.T. Centre, N. Group, F. Tekniker, D. Corporation, Mixed technologies for gas sensors microfabrication, (n.d.) 1–7.
[81] J. Zhu, J. Zhu, X. Liao, J. Fang, M. Zhou, Rapid synthesis of nanocrystalline SnO_2 powders by microwave heating method, Mater. Lett. 53 (2002) 12–19.
[82] A. Cirera, A. Vila, A. Dieguez, A. Cabot, Microwave processing for the low cost, mass production of undoped and in situ catalytic doped nanosized SnO_2 gas sensor powders, Sensors Actuators B 64 (2000) 65–69. doi:10.1016/S0925-4005(99)00485-2.
[83] F. Selmi, S. Komarneni, V.K. Varadan, V. V. Varadan, Microwave sintering of Sb-doped SnO_2, Mater. Lett. 10 (1990) 235–238. doi:10.1016/0167-577X(90)90024-G.
[84] N. Baik, G. Sakai, N. Miura, N. Yamazoe, Hydrothermally treated sol solution of tin oxide for thin-film gas sensor, Sensors Actuators B Chem. 63 (2000) 74–79. doi:10.1016/S0925-4005(99)00513-4.
[85] Z. Han, N. Guo, F. Li, W. Zhang, H. Zhao, Y. Qian, Solvothermal preparation and morphological evolution of stannous oxide powders, 2001. doi:10.1016/S0167-577X(00)00286-X.
[86] K.C. Song, J.H. Kim, Synthesis of high surface area tin oxide powders via water-in-oil microemulsions, Powder Technol. 107 (2000) 268–272. doi:10.1016/S0032-5910(99)00255-7.
[87] C. Shek, J.K. Lai, G.. Lin, Grain growth in nanocrystalline SnO_2 prepared by sol-gel route, Nanostructured Mater. 11 (1999) 887–893. doi:10.1016/S0965-9773(99)00387-6.
[88] D. Briand, M. Labeau, J.F. Currie, G. Delabouglise, Pd-doped SnO_2 thin films deposited by assisted ultrasonic spraying CVD for gas sensing: selectivity and effect of annealing, Sensors Actuators B Chem. 48 (1998) 395–402. doi:10.1016/S0925-4005(98)00102-6.
[89] N. Pinna, M. Niederberger, Surfactant-Free Nonaqueous Synthesis of Metal Oxide Nanostructures, Angew. Chemie Int. Ed. 47 (2008) 5292–5304. doi:10.1002/anie.200704541.
[90] S. Rani, S.C. Roy, M.C. Bhatnagar, Effect of Fe doping on the gas sensing properties of nano-crystalline SnO_2 thin films, Sensors Actuators, B Chem. 122 (2007) 204–210. doi:10.1016/j.snb.2006.05.032.
[91] J. Kaur, S.C. Roy, M.C. Bhatnagar, Highly sensitive SnO2 thin film NO_2 gas sensor operating at low temperature, Sensors Actuators, B Chem. 123 (2007) 1090–1095. doi:10.1016/j.snb.2006.11.031.
[92] J. Kaur, R. Kumar, M.C. Bhatnagar, Effect of indium-doped SnO_2 nanoparticles on NO2 gas sensing properties, Sensors Actuators, B Chem. 126 (2007) 478–484. doi:10.1016/j.snb.2007.03.033.
[93] J. Kaur, V.D. Vankar, M.C. Bhatnagar, Gas Sensing Properties of MoO_3 doped SnO_2 thin Films, World Acad. Sci. Eng. Technol. 43 (2008) 322–324.
[94] T. Krishnakumar, R. Jayaprakash, M. Parthibavarman, A.R. Phani, V.N. Singh, B.R. Mehta, Microwave-assisted synthesis and investigation of SnO_2 nanoparticles, Mater. Lett. 63 (2009) 896–898. doi:10.1016/j.matlet.2009.01.032.

[95] G. Neri, T. Krishnakumar, R. Jayaprakash, N. Pinna, A. Donato, N. Donato, G. Micali, Sb-SnO2-nanosized-based resistive sensors for NO_2 detection, J. Sensors. (2009). doi:10.1155/2009/980965.

[96] T. Krishnakumar, N. Pinna, K.P. Kumari, K. Perumal, R. Jayaprakash, Microwave-assisted synthesis and characterization of tin oxide nanoparticles, Mater. Lett. 62 (2008) 3437–3440. doi:10.1016/j.matlet.2008.02.062.

[97] R.C. Singh, M.P. Singh, O. Singh, P.S. Chandi, Influence of synthesis and calcination temperatures on particle size and ethanol sensing behaviour of chemically synthesized SnO_2 nanostructures, Sensors Actuators, B Chem. 143 (2009) 226–232. doi:10.1016/j.snb.2009.09.032.

[98] G.S. Devi, S. Manorama, V.J. Rao, High sensitivity and selectivity of an SnO_2 sensor to H_2S at around 100°C, Sensors Actuators B. 28 (1995) 31–37.

[99] S. Ray, P. Gupta, G. Singh, Electrical and Optical Properties of Sol-gel prepared Pd- doped SnO_2 Thin Films: Effect of Multiple Layersand its Use as Room Temperature Methane Gas Sensor, J. Ovonic Res. 6 (2010) 23–34.

[100] M. V. Vaishampayan, R.G. Deshmukh, I.S. Mulla, Influence of Pd doping on morphology and LPG response of SnO_2, Sensors Actuators, B Chem. 131 (2008) 665–672. doi:10.1016/j.snb.2007.12.055.

[101] R. Rella, A. Serra, P. Sicilian, L. Vasanelli, G. De, A. Licciulii, CO sensing properties of SnO_2 thin films prepared by the sol-gel process, Thin Solid Films. 304 (1997) 339–343.

[102] G. Zhang, M. Liu, Preparation of nanostructured tin oxide using a sol-gel process based on tin tetrachloride and ethylene glycol, J. Mater. Sci. 34 (1999) 3213–3219. doi:10.1023/A:1004685907751.

[103] R.H. Bari, S.B. Patil, A.R. Bari, Synthesis, characterization and gas sensing performance of SnO_2 thin films prepared by spray pyrolysis, Int. J. Smart Sens. Intell. Syst. 7 (2014) 610–629. ISSN 1178-5608.

[104] K. Kang, S.P.I.L. Lee, CO gas sensors operating at room temperature, J. Mater. Sci. 38 (2003) 4319–4323.

[105] S. Gnanam, V. Rajendran, Luminescence Properties of Eg- Assisted SnO_2 Nanoparticles by Sol-gel Process, J. Nanomater. 5 (2010) 699–704.

[106] W. Chen, H. Gan, W. Zhang, Z. Mao, Hydrothermal Synthesis and Hydrogen Sensing Properties of Nanostructured SnO_2 with Different Morphologies, J. Nanomater. 2014 (2014) 1–7. doi:10.1155/2014/291273.

[107] K. Anandan, V. Rajendran, Size controlled synthesis of SnO_2 nanoparticles:\rFacile solvothermal process, J. Non-Oxide Glas. 2 (2010) 83–89. http://www.chalcogen.ro/83_Anandan.pdf.

[108] G.E. Patil, D.D. Kajale, D.N. Chavan, N.K. Pawar, P.T. Ahire, S.D. Shinde, V.B. Gaikwad, G.H. Jain, Synthesis , characterization and gas sensing performance of SnO_2 thin films prepared by spray pyrolysis, Bull. Mater. Sci. 34 (2011) 1–9. doi:10.1007/s12034-011-0045-0.

[109] L. Tan, L. Wang, Y. Wang, Hydrothermal Synthesis of SnO_2 Nanostructures with Different Morphologies and Their Optical Properties, J. Nanomater. 2011 (2011) 1–10. doi:10.1155/2011/529874.

[110] S.P. Mondal, S.K. Ray, Temperature dependent growth and optical properties of SnO_2 nanowires and nanobelts, Bull. Mater. 33 (2010) 357–364. http://www.springerlink.com/index/0116478551026G34.pdf.

[111] V. Arivazhagan, S. Rajesh, Preparation of Nanocrystalline SnO_2 Thin Films For Micro Gas Sensors, 6 (2010) 221–226.

[112] R. Rai, Study of structural and electrical properties of pure and Zn-Cu doped SnO_2, Adv. Mater. Lett. 1 (2010) 55–58. doi:10.5185/amlett.2010.3101.

[113] G. Neri, T. Krishnakumar, R. Jayaprakash, N. Pinna, A. Donato, N. Donato, G. Micali, Sb-SnO_2-nanosized-based resistive sensors for NO_2 detection, J. Sensors. 2009 (2009). doi:10.1155/2009/980965.

[114] A.P. Rizzato, C. V. Santilli, S.H. Pulcinelli, D. Stuerga, D. Chaumont, V. Briois, Densification of Mn-Doped Tin Oxide Films by Conventional Heating and Microwave Heating Treatment, Phys. Scr. 2005 (2005) 291. doi:10.1238/Physica.Topical.115a00291.

[115] S. Mishra, C. Ghanshyam, N. Ram, S. Singh, R.P. Bajpai, R.K. Bedi, Alcohol sensing of tin oxide thin film prepared by sol-gel process, Bull. Mater. Sci. 25 (2002) 231–234. doi:10.1007/BF02711159.

[116] C. Wang, W. Zeng, L. Luo, P. Zhang, Z. Wang, Gas-sensing properties and mechanisms of Cu-doped SnO_2 spheres towards H2S, Ceram. Int. 42 (2016) 10006–10013. doi:10.1016/j.ceramint.2016.03.103.

[117] N. Bhardwaj, A. Pandey, B. Satpati, M. Tomar, V. Gupta, S. Mohapatra, Enhanced CO gas sensing properties of Cu doped SnO_2 nanostructures prepared by a facile wet chemical method, Phys. Chem. Chem. Phys. 18 (2016) 18846–18854. doi:10.1039/C6CP01758D.

[118] W.X. Jin, S.Y. Ma, Z.Z. Tie, J.J. Wei, J. Luo, X.H. Jiang, T.T. Wang, W.Q. Li, L. Cheng, Y.Z. Mao, One-step synthesis and highly gas-sensing properties of hierarchical Cu-doped SnO_2 nanoflowers, Sensors Actuators B Chem. 213 (2015) 171–180. doi:10.1016/j.snb.2015.02.075.

[119] S. Kim, W. Choi, H 2 S Micro Gas Sensor Based on a SnO_2 -CuO Multi-layer Thin Film, J. Mater. Sci. Eng. A. 13 (2012) 27–30.

[120] V. Kumar, S. Sen, K.P. Muthe, N.K. Gaur, S.K. Gupta, J. V. Yakhmi, Copper doped SnO_2 nanowires as highly sensitive H_2S gas sensor, Sensors Actuators, B Chem. 138 (2009) 587–590. doi:10.1016/j.snb.2009.02.053.

[121] A. Johari, A. Johari, M.C. Bhatnagar, M. Sharma, Structural, optical and ethanol sensing properties of Cu-doped SnO_2 nanowires, in: AIP Conf. Proc., American Institute of PhysicsAIP, 2014: pp. 306–308. doi:10.1063/1.4872582.

[122] A. Johari, A. Johari, M.C. Bhatnagar, M. Sharma, Structural, Optical and Sensing Properties of Pure and Cu-Doped SnO_2 Nanowires, J. Nanosci. Nanotechnol. 14 (2014) 5288–5292. doi:10.1166/jnn.2014.9142.

[123] S. Benzitouni, M. Zaabat, A. Khial, D. Rechem, A. Benaboud, D. Bouras, A. Mahdjoub, M. Toubane, R. Coste, U.M. Larbi Ben, O. El Bouaghi, High Sensitivity of Porous Cu-Doped SnO_2 Thin Films to Methanol, 5 (2016) 140–148. doi:10.4236/anp.2016.52016.

[124] T.V.K. Karthik, M. De La Luz Olvera, A. Maldonado, H. Gmezpozos, CO gas sensing properties of pure and Cu-incorporated SnO_2 nanoparticles: A study of Cu-induced modifications, Sensors (Switzerland). 16 (2016). doi:10.3390/s16081283.

[125] P.S. More, Y.B. Khollam, S.B. Deshpande, S.R. Sainkar, S.K. Date, R.N. Karekar, R.C. Aiyer, High-performance

temperature-selective SnO_2:Cu-based sensor, Mater. Lett. 57 (2003) 2177–2184. doi:10.1016/S0167-577X(02)01170-9.

[126] P.. More, Y.. Khollam, S.. Deshpande, S.. Date, R.. Karekar, R.. Aiyer, Effect of variation of sintering temperature on the gas sensing characteristics of SnO_2:Cu (Cu=9 wt.%) system, Mater. Lett. 58 (2004) 205–210. doi:10.1016/S0167-577X(03)00446-4.

[127] D. Singh, V.S. Kundu, A.S. Maan, Structural, morphological and gas sensing study of zinc doped tin oxide nanoparticles synthesized via hydrothermal technique, J. Mol. Struct. 1115 (2016) 250–257. doi:10.1016/j.molstruc.2016.02.091.

[128] I. Sakaguchi, N. Saito, K. Watanabe, Y. Adachi, T.T. Suzuki, Evaluation of sensor property for hydrogen and ethanol of zinc-doped tin-dioxide thin films fabricated by rf sputtering, J. Ceram. Soc. Japan. 124 (2016) 714–716. doi:10.2109/jcersj2.16015.

[129] R.H. Bari, S.B. Patil, Improved NO_2 sensing performance of nanostructured Zn doped SnO_2 thin films, Int. J. TechnoChem Res. Www.technochemsai.com. 1 (2015) 86–96.

[130] Q. Zhao, D. Ju, X. Deng, J. Huang, B. Cao, X. Xu, Morphology-modulation of SnO_2 Hierarchical Architectures by Zn Doping for Glycol Gas Sensing and Photocatalytic Applications, Sci. Rep. 5 (2015) 7874. doi:10.1038/srep07874.

[131] G. Singh, J. Kaur, R.C. Singh, Gas sensing behaviour of Zn doped SnO_2 nanostructures, in: AIP Conf. Proc., AIP Publishing LLCAIP Publishing, 2015: p. 30042. doi:10.1063/1.4929258.

[132] M. Kumar, Gas Sensing Properties of Zn-Doped Tin Oxide Nanoparticles with Methanol, INDIAN J. Appl. Res. X. 507 (2015) 2249–555.

[133] Y. Guan, D. Wang, X. Zhou, P. Sun, H. Wang, J. Ma, G. Lu, Hydrothermal preparation and gas sensing properties of Zn-doped SnO_2 hierarchical architectures, Sensors Actuators B Chem. 191 (2014) 45–52. doi:10.1016/j.snb.2013.09.002.

[134] L.K. Bagal, J.Y. Patil, K.N. Bagal, I.S. Mulla, S.S. Suryavanshi, Acetone vapour sensing characteristics of undoped and Zn, Ce doped SnO_2 thick film gas sensor, Mater. Res. Innov. 17 (2013) 98–105. doi:10.1179/1433075X12Y.0000000035.

[135] S. Tian, Y. Gao, D. Zeng, C. Xie, Effect of zinc doping on microstructures and gas-sensing properties of SnO_2 nanocrystals, J. Am. Ceram. Soc. 95 (2012) 436–442. doi:10.1111/j.1551-2916.2011.04957.x.

[136] W. Wang, Y. Tian, X. Li, X. Wang, H. He, Y. Xu, C. He, Enhanced ethanol sensing properties of Zn-doped SnO_2 porous hollow microspheres, Appl. Surf. Sci. 261 (2012) 890–895. doi:10.1016/j.apsusc.2012.08.118.

[137] P. Sun, L. You, Y. Sun, Novel Zn-doped SnO_2 hierarchical architectures: synthesis, characterization, and gas sensing properties, CrystEngComm. 14 (2012) 1701–1708. doi:10.1039/C1CE06197F.

[138] J.S. Bhat, K.I. Maddani, A.M. Karguppikar, Influence of Zn doping on electrical and optical properties of multilayered tin oxide thin films, Bull. Mater. Sci. 29 (2006) 331–337.

[139] Z.A. Ansari, S.G. Ansari, T. Ko, J.H. Oh, Effect of MoO_3 doping and grain size on SnO_2-enhancement of sensitivity and selectivity for CO and H_2 gas sensing, Sensors Actuators, B Chem. 87 (2002) 105–114. doi:10.1016/S0925-4005(02)00226-5.

[140] M. V. Vaishampayan, R.G. Deshmukh, P. Walke, I.S. Mulla, Fe-doped SnO_2 nanomaterial: A low temperature hydrogen sulfide gas sensor, Mater. Chem. Phys. 109 (2008) 230–234. doi:10.1016/j.matchemphys.2007.11.024.

[141] S. Bose, S. Chakraborty, B.K. Ghosh, D. Das, A. Sen, H.S. Maiti, Methane sensitivity of Fe-doped SnO_2 thick films, Sensors Actuators B Chem. 105 (2005) 346–350. doi:10.1016/j.snb.2004.06.023.

[142] N.S. Ramgir, Y.K. Hwang, S.H. Jhung, H.K. Kim, J.S. Hwang, I.S. Mulla, J.S. Chang, CO sensor derived from mesostructured Au-doped SnO_2 thin film, Appl. Surf. Sci. 252 (2006) 4298–4305. doi:10.1016/j.apsusc.2005.07.015.

[143] Z. Bin, Y. Chenbo, Z. Zili, T. Chunmin, Y. Liu, Investigation of the hydrogen response characteristics for sol-gel-derived Pd-doped, Fe-doped and PEG-added SnO_2 nano-thin films, Sensors Actuators B Chem. 178 (2013) 418–425. doi:10.1016/j.snb.2012.12.101.

[144] Z. Wang, L. Liu, Synthesis and ethanol sensing properties of Fe-doped SnO_2 nanofibers, Mater. Lett. 63 (2009) 917–919. doi:10.1016/j.matlet.2009.01.051.

[145] X.-T. Yin, X.-M. Guo, Sensitivity and selectivity of (Au, Pt, Pd)-loaded and (In, Fe)-doped SnO_2 sensors for H_2 and CO detection, J. Mater. Sci. Mater. Electron. 25 (2014) 4960–4966. doi:10.1007/s10854-014-2258-7.

[146] A. Gupta, M.C. Bhatnagar, P. Rajaram, Preparation of Undoped and Sb Doped Tin Oxide Films by Spray Pyrolysis for Gas Sensing Studies, Am. Int. J. Res. Formal, Appl. Nat. Sci. (2015) 46–50.

[147] I. Verma, R. Kumar, N. Verma, Synthesis and Characterization of Sb doping on thick film SnO_2 Gas Sensor by Sol-Gel Method, Int. J. Sci. Res. Eng. Technol. 1 (2012) 49–51.

[148] J. Kaur, V.D. Vankar, M.C. Bhatnagar, Effect of MoO_3 addition on the NO_2 sensing properties of SnO_2 thin films, Sensors Actuators, B Chem. 133 (2008) 650–655. doi:10.1016/j.snb.2008.03.042.

[149] J. Zhang, S. Wang, Y. Wang, Y. Wang, B. Zhu, H. Xia, X. Guo, S. Zhang, W. Huang, S. Wu, NO_2 sensing performance of SnO_2 hollow-sphere sensor, Sensors Actuators, B Chem. 135 (2009) 610–617. doi:10.1016/j.snb.2008.09.026.

[150] K. Jain, R.P. Pant, S.T. Lakshmikumar, Effect of Ni doping on thick film SnO_2 gas sensor, Sensors Actuators, B Chem. 113 (2006) 823–829. doi:10.1016/j.snb.2005.03.104.

[151] X. Liu, J. Zhang, X. Guo, S. Wu, S. Wang, Enhanced sensor response of Ni-doped SnO2 hollow spheres, Sensors Actuators, B Chem. 152 (2011) 162–167. doi:10.1016/j.snb.2010.12.001.

[152] Z. Lin, N. Li, Z. Chen, P. Fu, The effect of Ni doping concentration on the gas sensing properties of Ni doped SnO_2, Sensors Actuators, B Chem. 239 (2017) 501–510. doi:10.1016/j.snb.2016.08.053.

[153] Y. Chen, L. Yu, D. Feng, M. Zhuo, M. Zhang, E. Zhang, Z. Xu, Q. Li, T. Wang, Superior ethanol-sensing properties based on Ni-doped SnO_2 p-n heterojunction hollow spheres, Sensors Actuators, B Chem. 166–167 (2012) 61–67. doi:10.1016/j.snb.2011.12.018.

[154] R. Yogamalar, V. Mahendran, R. Srinivasan, A. Beitollahi, R.P. Kumar, A.C. Bose, A. Vinu, Gas-sensing properties of needle-shaped Ni-doped SnO_2 nanocrystals prepared by a simple sol-gel chemical precipitation method, Chem. - An Asian J. 5 (2010) 2379–2385. doi:10.1002/asia.201000358.

[155] M.M. Rahman, A. Jamal, S.B. Khan, M. Faisal, Highly sensitive ethanol chemical sensor based on Ni-doped SnO_2 nanostructure materials, Biosens. Bioelectron. 28 (2011) 127–134. doi:10.1016/j.bios.2011.07.024.

[156] R. Rai, Study of structural and electrical properties of pure and Zn-Cu doped SnO_2, 1 (2010) 55–58. doi:10.5185/amlett.2010.3101.

[157] J. Mrázek, V. Matejec, I. Kasik, M. Hayer, D. Berková, Application of the sol-gel method at the fabrication of microstructure fibers, J. Sol-Gel Sci. Technol. 31 (2004) 175–178. doi:10.1023/B:JSST.0000047982.14815.65.

[158] A. Mondal, D. Agrawal, A. Upadhyaya, M. Engineering, Microwave Heating of Pure Copper Powder With Different, (n.d.) 517–520.

[159] V. Subramanian, W.W. Burke, H. Zhu, B. Wei, Novel Microwave Synthesis of Nanocrystalline SnO_2 and Its Electrochemical Properties, J. Phys. Chem. C. 112 (2008) 4550–4556. doi:10.1021/jp711551p.

[160] F.I. Pires, E. Joanni, R. Savu, M.A. Zaghete, E. Longo, J.A. Varela, Microwave-assisted hydrothermal synthesis of nanocrystalline SnO powders, Mater. Lett. 62 (2008) 239–242. doi:10.1016/j.matlet.2007.05.006.

[161] S. Shi, J. Hwang, Microwave-assisted wet chemical synthesis : advantages , significance, and steps to industrialization, Mater. Charact. 2 (2003) 101–110.

[162] D.S. Wu, C.Y. Han, S.Y. Wang, N.L. Wu, I.A. Rusakova, Microwave-assisted solution synthesis of SnO nanocrystallites, Mater. Lett. 53 (2002) 155–159. doi:10.1016/S0167-577X(01)00468-2.

[163] A. Lagashetty, V. Havanoor, S. Basavaraja, S.D. Balaji, A. Venkataraman, Microwave-assisted route for synthesis of nanosized metal oxides, Sci. Technol. Adv. Mater. 8 (2007) 484–493. doi:10.1016/j.stam.2007.07.001.

[164] S. Das, A.K. Mukhopadhyay, S. Datta, D. Basu, Prospects of microwave processing An overview.pdf, Bull Mater Sci. 31 (2008) 943–956. doi:10.1007/s12034-008-0150-x.

[165] J. Gajendiran, V. Rajendran, Size controlled and optical properties of Zn- doped SnO_2 nanoparticles via sol-gel process, Optoelectron. Adv. Mater. Commun. 5 (2011) 44–48.

[166] H. Huang, S. Tian, J. Xu, Z. Xie, D. Zeng, D. Chen, G. Shen, Needle- like Zn-doped SnO_2 nanorods with enhanced photocatalytic and gas sensing properties, Nanotechnology. 23 (2012) 105502–105502. doi:10.1088/0957-4484/23/10/105502.

[167] P. Gupta, R. Vyas, B.L. Choudhary, K. Sachdev, D.S. Patil, S.K. Sharma, Synthesis and characterization of Pure and Doped SnO_2 Nanopowders, Int. J. Mod. Phys. Conf. Ser. 22 (2013) 452–457. doi:10.1142/S2010194513010507.

[168] E.R. Leite, M.I.B. Bernardi, E. Longo, J.A. Varela, C.A. Paskocimas, Enhanced electrical property of nanostructured Sb-doped SnO_2 thin film processed by soft chemical method, Thin Solid Films. 449 (2004) 67–72. doi:10.1016/j.tsf.2003.10.101.

[169] G.E. Patil, Kajale D D, Shinde S D, Bari R H, Chavan D N, Gaikwad V B, Jain G H, Effect of Annealing Temperature on Gas Sensing Performance of SnO_2 Thin Films Prepared by Spray Pyrolysis, Sensors & Transducers. 9 (2010) 96–108.

[170] E.N. Kaufmann, Characterization of Materials, 2008. http://medcontent.metapress.com/index/A65RM03P4874243N.pdf.

[171] M. Gaidi, A. Hajjaji, R. Smirani, B. Bessais, M.A. El Khakani, Structure and photoluminescence of ultrathin films of SnO_2 nanoparticles synthesized by means of pulsed laser deposition, J. Appl. Phys. 108 (2010). doi:10.1063/1.3485811.

[172] S.P. Mondal, S.K. Ray, J. Ravichandran, I. Manna, Temperature dependent growth and optical properties of SnO_2 nanowires and nanobelts, Bull. Mater. Sci. 33 (2010) 357–364. doi:10.1007/s12034-010-0054-4.

[173] P. Gupta, R. Vyas, B.L. Choudhary, K.V.R. Rao, K. Sachdev, D.S. Patil, S.K. Sharma, A comparative study of the sol-gel synthesized nanostructured SnO_2 powders, AIP Conf. Proc. 1536 (2013) 159–160. doi:10.1063/1.4810149.

[174] P. Hidalgo, R.H.R. Castro, A.C. V Coelho, D. Gouvêa, Surface segregation and consequent SO_2 sensor response in SnO_2-NiO, Chem. Mater. 17 (2005) 4149–4153. doi:10.1021/cm049020g.

[175] R.N. Mariammal, K. Ramachandran, B. Renganathan, D. Sastikumar, On the enhancement of ethanol sensing by CuO modified SnO_2 nanoparticles using fiber-optic sensor, Sensors Actuators B Chem. 169 (2012) 199–207. doi:10.1016/j.snb.2012.04.067.

[176] P. Chetri, A. Choudhury, Investigation of structural and magnetic properties of nanoscale Cu doped SnO_2: An experimental and density functional study, J. Alloys Compd. 627 (2015) 261–267. doi:10.1016/j.jallcom.2014.11.204.

[177] N. Talebian, F. Jafarinezhad, Morphology-controlled synthesis of SnO_2 nanostructures using hydrothermal method and their photocatalytic applications, Ceram. Int. 39 (2013) 8311–8317. doi:10.1016/j.ceramint.2013.03.101.

[178] G.-H. Lee, Effect of the N_2/O_2 ratio on the morphology of SnO_2 crystals synthesized through the thermal evaporation of Sn, Ceram. Int. 41 (2015) 12058–12064. doi:10.1016/j.ceramint.2015.06.021.

[179] X. Li, R. Deng, Y. Li, B. Yao, Z. Ding, J. Qin, Q. Liang, Effect of Mg doping on optical and electrical properties of SnO_2 thin films: An experiment and first-principles study, Ceram. Int. 42 (2016) 5299–5303. doi:10.1016/j.ceramint.2015.12.059.

[180] K. Sakthiraj, B. Karthikeyan, K. Balachandrakumar, Structural , Optical and Magnetic properties of Copper (Cu) doped Tin oxide (SnO_2) nanocrystal, 7 (2015) 1481–1487.

[181] M. Parthibavarman, V. Hariharan, C. Sekar, V.N. Singh, Effect of copper on structural, optical and electrochemical properties of SnO_2 nanoparticles, J. Optoelectron. Adv. Mater. 12 (2010) 1894–1898.

[182] M. Ma, Z. He, Z. Xiao, K. Huang, L. Xiong, X. Wu, Synthesis and electrochemical properties of SnO_2-CuO nanocomposite powders, Trans. Nonferrous Met. Soc. China. 16 (2006) 791–794. doi:10.1016/S1003-6326(06)60327-0.

[183] N. Saravanan, S. Shri Prasad, S. Ponnusamy, J. V., Ultrasonic-assisted wet chemical synthesis and characterization of Eu^{3+} doped\SnO_2 nanoparticles, Der Pharma Chem. 7 (n.d.) 1574–1577. (accessed February 12, 2017).

[184] A.S. Ahmed, M. Shafeeq M., M.L. Singla, S. Tabassum, A.H. Naqvi, A. Azam, Band gap narrowing and fluorescence properties of nickel doped SnO_2 nanoparticles, J. Lumin. 131 (2011) 1–6. doi:10.1016/j.jlumin.2010.07.017.

[185] L.M. Fang, X.T. Zu, Z.J. Li, S. Zhu, C.M. Liu, W.L. Zhou, L.M. Wang, Synthesis and characteristics of Fe^{3+}-doped SnO_2 nanoparticles via sol–gel-calcination or sol–gel-hydrothermal route, J. Alloys Compd. 454 (2008) 261–267. doi:10.1016/j.jallcom.2006.12.014.

[186] T. Krishnakumar, R. Jayaprakash, N. Pinna, A.R. Phani, M. Passacantando, S. Santucci, Structural, optical and electrical characterization of antimony-substituted tin oxide nanoparticles, J. Phys. Chem. Solids. 70 (2009) 993–999. doi:10.1016/j.jpcs.2009.05.013.

[187] M. Law, H. Kind, B. Messer, F. Kim, P. Yang, Photochemical Sensing of NO_2 with SnO_2 Nanoribbon Nanosensors at Room Temperature**, Angew. Chem. Int. Ed. 41 (2002) 2405.

[188] Z. Cao, J.R. Stetter, A selective solid-state gas sensor for halogenated hydrocarbons, Sensors Actuators B Chem. 5 (1991) 109–113. doi:10.1016/0925-4005(91)80229-D.

[189] V.R. Shinde, T.P. Gujar, C.D. Lokhande, Enhanced response of porous ZnO nanobeads towards LPG: Effect of Pd sensitization, Sensors Actuators B. 123 (2007) 701–706.

[190] H. Zhao, Y. Li, L. Yang, X. Wu, Synthesis, characterization and gas-sensing property for C_2H_5OH of SnO_2 nanorods, Mater. Chem. Phys. 112 (2008) 244–248. doi:10.1016/j.matchemphys.2008.05.039.

[191] X. Du, S.M. George, Thickness dependence of sensor response for CO gas sensing by tin oxide films grown using atomic layer deposition, Sensors Actuators B Chem. 135 (2008) 152–160. doi:10.1016/j.snb.2008.08.015.

[192] D. Manno, G. Micocci, R. Rella, A. Serra, A. Taurino, A. Tepore, Titanium oxide thin films for NH_3 monitoring: Structural and physical characterizations, J. Appl. Phys. 82 (1997) 54–60. doi:10.1063/1.365848.

[193] S.G. Ansari, P. Boroojerdian, S.R. Sainkar, R.N. Karekar, R.C. Aiyer, S.K. Kulkarni, Grain size effects on H_2 gas sensitivity of thick film resistor using SnO_2 nanoparticles, Thin Solid Films. 295 (1997) 271–276.

[194] S.F. Bamsaoud, S.B. Rane, R.N. Karekar, R.C. Aiyer, Nano particulate SnO_2 based resistive films as a hydrogen and acetone vapour sensor, Sensors Actuators B Chem. 153 (2011) 382–391. doi:10.1016/j.snb.2010.11.003.

[195] P. Sun, L. You, D. Wang, Y. Sun, J. Ma, G. Lu, Synthesis and gas sensing properties of bundle-like -Fe_2O_3 nanorods, Sensors Actuators B. 156 (2011) 368–374. doi:10.1016/j.snb.2011.04.050.

[196] X. Xu, P. Zhao, D. Wang, P. Sun, L. You, Y. Sun, X. Liang, F. Liu, H. Chen, G. Lu, Preparation and gas sensing properties of hierarchical flower-like In_2O_3 microspheres, Sensors Actuators B. 176 (2013) 405–412. doi:10.1016/j.snb.2012.10.091.

[197] L. You, X. He, D. Wang, P. Sun, Y.F. Sun, X.S. Liang, Y. Du, G.Y. Lu, Ultrasensitive and low operating temperature NO_2 gas sensor using nanosheets assembled hierarchical WO_3 hollow microspheres, Sensors Actuators, B Chem. 173 (2012) 426–432. doi:10.1016/j.snb.2012.07.029.

[198] S. Liu, M. Xie, Y. Li, X. Guo, W. Ji, W. Ding, C. Au, Novel sea urchin-like hollow core-shell SnO_2 superstructures: Facile synthesis and excellent ethanol sensing performance, Sensors Actuators, B Chem. 151 (2010) 229–235. doi:10.1016/j.snb.2010.09.015.

[199] N. Barsan, U. Weimar, Conduction model of metal oxide gas sensors, J. Electroceramics. 7 (2001) 143–167. doi:10.1023/A:1014405811371.

[200] L. Liu, S. Li, J. Zhuang, L. Wang, J. Zhang, H. Li, Z. Liu, Y. Han, X. Jiang, P. Zhang, Improved selective acetone sensing properties of CO-doped ZnO nanofibers by electrospinning, Sensors Actuators, B Chem. 155 (2011) 782–788. doi:10.1016/j.snb.2011.01.047.

[201] S.M. Rozati, E. Shadmani, Effect of Zn Concentration on Physical Properties of Nanostructure Tnin Oxide Films prepared by Spray Pyrolysis Technique, Dig. J. Nanomater. Biostructures. 6 (2011) 365–372.

[202] N. Yamazoe, K. Shimanoe, New perspectives of gas sensor technology, Sensors Actuators, B Chem. 138 (2009) 100–107. doi:10.1016/j.snb.2009.01.023.

[203] N. Barsan, D. Koziej, U. Weimar, Metal oxide-based gas sensor research: How to?, Sensors Actuators, B Chem. 121 (2007) 18–35. doi:10.1016/j.snb.2006.09.047.

[204] K. Fukui, M. Nakane, CO gas sensor based on Au-La_20_3 loaded SnO_2 ceramic, Sensors Actuators B. 2425 (1995) 486–490.

[205] C. Xu, J. Tamaki, N. Miura, N. Yamazoe, Grain size effects on gas sensitivity of porous SnO_2-based elements, Sensors Actuators B Chem. 3 (1991) 147–155. doi:10.1016/0925-4005(91)80207-Z.

[206] H. Gong, J.Q. Hu, J.H. Wang, C.H. Ong, F.R. Zhu, Nano-crystalline Cu-doped ZnO thin film gas sensor for CO, Sensors Actuators, B Chem. (2006). doi:10.1016/j.snb.2005.09.008.

[207] G.E. Patil, D.D. Kajale, S.D. Shinde, V.G. Wagh, V.B. Gaikwad, Synthesis of Cu-Doped SnO_2 Thin Films by Spray Pyrolysis for Gas Sensor Application, Adv. Sens. Technol. (2013) 299–311.

[208] R.S. Niranjan, V.A. Chaudhary, I.S. Mulla, K. Vijayamohanan, A novel hydrogen sulfide room temperature sensor based on copper nanocluster functionalized tin oxide thin films, Sensors Actuators B. 85 (2002) 26–32.

[209] T. Pagnier, M. Boulova, A. Galerie, A. Gaskov, G. Lucazeau, Reactivity of SnO_2-CuO nanocrystalline materials with H_2S: A coupled electrical and Raman spectroscopic study, Sensors Actuators B Chem. 71 (2000) 134–139. doi:10.1016/S0925-4005(00)00598-0.

[210] B. Wang, L. F. Zhu, Y. H. Yang, N. S. Xu, G. W. Yang, Fabrication of a SnO_2 Nanowire Gas Sensor and Sensor Performance for Hydrogen, J. Phys. Chem. C (ACS Publ. 112 (2008) 6643–6647. doi:10.1021/JP8003147.

[211] X. Liu, J. Zhang, X. Guo, S. Wu, S. Wang, Enhanced sensor response of Ni-doped SnO_2 hollow spheres, Sensors Actuators, B Chem. (2011). doi:10.1016/j.snb.2010.12.001.

Declaration

I herewith declare that I have produced this thesis without the prohibited assistance of third parties and without making use of aids other than those specified; notions taken over directly or indirectly from other sources have been identified as such. This thesis has not previously been presented in identical or similar form to any other Indian or foreign examination board.

This thesis work was conducted from July, 2010 to April, 2017 under the supervision of Prof. S. K. Sharma at Department of Physics, Malaviya National Institute of Technology Jaipur.

(PARUL GUPTA)

JAIPUR

Bio-data

Name: **PARUL GUPTA**
Email: parul.mnit@gmail.com

Educational Qualification:

- M.Sc. Physics, 2006-2008 (8.98 CGPA)
  Malaviya National Institute of Technology Jaipur
- B.Sc., University of Rajasthan, Jaipur, 2003-2006

Professional Experience:

- DST-INSPIRE Fellow- July, 2010 to June, 2014
- INUP student
- Guest Faculty in Department of Physics, MNIT Jaipur –
  August, 2008 to May, 2010

Computer skills:

- Programming languages: C / C++, AutoCAD
- Overview of DBMS
- Working knowledge of Research Softwares, Origin 9.0 etc.

Research Projects and Courses:

- Pre-Ph.D. course work conducted by MNIT Jaipur, covering study of various experimental techniques and numerical methods.
- Synthesis & Characterization of SnO_2 for Gas Sensing Application.
- SnO_2 Based Microwave Sintered Combustible Gas Sensors: Study of Grain Size Effects in Enhancing the Gas Sensing Behaviour DAE-BRNS Project.
- Oxidation of Amorphous Alloy $Ni_{44}Nb_{56}$ at Temperatures 573 K & 623 K.

Awards and Achievements:

- Awarded **DST- INSPIRE Fellowship**.
- Awarded **Gold Medal** for securing **highest marks in M.Sc. (Physics)** in M.N.I.T., Jaipur.
- **Best poster award** in National workshop "Nanoscience and Technology (NST-2013)" at NIT, Hamirpur.
- **Best oral award** in National conference "8th National Conference on Thermophysical Properties NCTP – 2015" at MNIT, Jaipur.

Conferences/ Workshops Attended:

- International Conferences 03
- National Conferences 01
- Workshops 03

- Short Term Course on "Characterization Techniques" 17-21 June, 2013.

List of publications from the thesis work

1. A study of oxygen gas sensing in Zn-doped SnO_2 nanostructures
   Parul Gupta, S.K. Sharma
   Materials Research Express, 4 (2017) 065010.

2. Effect of Temperature on Synthesis and Gas Sensing of Nanostructured SnO_2
   Parul Gupta, S.K. Sharma
   Advanced Science Letters, 22:11 (2016) 3743-3746.

3. Synthesis and Characterization of Pure and Zn-doped SnO_2 Nanopowders
   Parul Gupta, Rishi Vyas, B.L. Choudhary, K. Sachdev, D.S. Patil, S.K. Sharma
   International Journal of Modern Physics: Conference Series. 22 (2013) 452-457.

4. A Comparative Study of the Sol-Gel Synthesized Nanostructured SnO_2 Powders
   Parul Gupta, Rishi Vyas, B.L. Choudhary, K.V.R. Rao, K. Sachdev, D.S. Patil, S.K. Sharma
   AIP Conf. Proc. 1536 (2013) 159-160.

5. Sb-doped SnO_2 Nanostructures: Synthesis and H_2 Sensing Study
   Parul Gupta, S.K. Sharma
   (Manuscript submitted to Applied Materials Today)

Note: Two more manuscripts based on unpublished work pertaining to gas sensing behaviour for H_2, H_2S, CH_4 and microwave sintering effect are under preparation for submission to refereed journals.

Other publications list

1. Nitrogen dioxide induced conductivity switching in ZnO thin film
   Rishi Vyas, S. Sharma, **Parul Gupta**, A.K. Prasad, A.K. Tyagi, K. Sachdev, S.K. Sharma
   Journal of Alloys and Compounds 571 (2013) 6-11.

2. Enhanced NO_2 sensing using ZnO-TiO_2 nanocomposite thin films
   Rishi Vyas, S. Sharma, **Parul Gupta**, Y.K. Vijay, A.K. Prasad, A.K. Tyagi, K. Sachdev, S.K. Sharma
   Journal of Alloys and Compounds 554 (2013) 59-63.

3. CNT-ZnO nanocomposite thin films: O_2 and NO_2 sensing
   Rishi Vyas, S Sharma, **Parul Gupta**, A.K. Prasad, A.K. Tyagi, K. Sachdev, S.K. Sharma
   Adv. Mater. Res. 585 (2012) 235-239.

4. Synthesis and hydrogen sensing properties of CNT-ZnO nanocomposite thin films
   Rishi Vyas, S. Sharma, **Parul Gupta**, K. Sachdev, S.K. Sharma
   International Journal of Modern Physics: Conference Series. 22 (2013) 478-482.

5. A study on the origin of anomalous gas sensing behavior in sol-gel spin coated ZnO thin films
   Rishi Vyas, S. Sharma, **Parul Gupta**, A.K. Prasad, A.K. Tyagi, K. Sachdev, S.K. Sharma
   To be published in Institute of Physics Journal IOP Conference Series: Materials Science and Engineering

6. Plasma induced modifications on sin-coated ZnO thin films
   Rishi Vyas, **Parul Gupta**, S. Mathur, K. Sachdev, S.K. Sharma
   AIP Conf. Proc. 1349 (2011) 357-358.

7. Anomalous gas sensing behaviour of sol-gel spin coated ZnO thin films for H_2 and CH_4 exposure
   Rishi Vyas, S. Sharma, **Parul Gupta**, A.K. Prasad, S. Rajagoplan, M. Kamruddin, S.K. Dhara, A.K. Tyagi, K. Sachdev, S.K. Sharma
   International conference and workshop on nanostructured ceramics and other nanomaterials (ICWNCN-2012) organised by University of Delhi, Delhi during March 13-16, 2012.

8. Origin of high intensity A_1(LO) Raman vibration mode in sol-gel spin coated ZnO thin films
   Rishi Vyas, **Parul Gupta**, K. Sachdev, S.K. Sharma
   Current trends in Materials Research (CTMR-2012), organised by University of Rajasthan, Jaipur during March 17-19, 2012.

9. Corrosion Behaviour of Melt-spun Ribbon $Ti_{60}Ni_{40}$ in 1 M H_2SO_4 Aqueous Medium
   Shubhra Mathur, Rishi Vyas, **Parul Gupta**, Rohit Jain, K. Sachdev and S. K. Sharma
   in proceedings of National Conference on Emerging Trends of Research in Materials Science ETRMS-2011, SKIT Jaipur (2011) ISBN No. 978-93-5067-609-7.

10. Electrochemical behaviour of nanocrystalline states of the alloy $Ti_{60}Ni_{40}$ in 1 M HNO_3 aqueous medium
    Shubhra Mathur, Rishi Vyas, **Parul Gupta**, K. Sachdev and S. K. Sharma
    in proceedings of National Conference Emerging Interfaces of Physics and Technology, Vikram University, Ujjain (2011) 183-189.

Materials Research Express

PAPER

RECEIVED
17 March 2017

REVISED
20 April 2017

ACCEPTED FOR PUBLICATION
2 May 2017

PUBLISHED
5 June 2017

A study of oxygen gas sensing in Zn-doped SnO_2 nanostructures

Parul Gupta[1,2] **and S K Sharma**[1]

[1] Department of Physics, Malaviya National Institute of Technology, Jaipur-302 017 India
[2] Author to whom any correspondence should be addressed.

E-mail: parul.mnit@gmail.com

Keywords: XRD, nanostructures, electrical properties, gas sensing

Abstract

Sol–gel synthesis of pure and Zn-doped SnO_2 is demonstrated with variable concentration of Zn (1.5 wt%, 3 wt% and 4.5 wt%) for their potential oxygen sensing applications. X-ray diffraction measurements confirmed the tetragonal rutile type crystal structure of SnO_2 nanoparticles having particle sizes as 14 ± 1 nm, 12 ± 1 nm, 10 ± 1 nm and 9 ± 1 nm for the pure, 1.5 wt% Zn, 3 wt% Zn and 4.5 wt% Zn-doped SnO_2, respectively. The optical spectroscopy suggested an increase in the band-gap and oxygen deficiency with increase in Zn-doping in SnO_2. The *I–V* measurements yielded a high electrical resistance for 1.5 wt% Zn-doped SnO_2 as compared to other specimens. The gas sensing measurements revealed an enhanced sensitivity (37.6%) in 1.5 wt% Zn-doped SnO_2 for oxygen gas concentration in the range 5%–20% at 250 °C operating temperature in N_2 atmosphere (0.4 ± 0.03 mbar) along with reduced response time as compared to pure, 3 wt% Zn and 4.5 wt% Zn-doped SnO_2.

1. Introduction

Semiconducting metal oxides have attracted much research interest in view of their potential for technological applications in gas sensor, catalysis, solar cells, photoconductive device, liquid crystal display, gas discharge display, lithium- ion batteries etc [1–6]. It is due to their unique electrical, physical, chemical and magnetic properties in nanostructures form. Tin dioxide (SnO_2) is an n-type semiconductor, with a wide band gap ($E_g = 3.6$ eV, at 300 K). Gas sensing reactions generally take place on the surface, and thus the performance often depends on the effective surface area and surface defect concentration due to the adsorption-reaction-desorption process [7].

The semiconductor metal oxide gas sensor like SnO_2 and ZnO have been studied widely due to their response and range of conducting variability towards both the oxidizing and reducing gases. The practical performance of SnO_2 based sensors are related to its crystallinity, morphology, crystal size, presence of dopants, crystal defects and surface properties. These properties depend on the preparation methods and on conditions for specimen preparation [7, 8]. Sol–gel method is a relatively simple method for preparing chemically homogeneous, high purity nanoparticles at a comparatively lower temperature. Addition of adequate dopants drastically changes the properties, which may inhibit SnO_2 grain growth and modify the gas surface interactions [9]. Synthesis of SnO_2 nanomaterials doped with metal ions, such as Pd [10], Ni [11], Zn [12, 13] etc has been reported. Some reports suggested that the addition of cationic dopants with oxidation states lower than Sn^{4+}, such as Mn^{2+}, Cu^{2+} or Zn^{2+} produces high densification and reduced particle size [12, 14–16].

Several investigations on gas sensing behaviour studies of pure and doped SnO_2 have been reported and reviewed in the literature [17]. Zn-doped SnO_2 has been used for studying the gas sensing behaviour of both reducing and oxidizing gases, e.g. H_2 [18] and NO_2 [9]. It has been suggested that [9, 12, 19] Zn-doping (~2.6–3.0 wt% Zn) results in enhancement in conductivity improving SnO_2 gas sensing properties. To the best of our knowledge no data on gas sensing behaviour of oxygen in Zn-doped SnO_2 are available in the literature. However, oxygen gas sensing has been studied in pure SnO_2 thin film [20] and with other dopants like Li [21], Ga [22].

In the present work, pure and Zn-doped nanostructured SnO_2 powders were used for gas sensing studies. The aim of this work is to give an insight on how the Zn-doping concentrations (1.5, 3.0 and 4.0 wt%) influence the structural, optical, electrical properties and the gas sensing behaviour of SnO_2 specimens for oxygen. A part of this work relating to synthesis and characterization of specimens has earlier been reported [13].

2. Experimental

2.1. Synthesis

Nanostructured pure and Zn-doped SnO_2 powders were prepared using tin tetrachloride pentahydride ($SnCl_4 \cdot 5H_2O$) and an appropriate amount of zinc choride ($ZnCl_2$). The detailed synthesis process is reported earlier [13]. The as-synthesized nanopowders were pelletized in a hydraulic press at a pressure of 5 ton and then sintered at 400 °C in an open air tubular furnace for 3 h and the pellets were used for current–voltage (*I–V*), resistance–temperature (*R–T*) and gas sensing measurements.

2.2. Characterization

Pure and Zn-doped SnO_2 nanopowders were characterized using structural, optical and electrical characterization techniques. The crystal structure was characterized by x-ray powder diffraction (XRD) using PANalytical's X'Pert PRO-PW3040 diffractometer with Cu K_α x-ray radiation ($\lambda = 1.5406$ Å). UV–Vis and photoluminescence (PL) spectra were taken on UV-1800 spectrophotometer and Shimadzu make RF5301 PC spectrofluorophotometer (excitation wavelength 258 nm, xenon lamp), respectively.

The *I–V*, *R–T* and oxygen sensing measurements were performed by using Keithley 2400 SMU in two-point mode by sourcing voltage and measurement of current in a custom built chamber with substrate heater controlled by LabVIEW software. A precise amount of oxygen in nitrogen was administered through mass flow controllers into the chamber which is under a constant pressure maintained by a rotary pump. The electrode contacts were made using silver paste on pellets. The optimum operating temperature for sensing was chosen as 250 °C based on the poor observed response at temperatures below and above 250 °C. The gas sensing response was determined by calculating the sensitivity (S) to oxidizing gas using the expression:

$$S = (R_g - R_a)/R_a \quad (1)$$

where R_a is the resistance of the sample in air, and R_g is the resistance in the presence of test gas.

3. Results and discussion

3.1. X-ray diffraction

X-ray diffraction patterns of the pure and Zn-doped SnO_2 nanopowders with different Zn concentration i.e. 1.5 wt%, 3 wt% and 4.5 wt% are shown in figures 1(a)–(d). The XRD patterns were indexed to tetragonal rutile structure which is suggestive of the synthesis of pure SnO_2. FWHM of the diffraction peaks was found to increase with the addition of Zn, which is indicative of decrease in particle size. However, no peak pertaining to dopant Zn/ZnO phase in XRD pattern was observed.

The particle size estimated from Scherrer's formula [23] is shown in table 1. It is noteworthy here that Rozati *et al* [24] have also reported a similar decrease in particle size due to increase in Zn-doping concentration in their investigations.

3.2. Optical study

Figure 2 shows the UV–Vis spectra for pure and Zn-doped nanoparticles plotted as Tauc Plot [23] to deduce the band gap. The band gap is determined, when the straight portion of the $(\alpha h\nu)^2$ versust $h\nu$ plot is extrapolated to intersect the energy axis at $\alpha = 0$. The measured values of band gap are shown in table 1. The band gap was found to increase with increase in Zn-content in SnO_2 from 3.61 eV (pure SnO_2) to 3.78 eV (4.5 wt% Zn-doped SnO_2) and correlates with the reduced particle size as a result of Zn-doping. The increase in band gap due to reduced particle size has been attributed to quantum size effect [8, 25, 26].

Figure 3 shows PL emission spectra of nanostructured pure and Zn-doped SnO_2. The emission peak appearing in all spectra at ~367 nm is usually attributed to the free exciton electron hole recombination [25]. The broad emission peak is suggestive of the formation of oxygen deficient nanostructures SnO_2 [26].

3.3. *I–V* and *R–T* measurements

The current–voltage characteristics for pure and Zn-doped SnO_2 pellets are shown in figure 4. In the operating range of voltage and current, the current–voltage characteristics are linear, which is indicative of ohmic nature of specimens. Further, for 1.5 wt% Zn-doped SnO_2 sample a higher electrical resistance in comparison to 3 wt% Zn-doped, 4.5 wt% Zn-doped and pure SnO_2 sample is observed. Figure 5 shows resistance variation with temperature for pure and Zn-doped (1.5 wt%, 3 wt% and 4.5 wt%) SnO_2 specimens. The pure SnO_2 specimen is found to possess much lower resistance compared to doped SnO_2. It is observed from figure 5 that in 1.5 wt% Zn-doped specimens, initially the resistance decreases sharply with temperature and the rate of decrease slows down at higher temperatures. The decrease in resistance is due to the ionization of donor impurity atoms and defects present in the specimen with further increase in temperature the change in resistance becomes smaller.

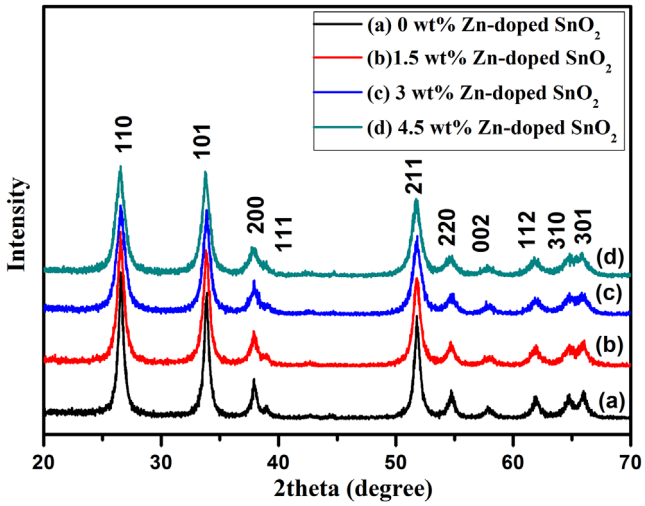

Figure 1. XRD of SnO_2 powder with (a) 0 wt% Zn, (b) 1.5 wt% Zn, (c) 3 wt% Zn, (d) 4.5 wt% Zn incorporation.

Table 1. Table showing variation in crystallite size and band gap with Zn concentration in SnO_2.

Zn-concentration in SnO_2 (wt%)	Crystallite size (nm)	Band-gap (E_g) (eV)
Pure	14 ± 1	3.61
1.5	12 ± 1	3.71
3	10 ± 1	3.75
4.5	9 ± 1	3.78

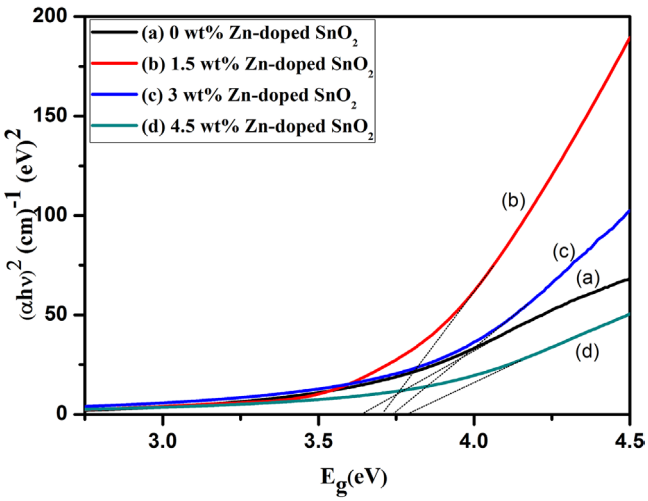

Figure 2. Tauc plot of SnO_2 powder with (a) 0 wt% Zn, (b) 1.5 wt% Zn, (c) 3 wt% Zn, (d) 4.5 wt% Zn incorporation.

In the operating temperature region, the good thermal stability has been suggested by *R–T* measurements [19]. Decrease in resistance with increase in temperature (above 50 °C), has also been attributed to negative temperature coefficient and semiconducting nature of pure and Zn-doped SnO_2 nanopowders [27].

3.4. Gas sensing measurements

As SnO_2 is an n-type semiconductor, its gas sensing characteristics originate from the reaction between the testing gases and the chemisorbed oxygen ions on the surface of SnO_2 nanoparticles, such as O_2^-, O^-, O^{2-} [28]. When O_2 in air is adsorbed on the surface of SnO_2 nanoparticles, the electrons in the specimens will be captured by oxygen species, reducing the charge carrier concentration and the conductivity of the specimens.

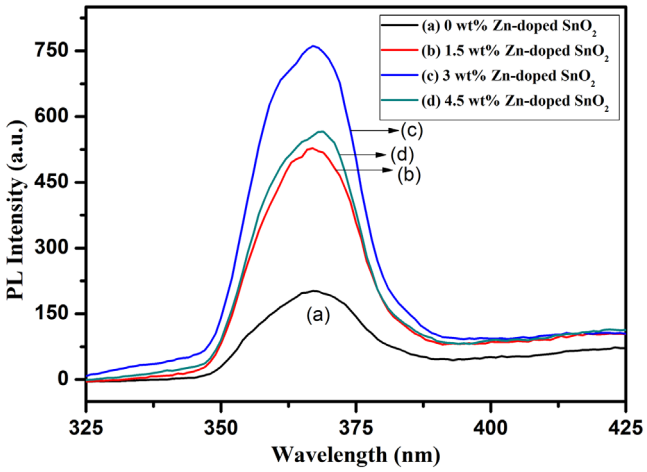

Figure 3. PL spectra of Zn-doped SnO_2 powder with (a) 0 wt% Zn (b) 1.5 wt% Zn (c) 3 wt% Zn (d) 4.5 wt% Zn incorporation.

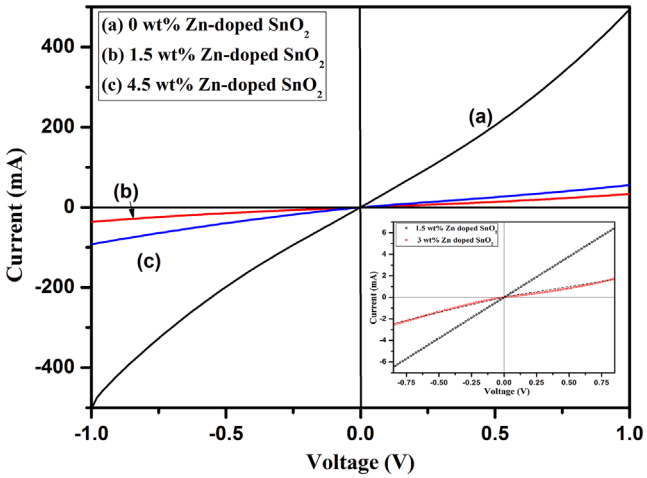

Figure 4. *I–V* measurements of SnO_2 samples with (a) 0 wt% Zn, (b) 1.5 wt% Zn, (c) 3 wt% Zn, (d) 4.5 wt% Zn incorporation.

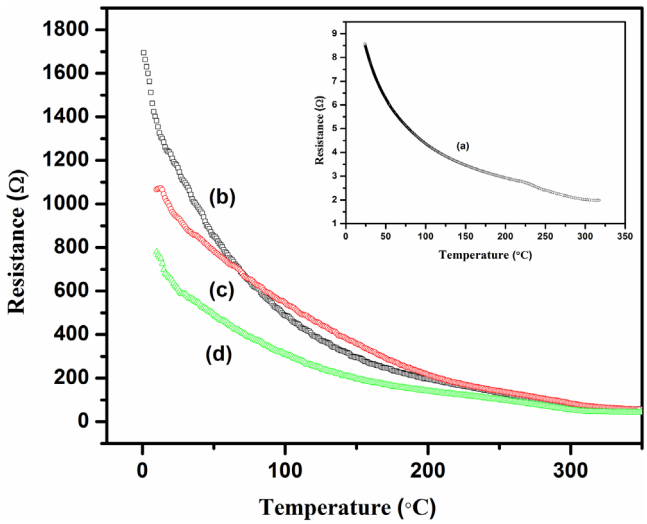

Figure 5. *R–T* measurements of Zn-doped SnO_2 samples with (a) 0 wt% Zn, (b) 1.5 wt% Zn, (c) 3 wt% Zn, (d) 4.5 wt% Zn incorporation.

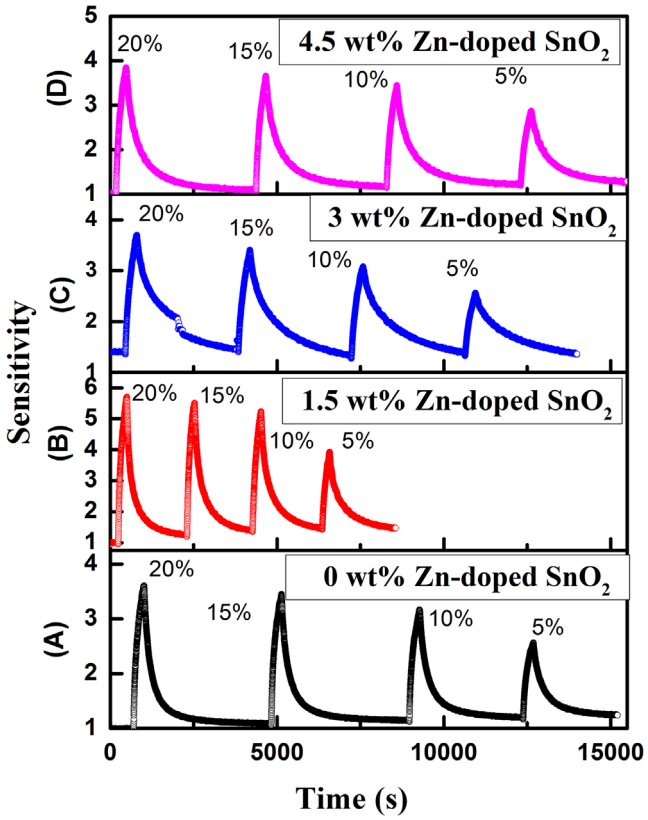

Figure 6. Gas sensing curves of Zn-doped SnO_2 samples for O_2 gas.

If the specimen is exposed to oxidizing gases, these gases can react with the oxygen species, and released electron is trapped by the oxygen species back to nanoparticles, resulting in the increase in resistance. Figure 6 shows the gas sensing characteristics of Zn-doped SnO_2 samples for O_2 gas (5% to 20%) at the operating temperature of 250 °C in N_2 atmosphere at (0.4 ± 0.03 mbar) pressure. These curves show increase in sensitivity as specimens are exposed to O_2 gas. For O_2 (5%–20%) exposure, sensitivity is found to increase with increase in in 1.5 wt% Zn doped specimen and the sensitivity decreases with further addition of Zn (3 wt% and 4.5 wt%) in SnO_2. The decrease in gas response for higher Zn concentration (3 wt% and 4.5 wt%) could be attributed to the fact that Zn atoms are most likely present in elemental form at grain boundaries, thus reducing the adsorption sites for gas sensing. This is supported by the observed decrease in resistance also for this specimen shown in figure 5. Thus, the 1.5 wt% addition of Zn in SnO_2 is observed to be most effective for enhancement in sensitivity for O_2 gas sensing among these Zn-doped SnO_2.

Response time for pure SnO_2, 1.5 wt% Zn-doped SnO_2, 3 wt% Zn-doped SnO_2 and 4.5 wt% Zn-doped SnO_2 are 152 s, 141 s, 172 s and 188 s, respectively. Recovery time for pure, 1.5 wt% Zn-doped SnO_2, 3 wt% Zn-doped SnO_2 and 4.5 wt% Zn-doped SnO_2 are 1011 s, 941 s, 1255 s and 1505 s, respectively. Thus response and recovery time are smaller for 1.5 wt% Zn-doped SnO_2 samples as compared to pure SnO_2, 3 wt% Zn-doped SnO_2 and 4.5 wt% Zn-doped SnO_2. From these measurements it is concluded that sensitivity is maximum for 1.5 wt% Zn doping with reduced response and recovery time, thus suggesting that 1.5 wt% Zn-doped samples exhibit good sensing behaviour for oxygen. It is worth mentioning here that no data on gas sensing behaviour of oxygen in Zn-doped SnO_2 are available in literature. However, Zn-doping has been found to increase the sensitivity in the case of an oxidizing gas NO_2 [9]. There are several studies of SnO_2 based gas sensors for the gas sensing behaviour where addition of dopant leads to increase in sensitivity of oxidizing gas NO_2 e.g.: In [29], ZnO [30], Fe_2O_3 [31] and Ru [32].

4. Conclusions

Pure SnO_2, 1.5 wt% Zn-doped SnO_2, 3 wt% Zn-doped SnO_2 and 4.5 wt% Zndoped SnO_2 nanopowders were synthesized by sol–gel method. With increase in doping concentration the size of crystallites decreases from 14 ± 1 nm to 9 ± 1 nm. UV–Vis spectroscopy suggested that the band gap increases with Zn-doping in SnO_2. Zn-doped specimens have low conductivity and good thermal stability at the operating temperature of 45 °C to 275 °C as suggested by *I–V* and *R–T* measurements. The Zn-doped specimens were tested for O_2 exposure for

their gas sensing application at operating temperature of 250 °C in N_2 atmosphere. The 1.5 wt% addition of Zn in SnO_2 is observed to be most effective for enhancement in sensitivity for O_2 gas sensing among pure and 3.0 wt% and 4.5 wt% Zn-doped SnO_2.

Acknowledgments

PG acknowledges DST-INSPIRE program of the Department of Science and Technology, Government of India, New Delhi for providing the research fellowship. PG is grateful to Mr Vikas Sharma (MNITJ) for optical analysis. The authors acknowledge facilities provided for characterization of specimens at University of Rajasthan, Jaipur.

References

[1] Radecka M, Przewoznik J and Zakrzewska K 2001 Microstructure and gas-sensing properties of (Sn,Ti) O_2 thin films deposited by RGTO technique *Thin Solid Films* **391** 247–54
[2] Pinna N, Neri G, Antonietti M and Niederberger M 2004 Nonaqueous synthesis of nanocrystalline semiconducting metal oxides for gas sensing *Angew. Chem., Int. Ed.* **43** 4345–9
[3] Miyauchi M, Nakajima A, Watanabe T and Hashimoto K 2002 Photocatalysis and photoinduced hydrophilicity of various metal oxide thin films *Chem. Mater.* **14** 2812–6
[4] Margalith T *et al* 1999 Indium tin oxide contacts to gallium nitride optoelectronic devices indium tin oxide contacts to gallium nitride optoelectronic devices **3930** 26–9
[5] Morales J, Vicente C P, Santos J and Tirado J L 1996 Electrochemical characteristics of crystalline and amorphous SnS_2 in lithium cells *J. Electrochem. Soc.* **143** 2847
[6] Sharma V, Vyas R, Bazylewski P, Chang G S, Asokan K and Sachdev K 2016 Probing the highly transparent and conducting SnO_x/Au/SnO_x structure for futuristic TCO *RSC Adv.* **6** 29135–41
[7] Huang H, Tian S, Xu J, Xie Z, Zeng D, Chen D and Shen G 2012 Needle-like Zn-doped SnO_2 nanorods with enhanced photocatalytic and gas sensing properties *Nanotechnology* **23** 105502
[8] Gajendiran J and Rajendran V 2011 Size controlled and optical properties of Zn-doped SnO_2 nanoparticles via sol–gel process *Optoelectron. Adv. Mater. Commun.* **5** 44–8
[9] Bari R H and Patil S B 2015 Improved NO_2 sensing performance of nanostructured Zn doped SnO_2 thin films *Int. J. TechnoChem Res.* **1** 86–96
[10] Tsang S C, Bulpitt C D A, Mitchell P C H and Ramirez-Cuesta A J 2001 Some new insights into the sensing mechanism of palladium promoted tin (IV) oxide sensor *J. Phys. Chem.* B **105** 5737–42
[11] Hidalgo P, Castro R H R, Coelho A C V and Gouvêa D 2005 Surface segregation and consequent SO_2 sensor response in SnO_2–NiO *Chem. Mater.* **17** 4149–53
[12] Kumar M 2015 Gas sensing properties of Zn-doped tin oxide nanoparticles with methanol *Indian J. Appl. Res.* X **507** 2249–555
[13] Gupta P, Vyas R, Choudhary B L, Sachdev K, Patil D S and Sharma S K 2013 Synthesis and characterization of pure and Zn-doped SnO_2 nanopowders *Int. J. Mod. Phys. Conf. Ser.* **22** 452–7
[14] Wang W, Tian Y, Li X, Wang X, He H, Xu Y and He C 2012 Enhanced ethanol sensing properties of Zn-doped SnO_2 porous hollow microspheres *Appl. Surf. Sci.* **261** 890–5
[15] Benzitouni S *et al* 2016 High sensitivity of porous Cu-doped SnO_2 thin films to methanol *Adv. Nanopart.* **5** 140–8
[16] Scarlat O, Mihaiu S, Aldica G, Groza J and Zaharescu M 2004 Semiconducting densified SnO_2-ceramics obtained by a novel sintering technique *J. Eur. Ceram. Soc.* **24** 1049–52
[17] Das S and Jayaraman V 2014 SnO_2: a comprehensive review on structures and gas sensors *Prog. Mater. Sci.* **66** 112–255
[18] Sakaguchi I, Saito N, Watanabe K, Adachi Y and Suzuki T T 2016 Evaluation of sensor property for hydrogen and ethanol of zinc-doped tin-dioxide thin films fabricated by RF sputtering *J. Ceram. Soc. Japan* **124** 714–6
[19] Rai R 2010 Study of structural and electrical properties of pure and Zn–Cu doped SnO_2 *Adv. Mater. Lett.* **1** 55–8
[20] Cukrov L M, McCormick P G, Galatsis K and Wlodarski W 2001 Gas sensing properties of nanosized tin oxide synthesised by mechanochemical processing *Sensors Actuators* B **77** 491–5
[21] Sberveglieri G, Faglia G, Groppelli S, Nelli P and Perego C 1993 Oxygen gas sensing properties of undoped and Li-doped SnO_2 thin films *Sensors Actuators* B **13–4** 117–20
[22] Tiburcio-Silver A and Sánchez-Juárez A 2004 SnO_2:Ga thin films as oxygen gas sensor *Mater. Sci. Eng.* B **110** 268–71
[23] Gaidi M, Hajjaji A, Smirani R, Bessais B and El Khakani M A 2010 Structure and photoluminescence of ultrathin films of SnO_2 nanoparticles synthesized by means of pulsed laser deposition *J. Appl. Phys.* **108** 63537
[24] Rozati S M and Shadmani E 2011 Effect of Zn concentration on physical properties of nanostructure tin oxide films prepared by spray pyrolysis technique *Dig. J. Nanomater. Biostruct.* **6** 365–72
[25] Tan L, Wang L and Wang Y 2011 Hydrothermal synthesis of SnO_2 nanostructures with different morphologies and their optical properties *J. Nanomater.* **2011** 1–10
[26] Mondal S P, Ray S K, Ravichandran J and Manna I 2010 Temperature dependent growth and optical properties of SnO_2 nanowires and nanobelts *Bull. Mater. Sci.* **33** 357–64
[27] Parthibavarman M, Hariharan V, Sekar C and Singh V N 2010 Effect of copper on structural, optical and electrochemical properties of SnO_2 nanoparticles *J. Optoelectron. Adv. Mater.* **12** 1894–8
[28] Law M, Kind H, Messer B, Kim F and Yang P 2002 Photochemical sensing of NO_2 with SnO_2 nanoribbon nanosensors at room temperature *Angew. Chem., Int. Ed.* **41** 2405
[29] Kaur J, Kumar R and Bhatnagar M C 2007 Effect of indium-doped SnO_2 nanoparticles on NO_2 gas sensing properties *Sensors Actuators* B **126** 478–84
[30] Hwang I-S, Kim S-J, Choi J-K, Choi J, Ji H, Kim G-T, Cao G and Lee J-H 2010 Synthesis and gas sensing characteristics of highly crystalline ZnO–SnO_2 core–shell nanowires *Sensors Actuators* B **148** 595–600
[31] Rumyantseva M, Kovalenko V, Gaskov A, Makshina E, Yuschenko V, Ivanova I, Ponzoni A, Faglia G and Comini E 2006 Nanocomposites SnO_2/Fe_2O_3: sensor and catalytic properties *Sensors Actuators* B **118** 208–14
[32] Ramgir N S, Mulla I S and Vijayamohanan K P 2005 A room temperature nitric oxide sensor actualized from Ru-doped SnO_2 nanowires *Sensors Actuators* B **107** 708–15

A Comparative Study of the Sol-Gel Synthesized Nanostructured SnO_2 Powders

Parul Gupta[1,*], Rishi Vyas[1], B. L. Choudhary[2], K.V. R. Rao[2], K. Sachdev[1], D. S. Patil[3] and S. K. Sharma[1]

[1]*Department of Physics, Malaviya National Institute of Technology, Jaipur-302 017 (INDIA)*
[2]*Department of Physics, University of Rajasthan, Jaipur- 302 004 (INDIA)*
[3]*Laser & Plasma Technology Division, BARC, Trombay, Mumbai -400 085 (INDIA)*
** Email.: parul.mnit@gmail.com*

Abstract. SnO_2 nanopowders were synthesized by different sol-gel preparation methods using $SnCl_4.5H_2O$ and variable concentration of ammonia water as precursor in different solvents in order to obtain different particle size for their gas sensing applications. These nanopowders were characterized by X- ray diffraction (XRD), Scanning electron microscopy (SEM), UV-Vis spectroscopy and PL spectroscopy. XRD study confirmed the formation of SnO_2 nanoparticles and particle size was estimated using Scherrer's formula. SEM micrographs also suggested the formation of well crystallized, finer grain size and slightly agglomerated nanoparticles. UV-Vis spectroscopy was used to deduce the band gap of nanostructured SnO_2. PL spectroscopy suggested the formation of oxygen deficient nanostructured SnO_2. A comparative study of these measurements carried out on synthesized SnO_2 nanopowders by different methods, in order to obtain suitable properties for their gas sensing applications, is presented and discussed in the paper.

Keywords: SnO_2, nanopowder, XRD, sol-gel route.
PACS: 81.05 Je, 81.07 Wx, 61.05 Cp, 81.20 Fw.

INTRODUCTION

Tin dioxide (SnO_2) is a wide band gap n - type semiconducting material. It has been widely studied over decades because of its wide range of applications as gas sensors, solar cells, transistors, electrodes, LCDs and catalysts [1]. Nanoparticles of SnO_2 have mostly been produced by sol-gel, spray pyrolysis, solvothermal and microwave methods [2-3]. In the present work we have employed sol-gel method, which is simple, inexpensive and offers ability to control the grain size, to synthesize nanoparticles of SnO_2. The objective of the work focused on the comparative study of the structural and optical properties of SnO_2 nanopowders prepared by different routes along with the commercially available SnO_2 (Alfa Aesar-99.99%).

EXPERIMENTAL PROCEDURE

The following routes were employed to synthesize nanostructured SnO_2 powder:

1. Optimized quantity of ammonia water is added to the 0.1 M $SnCl_4.5H_2O$ and hence a precipitate is obtained which further filtered/dried [4].
2. 0.1 M $SnCl_4.5H_2O$ in 50 ml D. I. water and ethylene glycol mixture were mixed as 1:1 and an optimized quantity of 0.1 M ammonia water was added to the above solution. The resulting gel was filtered/dried [5].
3. 0.1 M $SnCl_4.5H_2O$ was neutralized with aqueous NH_3 solution to obtain a precipitate. The resulting precipitate was filtered/ dried [6].

SnO_2 powders as synthesized by the above methods were annealed at 600°C for 3 hours.

The crystalline structure of SnO_2 nanopowders was characterized by XRD using PANalytical's X'Pert PRO- PW3040 Diffractometer with CuKα X-ray radiation (λ = 1.5406 Å) . The SEM images were recorded by ZEISS make EVO18 model. UV-Vis measurements were made with a UV-1800 spectrophotometer. PL measurements were carried out at RT using 275 nm as excitation wavelength with a Shimadzu make RF5301 PC spectrofluorophotometer.

RESULTS AND DISCUSSION

Fig. 1 shows the XRD patterns of differently synthesized SnO_2 nanopowders. All of the peaks in the XRD spectra were indexed to tetragonal rutile structure which is suggestive of the synthesis of pure nanostructured SnO_2. No characteristic peaks of other impurities were observed, indicating that the product has high purity. The crystallite size was estimated using the Scherrer's formula [7] and is given in Table 1.

Proceeding of International Conference on Recent Trends in Applied Physics and Material Science
AIP Conf. Proc. 1536, 159-160 (2013); doi: 10.1063/1.4810149

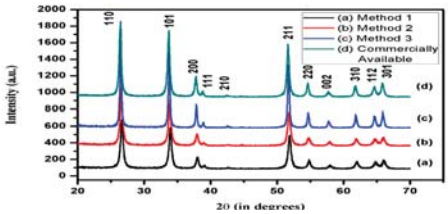

FIGURE 1. XRD of pure SnO_2 powder prepared by three different methods (1-3) and compared to the commercially available SnO_2 nanopowder

SEM micrographs of pure SnO_2 pellets are shown in Fig. 2. As shown in Fig. 2 (a) and 2 (b), the as synthesized samples consist of fine tiny nanoparticles, seem to be well crystallized with slightly agglomerated nanoparticles having small crystallite size. SEM micrograph of Method 3 showed similar morphology as Fig. 2 (a), with comparatively larger grains.

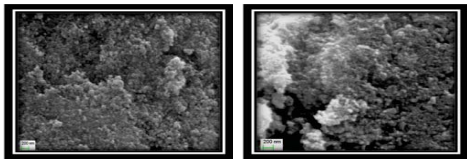

(a) Method 1 (b) Method 2

FIGURE 2. SEM micrograph of SnO_2 nanopowder synthesized by (a) method 1, (b) method 2

UV-Vis and PL spectroscopy were used to characterize the optical properties of SnO_2 nanopowders. UV-Vis spectroscopy gave the optical absorption spectra of SnO_2 nanoparticles. Fig. 3(A) shows the Tauc plot [7] of pure SnO_2 nanopowders. The band gap for each specimen, given in Table 1, is found to be particle size dependent. The increase in band gap with decrease in particle size has been attributed to quantum size effect [8].

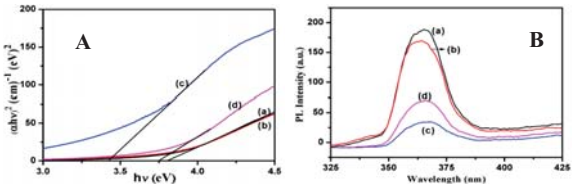

FIGURE 3. Tauc Plot (A) and PL spectra (B) of SnO_2 nanopowders synthesized by (a) method 1, (b) method 2, (c) method 3, (d) commercially available

Fig. 3(B) shows PL emission spectra, the emission peak appearing in all spectra at ~ 366 nm is usually attributed to the free exciton electron hole recombination [8]. The broad emission peak is suggestive of the formation of oxygen deficient nanostructured SnO_2 [9]. It also has been found that as the particle size increases the PL intensity decreases. It is noted here that method 1 and 2 yielded almost same particle size while method 3 gave larger sized nanoparticles of SnO_2 after the same annealing treatment at 600°C. Further, it was relatively easier to synthesize SnO_2 nanopowder using method 1 in comparison to method 2 and 3. In addition, the particle size control was found to be much better in case of method 1 during repeated synthesis of SnO_2.

TABLE 1. Crystallite size & band gap estimation using Scherrer's Formula & UV-Vis respectively

Method	Crystallite size	E_g using UV-Vis
1.	17~ 18 nm	3.78 eV
2.	18~ 19 nm	3.78 eV
3.	32~35 nm	3.40 eV
Co. Available	21~22 nm	3.75 eV

CONCLUSIONS

Pure SnO_2 nanopowders were successfully synthesized by different sol-gel routes. It is found that the samples have tetragonal rutile structure with no impurity. Surface morphology of pellets showed fine tiny nanoparticles, with slight agglomeration. UV-Vis spectroscopy suggested the band gap, which increases with decreasing particle size. Among all three routes employed for synthesis, method 1 showed better control over particle size in repeated synthesis.

ACKNOWLEDGMENTS

Authors (PG & RV) are grateful to the DST-INSPIRE and DAE/BRNS for providing the financial support.

REFERENCES

1. Radheshyam Rai, *Advd. Maters. Letters*, **1** 55-58 (2010).
2. J.Gajendiran, V. Rajendran, *Optoelec. Advd. Maters*., **5 (1)** 44-48 (2011).
3. J. Kaur, R. Kumar, M.C. Bhatnagar, *Sens. Actuators B,* **126** 478-484 (2007).
4. R.C. Singh, M.P. Singh, O. Singh, P.S. Chandi, *Sens. Actuators B*, **143** 226-232 (2009).
5. S. Gnanam, V. Rajendran, *Digest J. of Nanomaterials & Biostructures,* **5(3)** 699-704 (2010).
6. G.S. Devi, S. Manorama, V.J. Rao, *Sens. Actuators B,* **28** 31-37 (1995).
7. M.Gaidi, A. Hajjaji, R.Smirani, B.Bessais, M.A. El Khakni, *J. Applied Phys.* **108** 063537 (2010).
8. L. Tan, L. Wang, Y. Wang, *Hindawi Pub. Corp., J. Nanomaterials* (2011).
9. S.P. Mondal, S.K. Ray, J. Ravichandran, I. Manna, *Bull. Mater. Sci.*, **33** 357-364 (2010).

International Conference on Ceramics, Bikaner, India
International Journal of Modern Physics: Conference Series
Vol. 22 (2013) 452–457

DOI: 10.1142/S2010194513010507

SYNTHESIS AND CHARACTERIZATION OF PURE AND Zn-DOPED SnO_2 NANOPOWDERS

PARUL GUPTA

Department of Physics, Malaviya National Institute of Technology, JLN Marg, Jaipur, Rajasthan 302017, India
parul.mnit@gmail.com

RISHI VYAS

Department of Physics, Malaviya National Institute of Technology, JLN Marg, Jaipur, Rajasthan 302017, India
mail2rishivyas@gmail.com

B. L. CHOUDHARY

Department of Physics, University of Rajasthan, Jaipur, Rajasthan 302004, India
blcphysics@gmail.com

K. SACHDEV

Department of Physics, Malaviya National Institute of Technology, JLN Marg, Jaipur, Rajasthan 302017, India
sach_kanu@yahoo.co.in

D. S. PATIL

Department of Laser & Plasma Technology Division, BARC, Trombay, Mumbai -400085, India
dspatil@barc.gov.in

S. K. SHARMA

Department of Physics, Malaviya National Institute of Technology, JLN Marg, Jaipur, Rajasthan 302017, India
sksh@aol.in

Pure and 4.5 wt% Zn- doped SnO_2 nanopowders were synthesized by sol-gel method. These nanopowders were characterized by X- ray diffraction, Scanning electron microscopy, UV-Vis spectroscopy, I-V measurements and R-T measurements. XRD results confirmed the formation of tetragonal rutile type SnO_2 with the average crystallite size of 14 ± 1 nm which decreased to 9 ± 1 nm with 4.5 wt% Zn addition. Increase in band gap is observed from UV-Vis spectroscopy. Electrical characterizations revealed increase in resistivity with Zn addition. Temperature dependent resistance measurement showed that both the pure and the Zn- doped samples are suitable for gas sensing applications. A detailed study of these synthesized nanostructured samples is presented and discussed in the paper.

Keywords: SnO_2; nanopowder; sol-gel route.

1. Introduction

Nanostructured metal oxides have attracted an extensive research interest due to their unique electrical, physical, chemical and magnetic properties as well as their potential for technological applications[1]. Tin oxide (SnO_2) is a wide band gap (E_g = 3.6 eV, at 300K) semiconductor with n-type conduction due to the existence of intrinsic defects and has been widely used in many fields, such as gas sensors[2], catalysis[3], optoelectronics[4].

It is generally accepted that the practical performances of SnO_2 based sensors are relative to its crystallinity, morphology, crystal size, presence of dopants, crystal defects and surface properties, etc., which ultimately depend on the preparation methods and conditions [5]. Among all processes for synthesis of SnO_2 nanostructures sol-gel[5, 6] method is a relatively simple way of preparing chemically homogeneous, high purity nanoparticles at lower temperatures. It has been found that some properties can be drastically changed by the addition of adequate dopants. Synthesis of SnO_2 nanomaterials doped with metal ions, such as Zn[7-10], Pd[11], Ni[12] etc. has been reported.

In the present work, pure and Zn (4.5 wt%)- doped nanostructured SnO_2 powders were synthesized using sol-gel process. The aim of this work is to give an insight on how the Zn- doping influence the structure, optical and electrical properties of the SnO_2 nanopowder. Other reports[9-10] on Zn- doping (~ 2.6 - 3wt % Zn) suggested that addition of Zn improves the SnO_2 properties with low electrical conductivity. The selection is based on ionic radius of Sn^{4+} (r = 0.71Å) and Zn^{2+} (r = 0.74 Å) which are close to each other and with the substitution of Sn^{4+} ions with Zn^{2+} ions, the broken bond is produced, which acts as acceptor energy level near the valence band. These levels accept electrons from the valence band and thus increase the hole concentration or p- type conductivity[8].

2. Experimental

For the preparation of nanostructured SnO_2 powder, a very small quantity of hydrochloric acid was added to $SnCl_4$ solution to prevent it from rapid hydrolysis. The aqueous ammonia solution was added drop-wise into the aforesaid solution under vigorous stirring at room temperature till the pH of the solution reaching about 2.8. The resultant white solution was heated at 60°C for 30 min under vigorous stirring. After aging for two days, the gel was filtered /washed and dried. Then the final product was annealed at 600°C for 2 hours.

For preparation of Zn- doped SnO_2 nanopowder, an appropriate amount of $ZnCl_2$ was added to the pH balanced solution and mixture was stirred for 2 hours at 60°C before aging[5], rest procedure is same as pure SnO_2. The as synthesized nanopowders were pelletized using hydraulic press machine.

The crystalline structure of both pure and doped SnO_2 nanopowders was characterized by X-ray powder diffraction (XRD). XRD pattern was collected using PAN alytical's X'Pert PRO-PW3040 diffractometer with CuK_α X-ray radiation (λ = 1.5406 Å). The morphology of the sample was recorded using ZEISS make EVO18 model Scanning Electron Microscope (SEM). UV-Vis measurements were made with a UV-1800

spectrophotometer. The I-V and R-T measurements were performed by using Keithley 2400 SMU in a custom built chamber.

3. Results and Discussion

The XRD patterns of the as-synthesized pure and Zn- doped SnO_2 nanopowders are shown in Fig. 1 (a-b). The XRD patterns of samples exhibited sharp diffraction peaks, which indicate a good crystallinity of the samples. All of the peaks in the spectrum [Fig. 1 (a)] were indexed to tetragonal rutile structure which is suggestive of the synthesis of pure SnO_2 powder. The addition of Zn (4.5 wt%) was found to increase the FWHM of diffraction peaks [Fig. 1 (b)] which is indicative of decrease in particle size. Moreover, XRD pattern did not exhibit any additional peak pertaining to Zn/ ZnO phase as shown in Fig. 1. The crystallite size was estimated by the peak width with using the Scherrer's formula[13].

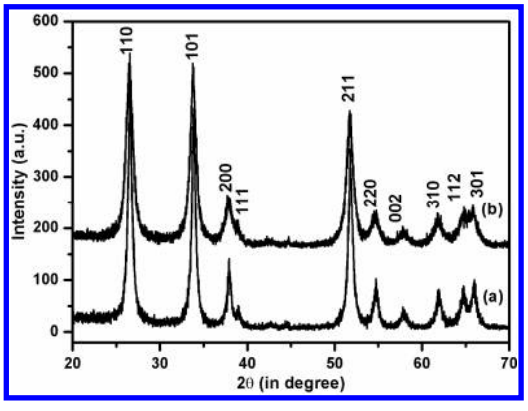

Fig. 1: XRD pattern of (a) Pure and (b) Zn- doped SnO_2 powder

The crystallite size in pure SnO_2 was found to be 14 ± 1 nm, and it decreased to 9 ± 1 nm in Zn- doped SnO_2. Rozati et al.[7] have also reported a decrease in crystallite size in SnO_2 specimens after Zn- doping.

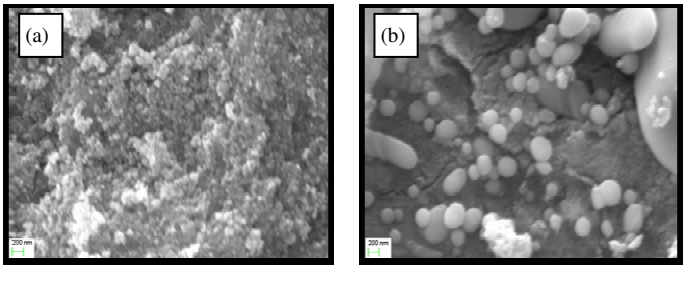

Fig. 2: SEM micrograph (a) Pure and (b) Zn- doped SnO_2 powder

Fig. 2 shows the SEM micrographs of pure and Zn- doped SnO_2 pellets made from pure and Zn- doped SnO_2 nanopowders. As shown in Fig. 2 (a), the as synthesized sample consists of fine tiny nanoparticles which are pressed down, and the surface of the pellet is approximately homogeneous with some agglomerates. In Fig. 2(b) Zn- doping is observed to introduce unique surface morphology consisting of globules agglomerates in Zn- doped SnO_2 pellets. Similar type of unique structures have also been reported in other studies[7, 14] on Zn- doping in SnO_2. These unique structures are expected to grow during post annealing process.

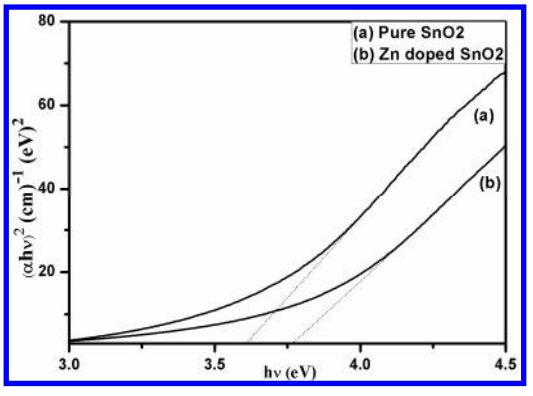

Fig. 3: Tauc Plot of Pure and Zn- doped SnO_2 powder

Fig. 3 shows the Tauc plot[13] of the pure and the Zn- doped SnO_2 nanoparticles. The band gap is found to increase with Zn- content in SnO_2 from 3.6 eV (pure SnO_2) to 3.78 eV (Zn-doped SnO_2). The increase in band gap might have resulted from the reduced particle size which is a common result due to quantum size effect[5, 15 - 16].

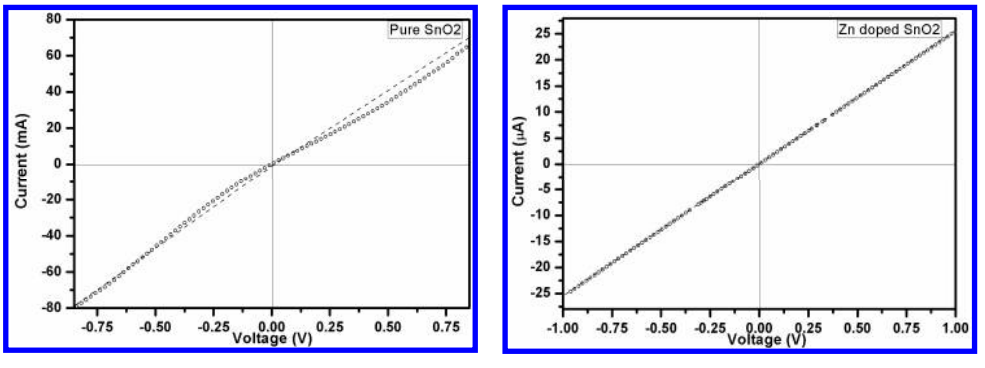

(a) (b)

Fig. 4: I-V measurements of (a) Pure SnO_2 and (b) Zn- doped SnO_2 samples

The current-voltage characteristics for pure and Zn- doped SnO_2 pellets are shown in Fig. 4. The current–voltage characteristics are almost linear in the operating range of voltage and current, which is indicative of ohmic nature. Further, in pure SnO_2 to Zn-doped specimens the resistance of the samples is found to increase from ~ 15 Ω to ~38 KΩ at room temperature.

Fig. 5 shows resistance variation with temperature for pure and Zn- doped SnO_2 specimens. In pure SnO_2 specimens the resistance of sample decreases very slowly with temperature and at high temperatures a faster decrease is seen. But, in Zn- doped specimen, initially the resistance decreases sharply with temperature and the rate of decrease slows down at higher temperatures. It is most likely due to result of the ionization of donor impurity atoms and defects present in the specimen, and consequently with further increase in temperature the change in resistance becomes smaller. It has been reported[17] that electrons of donor level are ionized completely, and the electronic concentration of intrinsic excitation is less than the concentration of donor at this temperature region with increasing temperature. R-T measurements suggest that the samples have good thermal stability in the operating temperature region[9]. The decrease in resistance with increase in temperature (above 45°C) could also be attributed to negative temperature coefficient and semiconducting nature of pure and Zn- doped SnO_2 nanopowder[18]. It is worth mentioning from the data reported here that 4.5 wt% Zn- doped SnO_2 showing a large increase in resistivity and good thermal stability may depict interesting behavior in gas sensing applications.

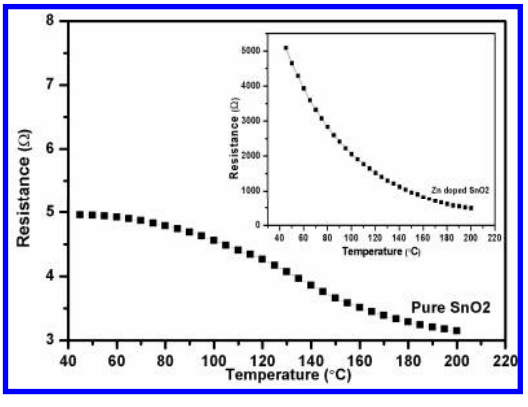

Fig. 5: R-T measurements of Pure and Zn- doped SnO_2 samples

4. Conclusions

Pure and 4.5 wt % Zn- doped SnO_2 nanopowders with tetragonal phase were synthesized by sol-gel method. It is found that the phase of the sample does not change with the introduction of 4.5 wt % Zn, but the crystallite size decrease from 14 ± 1 nm to 9 ± 1 nm. Surface morphology of pellets showed fine tiny nanoparticles, with certain clustering and agglomeration. UV-Vis spectroscopy suggested the band gap, which decreases with Zn-

doping. From I-V and R-T measurements it is found that Zn- doped specimens have low conductivity and good thermal stability at the operating temperature of 45°C to 200°C.

Acknowledgments

Authors (PG & RV) are grateful to the DST-INSPIRE and DAE/BRNS for providing the financial support.

References

1. H. J. Ahn, H. C. Choi, K. W. Park, S. B. Kim and Y. E. Sung, J. of Physical Chem. B **108** (28), 9815 (2004).
2. N. Pinna, G. Neri, M. Antonietti and M. N. Angewandte, Chemie Int. Edn. **43**, 4345 (2004).
3. M. Miyauchi, A. Nakajima, T. Watanable and K. Hashimoto, Chem. of Mater. **14**, 2812 (2002).
4. J.W. Mayer and T.L. Alford, J.App. Phy. **98**, 083705 (2005).
5. J. Gajendiran and V. Rajendran, Optoelectro. & Adv. Mater.- Rapid Comm. **5** (1), 44 (2011).
6. C. Terrier, J. P. Chatelon, R. Berjoan and J. A. Roger, Thin Solid Films, **263** (1), 37 (1995).
7. S.M. Rozati and E. Shadmani, Dig. J. Nanomaterials & Biostructures **6**(2), 365 (2011).
8. J. S. Bhat, K. I. Maddani and A.M. Karguppikar, Bull. Mater. Sci. **29** (3), 331(2006).
9. Radheshyam Rai, Adv. Mat. Lett. **1**(1), 55 (2010).
10. I. Saadeddin, H.S. Hilal, B. Pecquenard, J. Marcus, A. Mansouri, C. Labrugere, M.A. Subramanian and G. Campet, Solid State Sci. **8,** 7 (2006).
11. S. C. Tsang, C. D. A Bulpitt, P. C. H. Mitchell and A. J. Ramirez-Cuesta, J. Phys. Chem. B **105**, 5737 (2001).
12. P. Hidalgo, R. H. R Castro, A. C. V. Coelho and D. Gouvea, Chem. Mater. **17**, 4149 (2005).
13. M.Gaidi, A. Hajjaji, R.Smirani, B.Bessais and M.A. El Khakni, J. App. Phys. **108**, 063537, (2010).
14. N.D. Md Sin, M.H. Mamat, M.Z. Musa, Abdul Aziz A. and M.Rusop, IEEE – BEIAC (2012).
15. L. Tan, L. Wang and Y. Wang, Hindawi Pub. Corp., J. Nanomaterials, (2011).
16. S.P. Mondal, S.K. Ray, J. Ravichandran and I. Manna, Bull. Mater. Sci., **33**, 357 (2010).
17. A.C. Bose, P. Balaya, P. Thangaduri and S.J. Ramasamy, Phys. Chem Solids **64**, 259 (2003).
18. M. Parthibavarman, V. Hariharan, C. Sekar and V. N. Singh, J. of Optoelectro. Adv. Mater. **12** (9), 1894 (2010).

Effect of Temperature on Synthesis and Gas Sensing of Nanostructured SnO_2

Authors: Gupta, Parul; Sharma, S. K
Source: Advanced Science Letters, Volume 22, Number 11, November 2016, pp. 3743-3746(4)
Publisher: American Scientific Publishers
DOI: https://doi.org/10.1166/asl.2016.8070

Nanoparticles of SnO_2 have been synthesized using the sol–gel method. In this work, the growth of nanoparticles has been investigated at different annealing temperatures (ranging from 600 °C to 900 °C). Their structural and morphological analysis was carried out by using X-ray diffraction (XRD) and scanning electron microscopy (SEM). XRD results showed that the nanoparticles are highly crystalline with tetragonal rutile phase. The degree of crystallinity and grain size calculated from the XRD patterns has been found to be increasing with annealing temperature. The annealing temperature has been found to be playing a critical role of controlling nanostructure size. The SEM micrographs revealed the growth of nanoparticles at different annealing temperatures. UV-Vis spectroscopy has been used to deduce the band gap of nanostructured SnO_2. These pellets were tested for current–voltage (*I–V*) measurements and also tested for gas sensing of H_2 (1%) gas at an operating temperature of 300 °C. The investigations show that the sensing response of specimens is size dependent. A detailed study of these synthesized nanostructured samples is presented and discussed in the paper.

Keywords: Annealing; Gas Sensing; Nanoparticles; Recovery; Resistance; Response; SEM; Sensitivity; SnO2; Sol-Gel; XRD

Document Type: Research Article

Affiliations: Department of Physics, Malaviya National Institute of Technology Jaipur 302017, Rajasthan, India

Publication date: November 1, 2016